



HAL
open science

Analyse InSAR des déformations de volcans actifs: le Piton de la Fournaise (Réunion) et le Llaima (Chili)

Yu Chen

► **To cite this version:**

Yu Chen. Analyse InSAR des déformations de volcans actifs: le Piton de la Fournaise (Réunion) et le Llaima (Chili). Volcanologie. Université Toulouse 3 Paul Sabatier (UT3 Paul Sabatier), 2017. Français. NNT: . tel-01501284

HAL Id: tel-01501284

<https://theses.hal.science/tel-01501284>

Submitted on 4 Apr 2017

HAL is a multi-disciplinary open access archive for the deposit and dissemination of scientific research documents, whether they are published or not. The documents may come from teaching and research institutions in France or abroad, or from public or private research centers.

L'archive ouverte pluridisciplinaire **HAL**, est destinée au dépôt et à la diffusion de documents scientifiques de niveau recherche, publiés ou non, émanant des établissements d'enseignement et de recherche français ou étrangers, des laboratoires publics ou privés.



THÈSE

En vue de l'obtention du

DOCTORAT DE L'UNIVERSITÉ DE TOULOUSE

Délivré par :

Université Toulouse 3 Paul Sabatier (UT3 Paul Sabatier)

Présentée et soutenue par :

Yu CHEN

le jeudi 16 mars 2017

Titre :

Analyse InSAR des déformations de volcans actifs: le Piton de la Fournaise
(Réunion) et le Llaima (Chili)

École doctorale et discipline ou spécialité :

ED SDU2E : Sciences de la Terre et des Planètes Solides

Unité de recherche :

Géoscience Environnement Toulouse (UMR 5563)

Directeur/trice(s) de Thèse :

José DARROZES
Dominique REMY

Jury :

Patrick BACHELERY
Myriam SCHMUTZ
Michel RABINOWICZ
Sylvain BONVALOT
José DARROZES
Dominique REMY

Professeur LMV, Clermont-Ferrand
Professeur EA, Pessac
Professeur UPS, Toulouse
DR IRD-GET, Toulouse
MC UPS, Toulouse
IR IRD-GET, Toulouse

Rapporteur
Examineur
Examineur
Examineur
Invité, directeur de thèse
Invité, co-directeur de thèse

ABSTRACT

We address in this dissertation the use of Interferometric Synthetic Aperture Radar (InSAR) to measure and characterize the ground surface deformation at two volcanoes – Piton de la Fournaise (La Réunion Island, France) and Llaima (Chile).

For Piton de la Fournaise, we analyzed the spatial pattern and temporal evolution of the ground displacement between the historical March-April 2007 eruption and October 2014, based on continuous measurements recorded by GNSS stations and X band COSMO-SkyMed and TerraSAR-X/TanDEM-X time series analysis. For the processing of radar data, we adopted a classical InSAR time series approach that exploits the information redundancy in the interferograms and we implemented an original method for correcting artifacts based on the principal component decomposition. The spatial and temporal complexity of the obtained deformation field indicates that an important part of the volcanic edifice is affected by deformations of various origins that overlap spatially and temporally. We observe also subsidence processes that are not accompanied by horizontal displacements in recent lava fields. We show that there exists a linear relationship between the subsidence and the thickness of lava and that the amplitude of subsidence decreases with time. These relationships allow us to construct an empirical law to estimate the contribution of post-lava emplacement process in the deformation field. We also observe that the Central Cone subsides persistently during the study period. We interpret this subsidence as the expression of a relaxation of the stresses caused by the Dolomieu collapse during the March-April 2007 eruption. Finally, we show that a widespread time-dependent moving sector on the Eastern Flank is affected by downslope motion during the 2007-2014 period. The uncertainties on both the structure and rheology parameters of the edifice leads us to explore different hypotheses to explain the origin of this flank motion which could be controlled by the frictional properties of the rocks along one or more fault planes, or be the expression of a dependent ductile deformation of the viscosity of the medium.

Llaima is a large Andean stratospheric volcano whose deformation processes are poorly understood not only because of the complexity of its functioning mode but also because of the absence of observation networks on the ground. In this context, the potential of radar data for monitoring the ground deformations of these volcanoes is a main scientific interest. However,

the complex environment conditions (steep slopes, snow- or ice-capped summit, dense vegetation cover, and strong tropospheric artifacts) and limited amount of available radar data make it challenging to accurately measure ground displacement with InSAR. To overcome these difficulties, we first perform a detailed analysis of the water vapor variations using Medium-Resolution Imaging Spectrometer (MERIS) and Moderate Resolution Imaging Spectroradiometer (MODIS) near-infrared water vapor products to study the impact of these variations on radar measurements. By using the results of this analysis as a constraint, we implemented an inversion of the radar data acquired between 2003 and 2011 to determine the atmospheric contribution and volume variations of a magmatic source located at a 7 km depth, which allows us to explain the interferometric signals observed during the study period. The results of this inversion show that no deformation caused by a pressure change of this source is detected during the eruptive period of 2008, contrary to what was stated in a previous study. On the other hand, it is possible that an uplift of the edifice preceded the March 2009 eruption. But the variation in volume of the estimated magma chamber ($12 \times 10^6 \text{ m}^3$) is less than the margin of error determined by least square adjustment.

Key words: InSAR; Volcano deformation; Piton de la Fournaise; Llaima; InSAR time series; InSAR artifact correction; Tropospheric phase delay; Lava flow subsidence; Volcano flank motion

RESUME

Les études des déformations de surface en relation avec l'activité volcanique permettent de quantifier les phénomènes de transfert de magma qui s'opèrent dans les structures superficielles et profondes d'un édifice volcanique. Ces études s'appuient essentiellement sur l'utilisation de séries temporelles acquises par des réseaux de récepteurs GNSS installés sur les flancs de l'édifice volcanique et sur l'utilisation d'images acquises par des satellites équipés de capteurs à ouverture de synthèse. Les objectifs de ce travail ont été de mettre en œuvre sur deux des volcans les plus actifs du monde des méthodes numériques pour détecter, analyser et interpréter les déformations du sol associées à l'activité.

Sur le Piton de la Fournaise, nous avons analysé l'évolution spatiale et temporelle du champ de déplacement entre l'éruption historique d'avril 2007 et octobre 2014 à partir de l'analyse de mesures continues acquises par les stations GNSS et de longues séries temporelles d'images radar Cosmos-SkyMed et TerraSAR acquises en bande X. Pour le traitement des données radars, nous avons adopté une approche classique qui exploite la redondance d'information dans les interférogrammes et nous avons mis en œuvre une méthode originale de correction des effets troposphériques reposant sur la décomposition des signaux radars en valeurs singulières. La complexité spatiale et temporelle du champ de déplacement obtenu indique qu'une partie importante de l'édifice volcanique est affectée par des déformations d'origines diverses qui se superposent spatialement et temporellement. Ainsi, on observe des processus de subsidence qui ne s'accompagnent pas de déplacements horizontaux sur les coulées de lave récentes. Nous montrons qu'il existe une relation linéaire entre cette subsidence et l'épaisseur de la coulée et que son amplitude décroît avec le temps. Ces relations nous permettent de construire une loi empirique pour estimer la contribution de ce processus dans le champ de déformation. Nous observons également que le cône central subside de manière persistante durant la période étudiée. Nous interprétons cette subsidence comme l'expression d'une relaxation des contraintes provoquée par l'effondrement de plus de 350 m du Dolomieu survenu lors de l'éruption d'avril 2007. Enfin, nous montrons qu'une large partie du flanc est de l'édifice volcanique est affectée d'un mouvement lent le long de la pente entre 2007 et 2014. L'absence d'évidences sur la structure et sur la rhéologie de l'édifice nous amène à explorer différentes hypothèses pour expliquer l'origine de ce glissement qui pourrait être contrôlé par

les propriétés frictionnelles des roches le long d'un ou de plusieurs plans de faille, ou bien être l'expression d'une déformation ductile dépendante de la viscosité du milieu.

Le Llaima est un large strato-volcans andin dont les processus de déformations sont mal compris à cause principalement de la complexité de son mode de fonctionnement mais, également, aussi par l'absence de réseaux d'observation au sol. Dans ce contexte, les potentialités des données radar pour le suivi des déformations de surface de ces volcans constituent un intérêt scientifique majeur. Néanmoins, le nombre limité d'images radars disponibles, les conditions environnementales spécifiques (relief abrupt, présence de neige, végétation, glacier) et l'impact des effets troposphériques sur les données radars constituent des limites importantes à l'utilisation de cette technique. Dans un premier temps, nous avons réalisé une analyse détaillée des variations de la vapeur d'eau dans la troposphère en utilisant des images MERIS (Medium-Resolution Imaging Spectrometer) et MODIS (Moderate resolution Imaging Spectroradiometer) pour étudier l'impact de ces variations sur les mesures radars. En utilisant comme contrainte les résultats de cette analyse, nous avons procédé à l'inversion de données radars acquises entre 2003 et 2011 pour déterminer la contribution atmosphérique et les variations de volumes d'une source magmatique situées à 7 km de profondeur permettant d'expliquer les signaux interférométriques observés durant la période étudiée. Les résultats de cette inversion montrent qu'aucune déformation provoquée par un changement de pression de cette source est détectée durant la période éruptive de 2008, contrairement à ce qui avait été affirmé dans une précédente étude. Par contre, il est possible qu'une surrection de l'édifice ait précédé l'éruption de mars 2009, mais néanmoins la variation de volume de la chambre magmatique estimée ($12 \times 10^6 \text{ m}^3$) est inférieure à la marge d'erreur déterminée par l'ajustement par moindres carrés.

ACKNOWLEDGEMENTS

This dissertation concludes three years of my study and research at University of Toulouse (Université Toulouse 3 Paul Sabatier), where I sincerely appreciate the opportunity of pursuing my doctoral degree. I would like to take this opportunity to express my heartfelt gratitude to all those who helped me reach this point.

First and foremost, my deepest gratitude goes to my advisors, Dr. José Darrozes and Dr. Dominique Remy, who have given me invaluable guidance, constant support and tireless mentorship throughout the entire process. This thesis contains their thousands of corrections and constructive suggestions. I have to say that this thesis is born from their insightful instructions and warm encouragements. Dr. José Darrozes is the one who offered me the opportunity of PhD study at University of Toulouse. He has always been generous to support me at various points. He encourages me to participate international congresses, which helps construct and enrich the knowledge of my specialty. Dr. Dominique Remy is the one who gives me inspirations of the thesis topic. I cannot thank him enough for having been extremely kind and patient with me. He spent a lot of time guiding me in a right direction, answering questions and providing useful suggestions. I have benefited tremendously from his critical thinking and insightful viewpoint. His characteristics such as being always ready for intensive discussion and open for new idea are always inspiring me.

Moreover, I am grateful to Dr. Jean-Luc Froger for providing valuable data and information on my PhD subject. This thesis could not have come this far without his insightful and constructive comments. Thank him also for the cordial hospitality during our business trip to Clermont Ferrand. Very special thanks go to Dr. Aline Peltier who has processed the GNSS data completing the dataset of this thesis. She also gives extraordinary insights and helpful comments on my paper. I really admire her for her scientific and rigorous attitude, and high efficient working style. I also thank Dr. Sylvain Bonvalot, Dr. Nicolas Villeneuve, and Dr. Hugo Perfettini for fruitful discussions on my paper.

And also, the Chinese Scholarship Council (CSC) is greatly acknowledged for providing me three years of PhD scholarship. I would like to thank as well for the generosity of the Agence Nationale de la Recherche (ANR) through the framework of GEOSUD, ANR-10-EQPX-20 project,

ASI through the CSK 2080 project for CSK images, the Deutsches Zentrum für Luft- und Raumfahrt (DLR) for TSX/TDX images through the LAN 0237 project, the European Space Agency (ESA) for ASAR data through the project Envisat-AO#857 and Category 1 #2899, and the Japanese Aerospace Exploration Agency (JAXA) for ALSO PALSAR data through the project #1142. The GNSS data were collected by Observatoire Volcanologique du Piton de la Fournaise/ Institut de Physique du Globe de Paris (OVPF/IPGP). Southern Andean Volcano Observatory (OVDAS) OVDAS Loretto Cordoba SERNAGEOMIN for provided us GPS data and useful information concerning the activity of Llaima.

Besides, I extend my great gratitude to all my friends, who have given me a lot of supports and encouragements in their own ways, which propels me forward throughout the arduous but wonderful journey. Chuanbo Guo; Huihui Li; Jing Ye; Long Qu; Bing Zhou; Rui Xue; Ruixi Zhao; Yu Zhao; Yingning He; Jing Sheng; Ping Li; Yi Wang; Lu Peng; Buyun Du; Hongmei Xu; Le Yao; Xing Huang; Wei Yuan; Chuxian Li; Xu Yang; Zukun Qu; Caiyang Feng; Yan Huang; Youcun Liu; Jiubin Chen; Miao Deng; Peng Xiao; Yijing Wang; Daqing, Liu; Huanhuan Lu; Yolande Traoré; Lan Vu Phuong; Cam Chi Nguyen, etc..

At last, I thank my parents, Tiejun Chen and Zhihua Yu, for their regretless support, understanding and endless love to me. I would like to say “Je t’aime” to my perfect husband, Xiaojun Feng, who has been a superman giving me constant support, and who has been my personal chef carefully planning the diet during my whole pregnancy, even though he is also in the last year of his PhD study. I want to thank our baby boy coming in October 2016, Lucas Feng, for being an amazing surprise in our lives. I enjoy both happiness and challenges that he has brought in the last year of my PhD study. I believe that it’s going to be the best graduation present for both of us!

TABLE OF CONTENTS

.....	1
ABSTRACT	1
RESUME	3
ACKNOWLEDGEMENTS	5
TABLE OF CONTENTS	7
CHAPTER 1 : INTRODUCTION	13
1.1 DEVELOPPEMENT DE L'INTERFEROMETRIE RADAR SATELLITAIRE	15
1.2 UTILISATION DE INSAR POUR LE SUIVI DES DEFORMATIONS VOLCANIQUES.....	17
1.3 DEUX CAS D'ETUDES : PITON DE LA FOURNAISE (LA REUNION, FRANCE) ET LLAIMA (CHILI).....	19
1.4 PLAN DU MANUSCRIPT	21
1.5 CADRE DU PROJET	21
1.1 DEVELOPMENT OF INTERFEROMETRIC SYNTHETIC APERTURE RADAR	23
1.2 INSAR MONITORING VOLCANO DEFORMATION	26
1.3 TWO CASE STUDIES: PITON DE LA FOURNAISE (LA REUNION, FRANCE) AND LLAIMA (CHILE)	27
1.4 THESIS ROADMAP	29
1.5 PROJECT FRAMEWORK	29
CHAPTER 2 : PRINCIPLES, DATA & METHODOLOGY	31
2.1 PRINCIPLES OF INSAR.....	32
2.1.1 <i>Synthetic Aperture Radar (SAR)</i>	32
2.1.1.1 Formation of SAR images.....	34
2.1.2 <i>Interferogram</i>	36
2.1.3 <i>Coherence</i>	38
2.1.4 <i>Composition of the interferometric phase</i>	40
2.2 DATA USED IN THE STUDY	43
2.2.1 <i>SAR data</i>	43
2.2.1.1 TSX/TDX and CSK data	44
2.2.1.2 ENVISAT-ASAR data	47
2.2.1.3 ALOS-PALSAR data	48
2.2.2 <i>GNSS data</i>	49
2.3 INSAR PROCESSING.....	51

2.3.1	<i>Coregistration of SAR images</i>	52
2.3.2	<i>Filtering in range and azimuth</i>	53
2.3.3	<i>Interferogram generation</i>	55
2.3.4	<i>Interferogram unwrapping</i>	56
2.3.5	<i>Mitigation of non-deformation contribution</i>	58
2.3.6	<i>3D displacement calculation</i>	58
2.4	INSAR TIME SERIES ANALYSIS (STAMPS/MTI-SB)	60
2.4.1	<i>SB interferograms formation</i>	61
2.4.2	<i>SDFP pixel selection</i>	62
2.4.3	<i>Estimation of orbital ramp and spatially-correlated DEM error</i>	64
2.4.4	<i>Inversion of SB interferograms to time series</i>	64
2.5	ATMOSPHERIC CONTRIBUTION	65
2.5.1	<i>Origin of atmospheric phase delay</i>	65
2.5.2	<i>Distribution of tropospheric phase delay</i>	67
2.5.3	<i>Tropospheric delay correction methods</i>	69
PART I – PITON DE LA FOURNAISE		73
CHAPTER 3 : STUDY AREA & THE MARCH-APRIL 2007 ERUPTION		73
3.1	OVERVIEW OF PITON DE LA FOURNAISE	74
3.1.1	<i>La Réunion Island</i>	74
3.1.2	<i>Structure of Piton de la Fournaise</i>	75
3.1.3	<i>Eruptive activity of Piton de la Fournaise</i>	77
3.1.4	<i>InSAR observations at Piton de la Fournaise</i>	79
3.2	THE HISTORICAL MARCH-APRIL 2007 ERUPTION	80
3.3	ONE YEAR POST-ERUPTIVE DISPLACEMENT	83
3.4	DISCUSSION	89
CHAPTER 4 : LONG-TERM GROUND DISPLACEMENT BETWEEN 2009 AND 2014		93
LONG-TERM GROUND DISPLACEMENT OBSERVATIONS USING INSAR AND GNSS AT PITON DE LA FOURNAISE		
VOLCANO BETWEEN 2009 AND 2014		
		95
	ABSTRACT	96
4.1	INTRODUCTION	96
4.2	DATA	100
4.2.1	<i>SAR data</i>	100
4.2.2	<i>GNSS data</i>	101
4.3	INSAR PROCESSING	102

4.3.1	<i>InSAR time series generation</i>	102
4.3.2	<i>InSAR artifact analysis</i>	106
4.3.3	<i>InSAR artifact correction approach</i>	109
4.3.3.1	Estimation of Long-Term Displacement Model	109
4.3.3.2	Stratified Delay Mitigation.....	112
4.3.4	<i>InSAR 2-dimensional (2D) ground displacement</i>	115
4.4	GROUND DISPLACEMENT ANALYSIS	119
4.4.1	<i>Displacement of the Central Cone</i>	119
4.4.2	<i>Displacement of the Eastern Flank</i>	122
4.4.3	<i>Displacement on recent lava flows</i>	123
4.5	DISCUSSION	127
4.5.1	<i>Ongoing post-eruptive displacement</i>	128
4.5.2	<i>Possible origins of eastward motion</i>	130
4.6	CONCLUSIONS	133
4.7	ACKNOWLEDGEMENTS.....	134
4.8	SUPPLEMENTARY MATERIAL.....	135
4.8.1	<i>Presentation of the stratified tropospheric artifact</i>	135
4.8.2	<i>PCAIM decomposition</i>	137
4.8.3	<i>Merging of TSX and CSK time series</i>	139
4.8.4	<i>Relative error in components of the ground displacement</i>	140
4.8.5	<i>Correlation between E-W displacement and slope</i>	141
4.9	EFFECTIVENESS TESTS.....	141
4.9.1	<i>Effectiveness of GAMs for mitigating atmospheric artifact</i>	141
4.9.2	<i>Effectiveness of the proposed artifact correction method</i>	148
4.9.2.1	Three sets of InSAR time series	148
4.9.2.2	Comparison between two methods	150

CHAPTER 5 : COMPARISON OF DISPLACEMENT BETWEEN 2007 – 2008 AND 2009 – 2014 ... 157

5.1	DISPLACEMENT OF THE CENTRAL CONE	158
5.1.1	<i>Eruptions between 2009 and 2004</i>	158
5.1.1.1	The November 2009 eruption	160
5.1.1.2	The December 2009 eruption.....	163
5.1.1.3	The October 2010 eruption	166
5.1.1.4	The December 2010 eruption.....	170
5.1.1.5	The June 2014 eruption	173
5.1.1.6	Discussion	176
5.1.2	<i>Long-term displacement</i>	177

5.1.2.1	Spatial pattern	177
5.1.2.2	Temporal behavior	179
5.2	DISPLACEMENT OF THE EASTERN FLANK	182
5.2.1	<i>Spatial pattern</i>	182
5.2.2	<i>Temporal behavior</i>	184
5.3	DISCUSSION AND CONCLUSIONS.....	188
CHAPTER 6 : CHARACTERIZATION OF DISPLACEMENT IN LAVA FIELDS.....		189
6.1	DATA PROCESSING	192
6.1.1	<i>InSAR time series</i>	192
6.1.2	<i>Extracting single lava fields between March 1998 and April 2007</i>	194
6.1.3	<i>Estimating lava thickness</i>	195
6.2	RESULTS.....	196
6.2.1	Subsidence in lava fields outside the EFA	197
6.2.2	Subsidence in lava fields inside the EFA	202
6.3	DISCUSSION	206
6.4	CONCLUSIONS	210
PART II – LLAIMA.....		211
CHAPTER 7 : GROUND DISPLACEMENT AT LLAIMA OBSERVED BY INSAR		211
7.1	GENERAL BACKGROUND OF LLAIMA	212
7.2	INSAR OBSERVATIONS AT LLAIMA	213
7.3	REVISED INTERPRETATION OF RECENT INSAR SIGNALS OBSERVED AT LLAIMA VOLCANO (CHILE)	215
7.4	ANALYSIS OF TROPOSPHERIC ARTIFACT IN PALSAR INTERFEROGRAMS	232
7.5	PRE-ERUPTIVE INFLATION BEFORE THE APRIL 2009 ERUPTION?	234
7.5.1	<i>Problem definition</i>	234
7.5.2	<i>Solving method</i>	236
7.5.3	<i>Results</i>	239
7.5.4	<i>Discussion and conclusions</i>	240
CHAPTER 8 : CONCLUSIONS & PERSPECTIVES.....		243
REFERENCES.....		253
APPENDIX		279
APPENDIX 1. SUMMARY OF SAR ACQUISITIONS OF TSX/TDX AND CSK DATA.....		279
APPENDIX 2. TSX/TDX ASCENDING INTERFEROGRAMS		281
APPENDIX 3. TSX/TDX DESCENDING INTERFEROGRAMS		289

APPENDIX 4. CSK ASCENDING INTERFEROGRAMS	294
APPENDIX 5. CSK DESCENDING INTERFEROGRAMS	300
APPENDIX 6. SUBSET OF VERTICAL (U-D) COMPONENT OF GROUND DISPLACEMENT FOR TSX/TDX – CSK MERGED INSAR TIME SERIES.....	306
APPENDIX 7. SUBSET OF HORIZONTAL (E-W) COMPONENT OF GROUND DISPLACEMENT FOR TSX/TDX – CSK MERGED INSAR TIME SERIES	307
APPENDIX 8. EXAMPLES FOR EFFECTIVENESS TEST OF GAMs (CASES 3 - 5).....	308
APPENDIX 9. ORAL PRESENTATION AND ABSTRACT IN EGU 2015, VIENNA, AUSTRIA.....	311
APPENDIX 9. POSTER PRESENTATION AND CONFERENCE PAPER IN IGARSS 2015, MILAN, ITALY	313

CHAPTER 1 : INTRODUCTION

CHAPTER 1: INTRODUCTION

Les volcans sont parmi les plus impressionnants des phénomènes naturels, leurs éruptions et les menaces associées sont très dangereuses et causent des pertes en vie humaines et des dommages économiques aux communautés du monde entier. Il est donc essentiel de surveiller et d'étudier très attentivement les volcans. Les scientifiques ont besoin d'utiliser une variété de techniques qui permettent d'enregistrer l'activité à l'intérieur d'un volcan. Pour cela la surveillance des volcans nécessite différents types d'observations (**Figure 1.1**): l'analyse des gaz et de la chimie des roches volcaniques (Giggenbach et Le Guern, 1976; Symonds et al., 1994; King et al., 2004; Le maitre, 2002; Machado et al., 2008), les effets des séismes volcanotectoniques (Chouet et al., 1994; Lahr et al., 1994; Roman et Cashman, 2006), les vitesses et directions de déplacement liées aux mouvements de terrain (Matsushima et Takagi, 2000; Aloisi et al., 2003; Battaglia et al., 2003), et les mesures de télédétection (Francis, 1989; Massonet et al., 1995; Mougénis-Mark et al., 2000; Remy et al., 2003; Harris, 2013; Reynolds et al., 2015).

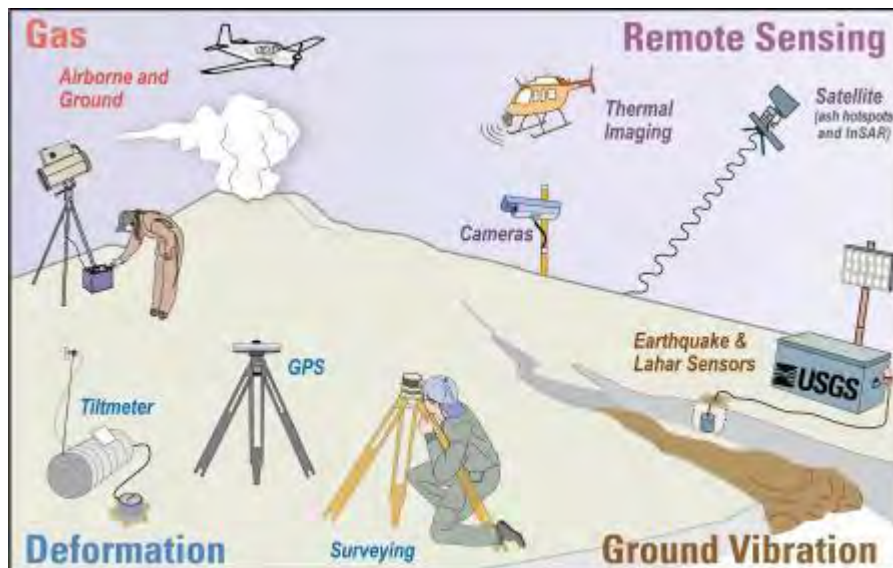


Figure 1.1 Exemple du programme USGS Volcano Hazard utilisé pour la surveillance des volcans. (<http://volcanoes.usgs.gov/vhp/monitoring.html>)

1.1 Développement de l'interférométrie radar satellitaire

L'interférométrie radar à ouverture de synthèse, plus connue sous sa dénomination anglo-saxonne Interferometric Synthetic Aperture Radar (InSAR) est l'une des techniques les plus utilisées actuellement en géodésie pour mesurer les déformations de la croûte terrestre en relation avec l'activité tectonique ou volcanique. L'interférométrie est une technique qui, en supprimant par différence de deux images SAR la contribution de la phase de réflexion, permet, lorsque certaines conditions sont réunies, d'exploiter la partie géométrique de la phase mesurée. Les images peuvent être acquises au même instant, généralement pour constituer des Modèles Numériques de Terrain (MNT) ou bien à des instants différents pour suivre les déplacements de surface survenus entre les deux acquisitions.

La réalisation de MNT a été l'une des premières applications de l'interférométrie radar. En effet, cette technique permet de produire des représentations de la topographie terrestre avec des précisions comparables à celles obtenues par des techniques optiques classiques. L'un des exemples le plus marquant a été la réalisation du MNT couvrant une large partie de la superficie terrestre : le SRTM (Shuttle Radar Topography Mission, NASA; [Farr & Kobrick, 2000](#)), obtenu à partir du traitement d'images acquises avec différents angles d'incidence par deux capteurs radar à ouverture de synthèse embarqués sur un satellite. Le MNT obtenu donne une estimation de l'altitude avec une précision métrique pour une résolution horizontale d'initialement 90 m. Actuellement, il existe une mission qui à partir des données acquises par la constellation de satellites TerraSAR-X, dans le cadre de la mission TanDEM-X, permet d'obtenir des MNT de haute résolution à travers le monde.

Le suivi des déplacements de la surface terrestre par interférométrie radar a débuté principalement avec le lancement du satellite ERS-1 en 1992. L'interférométrie permet de détecter un déplacement relatif entre deux points de la surface imagée de l'ordre d'une fraction de la longueur d'onde utilisée par le capteur (23 cm en bande L, 6 cm en bande C et 3 cm en bande X). Elle permet ainsi, théoriquement, d'obtenir des mesures de déplacements de la surface terrestre avec une précision centimétrique, voire millimétrique. L'un des premiers exemples de l'utilisation de la technique interférométrique pour imager les déplacements de

surface terrestre provoqués par le séisme de Landers (Californie) survenu en 1992 a été présenté par Massonnet et al. (1993). Les auteurs de cette étude ont pu ainsi produire une cartographie des déplacements provoqués par la rupture sismique à partir de deux images acquises avant et après le séisme par le satellite ERS-1. Depuis, de nombreuses études ont montré que cette technique était devenue incontournable pour étudier les champs de déformations et son utilisation s'est généralisée dans le cadre des géosciences aussi bien pour étudier les déformations volcaniques (e.g. Lu et al., 1997; Lanari et al., 1998; Pritchard & Simons, 2002, 2004; Froger et al., 2004; Brooks et al., 2008), les mouvement de glacier (e.g. Joughin et al., 1995; Kumar et al., 2011), les déformations d'origine sismique (e.g. Simons et al., 2002; Fialko et al., 2005; Chlieh et al., 2011; Bignami et al., 2012; Remy et al. 2016), les déformations d'origine anthropique telles que les phénomènes de subsidence en ville (e.g. Amelung et al., 1999), ou liées à l'activité minière (e.g. Gourmelen et al., 2007; Herrera et al., 2007), etc.. Tous ces études ont ainsi montré, le fort potentiel de l'interférométrie radar qui permet de cartographier la distribution spatiale des déformations avec un niveau de précision élevé, et souligner la complémentarité de cette technique avec d'autres techniques géodésiques telle que le GNSS (Global Navigation Satellite System).

Néanmoins malgré ce fort potentiel, l'interférométrie radar classique présente de nombreuses limitations qui sont principalement : le nombre parfois limité d'acquisitions d'images radars sur certaines cibles ; la perte de cohérence provoquée par le changement des caractéristiques de la surface terrestre imagée (présence de neige, végétation, etc..) ; les artefacts provoqués par les variations des propriétés atmosphériques ; et enfin les erreurs d'altitudes des Modèles Numériques de Terrain (MNT) utilisés pour estimer la contribution de la topographie dans le signal interférométrique. C'est ainsi, qu'au début des années 2000 et grâce au nombre de plus en plus important d'images disponible, des méthodes basées sur l'analyse statistique de mesures temporelles InSAR ont été développées telles que : Persistent Scatterers InSAR (PS-InSAR), Small Baseline InSAR (SB-InSAR) et Multi-Temporal InSAR (MT-InSAR) avec comme objectifs de surmonter ces limites et de mieux analyser la dynamique spatio-temporelle des champs de déformation observés (Ferretti et al., 2001; Berardino et al., 2002; Usai et al., 2003; Lanari et al., 2004a; Hooper et al., 2004, 2007; Hooper, 2008; Ferretti et al., 2011;). Ces différentes techniques d'analyse de mesures InSAR ont été utilisées avec succès pour déterminer des vitesses de déplacement et leurs variations dans différentes études (e.g. Lanari

et al., 2004b; Anderssohn et al., 2009; Lauknes et al., 2010; Peltier et al., 2010a; Heleno et al., 2011; Osmanoglu et al., 2011; Bovenga et al., 2012; Chaussard et al., 2014; Sun et al., 2015).

C'est ce rôle incontournable de l'interférométrie en géodésie qui a amené de nombreuses agences spatiales à lancer un nombre de plus en plus important de satellites équipés de capteurs radars à ouverture de synthèse opérant à différentes longueurs d'onde pour ne citer que les principales :

- en bande X (3 cm)
 - la constellation COSMO-SkyMed se composant de 4 satellites (Agence Spatiale Italienne) ; la constellation TerraSAR/TanDEM-X avec deux satellites (Allemagne), le satellite coréen KOMPSAT-5
- en bande C (5 cm)
 - RADARSAT-2 (Canada); Sentinel-1A and -1B de l'Agence Spatiale Européenne; RISAT-1 (Inde)
- en bande L (21 cm)
 - ALOS-2 (Japon).

1.2 Utilisation de InSAR pour le suivi des déformations volcaniques

En comparaison avec les instruments géodésiques installés au sol (inclinomètres, théodolite, stations sismiques et réseau GNSS), la technique InSAR est particulièrement intéressante car elle permet d'obtenir une cartographie précise du champ de déformation d'un édifice volcanique et peut être utilisée même sur des volcans où l'installation de système d'acquisition au sol est complexe à mettre en œuvre. C'est pour cette raison que l'interférométrie est utilisée de manière systématique pour la surveillance de nombreux volcans actifs à travers le monde comme le mont Etna, le Stromboli (Italie), Kilauea (Hawaii), de nombreux volcans andésitiques de la cordillère andine (Le Llaima, Lastarria, Lascar, etc..) et bien sur le Piton de la Fournaise (La Réunion) (e.g. Pritchard & Simons, 2002, 2004; Antonello et al., 2004; Palano et al., 2008; Neri et al., 2009; Fournier et al., 2010; Fukushima et al., 2010; Shirzaei et al., 2013; Di Traglia et al., 2014; Froger et al., 2015; Jo et al., 2015; Remy et al., 2015). Les

déformations en surface générées par l'activité volcanique, qui sont observées par InSAR, constituent des observations indispensables pour mieux comprendre les mécanismes qui en sont à l'origine. Ces origines sont diverses et les déformations peuvent être provoquées par l'activité magmatique (e.g. [Chadwick et al., 2006](#); [Lundgren et al., 2013](#)), par des phénomènes de compactions thermomécaniques de coulées de lave associés à la fluxion du substratum, (e.g. [Briole et al., 1997](#); [Stevens et al., 2001a](#); [Bato et al., 2016](#); [Chaussard, 2016](#); [cette étude](#)), ou à des glissements de flanc (e.g. [Solaro et al., 2010](#); [Intrieri et al., 2013](#); [Froger et al., 2015](#)). Ainsi des observations périodiques du champ de déformation des édifices volcaniques permettent de mieux appréhender l'ampleur des phénomènes, leurs dynamiques temporelles et par conséquent de mieux comprendre un système volcanique avec comme corolaire une amélioration de la gestion du risque associé à l'activité volcanique.

Néanmoins, à cause des caractéristiques spécifiques de la plupart des édifices volcaniques, la mise en œuvre de l'interférométrie radar pour le suivi de l'activité volcanique reste dans la plupart des cas très difficile ([Zebker et al., 1997](#); [Remy et al., 2003](#); [Doin et al., 2009](#); [Pinel et al., 2011](#); [Hooper et al., 2012](#)). Les pentes importantes d'un édifice volcanique peuvent conduire à des pertes de cohérence d'origine géométrique réduisant notablement la surface du champ de déplacement mesuré par InSAR. De nombreux édifices volcaniques sont situés dans des zones climatiques caractérisées par de fortes précipitations favorisant le développement d'une végétation épaisse entraînant la perte de cohérence à l'onde radar ([Pinel et al., 2011](#)). Dans d'autres cas, cette perte de cohérence peut être provoquée par la présence de neige ou de calotte glaciaire au sommet du volcan ([Lu & Dzurisin, 2014](#)). De plus, les variations spatiales et temporelles de l'indice de réfraction de la couche basse de la troposphère peuvent provoquer de forts artefacts dans les interférogrammes, notamment dans les zones volcaniques caractérisées par des variations de relief importantes ([Beauducel et al., 2000](#); [Remy et al., 2015](#)). Les signaux d'origine troposphérique peuvent biaiser significativement le signal observé. Ils doivent donc être étudiés avec la plus grande attention, car s'ils ne sont pas pris en compte ou sous-estimés ils peuvent conduire à de graves erreurs d'interprétation.

1.3 Deux cas d'études : Piton de la Fournaise (La Réunion, France) et Llaima (Chili)

L'objectif principal de ce travail de thèse est de suivre et d'interpréter les déplacements de surface sur deux édifices volcaniques par InSAR pour apporter des éléments nouveaux qui permettront de mieux comprendre les mécanismes et les processus à l'origine des déplacements éventuellement observés. Pour parvenir à cet objectif, nous avons notamment étudié très finement les éventuels effets de sites qui peuvent conduire à des interprétations erronées sur ces deux sites volcaniques.

Le Piton de la Fournaise est l'un des plus active volcan basaltique du monde, avec 44 éruptions qui sont survenues entre 1998 et 2015 ([Roult et al., 2012](#); [observation of Observatoire Volcanologique du Piton de la Fournaise](#)). L'activité récente du volcan se concentre principalement dans la zone sommitale du cône centrale et/ou sur ses flancs. Exceptionnellement, des fissures se sont ouvertes loin du cône central à des altitudes moins élevées dans la plaine des Osmondes ou dans la zone du Grand Brulé ([Peltier et al., 2009a](#)). Parmi les éruptions récentes, la crise éruptive survenue entre mars et avril 2007 est considérée comme l'une des plus importantes observée sur ce volcan depuis plus d'un siècle. Le flot de lave, sorti à une altitude basse (650 m) dans le Grand Brulé, a produit un volume estimé à 210×10^6 m³. Cette éruption s'est également accompagnée de l'effondrement de plus de 350 m du cratère du Dolomieu suite à la vidange de la chambre magmatique (e.g. [Staudacher et al., 2009](#); [Bachèlery et al., 2010](#)). Un aspect intéressant concerne le fort déplacement (~ 1.4 m de déplacement vers l'Est et 0.37 m de soulèvement) affectant une large part du flanc est de l'édifice observé durant cette phase éruptive ([Augier, 2011](#); [Froger et al., 2015](#)). De plus, des études récentes ([Augier, 2011](#); [Froger et al., 2015](#)) ont montré que le glissement du flanc est initié en 2007 avait continué au moins jusqu'en juillet 2008 (0.18 m de déplacement vers l'Est) associé à une forte subsidence (0.35 m). L'un des objectifs de ce travail de thèse est donc d'apporter des éléments d'observations nouveaux pour permettre de mieux cerner la dynamique et l'emprise spatiale de ce glissement. Outre une meilleure caractérisation de cet aléa, il y a bien sûr une volonté de mieux appréhender le risque associé à ce phénomène qui pourrait entraîner une large déstabilisation du flanc de l'édifice et provoquer un raz de marée ([McGuire, 1996](#)). Le principal challenge d'une étude des déplacements de surface du Piton de la

Fournaise est d'être capable de réduire au maximum l'impact des effets troposphériques corrélés au relief dans les interférogrammes. En l'absence de données extérieures permettant de réduire la variance du bruit d'origine atmosphérique de manière indépendante, nous avons adopté la stratégie suivante. Nous utilisons la chaîne de programme Stanford Method for Persistent Scatterers (StaMPS; Hooper et al., 2012) que nous avons modifiée pour mettre en oeuvre une méthode originale de correction des effets troposphériques reposant sur l'utilisation d'une décomposition en valeurs singulières (Component Analysis-based Inversion Method package PCAIM; Kositsky and Avouac, 2010) pour discriminer les déplacements persistants dans le temps des signaux d'origine troposphérique.

Le second site étudié est le Llaima qui est non seulement l'un des volcans les plus imposants, mais également le plus actif des volcans situés en Amérique du Sud, avec un nombre record d'environ 50 éruptions répertoriées entre 1640 et 2009 (Naranjo & Moreno, 1991; Naranjo & Moreno, 2005; Moreno et al., 2009). Son activité récente se caractérise par des éruptions de faibles intensités entre 1979 et 2003 (11 éruptions avec $VEI \leq 2$) suivies par des éruptions plus explosives entre mars 2007 et juin 2009 (avec des VEI compris entre 2 et 3) (Smithsonian Institution Global volcanism rapport sur <http://www.volcano.si.edu>). Ce volcan andésitique se caractérise par des flancs très pentus et par la présence d'un glacier sur son sommet. A cause de la présence de ce glacier même des éruptions de faibles intensités (comme celles de janvier 2008 ou avril 2009) provoquent la formation de lahars qui peuvent entraîner des dommages importants. Ainsi la détection de déformation avant une crise éruptive constitue une information importante pour la mise en place d'un plan d'alerte à l'aléa volcanique dans la région. Sur cet édifice volcanique, nous effectuons une analyse précise des variations du contenu en vapeur d'eau de la couche basse de la troposphère en utilisant des observations MERIS (Medium-Resolution Imaging Spectrometer) et MODIS (Moderate Resolution Imaging Spectroradiometer (MODIS), qui permettent de mieux contraindre les résultats de l'inversion des mesures InSAR acquises sur ce site. Cette analyse et les résultats des inversions nous amènent à reconsidérer les conclusions de l'étude de Bathke et al. (2011).

1.4 Plan du manuscrit

Ce manuscrit est composé de six chapitres qui suivent cette introduction. Dans le chapitre 2, nous commençons par présenter les concepts de base de la technique InSAR. Nous détaillons les méthodes et présentons les données radars qui ont été utilisées dans ce travail de thèse. Nous aborderons également dans ce chapitre les aspects théoriques concernant les effets atmosphériques et leurs impacts sur la précision des mesures InSAR. Les chapitres 3 à 6 concernent l'étude que nous avons réalisée durant cette thèse sur le Piton de la Fournaise. Dans un premier temps, nous aborderons rapidement le contexte géodynamique et structural de cet édifice volcanique. Puis nous présenterons une analyse détaillée des principales caractéristiques de l'éruption historique survenue en 2007 basée sur une étude bibliographique et sur les résultats à partir de l'analyse des déplacements de surface observés entre avril 2007 et juillet 2008 par le satellite ENVISAT. Le chapitre 4 concerne l'analyse des déplacements du Piton de la Fournaise persistants durant la période 2009 – 2014. Ce chapitre est composé d'un résumé et d'un article soumis à la revue Remote Sensing Environment en octobre 2016. Dans le chapitre 5, nous discutons les similitudes et les différences principales des champs de déplacement entre 2007-2008 et 2009 - 2014 périodes. Dans le chapitre 6, nous présenterons une analyse des déplacements provoqués par la mise en place des coulées de lave récentes. L'étude réalisée sur le Llaima sera présentée dans le chapitre 7. Enfin, un dernier chapitre sera consacré aux conclusions et perspectives de ce travail de thèse.

1.5 Cadre du projet

Ce projet de thèse a été pris en charge par le Chinese Scholarship Council (CSC). Cette étude a été réalisée pour une partie dans le cadre d'un projet GEOSUD ANR-10-EQPX-20. Les données radar CosmosSkymed ont été obtenues dans le cadre d'un appel d'offre de l'Agence Spatiale Italienne (CSK 2080 project) et les données radar TerraSAR X dans le cadre d'un appel d'offre du DLR (Deutsches Zentrum für Luft- und Raumfahrt) : projet LAN 0237. Les données ENVISAT ont été acquises dans le cadre des projets de l'Agence Spatiale Européenne Envisat-AO#857, Category 1 #2899 et les données ALOS dans le cadre de l'appel d'offre de l'agence spatiale Japonaise (JAXA) à travers le projet #1142. Les observations GNSS ont été acquises par

CHAPTER 1: INTRODUCTION

le réseau de stations mis en place par l'Observatoire Volcanologique du Piton de la Fournaise et l'Institut de Physique du Globe de Paris (OVPF/IPGP). Les données GNSS et les rapports des missions de terrain effectués sur le Llaima durant l'éruption de janvier 2008, nous ont été fournis par le Southern Andean Volcano Observatory (OVDAS).

Volcanoes are among the most impressive natural phenomena. Both their eruptions and their associated hazards are very dangerous and cause loss of life and economic damage to communities around the world. It is therefore essential to carefully monitor and study volcanoes. Scientists need to use a variety of techniques that can record activities inside a volcano. Volcano monitoring include various type of observations (**Figure 1.1**): volcanic gases and rock chemistry (Giggenbach & Le Guern, 1976; Symonds et al., 1994, King et al., 2004; Le maitre, 2002; Machado et al., 2008), volcano-tectonic earthquakes activity (Chouet et al., 1994; Lahr et al., 1994; Roman & Cashman, 2006), ground displacements (Matsushima & Takagi, 2000; Aloisi et al., 2003; Battaglia et al., 2003), remote sensing observations (Francis, 1989; Massonet et al., 1995; Mougénis-Mark et al., 2000; Remy et al., 2003; Harris, 2013; Raynolds et al., 2015).

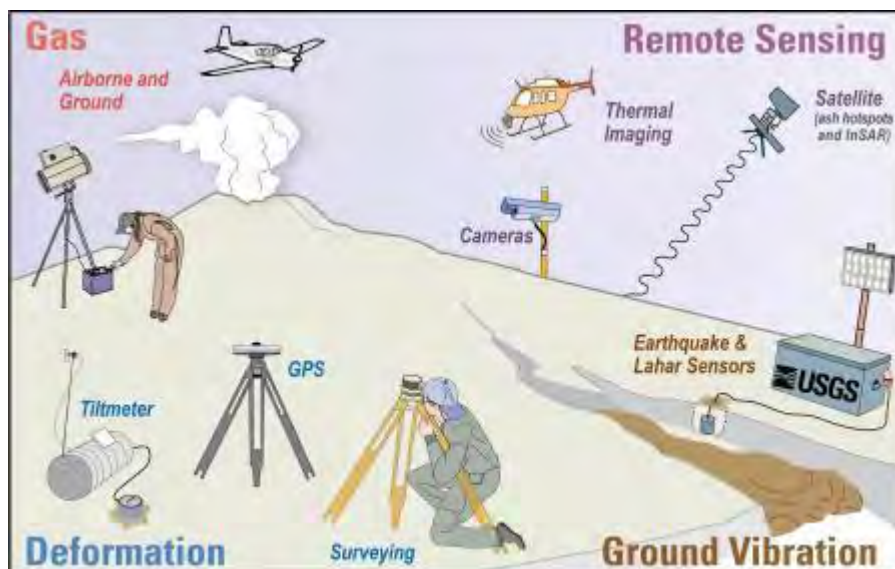


Figure 1.1 Example of the USGS Volcano Hazard Program employed for volcano monitoring. (<http://volcanoes.usgs.gov/vhp/monitoring.html>)

1.1 Development of Interferometric Synthetic Aperture Radar

Interferometric Synthetic Aperture Radar (InSAR), also referred to as SAR Interferometry, is a recently developed technique of geodesy, based on the phase difference between two SAR images. These images taken over a same region can be acquired at the same time by two

antennas or acquired at two different times, making it possible to measure the topography or the ground deformation of an area, especially the inaccessible areas.

The estimation of topography had been the main focus for the early applications (in the 1970s and 1980s) of InSAR, yielding elevation accuracies comparable with optical methods. One of the most valuable examples of application of InSAR to measure the topography is the construction of a global Digital Elevation Model (DEM) (Shuttle Radar Topography Mission, NASA; [Farr & Kobrick, 2000](#)), by treatment of SAR images simultaneously acquired with two different viewing angles. The obtained DEM is an estimate of the altitude at each point of the world, with a metric precision and a spatial resolution of 30 m on the territory of the United States of American and 90 m on the rest of the world. This mission has been ranked among the most successful missions in NASA. Acquiring almost simultaneously the SAR data can also be accomplished by the missions involving tandem satellites such as TerraSAR-X/TanDEM-X.

With development of geodetic technique in the late 1980s, the geophysical applications of InSAR and Differential InSAR (hereafter using the term InSAR representing the both) enabled geodesists, since the early 1990s and the launch of the ERS-1 satellite, to monitor displacement of ground surface ([Massonnet & Rebaute, 1985](#); [Gabriel et al., 1989](#); [Massonnet et al., 1993](#)). The relative LOS movement of scatters with respect to a reference location in the image could be measured as a fraction of the wavelength, yielding cm to mm accuracies for L-band, C-band, and X-band radars ([Gabriel et al., 1989](#)). One of the first spectacular examples of InSAR measuring ground deformation was reported by Massonnet et al. ([1993](#)) concerning the displacement field of the Landers, Californie earthquake. They produced a displacement map in the area associated with the seismic rupture, based on two acquisitions of ERS-1 satellite acquired before and after the earthquake. Since then, numerous InSAR studies have been carried out focusing on ground deformation associated with various natural causes or human activities, such as volcano dynamics (e.g. [Lu et al., 1997](#); [Lanari et al., 1998](#); [Pritchard & Simons, 2002, 2004](#); [Froger et al., 2004](#); [Brooks et al., 2008](#)), glacier movement (e.g. [Joughin et al., 1995](#); [Kumar et al., 2011](#)), earthquakes (e.g. [Simons et al., 2002](#); [Fialko et al., 2005](#); [Bignami et al., 2012](#)), urban subsidence (e.g. [Amelung et al., 1999](#)), mining activity (e.g. [Gourmelen et al., 2007](#); [Herrera et al., 2007](#)), etc.. These works thus highlighted the main contribution of InSAR compared with other geodetic techniques (e.g. the Global Positioning System), which is, the

excellent resolution and high spatial coverage making it possible to quantify the spatial variability of numerous phenomena.

Despite many successes, the standard InSAR techniques faced challenges with the increasing requirement of measurement accuracy. The main limitations of standard InSAR are, the phase noise due to changes in the scattering properties of the Earth's surface with time, the artifact due to variation in atmospheric properties, and even the errors in surface elevation determination. Therefore, in late 1990s and 2000s, the advanced InSAR time series techniques such as Persistent Scatterers InSAR (PS-InSAR), Small Baseline InSAR (SB-InSAR) and Multi-Temporal InSAR (MT-InSAR) were developed aiming to overcome the shortcomings of standard InSAR techniques and to better interpret time-dependent deformation behaviors by processing multiple acquisitions in time (Ferretti et al., 2001; Berardino et al., 2002; Usai et al., 2003; Lanari et al., 2004a; Hooper et al., 2004, 2007; Hooper, 2008; Ferretti et al., 2011). These different techniques for InSAR time series analysis have been successfully applied to measure mean velocities and/or incremental displacements in diverse applications (e.g. Lanari et al., 2004b; Anderssohn et al., 2009; Lauknes et al., 2010; Peltier et al., 2010a; Heleno et al., 2011; Osmanoglu et al., 2011; Bovenga et al., 2012; Chaussard et al., 2014; Sun et al., 2015).

The future developments of InSAR rely on mainly successful deployment of forthcoming SAR missions. Nowadays, the existing missions include the four COSMO-SkyMed satellites, the two TerraSAR/TanDEM-X spacecrafts and the Korean KOMPSAT-5 satellite in X band; the Canadian RADARSAT-2, the Sentinel-1A and -1B of the ESA and the Indian RISAT-1 in C band; the Japanese ALOS-2 in L band. In the upcoming years, the new X, C, and L band satellites such as, Sentinel-2, the Canadian RADARSAT Constellation Mission, the COSMO-SkyMed-2, SAOCOM, NISAR etc. have been commissioned. Additionally, the higher spatial resolution, the different frequency bands, the development of new methods for the analysis of InSAR data, the development of innovative approaches for jointly analyzing InSAR and other geodetic and/or geophysical data will be urgently required in terms of technical aspects (Stramondoa et al., 2016). Thus, the capabilities of InSAR are expected to be further exploited.

1.2 InSAR monitoring volcano deformation

Comparing with classical ground-based geodetic instruments that are widely used for volcano monitoring such as, theodolite, tiltmeters, electronic distance meter, seismic, and GNSS networks, the space-based technique, InSAR, is particularly valuable because it provides regional and spatially continuous measurements of ground surface displacement with unprecedented accuracy, and can be easily applied remotely for regions where there may be limitations for working on site with traditional instrumentations. At present, many active volcanoes in the world such as Etna (Italy), Stromboli (Italy), Kilauea (Hawaii), Piton de la Fournaise (La Réunion), and many andesitic volcano of the Andean Cordillera (the Llaima, Lastarria, Lascar, etc.), are regularly monitored by InSAR (e.g. Pritchard & Simons, 2002, 2004; Antonello et al., 2004; Palano et al., 2008; Neri et al., 2009; Fournier et al., 2010; Fukushima et al., 2010; Shirzaei et al., 2013; Di Traglia et al., 2014; Froger et al., 2015; Jo et al., 2015; Remy et al., 2015). The InSAR observed surface deformation alone is interesting, but more importantly, the interpretations are especially useful at volcanoes where surface displacement are associated with magma activity (e.g. Chadwick et al., 2006; Lundgren et al., 2013), movement of lava flows (e.g. Briole et al., 1997; Stevens et al., 2001a; Bato et al., 2016; Chaussard, 2016; this study), or flank instability (e.g. Solaro et al., 2010; Intrieri et al., 2013; Froger et al., 2015). Therefore, routinely monitoring surface deformation at volcanoes helps infer subsurface processes that cannot be directly observed and can improve our understanding of the state of volcano to further assess potential volcano hazard.

In spite of all the advantages of InSAR for monitoring surface deformation at volcanoes, their capability remains limited in some cases. Many volcanoes are located in intertropical or temperate areas where the frequent precipitations and fertile soils provide optimal conditions for the development of dense vegetation that can cause temporal decorrelation of interferometric phases (Pinel et al., 2011). Snow cover, summit ice caps can also contribute to temporal decorrelation (Lu & Dzurisin, 2014). In addition, spatial and temporal variations of the troposphere can induce strong tropospheric (long- and short-wavelength) artifacts on InSAR products (Beauducel et al., 2000; Remy et al., 2015). All these factors have negative impacts on InSAR applicability to volcano deformation monitoring, by reducing or even preventing the

ability to distinguish ground deformation signals from other radiometric contributions (Zebker et al., 1997; Remy et al., 2003; Doin et al., 2009; Pinel et al., 2011; Hooper et al., 2012).

1.3 Two case studies: Piton de la Fournaise (La Réunion, France) and Llaima (Chile)

The main objective of this dissertation is to monitor and interpret the ground deformation at both Piton de la Fournaise and Llaima volcanoes by taking full advantage of InSAR data acquired by different satellites. We are aiming to provide accurate results and valuable insights for understanding the state of volcano and the subsurface processes.

Piton de la Fournaise is one of the most active basaltic volcanoes in the world with 44 occurrences of eruption between 1998 and 2015 (Roult et al., 2012; [observation of Observatoire Volcanologique du Piton de la Fournaise](#)). Most of the recent activity occurred either in the summit crater or directly on the flank of the Central Cone. Exceptionally, fissures opened at low elevation far from the Central Cone in the Plaine des Osmondes or in the Grand Brulé (Peltier et al., 2009a). Among all the recent eruptions, the March-April 2007 eruption is considered as the largest eruption ever observed at this volcano during the 20th and 21th centuries, characterized by a distal effusion of $210 \times 10^6 \text{ m}^3$ volume of lava at low elevation in the Grand Brulé and a 340 m consequent collapse of the Dolomieu crater (e.g. Staudacher et al., 2009; Bachèlery et al., 2010). A notable widespread downslope motion (up to 1.4 m to the east and up to 0.37 m of uplift) affecting the Eastern Flank during co-eruptive period was observed by previous studies (Augier, 2011; Froger et al., 2015). Moreover, this downslope movement of the Eastern Flank had lasted from the end of the eruption to at least July 2008, with overall up to 0.18 m to the east and up to 0.35 m of subsidence during this one-year post-eruptive period (Augier, 2011; Froger et al., 2015). Therefore, it is essential and urgent to characterize and interpret the ground deformation field at Piton de la Fournaise, in particular on the Eastern Flank, in order to reduce the possibility of flank instabilities, which can result in large catastrophic flank destabilizations and tsunamis (McGuire, 1996). The main challenge in using InSAR data to study ground deformation at Piton de la Fournaise is the topography-correlated displacement. Further, the external data-based atmospheric artifact correction methods are inapplicable due to the

unavailability of external data corresponding to the InSAR data over Piton de la Fournaise. In order to overcome these difficulties, we adopt an enhanced Small Baselines (SB) -InSAR method based on Stanford Method for Persistent Scatterers (StaMPS; [Hooper et al., 2012](#)) to perform a detailed time series analysis on SAR data acquired over Piton de la Fournaise. We propose a new correction approach grounded on a principal component decomposition implemented in Principal Component Analysis-based Inversion Method package (PCAIM; [Kositsky and Avouac, 2010](#)) for discriminating the displacement signal from artifact in interferograms. This approach is proved to be efficient for the case of this study, allowing us to finally obtain high-precision InSAR time series maps of ground displacement at Piton de la Fournaise.

Llaima is not only one of the biggest volcanoes in Chile but also one of the most historically active volcanoes in South America with a record of around 50 documented eruptions between 1640 and 2009 ([Naranjo & Moreno, 1991](#); [Naranjo & Moreno, 2005](#); [Moreno et al., 2009](#)). Its recent activity has been characterized by relatively small eruptions between 1979 and 2003 (11 eruptions with $VEI \leq 2$) and by a slight increase in explosivity for the last eruptive cycle, between March 2007 and June 2009 (with $2 \leq VEI \leq 3$) ([Smithsonian Institution Global volcanism report available at <http://www.volcano.si.edu>](#)). Differing from basaltic volcano Piton de la Fournaise, the andesitic volcano Llaima has steep slopes and large scale near-summit glaciers. Thus, relatively minor eruptions can create hazards (as the eruptions in January 2008 and April 2009) due to the presence of large scale near-summit glaciers, which are highly susceptible to melting and lahar generation during energetic fountaining ([Bouvet de Maisonneuve et al., 2012](#)). Therefore, detecting ground deformation at Llaima volcano can contribute to preventing potential damage to local population and property. For Llaima, we first perform a careful analysis of the water vapor variations using Medium-Resolution Imaging Spectrometer (MERIS) and Moderate Resolution Imaging Spectroradiometer (MODIS) near-infrared water vapor products, and then we invert wrapped interferograms for both topographic correlated phase delays and a simple model source strength. Rigorous analysis allows us to reach a revised interpretation with respect to that of [Bathke et al. \(2011\)](#).

For Llaima, the specific environmental conditions (steep slopes, snow- or ice-capped summit, dense vegetation cover, and strong tropospheric artifacts) and limited amount of available SAR data make it challenging to accurately measure ground displacement with InSAR.

This is the main reason leading Fournier et al. (2010) and Bathke et al. (2011) to deliver opposite interpretations on the deformation signals during the 2008 eruptive period.

1.4 Thesis Roadmap

This dissertation is organized in six chapters which follow this introduction. We first summarize the basics of InSAR in Chapter 2. We then present the data used in this work. We further describe the procedures of conventional InSAR and time series InSAR processing by providing some examples derived from the studied data. The atmospheric contribution that is often the main artifact source to InSAR processing is finally introduced in Chapter 2. Chapter 3, 4, 5 and 6 compose the studies carried out at Piton de la Fournaise. In Chapter 3, in a first step, we briefly address the geodynamic and structural context of this volcanic edifice. Then we present a detailed analysis of the main features of the 2007 historical eruption based on a bibliographic study and on the results from the analysis of the surface displacements observed between April 2007 and July 2008 by the ENVISAT satellite. Chapter 4 deals with the analysis of persistent displacement at Piton de la Fournaise during the 2009 – 2014 period. This chapter consists of a summary of the paper submitted to the Remote Sensing Environment in October 2016. In Chapter 5, we discuss the main similarities and differences of the displacement between 2007 – 2008 and 2009 – 2014 periods. In Chapter 6 we present an analysis of the displacements caused by recent lava flows. The study on Llaima will be presented in Chapter 7. Finally, a final chapter will be devoted to the conclusions and perspectives of this study.

1.5 Project framework

This work is funded by the Chinese Scholarship Council (CSC). CSK data were provided by the Agence Nationale de la Recherche (ANR) through the framework of GEOSUD, ANR-10-EQPX-20 project, ASI through the CSK 2080 project, TSX/TDX data by the Deutsches Zentrum für Luft- und Raumfahrt (DLR) through the LAN 0237 project, ASAR data by the European Space Agency (ESA) through the project Envisat-AO#857 and Category 1 #2899, and PALSAR data by the Japanese Aerospace Exploration Agency (JAXA) through the project #1142. The GNSS data were collected by Observatoire Volcanologique du Piton de la Fournaise/ Institut de Physique du

CHAPTER 1: INTRODUCTION

Globe de Paris (OVPF/IPGP). The GPS data and field mission reports on the Llama during the January 2008 eruption were provided by the Southern Andean Volcano Observatory (OVDAS).

CHAPTER 2 : PRINCIPLES, DATA & METHODOLOGY

2.1 Principles of InSAR

2.1.1 Synthetic Aperture Radar (SAR)

Synthetic Aperture Radar (SAR) is a specific form of radar systems which is used to create images of objects. SAR is typically mounted on a moving platform such as an aircraft or spacecraft, and has its origins in an advanced form of side-looking airborne radar (SLAR). It uses the motion of the radar antenna over a targeted region to provide finer spatial resolution than is possible with conventional beam-scanning radars. It is in 1951 that the mathematician Carl A. Wiley introduced the first time the principle of SAR, which allowed bypassing the technical problem of building a kilometric antenna (in the case of Real Aperture Radar (RAR)) while improving the azimuth resolution (Curlander & McDonough, 1991).

Satellites equipped with SAR sensors have been launched sequentially in last decades, such as the ESR-1, 2, ENVISAT and Sentinel-1, 2 of the European Space Agency (ESA); the RADARSAT-1, 2 of the Canadian Space Agency (CSA); the ALOS-PALSAR 1 and 2 of the Japan Aerospace eXploration Agency (JAXA), the Cosmo-SkyMed Constellation of the Italian Space Agency (ASI), and the TerraSAR-X/TerraDEM-X of the German Aerospace Center (DLR), etc. (Figure 2.1). All of these satellites orbit the earth on a near-polar orbit at an altitude ranging from 200 to 800 km above the earth's surface, depending on the satellite platform carrying the SAR sensor.

Comparing with the optical-mechanical sensors working in the visible and infrared parts of the electromagnetic spectrum of the sun (passive satellite), SAR sensors' illuminating source is microwave energy created by the satellite itself (active satellite). The passage of the SAR signal through the medium is unaffected by darkness or clouds or fog (all weather), in terms of visibility of the ground surface. Therefore, SAR can function 24 hours per day and 365 days per year. The radar signals are emitted with a specific central frequency and the radar systems are associated with specific bands of electromagnetic spectrum (Figure 2.1), such as L-band (1-2 GHz, ~ 24 cm wavelength, e.g. ALOS, JERS 1), S-band (7.5-15cm, e.g. ALMAZ) C-band (5-6 GHz, ~

CHAPTER 2: PRINCIPLES, DATA & METHODOLOGY

6 cm wavelength, e.g. ERS-1, 2, ENVISAT and RADARSAT-1, 2) and X-band (8-12 GHz, ~ 3 cm wavelength, e.g. Cosmo-SkyMed and TerraSAR-X/TerraDEM-X).

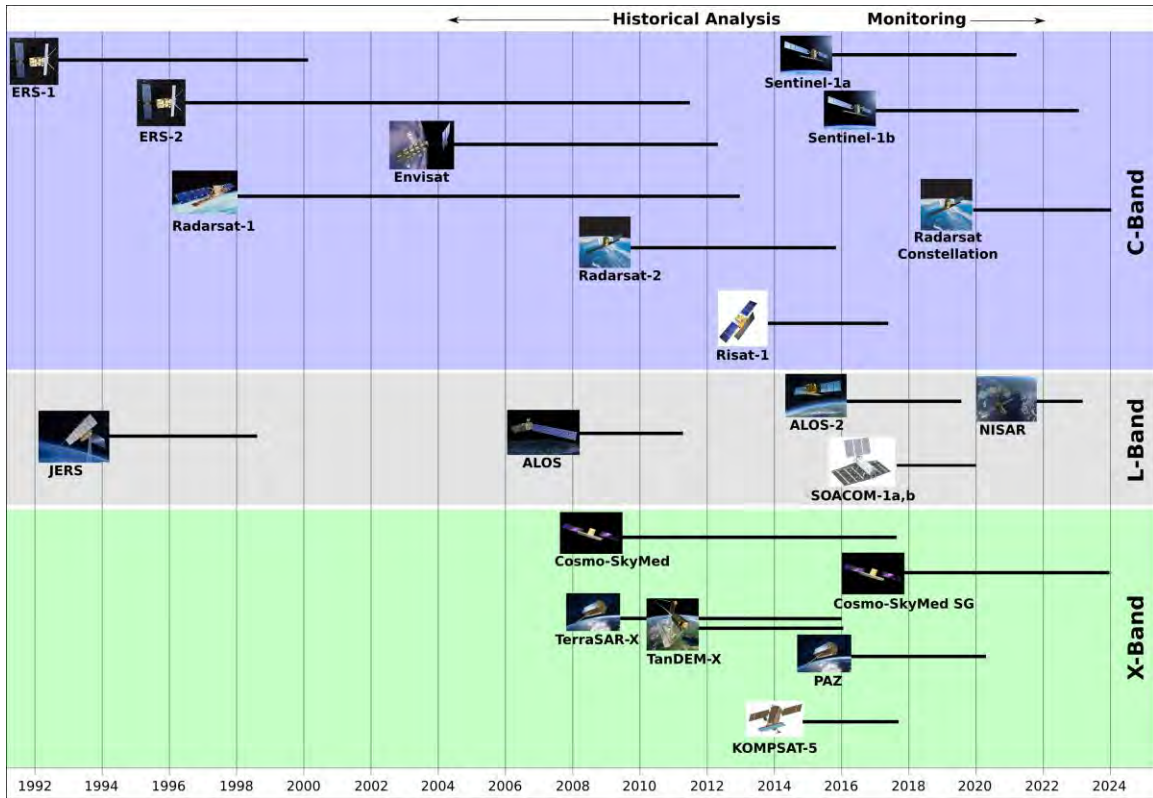


Figure 2.1 Main SAR satellite missions since 1992.

2.1.1.1 Formation of SAR images

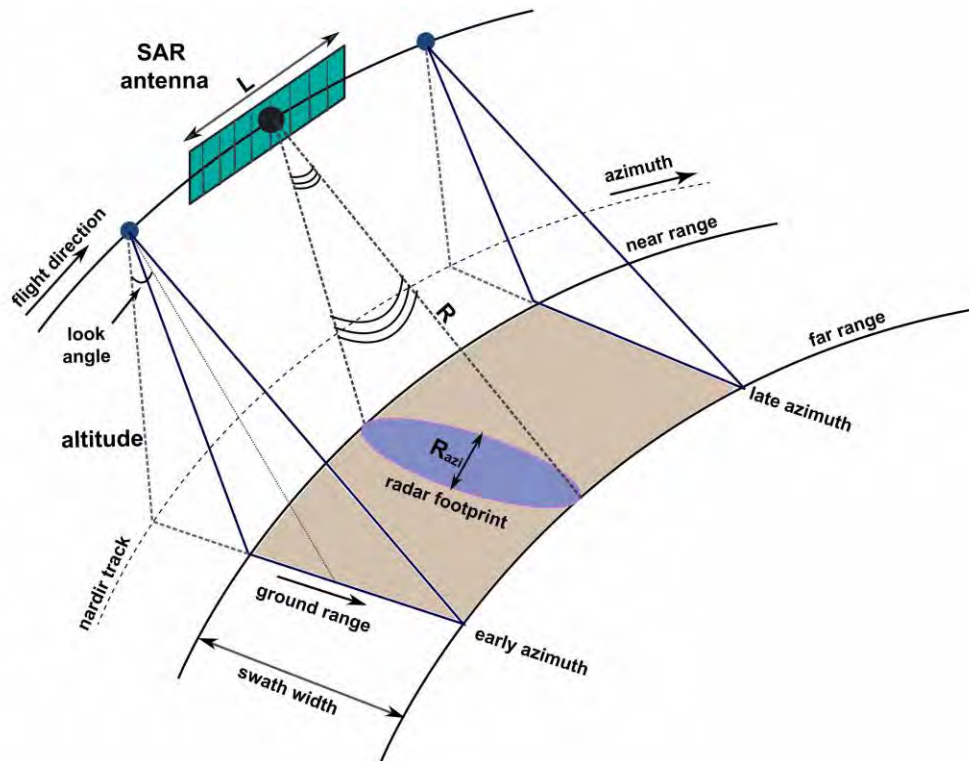


Figure 2.2 Imaging geometry of a SAR acquisition. The footprint of a single pulse is indicated by the purple shaded area. The whole SAR image starts in azimuth at the “early azimuth” time, and lasts until the “late azimuth” time. In range direction, it covers an interval from “near range” to “far range”, which corresponds to the light brown shaded area. (Hanssen, 2001).

The side-looking radar sensors emit millions of signals toward the earth along the line of sight (LOS) (**Figure 2.2**). Some of the signals are absorbed in non-reflective materials (e.g. vegetation); some of them are reflected away from satellite, and some return back to the satellite, referred to as backscattered signals. The backscattered signals are integrated to form a map by the processors on board the satellite. The side-looking configuration of SAR image acquisition (**Figure 2.2**) allows a direct discrimination between two points located at a same distance from the satellite. With such a configuration, the area illuminated by the pulse of electromagnetic wave is elliptical and dependent on the sensor-target distance. The horizontal resolution in range direction (i.e. the direction perpendicular to the satellite trajectory), related to the sensor-target distance, is proportional to the time that the transmitted signal takes to travel the sensor-target-sensor distance (double time). A metric resolution in range can be

achieved by transmitting a long pulse with a linearly modulated frequency, also called chirp (Hanssen, 2001). The resolution in azimuth direction (i.e. the direction parallel to the satellite trajectory) is defined by the Pulse Repetition Frequency (PRF) that is the rate at which the pulses are transmitted. Another important frequency in SAR system is Doppler Central Frequency (Doppler Central Frequency) that defines the operation wavelength of the system and characterizes its propagation and penetration features, as well as the sensitivity of the system in interferometric applications (Massonnet & Feigl., 1998).

Every pixel of a SAR image is characterized by two essential properties: amplitude and phase. Amplitude is associated with the energy of the backscattered signal. A signal is transmitted at a specific energy level when it leaves the sensor. The energy level is changed while the signal reaching the objects on the ground surface. The changing extent is depending on the reflective quality of the object. For example, hard objects (e.g. rocks, buildings) have a high reflective quality, so the amplitude of the reflected signal will be higher than background. To the contrary, soft objects (e.g. wood, crops) have a lower capacity to reflect the incident signals, thereby the amplitude of the reflected signal will be strongly diminished. **Figure 2.3a** corresponds to an amplitude image. The phase values recorded by SAR systems is related to the sensor-target distance and is the key element of the interferometric measurement, in which the signals can be considered as sinusoidal waves, one cycle ($-\pi$ to π) corresponding to the wavelength. **Figure 2.3b** shows a phase image of SAR. The Interferometric SAR (InSAR) will be explained later in next subsection.

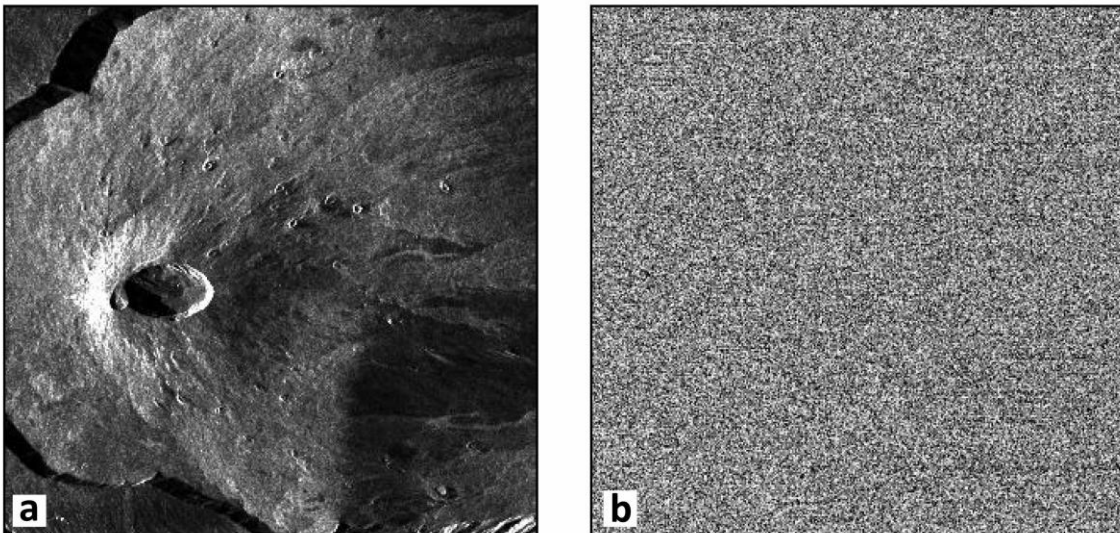


Figure 2.3 An example of SAR image acquired on 9 October 2011 by TanDEM-X ascending satellite over Piton de la Fournaise volcano. (a) Amplitude image. (b) Phase image.

2.1.2 Interferogram

As already mentioned previously, the radar signal is an electromagnetic wave that can be described by a complex number characterized by an amplitude and a phase. The phase carries the information on the path traveled by the wave. From this kind of information, it is possible to measure topography or the deformation of the surface.

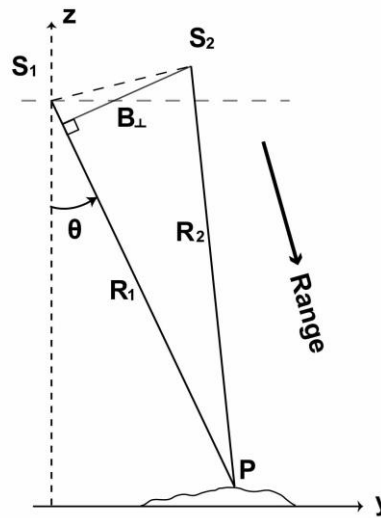


Figure 2.4 Acquisition geometry of two SAR images. S_1 and S_2 represent the location of satellite during the two acquisitions. R_1 and R_2 represent the distances of S_1P and S_2P respectively. B_{\perp} is the perpendicular baseline and θ represents the incidence angle.

With two repeat-pass SAR acquisitions (**Figure 2.4**) over the same area, an interferometric combination is formed by multiplying one SAR image by the complex conjugate of the other. The 2D array of phase differences ranging from $-\pi$ to $+\pi$ in the product image is the so-called an interferogram (**Equation 2.1**, **Figure 2.5**). For one single pixel of the interferogram, the interferometric phase corresponds to the path length (satellite-target) difference of the electromagnetic wave transmitted by the satellite between two different epochs. For a single acquisition, the interferometric phase difference between two pixels corresponds to the path length difference of the electromagnetic wave between two pixels.

Thus the interferogram is a measurement of the spatial and temporal variation of the modification of the mean free path of the electromagnetic wave in a pixel relative to other pixels.

$$\phi = \phi_1 - \phi_2 = -\frac{4\pi}{\lambda} \Delta R + \alpha \quad (2.1)$$

Where ϕ represents the interferometric phase; ϕ_1 and ϕ_2 are the phases of the first and the second acquisition; λ corresponds to the wavelength; $\Delta R = R_1 - R_2$, denotes the path length difference; α represents the phase shift due to different dispersion conditions.

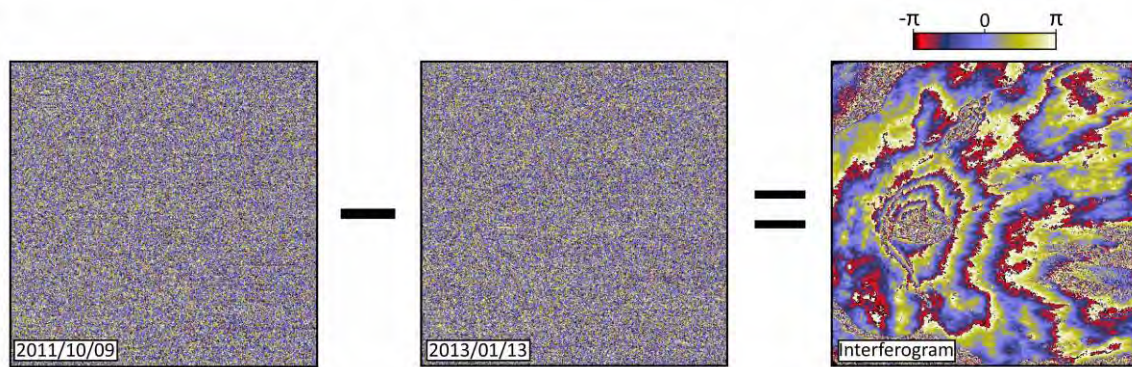


Figure 2.5 An example of two SAR phase images forming an interferogram by subtraction. The SAR images are acquired on 9 October 2011 and 13 January 2013 by TanDEM-X satellite over Piton de la Fournaise volcano.

The two-dimensional radar wave is coherent when it reaches the earth surface. But after being backscattered, it loses its coherence. In fact, the information provided by each pixel in the SAR image correspond to the total contributions of the reflectors within a target cell (Massonnet & Feigl, 1998; Rosen et al., 2000). A SAR image then represents an incoherent image that has no a priori sense. However, considering a second image of the same nature, which contains the same information as the first, with the only difference that the surface has been modified, makes it possible to compute the coherence. The useful information is carried by the difference of the two image, not by a single image (Figure 2.5).

The inspection and analysis of an interferogram is not a trivial task to perform for non-specialists. Apart from noise and decorrelation effects, the interferometric phase are a blend of different signal contributions, as will be discussed later.

2.1.3 Coherence

When an area on the ground appears to have the same surface characterization in all SAR images under analysis, then the images are said to be coherent. If the land surface is disturbed between two acquisitions (e.g. vegetation changed with seasons; mountain has been covered by snow, etc.), those areas will decorrelate (or be incoherent) in the InSAR analysis, leading to noise and no useful information being obtainable.

The coherence of a pixel in an interferogram can be expressed by a value ranging from 0 to 1. It can be defined as the correlation coefficient on a small cell (typically 3×3 pixels) of the interferometric phase:

$$\gamma = \frac{\sum_{cell} u_1 u_2^*}{\sqrt{\sum_{cell} u_1 u_1^* \sum_{cell} u_2 u_2^*}} \quad \gamma \in [0, 1] \quad (2.2)$$

Where, u_1, u_2 are the two complex SAR images (amplitude and phase); u_1^* is the conjugate complex of u_1 ; γ represents the correlation coefficient (coherence). The value of γ close to 1 indicate good coherence of the cell. To the contrary, the value of γ close to 0 indicates the coherence is lost, and it is impossible to detect the relative movement of one pixel with respect to its neighbors. In general, accurate information related to deformation is measurable when the coherence lies 0.5-1. When the coherence gets lower than 0.5, meaningful results can still be produced but it will be affected by varying levels of noise depending the coherence value.

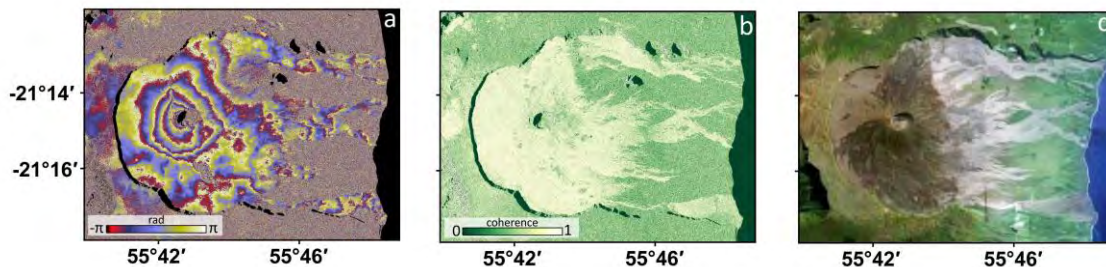


Figure 2.6 Coherence of an interferogram over Piton de la Fournaise. (a) An Cosmo-SkyMed interferogram over Piton de la Fournaise covering the period from 15 February to 27 September 2011. (b) Coherence map of the interferogram. (c) Google Earth satellite image of Piton de la Fournaise.

Figure 2.6a is an interferogram of Piton de la Fournaise covering the period from 15 February to 27 September 2011. The colored bands, referred to as fringes, indicate areas where movement can be measured, revealing areas with high coherence in **Figure 2.6b** (corresponding to areas mainly covered by lava flow in **Figure 2.6c**). SAR images were acquired by Cosmo-SkyMed satellite for which one fringe corresponds to ~ 15 mm of phase change along the LOS. The highly speckled areas indicate where some form of decorrelation arose corresponding to areas with low coherence in **Figure 2.6b** (vegetated areas in **Figure 2.6c**). In these area, the noise level prevents the application of InSAR and no useful information can be extracted.

For an interferogram, its overall coherence is generally affected by: (1) topographic slope and orientation (steep slopes result in low coherence); (2) temporal baselines (the time between two image acquisitions, longer time intervals lead to lower coherence); (3) terrain properties; (4) spatial baselines (the distance between the satellite tracks during the two acquisitions, larger spatial baselines lead to lower coherence); (5) the Doppler center frequency that allows a precise location of the target in azimuth direction (if the recovery of the Doppler spectra of the two acquisition is not maximum, it will necessarily involve a loss of coherence); (6) thermal noise (associated with system characteristics, such as the parameters of antenna, the gain factors, etc.) (Hanssen, 2001; Ducret, 2013).

For one pixel or an area in the interferogram, the coherence is affected by several source of decorrelation: (1) vegetation. The vegetation usually changes a lot the appearance of the surface characterization as the leaves grow, die and move, which is a particular problem for C-band and X-band SAR sensors because of their shorter wavelength than L band. With a longer wavelength, L-band sensors can go through foliage, reflect off objects beneath the vegetation, and then back through the foliage; (2) erosion. In areas where erosion is prevalent, the surface characterization of land can be changed by rain, snowmelt or wind leading to decorrelation; (3) construction. The land surface is changing constantly due to the construction; (4) transient and rapid movement. The surface appearance can be totally destructed or changed by rapid motions such as earthquakes, volcano eruptions, landslides and tsunamis. Sometimes, InSAR can be successful when the rapid movement does not exceed one-half of the wavelength. Otherwise, decorrelation is likely to occur (Massonnet & Feigl, 1998; Hanssen, 2001).

2.1.4 Composition of the interferometric phase

The theoretical Interferometric phase (ϕ) is a combination of several contributions (Hanssen, 2001; Hopper et al., 2007):

$$\phi_{theo} = \phi_{defo} + \phi_{flat} + \phi_{topo} + \phi_{atmo} + \phi_{noise} \quad (2.3)$$

ϕ_{defo} is the phase due to LOS range change caused by ground deformation (due to tectonic or anthropogenic causes) between the two SAR acquisition times. It is the contribution we are interested in.

ϕ_{flat} is the phase contribution due to a curvature of the earth. The acquisition geometry of SAR introduces a signal into the interferogram, which is called “flat earth” (ϕ_{flat}). It corresponds to numerous interferometric fringes parallel to satellite flight direction. If we consider two point P and P' located at the same altitude (**Figure 2.7a**), the path S_1P (S_2P) will be longer than the path S_1P' (S_2P'). This path difference (ΔR_{SR}) will introduce a phase shift in range, which can be estimated using satellite orbits:

$$\phi_{flat} = \frac{4\pi}{\lambda} \frac{B_{\perp}}{R_1 \tan \theta} \Delta R_{SR} \quad (2.4)$$

Where in **Equation 2.4** λ corresponds to the wavelength; R_1 denotes the satellite-target path length of the first acquisition; θ is the look angle; B_{\perp} is the perpendicular baseline between two acquisitions. The operation that corrects the interferogram from the phase contribution of “flat earth” is called interferogram flattening.

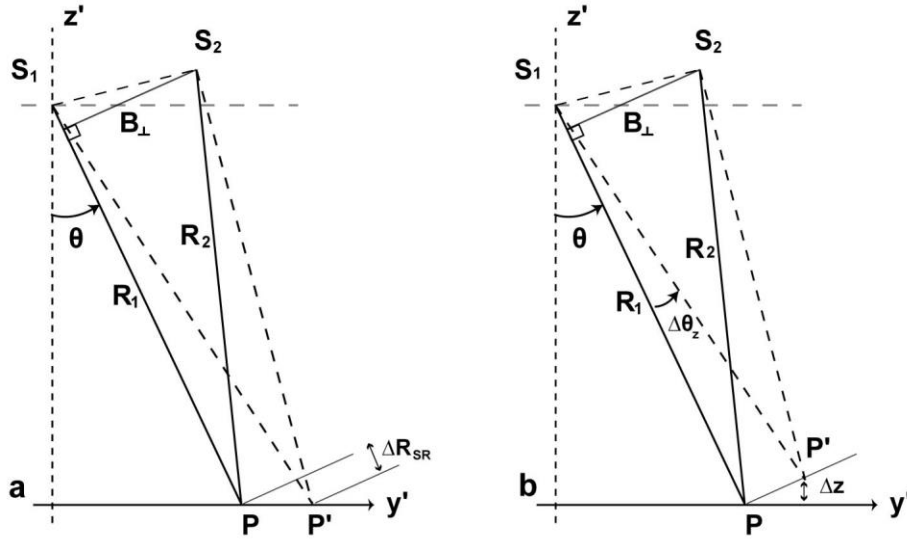


Figure 2.7 Interferometric phase contribution due to the “flat earth” and topography. (a) Acquisition geometry of two SAR images assessing the estimation of the “flat earth” term. (b) Acquisition geometry of two SAR images assessing the estimation of the topographic term. S_1 and S_2 represent the location of satellite during the two acquisitions. R_1 and R_2 represent the distances of S_1P and S_2P respectively. B_{\perp} is the perpendicular baseline and θ represents the incidence angle. ΔR_{SR} (a) is the path difference between S_1P (S_2P) and S_1P' (S_2P'), where P and P' represent two points located at the same altitude. Δz (b) is the height difference between the two points P and P' located at different altitude (Hanssen, 2001).

ϕ_{topo} is the phase contribution due to the height of target above a reference surface that is typically the reference geoid. Topography also introduce a variation of look angle resulting in a phase difference between two points P and P' (Figure 2.7b). This term of phase can be expressed as:

$$\phi_{topo} = \frac{4\pi}{\lambda} \frac{B_{\perp}}{R_1 \sin \theta} \Delta z \quad (2.5)$$

When $\phi_{topo} = 2\pi$,

$$\Delta z_{2\pi} = \frac{\lambda R_1 \sin \theta}{2 B_{\perp}} \quad (2.6)$$

Where $\Delta z_{2\pi}$, the altitude of ambiguity, i.e. the elevation change correspondent to a 2π phase shift, is a parameter proposed by Massonnet & Rabaute (1993) to reflect the sensibility of interferometric phase to altitude variation. $\Delta z_{2\pi}$ is inversely proportional to the perpendicular

baseline (B_{\perp}). In a topography measurement, if the B_{\perp} is too short, the interferometric phase will be less sensitive to the altitude variation and the measured altitude will be less accurate; but if the B_{\perp} is too long exceeding a certain limit, the interferometric signals will decorrelate and no fringes can be generated.

In the “two-pass” InSAR, the topographic phase contribution can be simulated and eliminated by using a DEM (Zebker & Goldstein, 1986).

ϕ_{atmo} is the phase linked to the spatio-temporal variations of the refractive index of atmosphere. This component of interferometric phase will be discussed in detail in Section 2.5.

ϕ_{noise} is the noise term due to variability in scattering, thermal noise, coregistration errors and uncertainty in the position of the phase center in azimuth (Hooper et al., 2007).

However, after the correction of ϕ_{flat} and ϕ_{topo} , some error sources such as orbital errors and DEM errors are always introduced in the observed interferometric phase (ϕ_{obs}):

$$\phi_{obs} = \phi_{defo} + \phi_{atmo} + \Delta\phi_{orbit} + \Delta\phi_{dem} + \phi_{noise} \quad (2.7)$$

where, ϕ_{orbit} is the phase component due to the errors in satellite state vectors. If the two orbits during the two acquisitions are strictly parallel, fringes parallel to these orbits are observed in the interferogram. These fringes reflect a linear evolution of the phase. However, an exact parallel between the orbits is barely the case, hence the associated fringes generally present a certain number of incurvations. Nevertheless, the linear trend is well conserved in the first order.

The simplest way to reduce these residual orbital fringes is to use the precise location of the orbits, which are generally re-calculated several hours to several days after the satellite passes over the area of interest. However the re-estimations of precise satellite orbit are only available for satellites of ESA. In most cases, the orbital fringes are simulated by empirical functions, for example a linear equation: $\phi_{orbit} = ax + by + l$, where x and y correspond the coordinates of pixel in the interferogram, and a , b , and l are parameters for estimating.

ϕ_{dem} represents the residual phase due to look angle error that is due almost entirely to error in the DEM, thereby, ϕ_{dem} is commonly referred to as DEM error. As shown in **Equation**

2.5. The topographic phase (ϕ_{topo}) is proportional to the perpendicular baseline B_{\perp} between the two SAR images forming the interferogram. Therefore errors in the DEM lead to baseline-dependent phase residual in the interferograms, which results in errors in the measurement of ground displacement (Berardino et al., 2002; Hooper et al., 2007). This part of phase contribution can be estimated based on its dependency on B_{\perp} (Hooper et al., 2007; Fattahi & Amelung, 2013).

2.2 Data used in the study

The images acquired by SAR satellites and the data recorded by Global Navigation Satellite System (GNSS) are both used in this study.

2.2.1 SAR data

The SAR images used in this study were acquired by four earth observation satellites: COSMO-SkyMed (Constellation of Small Satellites for the Mediterranean basin Observation, hereinafter named CSK), TerraSAR-X/TanDEM-X (hereinafter named TSX/TDX), ENVISAT, and ALOS (Advanced Land Observing Satellite). The four satellites are all in sun-synchronous polar orbits. Ascending images are acquired when the satellite goes towards the North Pole. Descending images are acquired when the satellite goes towards the South Pole. The main features of the four satellites are illustrated in **Table 2.1**.

Satellite (Radar)	CSK	TSX/TDX	ENVISAT (ASAR)	ALOS (PALSAR)
Agency	ASI	DLR	ESA	JAXA
Launch date	June 2007, December 2007, November 2010 (CSK-1, 2, 4) ^a	June 2007/ June 2010	March 2002	January 2002 (ALOS-1) ^b
Band/Wavelength	X band/3.1 cm	X band/3.1 cm	C band/5.6 cm	L band/23.6 cm
Revisit time	16 days	11 days	35 days	46 days
Number of tracks ^c for PdF (A/D) ^d	1/1	1/1	3/2	-
Number of tracks for Llaima (A/D)	-	-	0/1	1/0

Table 2.1 Main features of the satellites used in this study.

^a number of satellites (The data used is acquired by CSK-1, 2, and 4).

^b The data used is acquired by the first satellite ALOS-1.

^c InSAR is applicable only when the two images are from the same orbital track.

^d A and D correspond respectively to Ascending and Descending pass.

2.2.1.1 TSX/TDX and CSK data

As X band satellites have been successively launched, the X band data has shown great potentialities for ground deformation monitoring. The X band data in the study provides an ~3 m spatial resolution (**Table 2.2**), which is much finer with respect to C band and L band data leading to an excellent performance not only on high coherency targets identification but also on high accuracy mapping and monitoring (Prati et al., 2010; Herrera et al., 2011; Bovenga et al., 2012). Furthermore, the advantage of frequent revisit over the same interesting zone (11 days for TSX/TDX and 16 days for CSK) makes it possible to understand the detailed temporal deformation behavior and identify a fast varying or non-linear deformation that might be suggested as linear trend by C-band data (Sansosti et al., 2010). Additionally, the shorter wavelength (~ 0.03 m) of X band makes it more capable than longer wavelength bands to detect low or very low amplitude displacement since the sensitivity to ground displacement increases as the wavelength decreases.

The introduction of the X band SAR data acquired by TSX/TDX and CSK satellites covering the Piton de la Fournaise volcano is detailed in **Table 2.2**.

Satellite		TSX/TDX		CSK	
Acquisition mode		StripMap	StripMap	StripMap (HIMAGE)	StripMap (HIMAGE)
Acquisition direction		Right side	Right side	Right side	Right side
Product type		SLC	SLC	SLC	SLC
Beam/ Swath/Track		strip_008/-/68	strip_010/-/121	-/15/-	-/18/-
Pass ^a		A	D	A	D
Incidence angle (°)		33.5	36.5	48.8	52.2
Resolution (m)	ΔR^b	3.23	1.94	3	3
	ΔA^c	3.3	3.3	3	3
Number of		56	34	43	43

acquisitions				
Time spans	2009/03/07 - 2014/11/15	2008/12/13 - 2014/10/06	2011/02/15 - 2014/09/19	2011/02/15 - 2014/09/19

Table 2.2 Summary of the X-band (TSX/TDX and CSK) data used for Piton de la Fournaise volcano.

^a A and D correspond respectively to Ascending and Descending pass.

^b ΔR represents the resolution in Range direction.

^c ΔA represents the resolution in Azimuth direction.

The TSX/TDX and the CSK satellites have similar acquisition modes including ScanSAR mode, StripMap mode and SpotLight mode (**Figure 2.8** and **Figure 2.9**). Both of 90 TSX/TDX and 86 CSK Single Look Complex (SLC) images were obtained in the StripMap mode and from Right-look side direction. In StripMap acquisition mode, the ground swath is illuminated with continuous sequence of pulses and the antenna beam is fixed in azimuth and elevation, which results in an image with continuous image quality in flight direction.

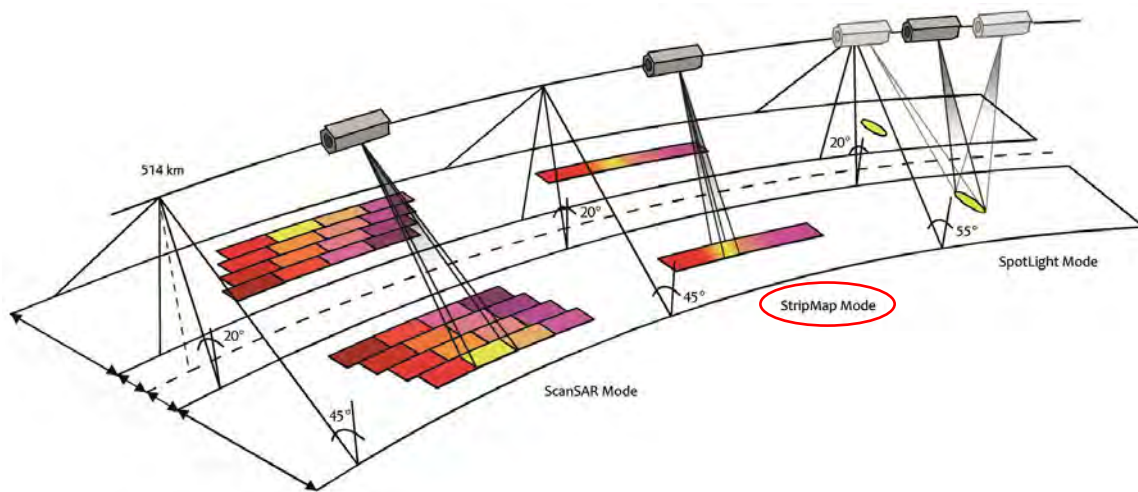


Figure 2.8 TerraSAR-X/TanDEM-X acquisition modes. The red ellipse indicates the acquisition mode of the CSK data used in this study.

56 of the TSX/TDX images were obtained from ascending pass spanning from 7 March 2009 to 15 November 2014, and 34 of them were acquired from descending pass spanning the period between 13 December 2008 and 6 October 2014. The CSK dataset is consist of 43

ascending and 43 descending images that share the same period of time (between 15 February 2011 and 19 September 2014).

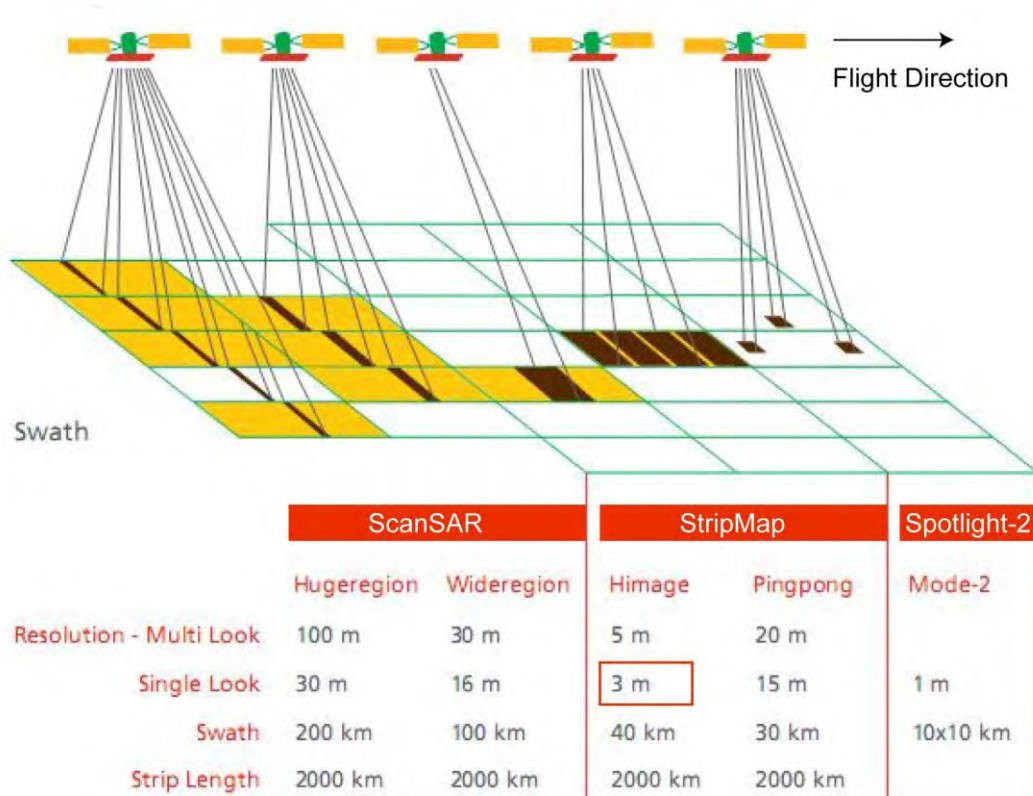


Figure 2.9 COSMO-SkyMed acquisition modes and related characteristics. The red rectangle indicates the acquisition mode of the TSX/TDX data used in this study.

Figure 2.10 illustrates the temporal distribution of the two satellites datasets. The detailed dates of the X band data is listed in [Appendix 1](#). The CSK-A and CSK-D share the exactly same acquisition dates. The minimum time interval between two acquisitions is 16 days. The data is evenly distributed between February 2011 and February 2012, and between June 2013 and September 2014. However, there is a time gap of more than one year between February 2012 and June 2013. One eruption at Piton de la Fournaise occurred (June 2014) during the CSK spanning period. Comparing with CSK data, the TSX/TDX data spans about two years longer. Its minimum time interval between two acquisitions is 11 days. The TSX/TDX-A data distributes relatively uniform except for the one year gap between October 2010 and October 2011. The TSX/TDX-D data concentrates in the first two years (2009-2011) but distributes sporadically during the rest years (2011-2015). 7 eruptions occurred during the TSX/TDX spanning period.

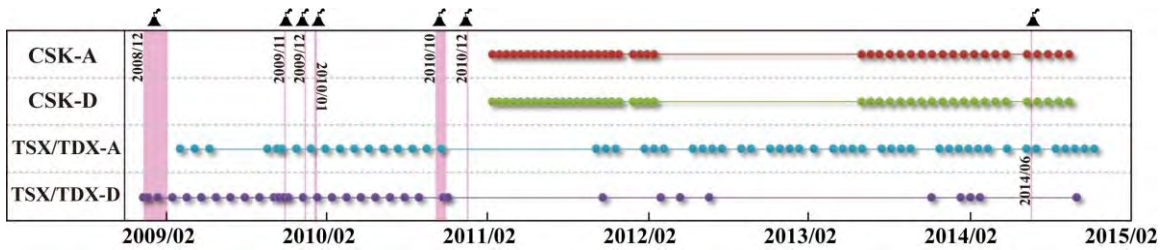


Figure 2.10 Temporal distribution of CSK and TSX/TDX data used for Piton de la Fournaise volcano. The pink areas indicate the period of eruptive activities during the study period. The CSK-A and -D represent CSK ascending and descending data (similarly for TSX/TDX-A and -D).

2.2.1.2 ENVISAT-ASAR data

The ASAR instrument on board the ENVISAT satellite operates as a conventional StripMap SAR or as a ScanSAR. The former includes Image Mode and Wave Mode, and the latter includes Wide Swath Mode, Global Monitoring Mode and Alternating Polarisation Mode. The used ASAR data over the Piton de la Fournaise volcano (**Table 2.3**) was acquired in the Image Mode, in which ASAR operates in one of seven predetermined swaths with either vertically or horizontally polarized radiation (see **Figure 2.11**).

Acquisition mode		StripMap (Image mode)				
Acquisition direction		Right side				
Swath		2	5	6	7	
Track		313	399	277	005	170
Pass ^a		A	A	D	D	A
Incidence angle (°)		20.9	39.0	40.4	44.0	45.9
Resolution (m)	ΔR^b	21.48	14.88	14.47	13.50	13.77
	ΔA^c	5.74	4.6	5.61	4.64	4.64
Number of acquisitions		5	6	5	4	6
Acquisition date		2007/04/24	2007/04/30	2007/04/22	2007/05/08	2007/04/14
		2007/05/25	2007/06/04	2007/05/27	2007/06/14	2007/05/19
		2007/08/07	2007/11/26	2007/11/18	2008/01/08	2007/06/03
		2007/09/11	2007/12/31	2008/01/27	2008/08/05	2007/07/28
		2008/05/13	2008/04/14	2008/08/24	-	2007/09/01
		-	2008/07/27	-	-	2008/07/12

Table 2.3 Summary of the ASAR data used for Piton de la Fournaise volcano.

^a A and D correspond respectively to Ascending and Descending pass.

^b ΔR represents the resolution in Range direction.

^c ΔA represents the resolution in Azimuth direction.

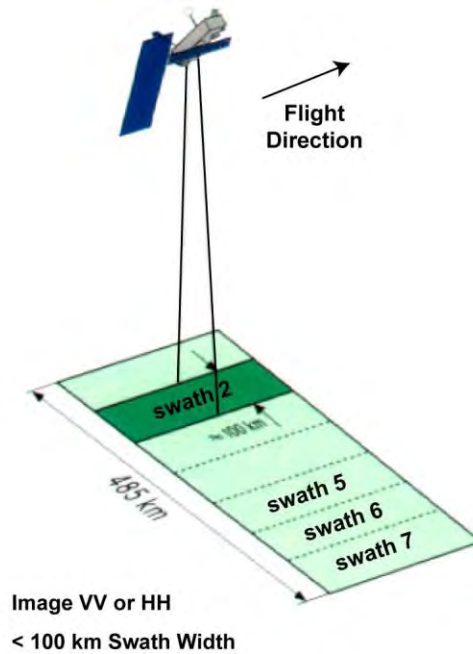


Figure 2.11 ASAR Image acquisition mode. (© ESA)

Six ASAR image acquired in Image mode, swath 2 and descending track 10 are analyzed in the Llama study case. The images are acquired between 2003 and 2008 (2003/11/25, 2004/03/09, 2007/04/03, 2007/05/08, 2008/01/08 and 2008/11/18).

2.2.1.3 ALOS-PALSAR data

PALSAR is an L band radar on board the ALOS satellite that can change off-nadir angle in the range from 9.7 to 50.8 degrees (**Figure 2.12**). PALSAR has a high resolution observation mode and a wide area observation mode (ScanSAR). Eight PALSAR images of ascending track 117 and seven of ascending track 116 acquired in the Fine Beam Single Polarization Mode (high resolution mode) between 2007 and 2011 (track 117: 2007/03/06, 2007/06/06, 2007/12/07, 2008/01/22, 2008/03/08, 2009/03/11, 2009/04/29, and 2011/03/17; track 116: 2007/02/17, 2007/04/04, 2007/11/20, 2008/02/20, 2009/02/22, 2011/01/13, and 2011/02/28) are used for

InSAR observation at Llaima volcano. The data was obtained at off-nadir 34.3 degrees where the spatial resolution can reach 10 m.

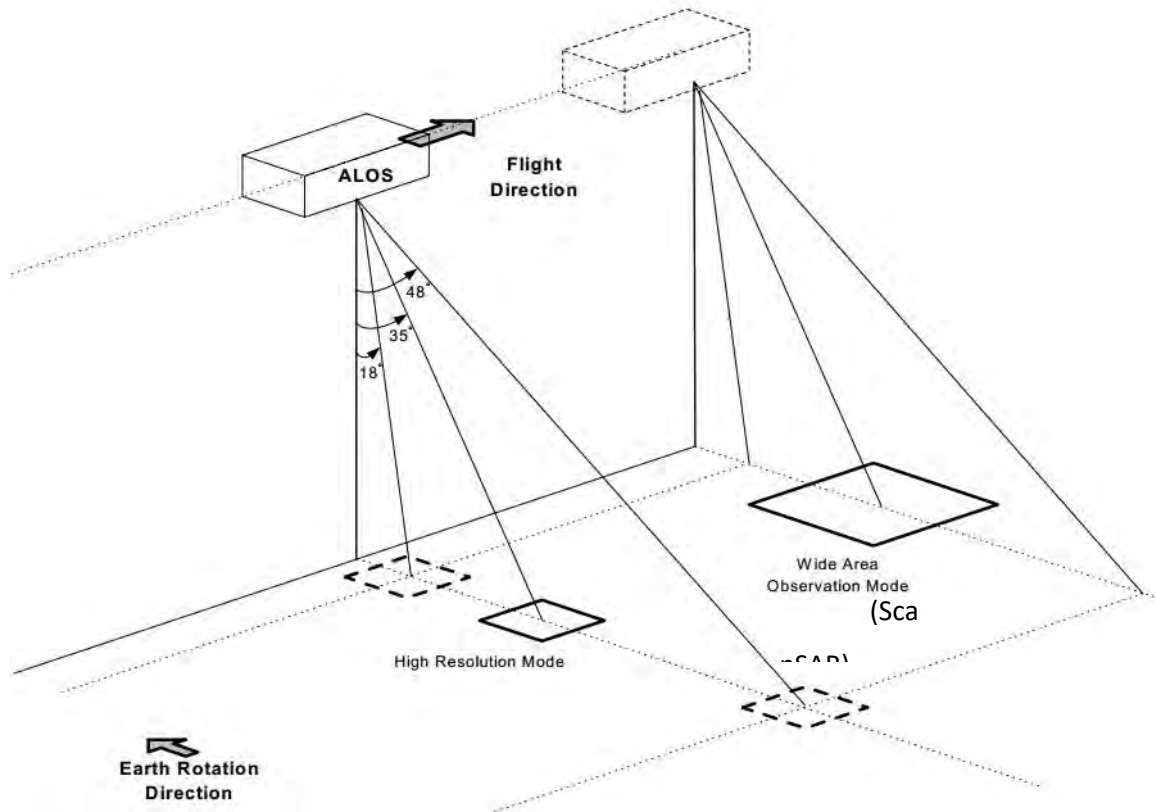


Figure 2.12 ALOS PALSAR observation concept. (© JAXA)

2.2.2 GNSS data

The permanent GNSS network is operated by the Volcanological Observatory of Piton de la Fournaise (OVPF). Piton de la Fournaise has been being monitored by GNSS technique since the first stations were installed in 2001-2002 (**Figure 2.13**). The stations around the summit craters (DERG, BORG, SNEG, and DSRG) and the reference station GITG located outside of the Enclos Fouqué caldera were not permanent until 2004 when the second reference station ENCG was installed. The network extended to the flank of the Central Cone in 2005-2006 when five stations were installed (FERG, FORG, FJSG, RIVG, and CHAG), and four of them were dismantled later and replaced by four new stations (FOAG, FJAG, RVLG, ENOG). Six stations have been progressively installed since 2009, 2 years after the historical eruption in March-April 2007. Two

stations outside of the Enclos Fouqué caldera and close to the coastline (CASG and TRCG) were installed in 2008 and 2010 respectively. With the newest four stations (FREG, PRAG, PBRG, FEUG) installed in 2012-2013, the density of the network is further increased. By the end of 2015, ten stations are located on the Central Cone, six on the Eastern Flank and eight outside of the Enclos Fouqué caldera (**Figure 2.13**; refer to <http://volobsis.ipgp.fr/index.php?page=gps> and <https://gpscope.dt.insu.cnrs.fr/chantiers/reunion/> for more information of GNSS network or download GNSS data). The densification of the GNSS network at Piton de la Fournaise allows improving the knowledge of sophisticated processes going on in the volcanic edifice with a sufficient space and time resolution (Got et al., 2013; Rivet et al., 2014; Peltier et al., 2015a).

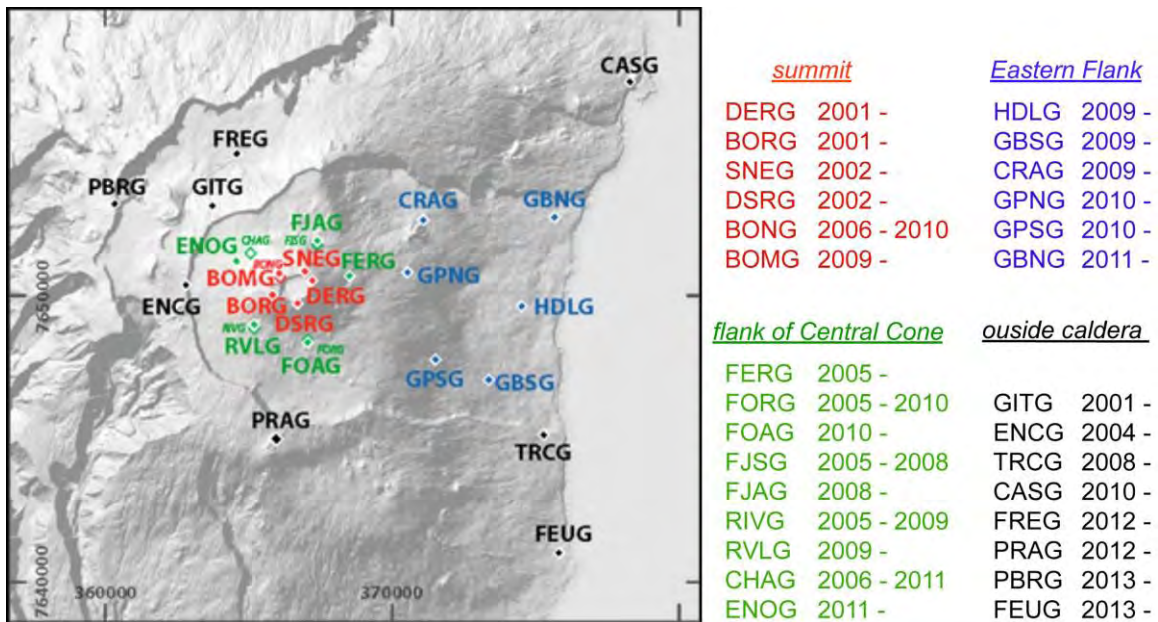


Figure 2.13 GNSS network (left) and the working period (right) at Piton de la Fournaise volcano (in red: the stations installed at the volcanic summit; in green: the stations installed on the flank of the Central Cone; in blue: the stations on the Eastern Flank; in black: the stations outside of the Enclos Fouqué caldera). The white diamonds with colored borders and labelled with small font size represent the dismantled stations. (Peltier et al., 2015a).

In this study, 6 GNSS stations located on the Eastern Flank (HDLG, GBSG, CRAG, GPNG, GPSG, and GBNG) are used in order to better understand the ground motions of the Eastern Flank and to validate the InSAR-derived results. The receivers record one measurement every 30 s. The daily GNSS solutions were processed using GAMIT/GLOBK software (Herring et al., 2010) by Peltier et al. (2015a). The 1σ accuracies of the daily positions are ~ 5 mm and ~ 10 mm for

horizontal and vertical components, respectively. The precise ground displacement time series in three dimensions (up-down, U-D; east-west, E-W; north-south, N-S) at each GNSS station were then obtained after having been corrected from plate motion using the data recorded at the REUN IGS station (**Figure 3.2**), that located about 15 km west of the volcanic summit and as the ground displacement observed at this station is considered to be mainly affected by the plate motion.

2.3 InSAR processing

The interferometric processing can start either with unfocused raw SAR data or focused complex SAR data (sometimes referred to as Single-Look Complex (SLC) data). The raw SAR data is often preferred over SLC data, because the price is usually cheaper, can be delivered faster, and exclude the possibility of different focusing strategies at the various processing facilities ([Hanssen 2001](#)). Whether the raw data or the SLC data is used, the InSAR processing steps are similar with only one exception, the azimuth filtering. The azimuth filtering is not necessary while using raw data because the mean of the Doppler Centroid Frequencies of both master and slave images can be used in image focusing. However for SLC data, the azimuth filtering is usually required to suppress the noise introduced by the non-overlapping parts of the image spectra since the data are focused with respect to the zero-Doppler Frequency. The InSAR processing steps is summarized in **Figure 2.14**.

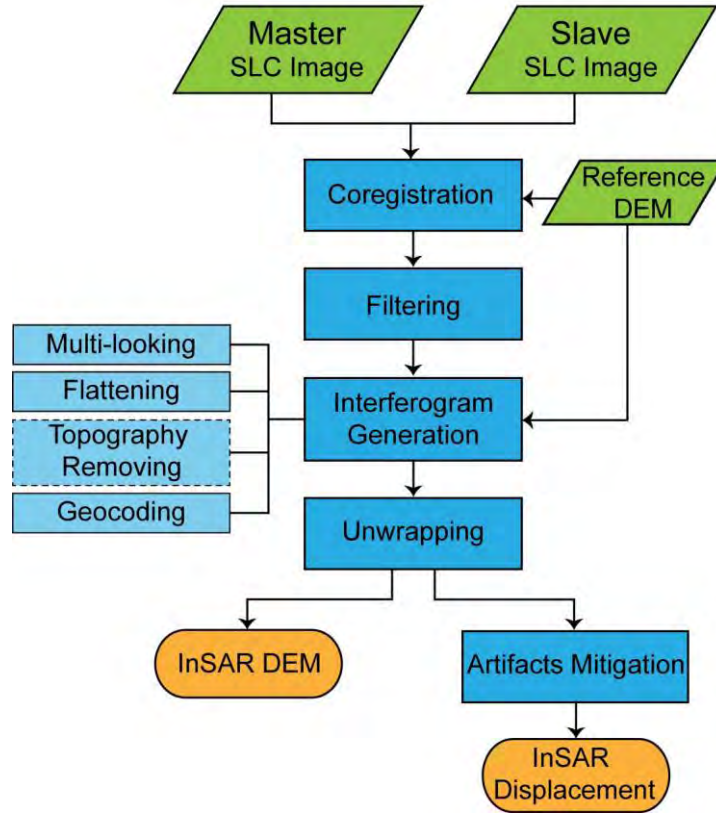


Figure 2.14 Flowchart of InSAR processing.

2.3.1 Coregistration of SAR images

The coregistration step is fundamental in interferogram generation, as it ensures that each ground target contributes to the same pixel in both SAR images. High precision InSAR requires subpixel-to-subpixel match between SAR image pairs. So the alignments of SAR images from two acquisitions, i.e. the coregistration, is an essential step for accurate determination of phase difference. The typical InSAR coregistration consists of two steps (Brown, 1992; Hanssen, 2001): (1) coarse coregistration; and (2) fine coregistration. In the coarse coregistration, the SAR images are coregistered at one/two pixels accuracy. One of the two SAR images is assigned as the master image (reference) and another one is the slave (match) image. In the process, the coarse image offsets in range and azimuth are searched for based on the cross-correlation of amplitude (Li & Goldstein, 1990) and then the slave image is shifted. The fine coregistration is implemented for subpixel accuracy. The subpixel (e.g. 1/10 pixel (Hanssen & Bamler, 1999)) tie points are searched for based on the cross-correlation of amplitude (Kwoh et al., 1994; Rufino et

al., 1998) or complex data (amplitude and phase) (Prati & Rocca, 1990). With the coordinates of these tie points in master and slave images, a polynomial function (e.g. **Equation 2.8**) can be estimated to make the transformation from the geometry of slave image to that of master image, in both range and azimuth directions. After the transformation equations are set up, the slave image is resampled according the subpixel transformation.

$$\begin{cases} X = Ax^2 + Bx + Cy + D \\ Y = Ex^2 + Fx + Gy + H \end{cases} \quad (2.8)$$

Where, (x, y) are the range and azimuth coordinates respectively of tie points of slave image; (X, Y) are the range and azimuth coordinates respectively of tie points of master image; $A, B, C, \dots H$ are the parameters to be estimated.

Generally, the use of a DEM enables improving the data coregistration accuracy especially working with high resolution data and in mountainous or hilly areas with large range of topography.

2.3.2 Filtering in range and azimuth

If the interferogram is generated without further processing, the phase noise in the interferogram can result in high number of residuals in the phase unwrapping, and thus hamper the data interpretation (Hanssen, 2001). Therefore, a spectral shift filtering is generally applied to the SAR images before interferogram generation aiming at eliminating the noise in the data and increasing the SNR (Signal-Noise-Ratio) of the product (Gatelli et al., 1994; Just & Bamler, 1994; Goldstein & Werner, 1998). This spectral shift filtering can be applied in range and azimuth directions based on slightly different approaches.

The origin of the spectral shift problem is the difference between the object spectrum and the data spectrum. The object spectrum is a property of its own, and the radar reflectivity of the object is independent of the imaging system. In contrast, the data spectrum is a characteristic of the image system, whose bandwidth contains the measurable width of the spectrum, and whose Nyquist frequency is determined by the system's sampling frequency (**Figure 2.15a**; Hanssen, 2001).

In the ideal case, the object spectrum should be mapped identically to the data spectrum in order to implement interferometry. However, in practice, the difference in the local incidence angles towards the two sensors (see **Figure 2.15b**; [Hanssen, 2001](#)) lead to a spectral shift (a wavenumber shift- the wavenumbers of the object spectrum have shifted to other frequencies in the data spectrum) in range direction. In **Figure 2.15a**, the correlated spectral contributions (overlapping spectral parts S_1 and S_2) correspond information, and the non-correlated spectral contributions (non-overlapping parts N_1 and N_2) can be considered as noise for interferometric purpose. Therefore, a bandpass filter is required to eliminate the two non-overlapping parts containing noise. This kind of filtering in range can yield a significant increase in correlation between two SAR images at the expense of a reduced resolution ([Gatelli et al., 1994](#)). So sometimes no filtering is preferred before interferogram generation in order to remain the finer resolution for identification of persistent scatterers ([Hooper et al., 2007](#)).

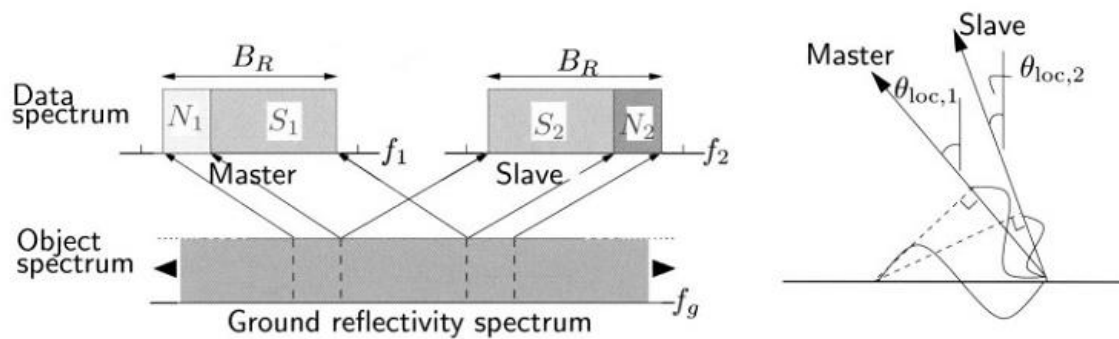


Figure 2.15 Mapping of the wavenumber domain in the object spectrum of the ground reflectivity spectrum to the frequency domain in the SAR data spectrum. (a) The same wavenumber shift in the two SAR data spectra is due to the different mapping of the object spectrum onto the data spectra of the two images. (b) The different local incidence angles, θ_{loc} , resulting in different projections, causes the wavenumber shift in range. ([Hanssen, 2001](#)).

The spectral shift in azimuth direction is due to a possible variation in the antenna pointing, for example the Doppler centroid between the two acquisitions. The difference of Doppler centroid frequencies is a result of a difference in the squint angle of the radar antennas (**Figure 2.16**; [Ferretti et al., 2007](#)). Similar as in range direction, the non-overlapping parts of the spectrum will result in noise in the interferogram. In order to remove these parts of spectrum, bandpass azimuth filtering can be performed. The filter bandwidth should keep the common bandwidth that is represented in the lower plot of Figure by the shade area.

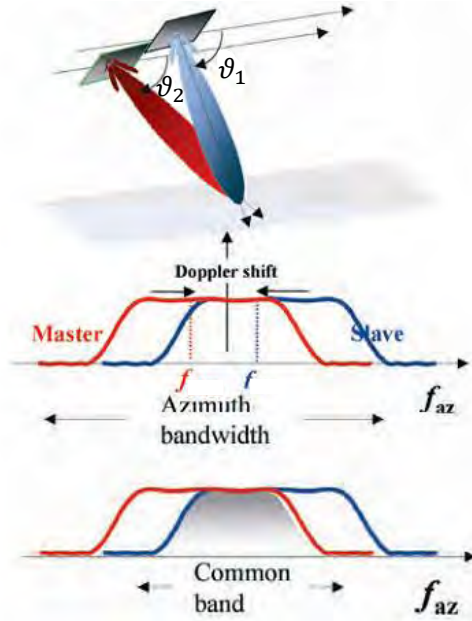


Figure 2.16 In azimuth direction, the shift is due to the change in squint angle (ϑ) during the two acquisitions. The filtering in azimuth direction is required to remove the uncorrelated spectral parts and remain the common band. (Ferretti et al., 2007).

2.3.3 Interferogram generation

After having been coregistered and filtered (in range and azimuth), the two SAR images (containing amplitude and phase) can be used for computing a complex interferogram (Gabriel & Goldstein, 1988):

$$y_1 y_2^* = |y_1| \exp(j\phi_1) |y_2| \exp(-j\phi_2) = |y_1| |y_2| \exp(j(\phi_1 - \phi_2)) \quad (2.9)$$

Where $\phi = \phi_1 - \phi_2$ is the interferometric phase (See **Equation 2.1**); y_1 and y_2 refer to the master and slave complex images respectively. Even though the interferometric phase ϕ is the most important information for InSAR, the complex interferogram is usually retained for future computations.

The complex interferogram obtained from **Equation 2.9** is usually noisy although the a prior filtering has been applied. It is common practice to decrease the noise level of the interferogram by simply averaging complex interferogram data in a specified window. This processing is defined as complex “multi-looking” (Goldstein et al., 1988; Lee et al., 1998), trading

geometric resolution for phase accuracy. Multi-looking can be performed simultaneously with the complex interferogram generation and it is in general applied to a range-azimuth ratio yielding approximately square pixels.

The interferogram can be flattened with respect to a reference ellipsoid such as WGS84 (see ϕ_{flat} in Section 2.1.4) and is corrected from topographic contribution based on a DEM (see ϕ_{topo} in Section 2.1.4) once it is generated. Geocoding is the last step in the interferogram generation chain show in the flowchart in **Figure 2.14** referring to a transformation of the radar coordinates (range/azimuth/height) to coordinates in a convenient geodetic reference system such as WGS84 (latitude/longitude/height above the reference ellipsoid).

2.3.4 Interferogram unwrapping

The interferogram provides an intrinsically ambiguous and relative information because the interferometric phase (ϕ) is measured modulo 2π rad (**Equation 2.10; Figure 2.17**). In order to obtain the absolute phase (ψ) along the LOS direction, the number of phase cycles n (fringes on the interferograms) needs to be properly defined. This process of seeking and adding the correct integer ambiguity number (n) of 2π to the interferometric fringes is called phase unwrapping (**Figure 2.17**).

$$\psi = \phi + 2\pi \cdot n \quad (2.10)$$

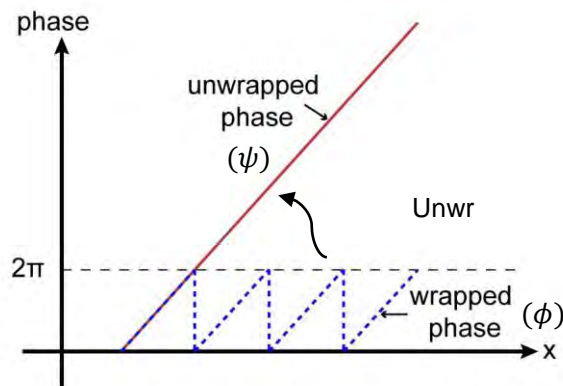


Figure 2.17 Schematic diagram of the interferometric phase unwrapping.

Figure 2.18 shows an example of unwrapping result based on an interferogram over Piton de la Fournaise volcano.

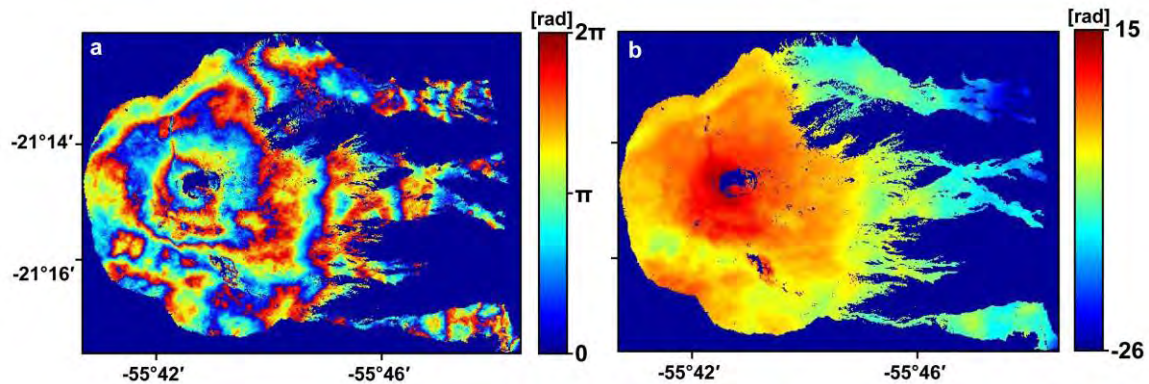


Figure 2.18 Example of wrapped and unwrapped interferograms over Piton de la Fournaise. (a) Wrapped interferogram computed from two CSK images (temporal baseline $B_t=64$ days, perpendicular baseline $B_{\perp}=217$ m). (b) Corresponding unwrapped interferogram.

Several algorithms for phase unwrapping have been developed, such as the branch-cut algorithm (Goldstein et al., 1988), least-square algorithm (Ghiglia & Romero, 1994, 1996; Pritt, 1996), minimal cost flow algorithm (Costantini, 1998; Chen & Zebker, 2000). Nowadays, the two dimensional (2D) statistical-cost network-flow unwrapping method, SNAPHU (Chen & Zebker, 2000), is widely accepted and used for interferogram unwrapping. Most recently, with the exciting areas turning to the InSAR time series analysis that provides three dimensional (3D) wrapped phase data, the third dimension being that of time. New algorithms thus have been developed taking advantage of the third dimension including branch-cut algorithms (Huntley, 2001; Cusack & Papadakis, 2002; Salfity et al., 2006), an integer least-square algorithm (Jenkinson, 2003), and the advanced 3D unwrapping algorithm (Hooper & Zebker, 2007), among which, the advanced 3D unwrapping algorithm (Hooper & Zebker, 2007) can be directly applied to InSAR time series and has been implemented in some InSAR time series analysis software, e.g. StaMPS/MTI for Persistent Scattered (PS), Small Baseline (SB), and Multi-Temporal (MT) InSAR processing (Hooper et al., 2012).

2.3.5 Mitigation of non-deformation contribution

Non-deformation phase contribution, including atmospheric artifacts (ϕ_{atmo}), orbital errors ($\Delta\phi_{orbit}$) and DEM error ($\Delta\phi_{dem}$), need to be estimated and corrected from the interferogram in order to retrieve the ground deformation. These non-deformation contribution, in particular the $\Delta\phi_{orbit}$ and ϕ_{atmo} are traditionally considered as the main limitation of InSAR measure long-wave length displacement. As already mentioned in [Section 2.1.4](#), the orbital errors can be simply modeled using a linear or quadratic surface that fits to the interferometric phases ([Massonnet & Feigl 1998](#)), and the DEM error is estimated based on its proportional dependency on the perpendicular baseline ([Hooper et al., 2007](#); [Fattahi & Amelung, 2013](#)). A variety of strategies are available to estimate the atmospheric artifacts including methods based on external data and methods based on the interferometric phase itself. Sometimes the orbital errors and the atmospheric artifacts are jointly estimated by an empirical function. The analysis of atmospheric component within the interferometric phase and the strategies to mitigate them will be emphatically discussed in [Section 2.5](#).

2.3.6 3D displacement calculation

The interferogram (free of all the non-deformation contributions) only provides the slant-range ground deformation along the LOS direction of the radar system. Interferograms derived from different tracks of satellite but covering the same deformation provide non-unique deformation signals. Therefore, interferograms need to be interpreted with care. Taking advantage of interferograms capturing the same deformation but along different LOSs, it is possible to recover theoretically the 3 dimensional (3D) components of displacement (east-west, north-south and up-down, hereinafter called EW, NS, and UD) ([Fialko et al., 2001](#); [Hanssen, 2001](#); [Wright et al., 2004](#)).

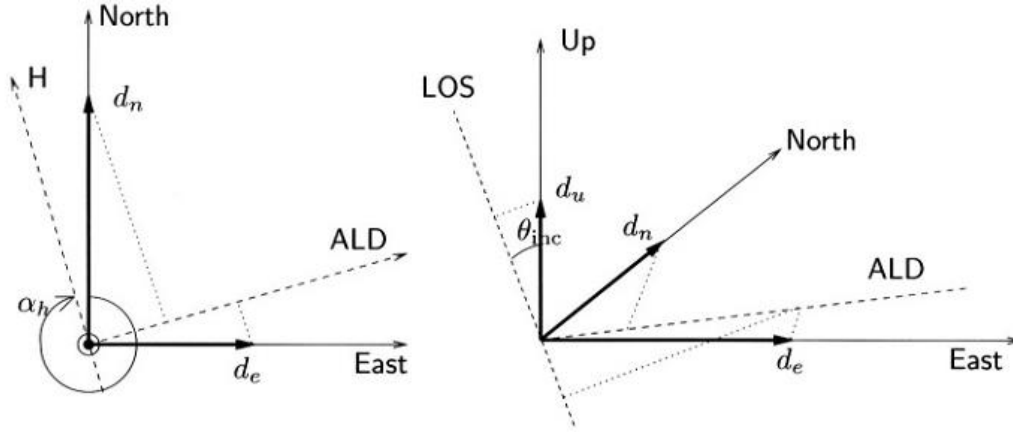


Figure 2.19 Projection of the 3D components of the ground displacement vector $\vec{d}_{3D} = (d_u, d_n, d_e)^T$ onto the satellite LOS direction. (a) Vertical view showing the North and East component of the displacement projection on the azimuth look direction (ALD) that is perpendicular to the satellite's heading (H). α_h indicates the heading angle. (b) The projection of the Up component to LOS shown in a 3D sketch. The incidence angle is indicated by θ_{inc} . (Hanssen, 2001).

Figure 2.19 shows the 3D displacement component ($d_{3D} = [d_u, d_n, d_e]^T$) projected to one slant-range component (d_1) in the LOS direction for a right-looking satellite (Hanssen, 2001). The projection can be expressed as follow:

$$d_1 = d_u \cos \theta_{inc} + \sin \theta_{inc} [d_e \sin(\alpha_h - 3\pi/2) - d_n \cos(\alpha_h - 3\pi/2)] \quad (2.11)$$

Where α_h represent the heading azimuth angle and; θ_{inc} denotes the incidence angle. The unit vector(v_1) pointing from the ground to the LOS direction (corresponding to d_1) is defined as follow:

$$v_1 = [v_1^u, v_1^n, v_1^e] \quad (2.12)$$

$$\begin{cases} v_1^u = \cos \theta_{inc} \\ v_1^n = -\sin \theta_{inc} \cos(\alpha_h - 3\pi/2) \\ v_1^e = \sin \theta_{inc} \sin(\alpha_h - 3\pi/2) \end{cases}$$

If we observed n slant-range displacement from different LOSs, i.e. $d_{los} = [d_1, d_2, \dots, d_n]^T$, with corresponding unit vectors $V = [v_1, v_2, \dots, v_n]^T$, the d_{3D} can be solved weight least-square solution (Wright et al., 2004):

$$d_{los} = V d_{3D} \quad (2.13)$$

$$d_{3D} = (V^T W_{los}^{-1} V)^{-1} V^T W_{los}^{-1} d_{los} \quad (2.14)$$

where W_{los} is the covariance matrix for the observed slant-range displacement. Then the covariance matrix for the estimated 3D displacement W_{3D} is:

$$W_{3D} = (V^T W_{los}^{-1} V)^{-1} \quad (2.15)$$

2.4 InSAR time series analysis (StaMPS/MTI-SB)

The InSAR time series analysis is a type of advanced InSAR techniques aiming to overcome shortcomings of standard InSAR technique. On analyzing multiple SAR images acquired from the same satellite track (in the same LOS geometry), a time series containing the spatio-temporal characteristics of the ground displacement can be retrieved by InSAR time series technique. Small Baseline (SB) InSAR is one of important InSAR time series techniques that have been recently developed and widely applied in various applications of ground deformation monitoring. Many open-source InSAR software packages that implement a wide range of SB methods have been developed, such as the StaMPS/MTI (Hooper et al., 2012) and the Generic InSAR Analysis Toolbox (GIAnt) built by three SB methods (conventional SB, New SBAS and Multiscale InSAR Time Series) (Berardino et al., 2002; Lanari et al., 2004a; Jolivet et al., 2012; Hetland et al., 2012). All the SB methods share the same fundamental concept, but each has its own advantages and limitations (Gong et al., 2016). Comparison of these SB InSAR methods has been carried out by Gong et al. (2016) in terms of the selection of coherent pixels and the performance in capturing ground deformation for further research reference.

In this dissertation, I present the SB algorithm implemented in the StaMPS/MTI package developed by Hooper et al. (2012), hereinafter named StaMPS/MTI-SB, since I applied a part of this treatment to the X-band SAR data acquired over the PdF volcano to generate the displacement time series (Chapter 4). The StaMPS/MTI-SB method differs from standard ones because it has fully taken advantage of two benefits of time series acquisitions. Firstly, most standard SB methods operate on multi-looked interferograms (e.g. Berardino et al., 2002; Lanari et al., 2004b; Hetland et al., 2012; Jolivet et al., 2012), while this method processes the single-look images that provide the highest resolution to improve the identification of coherent

pixels, referred to as the Slowly-Decorrelating Filtered Phase (SDFP) pixels (Hooper et al., 2012; Hooper, 2008). Secondly, this StaMPS/MTI-SB method takes the third dimension, the time, into account while unwrapping the phase, referred to as 3D unwrapping (Hooper & Zebker, 2007), making the unwrapped results more reliable.

The main processing steps of StaMPS/MTI-SB is illustrated in **Figure 2.20**. I highlight the main principles and treatment processes of StaMPS/MTI-SB in the following subsections and the application to PdF volcano will be introduced in [Chapter 4](#).

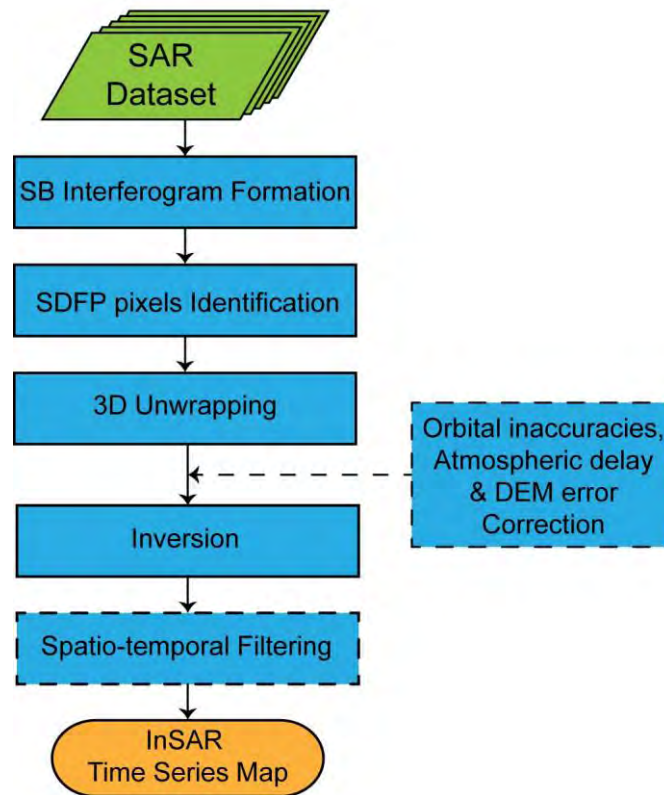


Figure 2.20 Flow chart of StaMPS/MTI-SB processing.

2.4.1 SB interferograms formation

The small baseline subset is a combination of multiple interferograms characterized by small perpendicular baselines (B_{\perp}), short temporal baselines (B_t) in order to minimize the spatial and temporal decorrelation. The formation of SB interferograms depends preliminarily on the determination of thresholds of three parameters, B_{\perp} , B_t , and γ (a coherence implying

the spatio-temporal decorrelation level of interferogram). The selection of thresholds of baselines ($B_{\perp,thr}$ and $B_{t,thr}$) can vary case by case depending on the type of SAR data used and the context of the study area. In general, the critical perpendicular baseline (B_{\perp}^c) and critical temporal baseline (B_t^c) provide references for adjusting the threshold. After an initial selection, the value of γ leads to further reduce the decorrelated image pairs. For an interferogram, $\gamma = (1 - B_{\perp}/B_{\perp,thr}) \times (1 - B_t/B_{t,thr})$, $\gamma \in [0, 1]$. The default threshold of γ is 0.5 in StaMPS/MTI package. One can adjust it according to related cases while ensuring that the resultant SB network contains no isolated clusters (Hooper, 2008). In theory, the more the coherent interferogram in SB network, the more accurate resultant time series will be obtained, because sufficient redundant information in a strong network avoids error propagation during the inversion from SB network to time series.

Before generation SB interferograms, a filtering in range is necessary to further reduce the geometric decorrelation, and a filtering in azimuth as well, to discard non-overlapping Doppler frequencies, as already mentioned in Section 2.3.2.

2.4.2 SDFP pixel selection

Searching for the Slowly-Decorrelating Filtered Phase (SDFP) pixel is the main target of StaMPS/MTI-SB method. The SDFP pixel differs from the Persistent Scatterer (PS) pixel (main target of PS-InSAR method) (Hooper et al., 2007) in several ways. The PS pixel, as a SAR ground resolution cell, should contain a persistently dominant scatterer that has consistent scattering properties with its phase decorrelates little with time. However, within a SDFP pixel, there should not necessarily be a dominant scatterer. Phase variation due to temporal decorrelation could be large, but it can be minimized by forming small spatial and temporal baseline interferograms. Pixels whose phase when filtered decorrelates little over short time intervals are defined as SDFP pixels (Hooper, 2008).

An initial subset of SDFP candidate pixels is firstly obtained in order to reduce the computational burden through analysis of amplitudes. The amplitude difference dispersion $D_{\Delta A}$ is considered as an indication of the phase stability. It is defined as $D_{\Delta A} \equiv \sigma_{\Delta A}/\mu_A$, where $\sigma_{\Delta A}$ denotes the standard deviation of the amplitude difference between two images forming the

interferogram, and μ_A is the mean amplitude (Hooper, 2008). The threshold of $D_{\Delta A}$ is empirically set as 0.6 to screen out the SDFP candidate pixels.

Then, a phase stability analysis of the SDFP candidate pixels is carried out. An estimate of decorrelation noise with a candidate pixel γ_x is used to indicate its phase stability level (Hooper et al., 2004, 2007; Hopper, 2008).

$$\gamma_x = \frac{1}{N} \left| \sum_{i=1}^N \exp\{\sqrt{-1}(\phi_{x,i} - \tilde{\phi}_{x,i} - \Delta\hat{\phi}_{dem,x,i}^u)\} \right| \quad (2.16)$$

Where, N is the number of SB interferograms, $\phi_{x,i}$ is the wrapped phase of pixel x in the i th flattened and topographically corrected interferogram that can be expressed in **Equation 2.17**; $\tilde{\phi}_{x,i}$ is the spatially-correlated terms estimated by bandpass filtering of neighboring pixels. It is supposed to include the ground displacement phase, atmospheric phase delay, orbital errors, and spatially-correlated DEM error; $\Delta\hat{\phi}_{dem,x,i}^u$ is the spatially-uncorrelated DEM error term that is estimated in this step based on its relationship with perpendicular baseline.

$$\phi_{x,i} = \phi_{defo,x,i} + \phi_{atmo,x,i} + \Delta\phi_{orbit,x,i} + \Delta\phi_{dem,x,i} + \phi_{noise,x,i} \quad (2.17)$$

Where, $\phi_{defo,x,i}$ is the phase change due to the displacement in the satellite LOS direction, $\phi_{atmo,x,i}$ is the atmospheric phase delay between passes, $\Delta\phi_{orbit,x,i}$ is the phase due to orbit inaccuracies, $\Delta\phi_{dem,x,i}$ is the phase due to the DEM error, $\phi_{noise,x,i}$ is the noise term.

The computation is iterative. Once the root mean square change in γ_x reaches to be small enough, the iteration stops. Therefore, every SDFP candidate pixel has a γ_x value representing its noise level. γ_x and $D_{\Delta A}$ are both taken into account for statistical analysis yielding a threshold function, $\gamma_x^{thresh}(D_{\Delta A})$, for SDFP pixel selection (Hooper et al., 2007; Hooper, 2008). The selected SDFP pixels in previous step are then refined and weeded by dropping those with relative large standard deviations of γ_x and those that are due to signal contribution from neighboring ground resolution cells (Hooper et al., 2007).

The phases of SDFP pixels are corrected using the estimate spatially-uncorrelated DEM error ($\Delta\hat{\phi}_{dem,x,i}^u$) calculated in previous selection steps.

2.4.3 Estimation of orbital ramp and spatially-correlated DEM error

Prior to the Inversion process, the StaMPS/MTI-SB estimates residual orbital ramp ϕ_{orbit} using a linear function correlating the two dimensional coordinates and the interferometric phases as explained in [Section 2.1.4](#). The following equation is used to estimate the spatially-correlated DEM error:

$$\{\phi_{sb} - \Delta\phi_{orbit}\} = Gm \quad (2.18)$$

Where the ϕ_{sb} is the interferometric phase from SB interferogram subset and ϕ_{orbit} is the estimated orbital phase ramp, $\{\phi_{sb} - \Delta\phi_{orbit}\}$ denotes a $N \times L$ matrix, G is a $N \times 3$ design matrix with ones in the first column, the perpendicular baselines (B_{\perp}) of SB interferograms in the second column and the temporal baselines (B_t) of the SB interferograms in the third column, the m is the $3 \times L$ matrix to be estimated, N and L donates the number of SB interferograms and the number of SDFP pixels.

In the resultant matrix m , the second row donates the DEM error in one-meter B_{\perp} for each SDFP pixel. The third row represents the velocity of the LOS displacement for each SDFP pixel, which is to say that the calculation of the DEM error of StaMPS/MTI-SB is based on an assumption of a linear displacement model.

2.4.4 Inversion of SB interferograms to time series

The InSAR time series generation is a process of inversion from the space of SB subset to the space of single-master subset (where all the maps are chronologically ordered relative to one single map from one certain epoch) based on the redundant information of SB subset. This inversion can be implemented before or after the mitigation of non-defomation contributions step depending on specific cases.

The inversion formulation is expressed as:

$$\phi_{sb} = G\phi_{ts} \quad (2.19)$$

Where, ϕ_{sb} is a $(N + 1) \times L$ matrix with the interferometric phase of each SDFP pixel from SB interferogram subset, ϕ_{sb} can be replaced by $\phi_{sb} - \phi_{art}$ if the corrected time series are required, where ϕ_{art} represents the phase due to artifacts including $\Delta\phi_{orbit}$, and/or ϕ_{atmo} and/or $\Delta\phi_{dem}$, ϕ_{ts} is a $(M \times L)$ matrix of the time series to be inverted and G is the $(N + 1) \times M$ design matrix with zeros, plus and minus ones, N , L and M donates the number of SB interferograms, the number of SDFP pixels and the number of SAR acquisitions respectively. The extra row of ϕ_{sb} and G makes it possible to fix the reference epoch of the time series.

StaMPS/MTI-SB solves the inversion by directly using the Least-Square adjustment (Hooper, 2008; Hooper et al., 2012), as there are no isolated clusters in SB interferograms network that provides full redundant information.

StaMPS/MTI-SB provides an independent program for atmospheric delay correction based on a simple linear model correlating the interferometric phase and the elevation. But this algorithm doesn't have a strong universality since it doesn't account for the cases where the phase-elevation correlation might be not simply linear and where the ground displacement might be correlation with elevation. Therefore, the atmospheric delay correction method would vary case by case.

StaMPS/MTI-SB provides as well a spatio-temporal filter to further reduce the residual artifact and noise level, which, in practice, is an optional step since sometimes interest signal could be reduced due to the filtering when parameters have not been properly set.

2.5 Atmospheric contribution

2.5.1 Origin of atmospheric phase delay

In repeat-pass InSAR measurement, the two interferometric SAR images are not simultaneously acquired. The propagation path of radar signal for each acquisition can be affected differently by the atmosphere, resulting in a visible consequence on the interferogram. This undesirable part of contribution in interferometric phase is the so-called atmospheric contribution or atmospheric phase delay. The atmospheric contribution was first identified in

1994 (Massonnet et al, 1994), and quickly confirmed as the major limitation of InSAR accuracy for topographic reconstruction as well as for deformation monitoring. Rosen et al. (1996) found that the phase delay due to atmospheric refractivity anomalies can reach the level of 12 cm peak-to-peak in LOS direction obviously contaminating the deformation signal over Kilauea volcano, Hawaii. Zebker et al. (1997) reported that the spatial and temporal changes of 20% in relative humidity lead to 10 cm errors in deformation measurement, and perhaps 100 m of error in derived topographic products for those interferograms with unfavorable baseline geometries.

The dominant source contributes to the atmospheric phase delay affecting the accuracy of InSAR measurement comes from the time and space variations of refractivity index in the neutral atmosphere, which is mainly confined to the troposphere (Goldstein, 1995; Massonnet & Feigl, 1995; Zebker et al., 1997; Hanssen, 2001). The refractivity index N in the troposphere can be expressed as (Bean & Dutton, 1968; Thayer, 1974; Hanssen, 2001; Puysegur et al., 2007; Doin et al., 2009):

$$N = k_1 \frac{P}{T} + \left(k_2 \frac{e}{T} + k_3 \frac{e}{T^2} \right) + k_4 W_{cl} + k_5 \frac{ne}{f^2} \quad (2.20)$$

Where $P = P_d + e$ is the total atmospheric pressure in Pa, P_d is the partial pressure of dry air, e is the partial pressure of water vapor in Pa, T is the absolute temperature in Kelvin, W_{cl} is cloud water content in kg/m^3 , ne is the electron density in the ionosphere and f is electro-magnetic wave frequency, the constants $k_1, k_2 \dots k_5$ are $k_1 = 0.776 \text{ K} \cdot \text{Pa}^{-1}$, $k_2 = -0.06 \text{ K} \cdot \text{Pa}^{-1}$, $k_3 = 3.75 \times 10^3 \text{ K}^2 \cdot \text{Pa}^{-1}$, $k_4 = 1.45 \times 10^3 \text{ m}^3 \cdot \text{kg}^{-1}$, and $k_5 = -4.03 \times 10^7 \text{ s}^2 \cdot \text{m}^3$ (Smith & Weintraub, 1953; Skone & Cannon, 1999; Solheim et al., 1999). The tropospheric phase delay ϕ_{trop} , at a specific height, $z = z_0$, corresponds to the integration of the refractivity between z_0 and the top of the troposphere z_{top} along the radar LOS (Hanssen, 2001).

$$\phi_{trop} = \frac{-4\pi}{\lambda} 10^{-6} (\cos \theta)^{-1} \int_{z=z_0}^{z=z_{top}} N(z) dz \quad (2.21)$$

Where θ is the incidence angle, λ is the radar wavelength, and $\frac{-4\pi}{\lambda}$ is a conversion factor to convert from range increase to phase delay.

The first term at the right-hand side of the Equation is often called “hydrostatic term” that corresponds to the effect of dry air and a partial effect of water vapor on refractivity. The second and the third term (in brackets) are the “wet term” related to the rest effect of water vapor contained in troposphere. The fourth term refers to the effect of liquid water contained in the clouds that the radar signal passes through, and the fifth term corresponds to the dispersive effect of ionosphere.

The “hydrostatic delay” yielded by the hydrostatic term has a very limited influence on interferograms, and can be safely ignored in case of about 50 km and smaller of interest area. Whereas, the wet terms, parametrized by temperature T and the partial pressure of water vapor e , is much more spatially variable than the hydrostatic term. The variations of the wet delay have a considerable effect on the observed phase delay. Bean & Dutton (1968) and Hall et al. (1996) reported that the effect of liquid water in clouds on atmospheric delay rarely exceeds 1 mm/km along the LOS direction. Thus this part is sometimes neglected when computing the perceptible water vapor, which however will result in an overestimation of less than 10% (Hanssen, 2001). Jolivet et al. (2014) nevertheless suggests that the hydrostatic delay should not be neglected because it accounts for about 15% of the variance reduction when surface temperature varies by more than 10 °C during the year. Ionospheric delay is electro-magnetic wavelength dependant (**Equation 2.20**) and L-band data are more affected by ionospheric effects than X or C-band data. Based on current theoretical considerations and experimental results, the hypothesis that, the ionospheric effect may induce long wavelength signals over a single SAR image but will not noticeably affect phase variations at spatial scales less than about 50 km (in particular for studies using C-band sensors), is currently adapted (Hanssen, 2001; Raucoule & De Michele, 2010).

2.5.2 Distribution of tropospheric phase delay

From the point of InSAR applications, the total tropospheric phase delay results from the combined effects stratification of the lower troposphere (called stratified delay) and turbulent mixing in the troposphere (called turbulent delay) (Hanssen, 2001; Emardson et al., 2003; Doin et al., 2009; Jolivet et al., 2014). On a single SAR image, the tropospheric contribution can be expressed as (Doin et al., 2009):

$$N(x, z) = \bar{N}(z) + \delta N(x, z) \quad (2.22)$$

Where $\bar{N}(z)$ is the average vertical stratified component of the image, $\delta N(x, z)$ denotes the deviation from the average profile, implying the local turbulent component at location x , and z is related to the elevation.

The turbulent component is due to the laterally variable turbulence of the troposphere or clouds, locally modifying the propagation speed of the radar wave. On the interferograms, it is reflected by a random signal (random in space and time) comparable to a medium extent of noise. **Figure 2.21a** shows an example of phase delay due to the turbulent mixing in troposphere. The temporal baseline is 24 days, and the perpendicular baseline is 33 m. The area extends from the west boundary of Enclos Fouqué Caldera to the sea. No ground displacement is expected to occur during this period. The contour is superimposed on the map. According to the **Figure 2.21c**, no clear correlation between interferometric phase and elevation is visible over the whole interferogram.

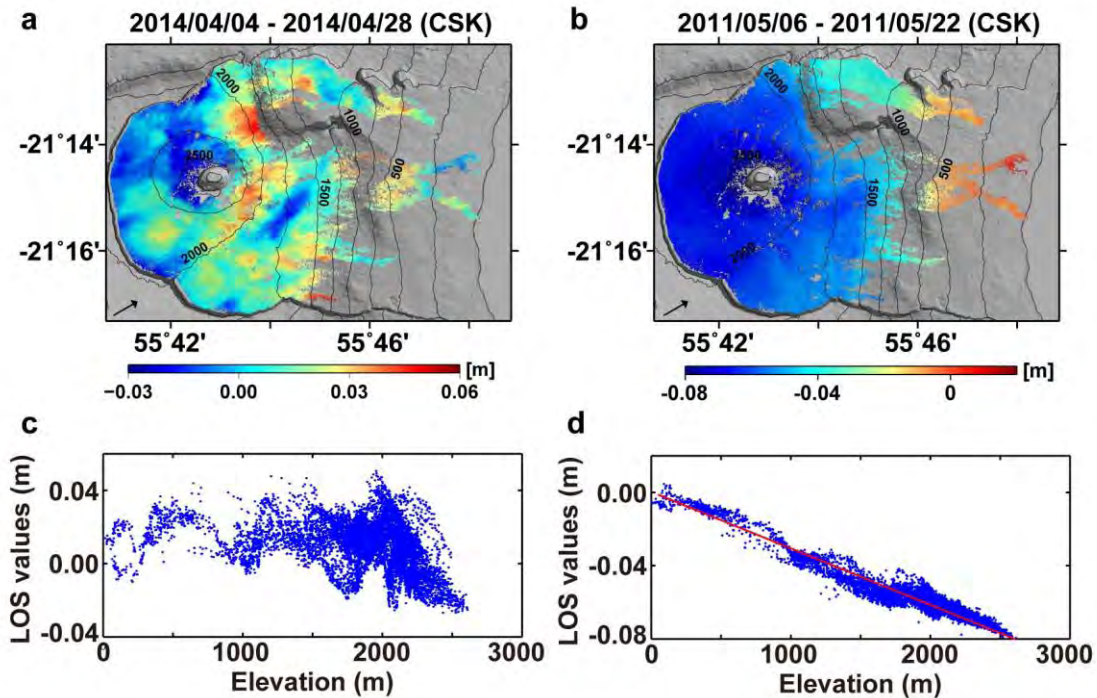


Figure 2.21 Example of two types of tropospheric phase delay. (a) A CSK interferogram spanning 24 days showing the turbulent component of tropospheric phase delay, and its correlation with topography showing in (c). (b) A CSK interferogram spanning 16 days showing the stratified component of tropospheric phase delay, and its correlation with topography showing in (d).

The stratified component results from vertical variation refractivity index of the troposphere. Temporal variations in the vertical stratification component lead to a phase delay within the interferometric phase that correlates with topography. **Figure 2.21b** shows an example of interferogram with stratified tropospheric delay. We estimate as well the coefficient of correlation between interferometric phase and elevation (**Figure 2.21d**). The phase-elevation plot reveals the clear correlation between phase and topography.

2.5.3 Tropospheric delay correction methods

Since the turbulent tropospheric delay is randomly distributed in time and space, it cannot be modeled, but it is possible to calculate the statistical characteristics of this random signal. In practice, we consider that the turbulent delay can be corrected by multiple InSAR processing, such as interferograms stacking ([Zebker et al., 1997](#); [Lasserre et al., 2007](#)) and InSAR time series analysis ([Ferretti et al., 2001](#); [Cavalié et al., 2007](#)).

The stratified delay has a temporally varying amplitude and sign as well, suggesting it should also be mitigated by interferograms stacking or by smoothing InSAR time series. However, it is clearly less efficient than for turbulent delay, as the stratified delay is not random in time but sometimes presents seasonal fluctuations, and its spatial pattern always mimics elevation ([Doin et al., 2009](#)). Therefore, properly estimation and correction of the stratified tropospheric delay is the main task for most InSAR studies.

Numerous methods focusing on the quantification and correction of the tropospheric delay from InSAR measurements have been proposed since 1990s. Those proposed methods can be divided into two groups, interferometric phase-independent methods and interferometric phase-dependent methods, relying on the dataset used for estimation of tropospheric delay.

The interferometric phase-independent methods work on the external datasets to compute synthetic tropospheric delay for corresponding interferogram and correct it directly. Numerous correction methods have been developed based on various external datasets, such as, (1) using Zenith Wet Delay (ZWD) data obtained from a network of Global Navigation Satellite System (GNSS) receivers in the area imaged by SAR ([e.g. Williams et al., 1998](#); [Webley et al., 2002](#); [Li, 2005](#); [Li et al., 2006a](#); [Onn & Zebker, 2006](#)); (2) using Medium Resolution Imaging

Spectrometer (MERIS) and/or Moderate Resolution Imaging Spectroradiometer (MODIS) data to analyze the magnitude and behavior of the water vapor variation that is considered as the main contribution to the tropospheric delay (e.g. Li, 2005; Li et al., 2006b, 2009, 2012a; Remy et al., 2011, 2015); (3) using Global Atmospheric Models (GAM, that provides estimates of temperature, water vapor partial pressure, and geopotential height of pressure levels, on a regular spatial grid at regular time steps) to predict delays at the time of SAR acquisitions and correct for the stratified tropospheric delays in SAR interferograms (Doin et al., 2009; Jolivet et al., 2011, 2014). The GAM models includes ERA-Interim (European Center for Medium-Range Weather Forecasts, ECMWF) (Dee et al., 2011), the North American Regional Reanalysis (NARR) (Mesinger et al., 2006), and the Modern Era-Retrospective Analysis for Research and Applications (MERRA) (Rienecker et al., 2011); and (4) using a combination of (1) and (2) (Puysségur et al., 2007), or of (2) and (3) (Walters et al., 2013). These methods, although can reduce the tropospheric delay in interferograms, they are often limited by the spatio-temporal collection of the corresponding external datasets since they are not always available for the time of each SAR acquisition (especially unlikely for InSAR time series studies) and the low spatial resolution is often not qualified for high accuracy InSAR measurements.

The interferometric phase-dependent methods use only the interferometric phases and the topography of the study area. It is based on the analysis of the phase delay to elevation relationship observed in individual interferograms (e.g. Beauducel et al., 2000; Remy et al., 2003; Taylor & Peltzer, 2006). The phase/elevation correlation $\phi_{trop} = f(z)$ can be linear or non-linear varying from case to case. A simple linear empirical function can be expressed as: $\phi_{trop} = K_{trop}z + \Delta\phi_0$, where K_{trop} is a constant to be estimated and used to model the tropospheric delay throughout the interferogram, and $\Delta\phi_0$ represents a constant shift. The phase-dependent methods based on empirical functions are uncomplicated and efficient to synthesize the stratified tropospheric delay with no need for collecting external datasets (that sometimes is difficult or even inaccessible). Despite all advantages, these methods have several limitations. First, this method is only applicable when a non-deformation area is available or the expected deformation signal do not correlates with topography. If deformation is expected to be present throughout the whole interferogram and to correlate with topography, such as over volcanoes or areas with wide range of topography (e.g. Delacourt et al., 1998; Elliott et al., 2008), the use of a priori deformation model is needed to pre-separate different contributing signals (e.g.

Cavalié et al., 2008; Chapter 4). Alternatively, Lin et al. (2010a) developed an approach that can be applied in a deforming area by using the insensitivity of a spatial frequency band to deformation. This method assume the empirical phase-elevation relationship holds for all spatial frequencies, but the deformation may only be significant in a certain frequency. The second limitation that using one single phase-elevation relationship over the whole interferogram sometimes results in inaccurate estimates due to the spatial variation of the stratified troposphere. This can be significant when a large area, say larger than tens of kilometers, is studied. To solve this problem, Bekaert et al. (2015) proposed and tested a novel power law correction method which can be applied in the presence of deformation, over a range of different time periods and in different atmospheric conditions.

All currently proposed methods for tropospheric delay correction are evidenced successful in corresponding cases, but few can be universally applicable. Their performance can vary from case to case and should be carefully evaluated for each.

In this dissertation, we applied the phase-independent method based on MERIS and MODIS near-infrared water vapor products to estimate the tropospheric delay in the InSAR data acquired over the Llaima volcano in Chile, which will be detailed in Chapter 7. We proposed a phase-dependent tropospheric correction method for the specific case of Piton de la Fournaise volcano in La Réunion Island. It is based on an a priori deformation model which is extracted by a principal component decomposition implemented in Principal Component Analysis-based Inversion Method package (PCAIM) (Kositsky & Avouac, 2010). This method is highlighted in Chapter 4.

PART I – Piton de la Fournaise

CHAPTER 3 : STUDY AREA & THE MARCH-APRIL 2007 ERUPTION

3.1 Overview of Piton de la Fournaise

3.1.1 La Réunion Island

La Réunion (an insular region of France) is an oceanic basaltic island lying on the geographical coordinates of 21°06'S, 55°36'E, in the southwest of the Indian Ocean (**Figure 3.1**). It is situated about 800 km east of Madagascar and about 175 km southwest of Mauritius, the nearest island. It is in the southeast extension of the volcanic Mascaren Plateau and located above a hotspot in the Earth's crust. This hotspot was proposed as the origin of the alignment of volcanic islands (the Mascaren Plateau, the Mauritius Island and La Réunion Island) (Duncan, 1981; Morgan, 1981).

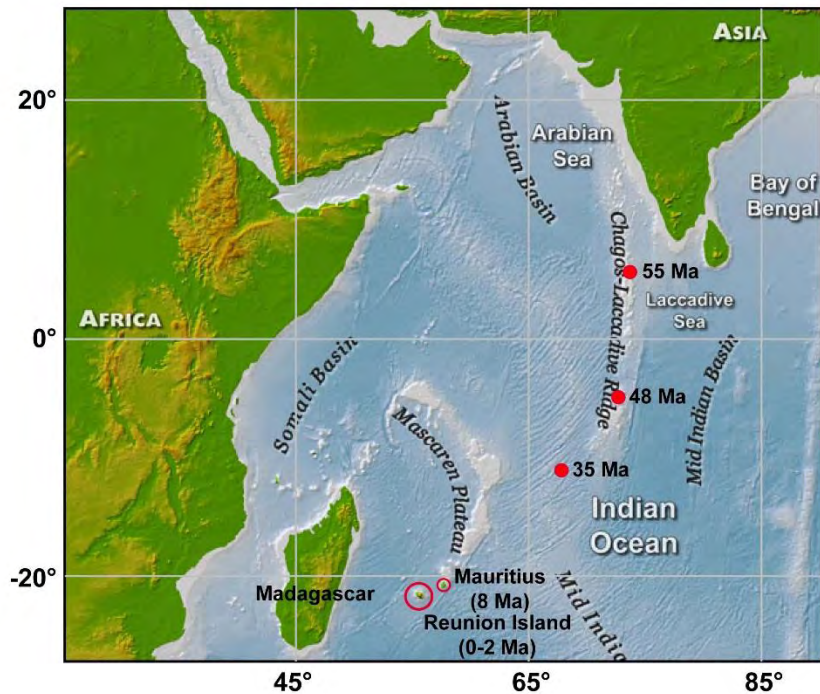


Figure 3.1 Location of La Réunion Island in Indian Ocean.

La Réunion Island (**Figure 3.2**) is 63 km long, 45 km wide and covers 2512 km². It is elliptical in shape with a NW-SE elongation. It rises above the ocean floor at a depth of 4000 m with a base of 200 km by 240 km. The island is composed by two shield volcanoes, Piton des Neiges and Piton de la Fournaise, whose highest elevations are 3070 m and 2632 m respectively.

Therefore the total height of La Réunion island can be more than 7000 m. The Piton des Neiges volcano forming the northwest part of the island is the older (about 2 Ma) and has been inactive for 12 000 years. The Piton de la Fournaise volcano, built to the southeast of the Piton des Neiges, occupies one third of the surface of the island and is still active today. The existence of the volcano Les Alizés that was recently proposed based on the interpretation of magnetic and gravity measurements (Malengreau et al., 1999) has improved the knowledge of the origin of the Piton de la Fournaise. Les Alizés is an ancient volcano on which the Piton de la Fournaise was built. Its activity could start 1.8 Ma ago earlier than that of Piton de la Fournaise and partially contemporary with that of Piton de Neiges.

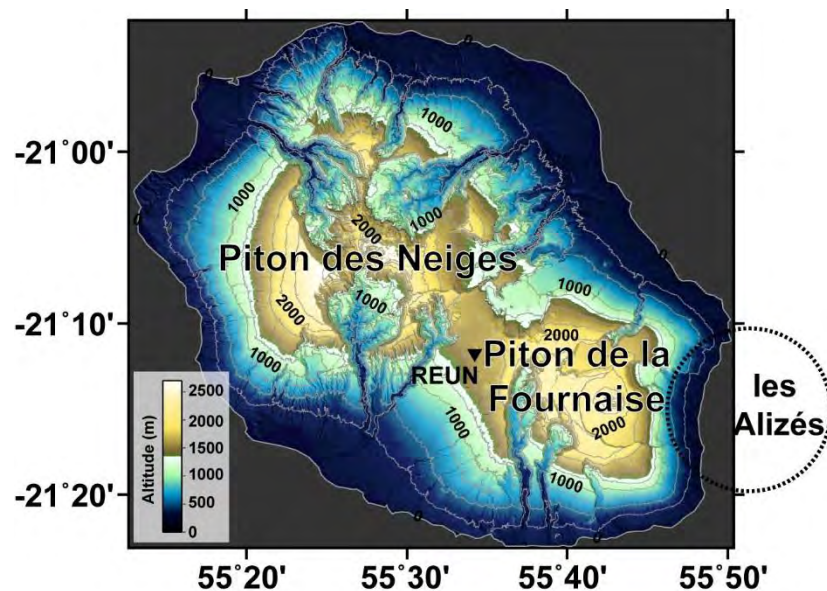


Figure 3.2 Topography of La Réunion Island and the location of volcanic edifices. Black triangle indicates the location of the REUN IGS station used in this dissertation for subtraction of the plate motion from GNSS data.

3.1.2 Structure of Piton de la Fournaise

The Piton de la Fournaise located in the south-eastern part of La Réunion Island, is an oceanic basaltic shield volcano whose activity began more than 540,000 years ago (Gillot & Nativel, 1989). It was built on the eastern flank of Piton des Neiges and on the western flank of Les Alizés, two older inactive volcanoes located on the western and the eastern parts of the island, respectively (Figure 3.2). The evolution of Piton de la Fournaise results from the

PITON DE LA FOURNAISE
CHAPTER 3: STUDY AREA & THE MARCH-APRIL 2007 ERUPTION

successive construction of several shield volcano calderas decentered with respect to each other (Bachèlery & Mairine, 1990). The first caldera was the caldeira des Remparts that rooted from a collapse of an ancient eruptive center 290 000 years ago. The activity of the ancient eruptive center likely stopped and a new eruptive center was developed to the east. The lava flows were channeled through the Rivière des Remparts, until the formation of the second caldera Morne Langevin, 220 000 years ago (Gillot & Nativel, 1989). The third caldera, the caldera Pas des Sables (Figure 3.3) was built 65 000 years ago containing the Plaine des Sables and the upper Rivière de l'Est (Gillot & Nativel, 1989; Staudacher et al., 1990). The fourth caldera called Enclos Fouqué (Figure 3.3) was formed 4500 years ago (Bachèlery, 1981; Gillot & Nativel, 1989; Staudacher & Allègre, 1993), and where the majority of the recent eruptive activities took place. The structure Enclos Fouqué- Grand Brûlé (Figure 3.3) is an EW elongated horseshoe shaped depression (~ 13×10 km) opened eastward to the Indian Ocean and surrounded by walls up to one hundred meters high. These walls are considered as the witness of a subsidence of the edifice resulting from either a caldera collapse (Bachèlery, 1981), or a slip of the Enclos Fouqué (Labazuy, 1996; Merle & Lénat, 2003; Oehler et al., 2004). Michon & Saint Ange (2008) explain the general morphology of the edifice by a gravitational spreading phenomenon in which several episodes of caldera collapse superimpose. These collapses can cause major faults crossing the eastern flank of the volcano (Michon & Saint Ange, 2008).

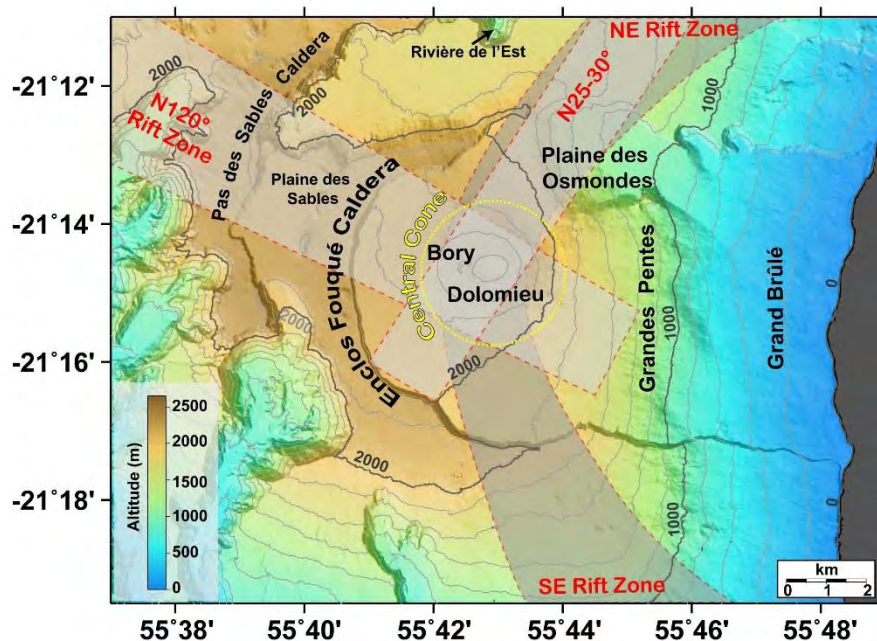


Figure 3.3 Topography and main structures of Piton de la Fournaise (N25-30 and N120 Rift Zones, light grey, after Michon et al., 2007a; NE and SE rift zones, dark grey, after Bachèlery, 1981).

Eruptions within Enclos Fouqué have contributed to the formation of a 400 m high Central Cone, 3 km in diameter, and an average slope of 15-20 ° (**Figure 3.3**), in the central part of the caldera. After experiencing many morphological changes (Bachèlery, 1981) induced by various episodes of collapse and fillers, the summit of the Central Cone presents its current form with two craters, which are the Bory crater (to the west, 200-350 m in diameter) and the Dolomieu crater (to the east, 700-1000 m in diameter). Comparing with Bory, Dolomieu is more active crater with numerous eruptions and crater collapses. Most recently in April 2007, the Dolomieu experienced a 340 m consequent collapse affecting its entire surface (Michon et al., 2009).

The Grandes Pentes and Grand Brûlé are both located in the eastern part of Piton de la Fournaise, separating the summit craters of the coast (**Figure 3.3**). The Grandes Pentes are a mountain rampart of La Réunion Island. They are characterized, as the name suggests, by steep slopes bending to the east at about 1000 m above sea level. They start at the east foot of the Central Cone overlooking a coastal area covered by forest and named Grand Brûlé. They are therefore in a sense an intermediate stage for vegetation within the caldera formed by the effusive-type volcano. The Grandes Pentes can reach an angle of thirty degrees and are sometimes considered as being the headwall scarps of the gravity faults (Lénat et al., 1990). Michon & Saint Ange (2008) have identified linear structures traversing the Grandes Pentes, which they interpret as normal faults that played a role in the slip during various episodes. The Grand Brûlé is located downstream from the Grandes Pentes, with slopes much lower than Grandes Pentes. The Grand Brûlé depression is interpreted as being the result of the last destabilization of the Eastern Flank (Chevallier & Bachèlery, 1981; Bachèlery & Mairine, 1990; Lénat et al., 1990; Bachèlery 1995; Labazuy, 1996; Lénat et al. 2001; Merle and Lénat 2003).

3.1.3 Eruptive activity of Piton de la Fournaise

Piton de la Fournaise is one of the most active volcanoes in the world with a high eruptive frequency (Peltier, et al., 2009a). During the period 1992-1998, the Piton de la Fournaise experienced a period of calm without any eruption, as the period 1966-1972. In Mars

1998, an eruption lasted 196 days breaking the silence of 6 years. Since this major eruption, a new cycle of intense activity (2 or 3 eruptions each year) began. With several exceptions, most recent eruptions occurred mainly either at the summit, inside the Dolomieu crater, or along the NE and SE rift zones (oriented N10 and N170, that defined by Bachèlery (1981)) and the N25-30 and N120 rift zones (that defined by Michon et al. (2007a)) (Figure 3.3). Two main eruptive periods of Piton de la Fournaise since 1972 was highlighted by Peltier et al. (2009a). They both lasted several decades and separated by the repose period of six years (1992-1998). From 1972 to 1992, eruptions were fed by the progressive drainage of a shallow magma reservoir that was occasionally recharged. Weak seismic and ground displacement eruptive precursors are the main characteristic of this period. The second period 1998-2007, especially after 2000, the behavior of the volcano was modified by the arrival of new magma into the shallow reservoir from a deeper one because of the opening of the conduit. Eruptions were therefore fed by a continuous recharge of the shallow reservoir, inducing continuous summit inflation, strong pre-eruptive seismicity and distal eruptions. The eruption from 2000 to 2007 exhibits three type of eruptions comprising (Peltier et al., 2009a): summit and proximal eruptions, two major types that commonly occur with eruptive fissures less than 2 km from the summit craters; distal eruptions, the third type with eruptive fissures on the Eastern Flank at low elevation, larger than 4 km away from the craters (e.g., December 2005 eruption and March-April 2007 eruption). These eruptions followed one another accomplishing eruptive cycles (a sequence of summit/near-summit, proximal eruptions, ending with distal, low-altitude eruptions on the Eastern Flank of the volcano). Five eruptive cycles have been defined during 2000-2007 period (Peltier et al., 2009a), which has been explained by the preferential motion of the Eastern Flank being the only direction with a free boundary condition (toward the sea). Such motion would lead to occurrence of distal eruptions on the Eastern Flank at the end of a cycle (Roult et al., 2012).

In March-April 2007, Piton de la Fournaise experienced an extraordinary eruption which is considered as the largest historical eruption ever observed during the 20th and 21st centuries, characterized by an effusion of $210 \times 10^6 \text{ m}^3$ volume of lava (Bachèlery et al., 2010) with a 340 m consequent collapse of the Dolomieu crater (Staudacher et al., 2009). Observations on the 2008 eruptions (Peltier et al., 2010b) showed that the functioning of the shallow magma feeding system changed significantly after the Dolomieu collapse in 2007. The 2008 eruptions (3

occurrences) were preceded by slighter and shorter time of summit inflation than eruptions in 2000-2007. Rare transient displacement was recorded in the minutes/hours before the fissures' opening (September and December eruptions), or even no significant ground displacement during the eruption (September eruption). These successive magma intrusion without reaching the ground surface results in the formation of temporal shallow magma storages that are the direct supply of the following eruptions.

3.1.4 InSAR observations at Piton de la Fournaise

As one of the most active volcanoes in the world, Piton de la Fournaise is monitored on a regular basis from space by the use of InSAR data since 1998. Thirty-five of the 44 eruptions that occurred between 1998 and 2015 were imaged using data provided by the Canadian RADARSAT-1 and RADARSAT-2 satellites (Sigmundsson et al., 1999; Fukushima et al., 2005, 2010), the European ENVISAT and SENTINEL-1 satellites (Froger et al. 2004, 2015; Tinard, 2007; Peltier et al., 2010a, 2016b), the Japanese ALOS-1 and ALOS-2 satellites (Augier et al., 2008; Froger et al., 2015; Peltier et al., 2016b), the German TerraSAR-X and TanDEM-X satellites (Froger et al., 2011; Bato et al., 2016) and the Italian Cosmo-SkyMed satellites (Bato et al., 2016). InSAR monitoring of Piton de la Fournaise became routine in 2003, initially through the Observatoire de Physique du Globe at Clermont-Ferrand, France. In 2010, this monitoring was integrated into the National Service for Volcanological Observations of the French National Institute for Earth Science and Astronomy under the name OI² (Observatoire InSAR de l'Océan Indien). Currently, the OI² database (<https://wwwobs.univ-bpclermont.fr/casoar>) includes around 1200 radar images of Piton de la Fournaise acquired by various radar satellites from February 2003. The resulting InSAR database represents an exceptional record of the ground surface displacements that have occurred at Piton de la Fournaise since 2003.

3.2 The historical March-April 2007 eruption

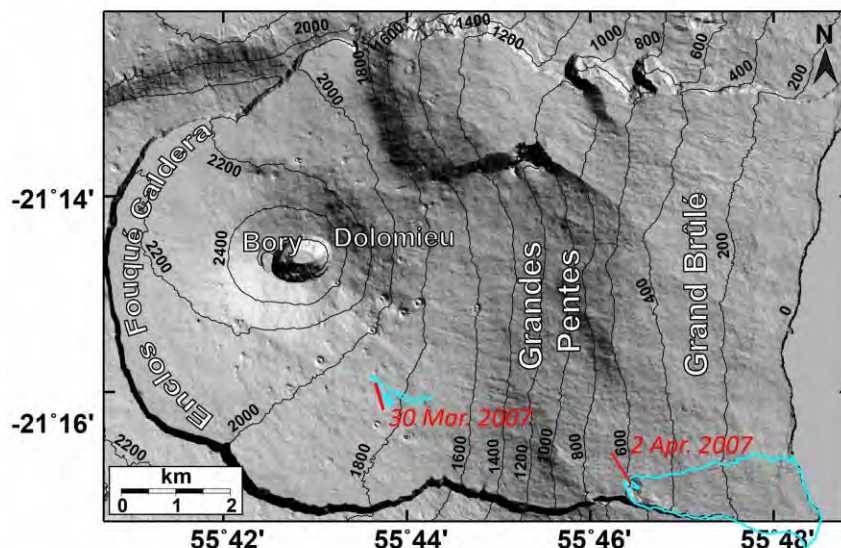


Figure 3.4 Location of the March-April 2007 eruption overlapping on the topography map of Piton de la Fournaise with 200 m elevation contours. The eruptive fissures are indicated by red lines and the lava flow contours are indicated by cyan lines. Map is projected in Geographic Lat/Lon referenced to WGS-84 Datum.

The 2006-2007 eruptions at Piton de la Fournaise were classified as one of the eruptive cycles that generally consist of several summit/proximal eruptions and a distal eruption ending a cycle (Peltier et al., 2009b). The March-April 2007 eruption was the distal eruption that ended the 2006-2007 eruptive cycle, preceded by 3 summit/proximal eruptions: the July-August 2006 proximal eruption, the August 2006-January 2007 summit eruption, and the February 2007 summit eruption (Peltier et al., 2009b). The first fissure of the March-April 2007 eruption opened on 30 March at 1900 m elevation (Figure 3.4) at the base of the southeastern Central Cone, following a one-month progressive increase in seismicity beneath the summit zone (Staudacher et al., 2009). A small lava flow (less than 10^6 m³; Staudacher et al., 2009; Figure 3.4) was formed during this ~ 10-hour-long phase. On 2 April, a new eruptive phase began by the opening of another fissure (Figure 3.4) at low elevation (~ 600 m) on the Southeastern Flank of Piton de la Fournaise, 7 km away from the summit in the Grand Brûlé. The eruption intensity was very high. The Dolomieu crater experienced a collapse (340 m in depth, $100\text{-}120 \times 10^6$ m³ in volume; Michon et al., 2007b) that was observed for the first time on 6 April. Concomitant to the Dolomieu collapse, lava fountains in the Grand Brûlé reached more than 200 m high

PITON DE LA FOURNAISE
CHAPTER 3: STUDY AREA & THE MARCH-APRIL 2007 ERUPTION

(Staudacher et al., 2009). The eruption continued until 1 May 2007. From 2 April to 1 May, a huge lava flow of ~ 1.8 km wide and up to 60 m thick at the costline was continuously emitted, with a total volume of 130×10^6 m³ (Staudacher et al., 2009). The March-April 2007 eruption is considered as the largest eruption ever observed at Piton de la Fournaise during the 20th and 21st centuries because of its unusual and unprecedented characteristics (the magnitudes of emitted lava volume and crater collapse).

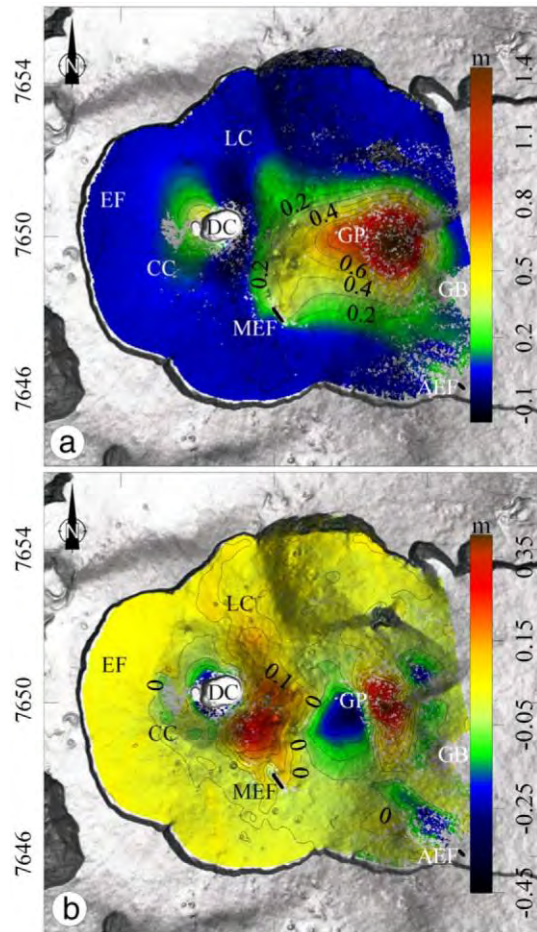


Figure 3.5 InSAR-derived early co-eruptive (March – April 2007) displacements draped on the shaded DEM. (a) East-West (E-W) component, contour interval is 0.1 m. (b) Vertical (U-D) component, contour interval is 0.05 m. (Froger et al., 2015).

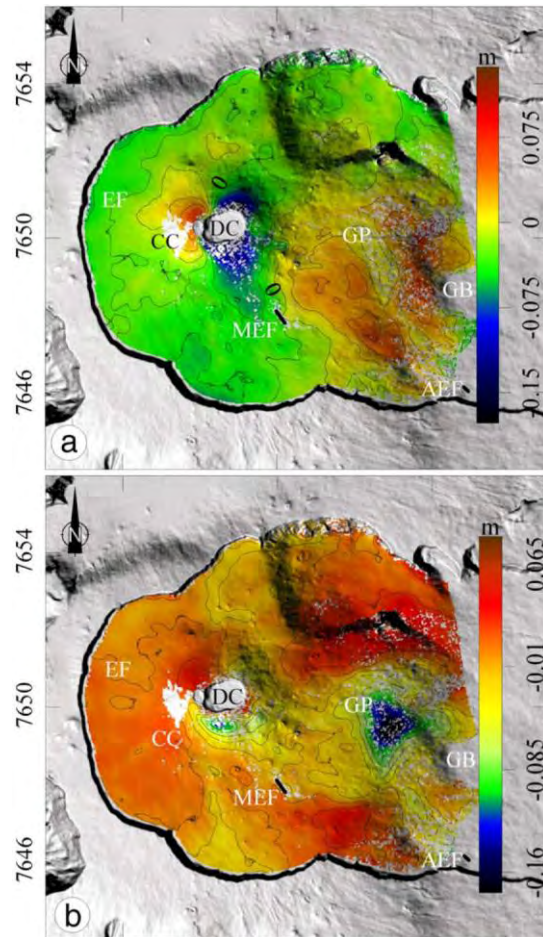


Figure 3.6 InSAR-derived late co-eruptive (April – May 2007) displacements draped on the shaded DEM. (a) East-West (E-W) component, contour interval is 0.02 m. (b) Vertical (U-D) component, contour interval is 0.05 m. (Froger et al., 2015).

Figure 3.5 and **Figure 3.6** display the early and late co-eruptive displacements of the March-April 2007 eruption derived using InSAR data by Froger et al. (2015). During the early co-eruptive period, the entire western part of the Central Cone is affected by both eastward and downward displacement, indicating subsidence with maximum of about 50 cm at the northwestern rim of the summit crater. The vertical component exhibits a maximum uplift of about 25 cm on the southeastern flank of the Central Cone (**Figure 3.5b**), which was interpreted by Froger et al. (2015) as being induced by the 30 March dyke intrusion. The Eastern Flank of the volcano is marked by a large displacement pattern. On the E-W component map (**Figure 3.5a**), the pattern is fan-shaped and covers an area of about 14 km², indicating an extensive eastward displacement with a maximum of up to 1.4 m. The vertical component map shows a more

complicated pattern, with subsidence of the Eastern Flank of up to 33 cm, intersected in its central part by uplift reaching 37 cm (**Figure 3.5b**).

During the late co-eruptive period, the Central Cone is affected by centripetal subsidence producing symmetrical displacement on the E-W displacement map (**Figure 3.6a**), and concentric downward displacement on the vertical displacement map (**Figure 3.6b**). The observed centripetal subsidence during both early and late co-eruptive periods suggests a shallow deformation source below the Central Cone. Froger et al. (2015) proposed a very shallow source with source center depth between 1858 m and 2378 m above sea level to explain this deformation of the Central Cone. The Eastern Flank display a large trapezoidal eastward displacement pattern that partly coincides with the early co-eruptive eastward displacement pattern (**Figure 3.5a**) in the area, although it extends significantly farther to the south. One import feature is that the magnitude of the displacement is about 15 to 20 times lower than that of early co-eruptive displacement, indicating that most of the eastward displacements on the Eastern Flank occurred early during the first days of the eruption.

These InSAR observations show that the Eastern Flank of Piton de la Fournaise was affected by a widespread seaward motion during the March-April 2007 eruption. Froger et al. (2015) proposed that this displacement is related to an intrusion within the Eastern Flank. The intrusion may have encountered and activated a pre-existing structural discontinuity (a detachment). While propagating to the east, it uplifted the central part resulting in the early co-eruptive uplift displacement of the Eastern Flank (**Figure 3.5b**). Then with the subsequent emission of lava through the 2 April fissure, the area that uplifted during the early co-eruptive period subsided during the late co-eruptive period (**Figure 3.6b**) due to the progressive withdrawal of magma (Froger et al., 2015).

3.3 One year post-eruptive displacement

To analyze the one year post-eruptive displacement triggered by the March-April 2007 eruption, we used a set of 21 interferograms formed with images acquired in 5 different tracks (both ascending and descending), including 4 for track 2313, 5 for track 5399, 4 for track 6277, 3 for track 7005, and 5 for track 7170 (**Table 2.3**). The interferograms were generated with the

DIAPASON© software ([CNES/Altamira-Information, 1996](#)) using two-pass method. The contribution of the orbital trajectories was modelled and removed using the ESA DORIS orbit state vectors. A 25 m DEM made by the French Geographic Institute was used to model and remove the topographic contribution in the interferograms.

Considering the acquisition dates are distinct between different tracks, we decided to divide all the interferograms into 6 groups in time (named by dates: 2007/04/15, 2007/05/15, 2007/06/15, 2007/11/15 and 2008/01/15) by calculating the difference between the slave date of the interferogram and the group dates respectively. The interferogram less than 15 days to a group date was subsumed into the corresponding group. One interferogram can belong to multiple groups. Eventually, each group contains at least one ascending and one descending track in order to compute 2D components of displacement maps.

We then obtained the maps of displacement components (U-D and E-W) using the formulation of Wright et al. ([2004](#)) (see [Section 2.3.6](#) for detail). The corresponding dates of maps were replaced by the group dates. All the maps were finally re-referenced to the map of 2007/04/15. The last date was approximated as 2008/07/26. The resultant 2D components of displacement time series maps are shown in **Figure 3.7** (U-D, vertical) and **Figure 3.8** (E-W, horizontal).

The post-eruptive U-D and E-W displacement components (**Figure 3.7** and **Figure 3.8**) show mainly a centripetal subsidence pattern on the Central Cone and a large scale trapezoidal seaward pattern on the Eastern Flank of Piton de la Fournaise. The centripetal subsidence of the Central Cone displays an asymmetrical pattern on the E-W displacement map, with up to 22 cm eastward on the western flank of the Central Cone and up to 12 cm westward on the eastern flank from April 2007 to July 2008 (**Figure 3.8**). On the U-D displacement map, the Central Cone show a concentric subsidence pattern with up to 27 cm downward displacement near the crater rim over this post-eruptive period (**Figure 3.7**). The limited scale of the centripetal subsidence pattern has been interpreted as being related to the released stress in a shallow source below the crater. The deflation of the shallow source following the Dolomieu crater collapse (2 April 2007) results in the ground surface displacement of the Central Cone ([Augier, 2011; Froger et al., 2015](#)). Given that the extension of the area of centripetal subsidence does not vary significantly between the co-eruptive and post-eruptive periods (**Figure 3.5 – Figure 3.8**), [Froger et al. \(2015\)](#)

assumed that the two displacement sources to be close or the same. The trapezoidal displacement pattern affects major part of the Upper and Middle Eastern Flank covering ~ 20 km² area. It is limited to the south by a sharp N120-125°E limit. To the east, the displacement does not extend to the Lower Eastern Flank. The entire trapezoidal area is affected by eastward and downward displacement indicating an overall downslope motion. The amplitude of downward displacement (maximum 28 cm) is larger than eastward displacement (maximum 17 cm) over almost the entire area between April 2007 and July 2008. This one year post-eruptive displacement of the Eastern Flank was interpreted as being produced by a set of normal faults that might have been activated by the EW extensional stress resulting from the detachment slip during the co-eruptive period ([Froger et al., 2015](#)).

PITON DE LA FOURNAISE
CHAPTER 3: STUDY AREA & THE MARCH-APRIL 2007 ERUPTION

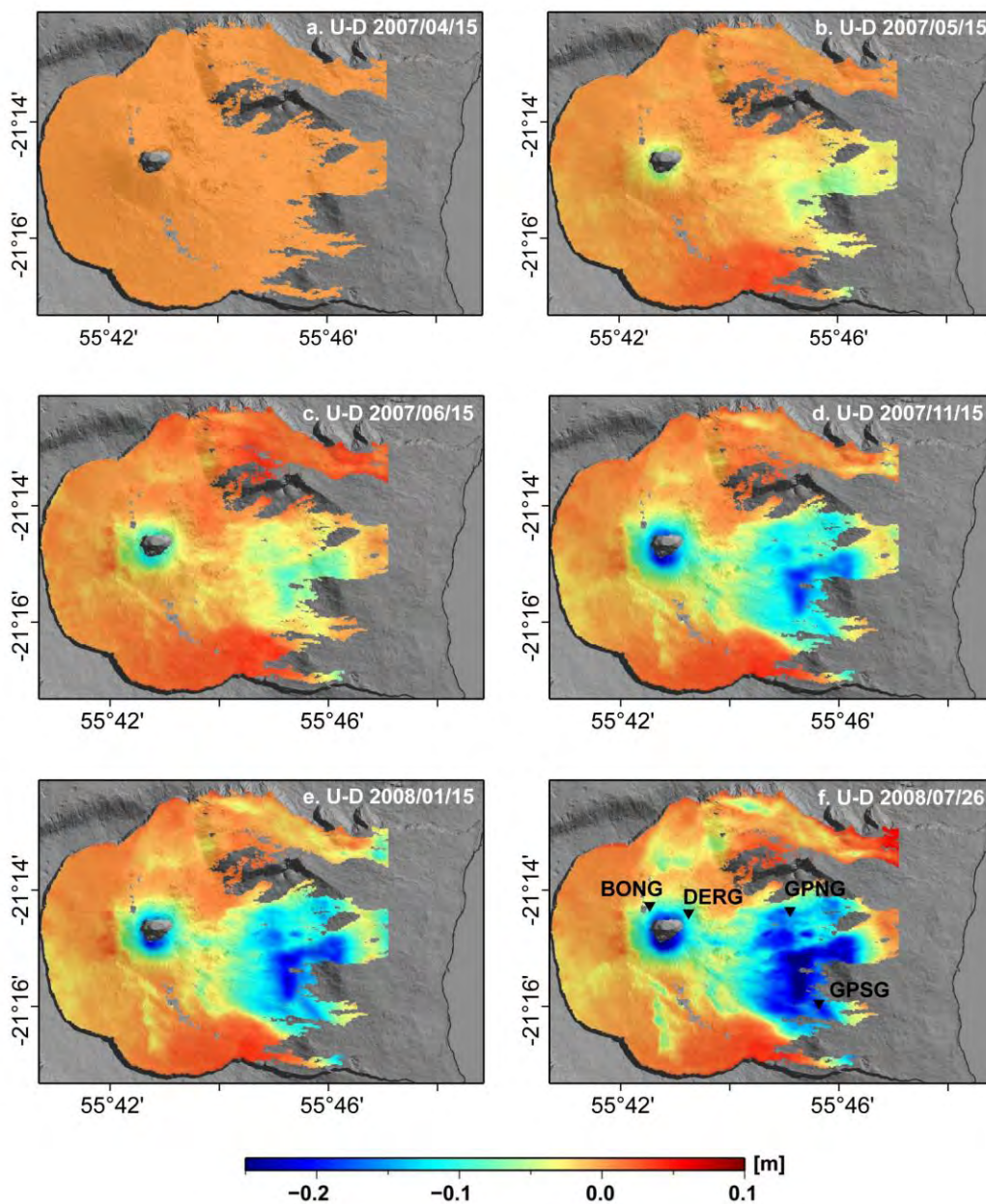


Figure 3.7 U-D component of post-eruptive ground displacement time series derived from ASAR data. All the maps are spatially referenced to a non-displacement zone that is located ~ 10 km away from volcanic craters, and temporally referenced to the first map in the time series (15 April 2007). Positive values represent upward displacement, while negative values represent downward displacement. Location of four GNSS stations (BONG, DERG, GPNG and GPSG) on the Central Cone and on the Eastern Flank are marked with black triangles in the last map (2008/07/26). Maps are draped on a shaded DEM and projected in Geographic Lat/Lon referenced to WGS-84 Datum.

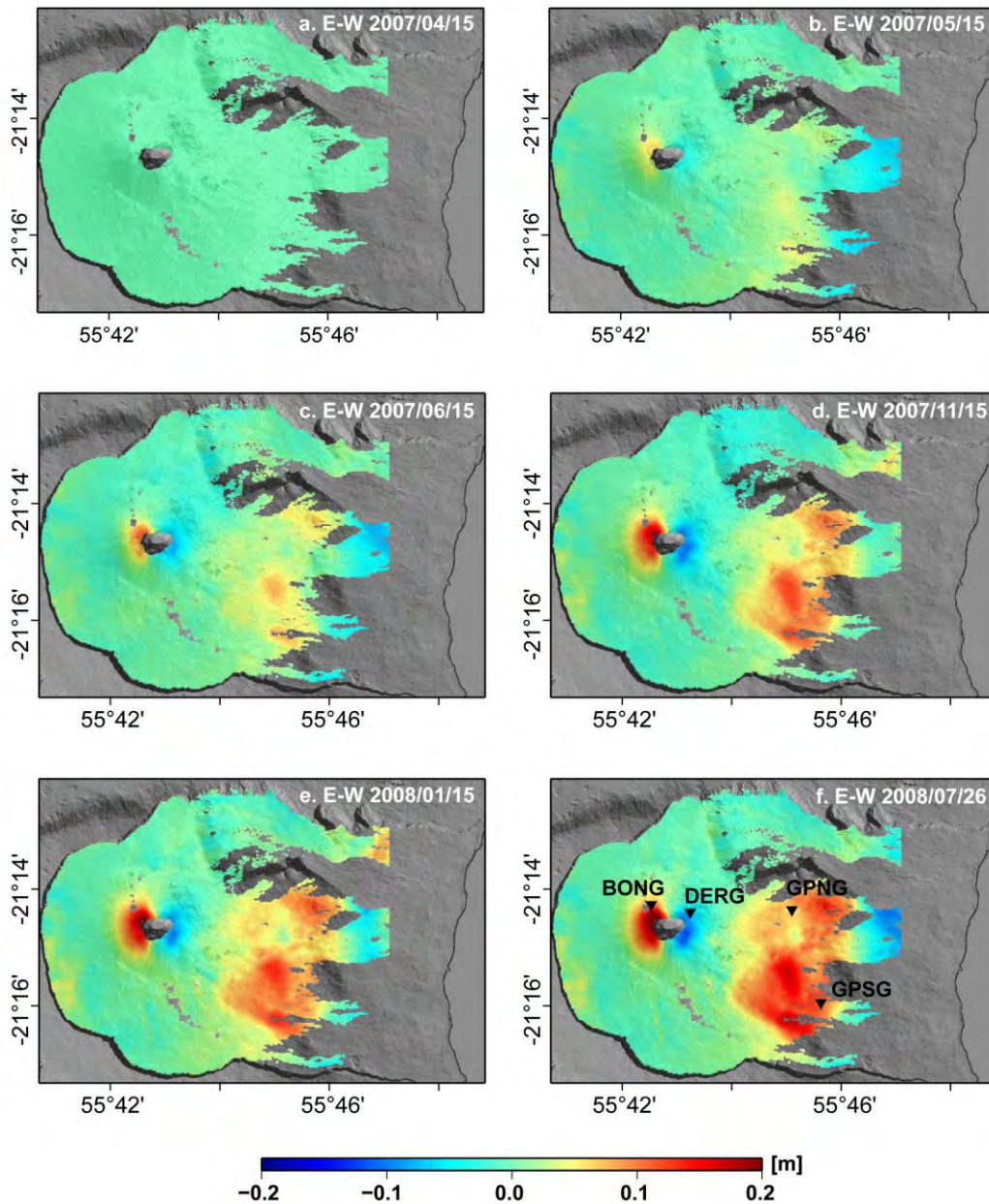


Figure 3.8 E-W component of post-eruptive ground displacement time series derived from ASAR data. All the maps are spatially referenced to a non-displacement zone that is located ~ 10 km away from volcanic craters, and temporally referenced to the first map in the time series (15 April 2007). Positive values represent eastward displacement, while negative values represent westward displacement. Location of four GNSS stations (BONG, DERG, GPNG and GPSG) on the Central Cone and on the Eastern Flank are marked with black triangles in the last map (2008/07/26). Maps are draped on a shaded DEM and projected in Geographic Lat/Lon referenced to WGS-84 Datum.

The **Figure 3.9** and **Figure 3.10** shows the ASAR-derived time series of four points right located at the position of GNSS stations (BONG, DERG, GPNG and GPSG), which illustrates the general temporal behavior of the ground displacement of the Central Cone and the Eastern Flank during the one year post-eruptive period (no eruptive event occurred). After the short-term and rapid rates motions during the co-eruptive period, the summit of the volcano deflates progressively inducing long-term and slow rates ground deformation following a more likely exponential than linear low in time in both U-D and E-W components (**Figure 3.9**). For the Eastern Flank, both U-D and E-W components present similar exponentially deforming trend with displacement rate decreasing with time, indicating that the large trapezoidal sector on the Eastern Flank of Piton de la Fournaise moves continuously downslope toward the sea, with an exponentially decreasing amplitude (Augier, 2011; Froger et al., 2015).

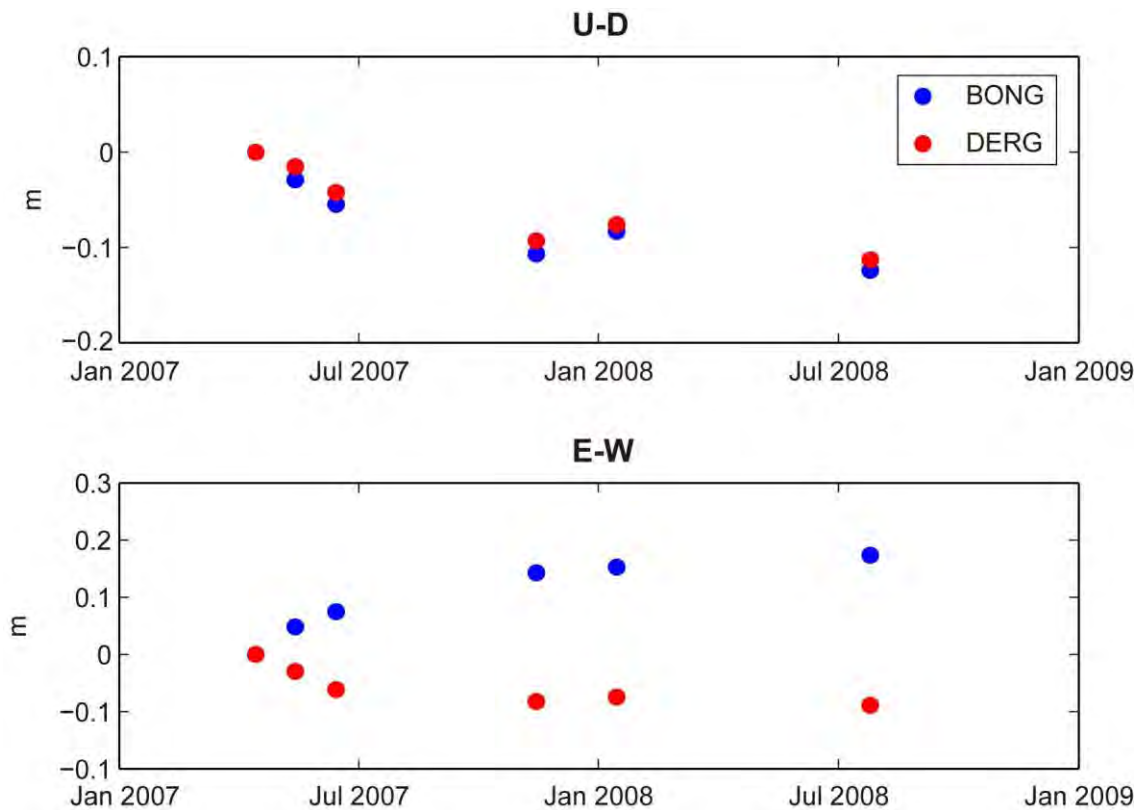


Figure 3.9 Temporal behavior of two points located at GNSS stations BONG and DERG on the Central Cone.

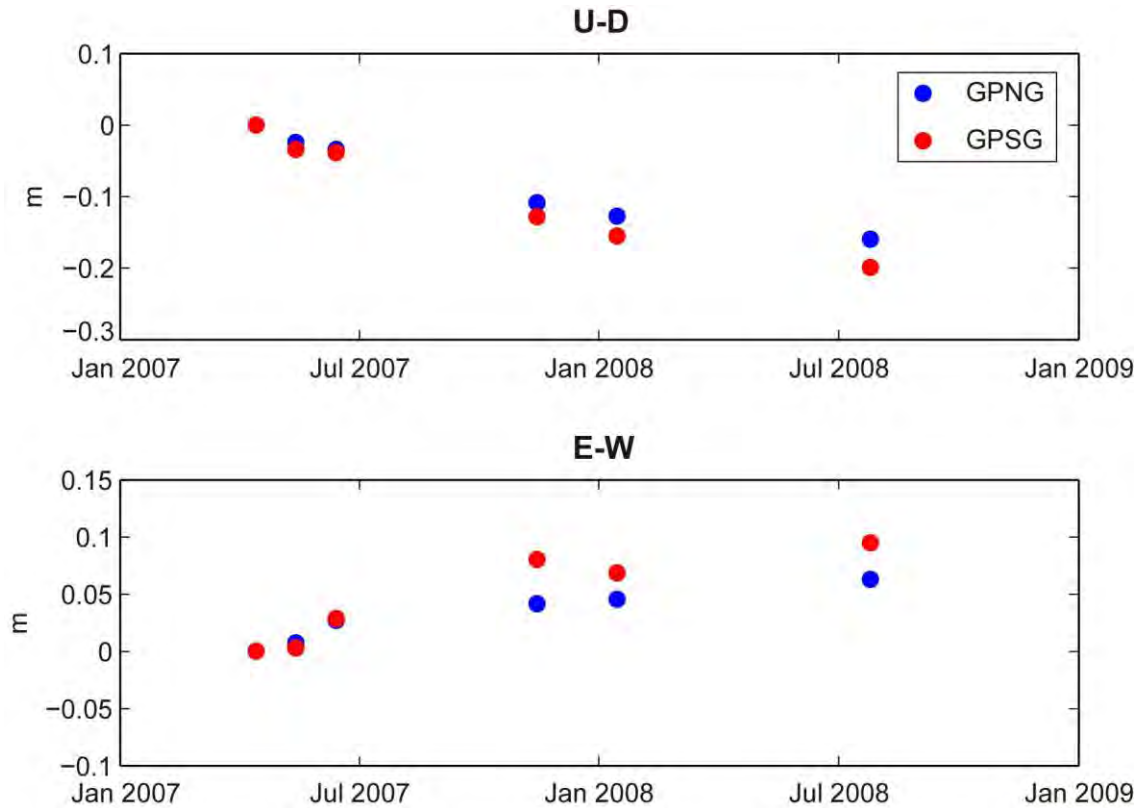


Figure 3.10 Temporal behavior of two points located at GNSS stations GPNG and GPSG on the Eastern Flank.

3.4 Discussion

The observations above during the co- and one year post-eruptive periods of the March-April 2007 eruption provide important insights:

1) The Central Cone displayed a centripetal subsidence during the co-eruptive period and it exponentially decreased during the one year post-eruptive period. The short scale InSAR signal that does not extend beyond the Central Cone suggests a very shallow displacement source (Froger et al., 2015). They proposed that the observed displacements are related to the sudden decompression of the hydrothermal system induced by the April 2007 Dolomieu collapse. This interpretation differs from that of Peltier et al (2008, 2009b) who proposed a shallow magma reservoir located between 0 and 1000 m above the sea level by modelling the GNSS data recorded during the 1998 – 2007 period. From tilt analysis and geochemical study,

Fontaine et al. (2014) and Di Muro et al. (2014) suggested that the 2007 eruptive sequence was triggered by a new magma input (at a depth of about 3.2 km below sea level; Fontaine et al., 2014) that pressurized the shallow part of the plumbing system.

2) The Eastern Flank of Piton de la Fournaise was affected by a widespread seaward motion during the March-April 2007 eruption and it kept deforming during the post-eruptive period, with an exponentially decreasing amplitude. This observed displacement is the first clear evidence of flank instability of Piton de la Fournaise. The deep mechanisms controlling the flank instability of Piton de la Fournaise is still the focus of debate. Got et al. (2013) proposed that the flank motion at Piton de la Fournaise may be controlled by flank eruptions, with high rates of co-eruptive flank displacement that decay over time. The displacement could occur due to a magma intrusion along a shallow interface such as a decollement or a detachment (Chaput et al., 2014a, 2014b; Froger et al., 2015), as already recognized at Piton des Neiges (the older twin of Piton de la Fournaise in La Réunion Island; Famin & Michon, 2010) and another basaltic volcano Kilauea (Got & Okubo, 2003). However, the existence of the interface beneath the Eastern Flank is still a subject of debate, which is mainly due to rareness of clear shallow seismicity below the Eastern Flank and that the earthquakes below the mobile flank are not aligned along a plane (Clarke et al., 2013; Peltier et al., 2015a, 2015b). Moreover, the Eastern Flank of Piton de la Fournaise shows no structural evidence for compression (contrast to Piton des Neiges), which led le Friant et al. (2011) to suggest that no decollement surface exists beneath the volcano. Peltier et al. (2015a) observed a slight acceleration of eastward motion at GPNG station from GNSS measurements during the eruptive/intrusive period spanning between October 2010 and February 2011. Then another acceleration of displacement was observed in April-mid May 2015 at Eastern Flank stations GPNG and HDLG (Peltier et al., 2016a). These accelerations of the Eastern Flank motion during pre-eruptive/eruptive periods and long-term motion during the rest periods show a deformation regime of the Eastern Flank – it relaxed the accumulated stress in or around the summit during rest periods and is accelerated by eruptive events (Peltier et al., 2015a). This highlights the importance of magmatic forces that could be the main process driving the flank instability of Piton de la Fournaise, although other processes such as gravitational force and lava flow cooling and contraction could also contribute to the deformation signal (Peltier et al., 2015b).

Whatever the processes controlling the Eastern Flank motion of Piton de la Fournaise, it is important to monitor the ground deformation of the edifice on a regular basis in order to prevent potential catastrophic hazards. Peltier et al. (2015a) observed easting and vertical displacements at four continuous GNSS stations located on the Eastern Flank of Piton de la Fournaise during 2010 – 2014 period (the 3 – 7 years after the March-April 2007 eruption). The authors suggest that it could be related to the ongoing sliding of the Eastern Flank that was triggered during the March-April 2007 eruption. Nevertheless, the study was based on measurements recorded at several GNSS stations, which is not capable enough for detecting large-scale deformation. Therefore, we will use InSAR technique to characterize the temporal and spatial behavior of the ground deformation fields at Piton de la Fournaise during the 7 years after the March-April 2007 eruption, aiming to improve the knowledge of the state of the volcano and the sophisticated processes going on in the volcanic edifice. This part of work will be presented in [Chapter 4](#).

**CHAPTER 4 : LONG-TERM GROUND
DISPLACEMENT BETWEEN 2009 AND 2014**

One of the main objective of the study is to monitor ground surface displacement at Piton de la Founaise during a long period of time in order to better understand the dynamic and the mechanism. Previous InSAR studies (Augier, 2011; Clarke et al., 2013; Froger et al., 2015) have shown a notable widespread motion (up to 1.4 m to the east and up to 0.37 m of uplift) affecting the Eastern Flank of Piton de la Fournaise during the co-eruptive period (See also Section 3.2), which was interpreted as seaward sliding of the Eastern Flank related to the activation of a detachment surface induced by a magmatic intrusion. Moreover, studies of Augier (2011) and Froger et al. (2015), and the analysis of ENVISAT time series in this thesis (Section 3.3) highlight that this downslope movement of the Eastern Flank lasted from the end of the eruption to at least July 2008, with an exponential time decay (up to 0.18 m to the east and up to 0.35 m of subsidence during a one-year post-eruptive period). More recently, four continuous GNSS stations located on the Eastern Flank of Piton de la Fournaise recorded easting and vertical displacements (up to ~ 0.02 m/yr to the east and up to ~ 0.025 m/yr of subsidence) between 2010 and 2014 (Peltier et al., 2015a). This observed eastward displacement led the authors to suggest that it could be related to the ongoing sliding of the Eastern Flank. However, this is only based on punctual measurements of several GNSS stations, which could only hint at the spatial distribution of displacement. It is thus essential to monitor and characterize the ground deformation of the volcano flank with high spatial resolution, in order to reduce the possibility of flank instability that could result in large catastrophic flank destabilizations and tsunami (McGuire, 1996). Different processes such as magmatic force, gravitational force, a pre-existing structural discontinuity and activated fault movement were proposed to attempt to explain the Eastern Flank motionf Piton de la Fournaise. But the deep mechanism is still the focus of debate according to current researches.

Therefore, the main objective of this chapter is to precisely describe and analyse the temporal and spatial variations of the long-term ground displacement that Piton de la Fournaise underwent after the March-April 2007 eruption by using large and dense X band InSAR time series. We also aim to make contributions to the interpretation of deformation signals and to provide useful implications for uncovering the processes accounting for the flank instability of Piton de la Founaise. This work is synthetized in the following research paper which is submitted to Remote Sensing of Environment.

Long-term ground displacement observations using InSAR and GNSS at Piton de la Fournaise volcano between 2009 and 2014

**Yu Chen ^a, Dominique Remy ^a, Jean-Luc Froger ^b, Aline Peltier ^c, Nicolas Villeneuve ^c,
José Darrozes ^a, Hugo Perfettini ^d, Sylvain Bonvalot ^a**

- (a) GET / UMR5563 (UPS, CNRS, IRD, CNES); Obs. Midi-Pyrénées, Université P. Sabatier, Toulouse, France.
- (b) LMV / UMR6524 (UBP, CNRS, IRD); Obs. de Physique du Globe de Clermont-Ferrand, Université B. Pascal, Clermont-Ferrand, France.
- (c) IPGP / UMR7154 (CNRS); Obs. Volcanologique du Piton de la Fournaise, Sorbonne Paris Cité, Paris, France.
- (d) ISTERRE / UMR5275 (UJF, CNRS, IRD); Obs. des Sciences de l'Univers de Grenoble, Université Joseph Fourier, Grenoble, France.

Remote Sensing of Environment

(Accepted with minor revision)

Abstract

Monitoring ground surface displacement of volcanoes over a long period of time helps improve understanding of the volcano structure, dynamics and mechanisms. In this paper, we investigate the spatio-temporal behavior of the long-term displacement field at Piton de la Fournaise volcano (La Réunion Island) by means of X-band InSAR and GNSS time series analysis from 2009 to 2014. We propose a new correction approach based on principal component analysis to mitigate the long-wavelength artifact in the interferograms over the study area. Our results show that most of the volcanic edifice including the Central Cone, the Eastern Flank and recent lava flow fields was affected by varying degrees of ground motion. More importantly, a widespread sector ($\sim 20 \text{ km}^2$) affected by time-dependent downward and eastward motion was observed on the Eastern Flank of Piton de la Fournaise. The combined analysis of InSAR and GNSS time series and previous studies allow us to confirm that this large mobile sector on the Eastern Flank underwent deformation for at least 7 years following the end of the large March-April 2007 eruption, including a stage of transient strain from the end of eruption to February 2011, followed by a stage of steady-state strain until late 2014. Several possible origins, including a pre-existing structural discontinuity, summit stress associated with magmatism, and activated fault movement are explored to explain the observed widespread long-term seaward motion that is considered to be direct evidence of potential flank instability.

Keywords: InSAR time series analysis, Piton de la Fournaise, Volcano ground displacement, InSAR artifact correction, Flank displacement

4.1 Introduction

Piton de la Fournaise (2632 m a.s.l., **Figure 4.1**), is a hotspot shield volcano forming the south-eastern part of La Réunion Island (**Figure 4.1b**), in the southwest Indian Ocean (**Figure 4.1a**; $21^{\circ}14'33''\text{S}$, $55^{\circ}42'32''\text{E}$). Most historical eruptions of Piton de la Fournaise have occurred in the Enclos Fouqué – Grandes Pentes – Grand Brûlé structure, an EW-elongated horseshoe-shaped depression ($\sim 13 \times 10 \text{ km}$) opening eastward to the Indian Ocean (**Figure 4.1c**). Although it has been proposed that this depression results from a caldera collapse ([Chevallier & Bachelery, 1981](#); [Duffield et al., 1982](#); [Bachelery & Mairine, 1990](#); [Bachelery, 1995](#)) or from flank collapses

PITON DE LA FOURNAISE
CHAPTER 4: LONG-TERM GROUND DISPLACEMENT BETWEEN 2009 AND 2014

(Lénat et al., 1990; Labazuy, 1996; Lénat et al., 2001), the origin of the Enclos Fouqué – Grandes Pentes – Grand Brûlé structure is still debated. However, the presence of debris avalanche deposits offshore of the Eastern Flank of Piton de la Fournaise provides proof of flank destabilisations moving down slope to the abyssal plain (Lénat et al., 1989; Labazuy, 1996; Le Friant et al., 2011).

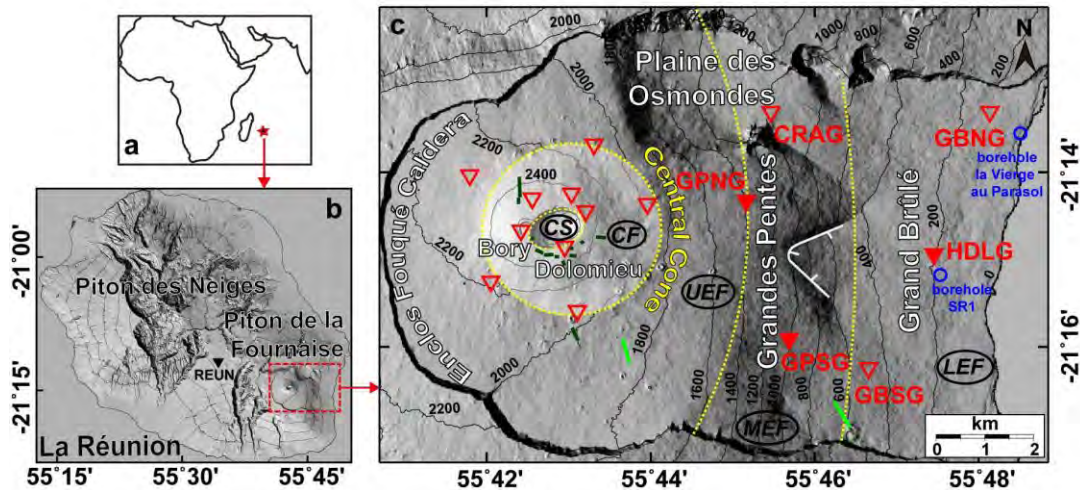


Figure 4.1 Shaded relief map of study area. (a) Location of La Réunion Island in the Indian Ocean. (b) Location of the Piton des Neiges and Piton de la Fournaise volcanoes on La Réunion Island, with location of the REUN IGS station (black triangle) used in this study for subtraction of the plate motion from GNSS data. (c) Shaded relief map of the Piton de la Fournaise volcano (the study area) with 200 m elevation contours and locations of the main areas mentioned in the paper: the Enclos Fouqué caldera, the Dolomieu and Bory caters, the Central Cone, the Plaine des Osmondes, the Grandes Pentes and the Grand Brûlé areas. CS, CF, UEF, MEF, and LEF refer respectively to Cone Summit, Cone Flank, Upper Eastern Flank, Middle Eastern Flank, and Lower Easter Flank; they are geographically divided by yellow dashed curves. Red triangles show the locations of the OVPF GNSS permanent stations inside the Enclos Fouqué caldera at the end of 2014; filled red triangles indicate the location of GNSS stations discussed in the paper. Blue circles indicate the locations of two boreholes in the Grand Brûlé area (Rançon et al., 1989). Dark green lines indicate the locations of eruptive fissures that opened during the study period. Light green lines indicate the locations of the March-April 2007 eruptive fissures. The white line with hatch marks indicates the V-shaped structure that was interpreted as the scar of a small-scale landslide by Bachèlery (1981). Maps are in Geographic Lat/Lon referenced to WGS-84 Datum.

In the upper part of the Enclos Fouqué – Grandes Pentés – Grand Brûlé structure, the Central Cone, built up by endogenous growth (e.g. [Annen et al., 2001](#); [Peltier et al., 2012](#)) and accumulation of volcanic products, exhibits an EW-elongated shape, with two pit-craters, the Bory crater to the west and the Dolomieu crater to the east. It is the site of the majority of historical activity, with eruptive fissures opening either in the summit crater or directly on the flank of the Central Cone. Occasionally, fissures have opened at low elevations far from the Central Cone in the Plaine des Osmondes or in the Grand Brulé (**Figure 4.1c**; [Peltier et al., 2009a](#)) and in rare cases (3% of the eruptions) outside the Enclos Fouqué – Grandes Pentés – Grand Brûlé structure ([Villeneuve & Bachèlery, 2006](#)).

After an unusually long dormant period of 63 months, Piton de la Fournaise was highly active between March 1998 and February 2011, with 39 eruptions and 8 intrusions ([Roult et al., 2012](#)). Then a ~ 3.5-year period of dormancy occurred. The eruption of 26 – 27 May 2016 is the sixth since activity resumed in June 2014. Most of the eruptions which have occurred since 1998 have fed lava flows that now cover a large portion of the Central Cone, Grandes Pentés, Grand Brûlé and Plaine des Osmondes areas.

Piton de la Fournaise is not only one of the most active basaltic volcanoes in the world but also one of the few that is monitored on a regular basis from space by the use of InSAR data. Thirty-five of the 44 eruptions that occurred between 1998 and 2015 were imaged using data provided by the Canadian RADARSAT-1 and RADARSAT-2 satellites ([Sigmundsson et al., 1999](#); [Fukushima et al., 2005, 2010](#)), the European ENVISAT and SENTINEL-1 satellites ([Froger et al. 2004, 2015](#); [Tinard, 2007](#); [Peltier et al., 2010a, 2016b](#)), the Japanese ALOS-1 and ALOS-2 satellites ([Augier, 2011, Peltier et al., 2016b](#)), the German TerraSAR-X and TanDEM-X satellites ([Froger et al., 2011](#); [Bato et al., 2016](#)) and the Italian Cosmo-SkyMed satellites ([Bato et al., 2016](#)). InSAR monitoring of Piton de la Fournaise became routine in 2003, initially through the Observatoire de Physique du Globe at Clermont-Ferrand, France. In 2010, this monitoring was integrated into the National Service for Volcanological Observations of the French National Institute for Earth Science and Astronomy under the name OI² (Observatoire InSAR de l’Ocean Indien). Currently, the OI² database (<https://wwwobs.univ-bpclermont.fr/casoar>) includes around 1200 radar images of Piton de la Fournaise acquired by various radar satellites from February 2003. The resulting InSAR database represents an exceptional record of the ground surface displacements that have occurred at Piton de la Fournaise since 2003.

The March-April 2007 eruption is considered to be the largest eruption observed at this volcano during the 20th and 21st centuries, and was characterized by a distal effusion of 210×10^6 m³ volume of lava, with a subsequent 340 m collapse of the Dolomieu crater (e.g. Staudacher et al., 2009; Bachèlery et al., 2010). Numerous studies have focused on investigating the displacement behavior of the volcanic edifice during and in months following this eruption using different techniques (such as, tiltmeters, Global Navigation Satellite Systems (GNSS), seismic networks, and InSAR), and on interpreting its origin and influence on the subsequent eruptive activities (Augier, 2011; Bachèlery et al., 2010; Michon et al., 2007b, 2009, 2011; Peltier et al., 2009b, 2010b, 2015a; Clarke et al., 2013; Got et al., 2013; Chaput et al., 2014a; Cayol et al., 2014; Rivet et al., 2014; Carrier et al., 2015; Froger et al., 2015, 2016). In particular, Augier (2011), Clarke et al. (2013) and Froger et al. (2015) produced InSAR-derived ground displacement maps that showed a notable widespread motion (up to 1.4 m to the east and up to 0.37 m of uplift during early co-eruptive period, and up to 0.07 m to the east and up to 0.18 m of subsidence during late co-eruptive period) affecting the Eastern Flank (See also Section 3.2), which was interpreted as seaward sliding of this flank related to the activation of a detachment surface induced by a magmatic intrusion. Another remarkable feature highlighted by these studies was that this downslope movement of the Eastern Flank lasted from the end of the eruption to at least July 2008 (up to 0.18 m to the east and up to 0.35 m of subsidence during a one-year post-eruptive period, with an exponential time constant of about 160 days; Augier, 2011; Froger et al., 2015; see also Section 3.3). More recently, four continuous GNSS stations located on the Eastern Flank of Piton de la Fournaise recorded easting and vertical displacements (up to ~ 0.02 m/yr to the east and up to ~ 0.025 m/yr of subsidence) between 2010 and 2014 (Peltier et al., 2015a). This observed eastward displacement led the authors to suggest that it could be related to the ongoing sliding of the Eastern Flank. Nevertheless, these point measurements of three-dimensional ground movements could only hint at the spatial distribution of displacement affecting the flank of the edifice. Accurate displacement maps with high spatial resolution are thus essential to better characterize the dynamics of the volcano flank, because the likelihood of continuous seaward motion of the Eastern Flank could raise the possibility of flank instability, which could result in large catastrophic flank destabilizations and tsunamis (McGuire, 1996; Kelfoun et al., 2010).

The objective of this study is to precisely describe and analyse the long-term ground motions that Piton de la Fournaise underwent after the March-April 2007 eruption. We focus particularly on characterizing the spatial pattern and temporal evolution of the previously observed seaward motion affecting the Eastern Flank. To achieve these goals, we adopted an enhanced Small Baselines (SB) -InSAR method based on the Stanford Method for Persistent Scatterers (StaMPS; [Hooper et al., 2012](#)) to perform a detailed time series analysis on a large quantity of X band SAR data provided by the COSMO-SkyMed and TerraSAR-X/TanDEM-X satellites. The data used in this study (including SAR data and GNSS data) are presented in [Section 4.2](#). We used a new correction approach ([Section 4.3](#)) based on a principal component decomposition method ([Kositsky and Avouac, 2010](#)) for discriminating the displacement signal from artifacts because we demonstrate that traditional artifact correction methods are inapplicable in the specific conditions of the study area. The results derived from InSAR and GNSS data ([Section 4.4](#)) based on qualitative analysis reveal a widespread time-dependent downward and eastward displacement affecting the Eastern Flank during the 2009-2014 period, which coincides with the trapezoidal pattern observed by [Augier \(2011\)](#) and [Froger et al. \(2015\)](#). Summit deflation and subsidence on lava flow fields is also observed during this study period. [Section 4.5](#) discusses the evidence which confirms that the large mobile sector of the Eastern Flank continued to deform for at least 7 years after 2007, and the possible origins of this deformation. [Sections 4.6](#) summarizes the conclusions. This paper provides essential insight not only to improve understanding of the spatio-temporal ground displacement behavior at Piton de la Fournaise volcano, but also for hazard assessment of potential flank destabilizations at other basaltic volcanoes.

4.2 Data

4.2.1 SAR data

For this study we use a large amount of X band SAR data acquired by the German Space Agency TerraSAR-X/TanDEM-X (hereafter abbreviated to TSX) satellite constellation and by the Italian Constellation of Small Satellites for the Mediterranean basin Observation (COSMO-SkyMed, hereafter named CSK). X band SAR data, thanks to their fine spatial resolution and their

high revisit frequency, provide the means for accurate detection of low amplitude displacement at high spatial and temporal resolution (Bovenga et al., 2012). The TSX dataset includes 56 acquisitions from ascending orbits (Acquisition mode: Stripmap; Beam: strip_008; Track: 68) from 7 March 2009 to 15 November 2014, and 34 acquisitions from descending orbits (Acquisition mode: Stripmap; Beam: strip_010; Track: 121) from 13 December 2008 to 6 October 2014. The CSK dataset includes 43 acquisitions from ascending orbits (Acquisition mode: Stripmap; Swath: 15) and 43 acquisitions from descending orbits (Acquisition mode: Stripmap; Swath: 18) both acquired between 15 February 2011 and 19 September 2014 (Table 4.1).

Satellite	Acquisition mode	Beam/Track (Swath)	Pass	Time spans	Incidence angle (deg)	Wavelength (m)	Ground resolution (m)	Acquisitions (number/hour-local)	Interferograms
TSX	Stripmap	strip_008/68	Ascending (Asc)	2009/03/07 - 2014/11/15	33.5	0.0310	Range: 3.23 Azimuth: 3.3	56/18:41	325
TSX	Stripmap	strip_010/121	Descending (Des)	2008/12/13 - 2014/10/06	36.5	0.0310	Range: 1.94 Azimuth: 3.3	34/05:52	196
CSK	Stripmap	-/15	Ascending (Asc)	2011/02/15 - 2014/09/19	48.8	0.0312	3	43/06:45	257
CSK	Stripmap	-/18	Descending (Des)	2011/02/15 - 2014/09/19	52.2	0.0312	3	43/17:26	244

Table 4.1 Summary of the processed SAR data. Ascending and descending CSK images are acquired at the same dates.

4.2.2 GNSS data

The permanent GNSS network operated by the Piton de la Fournaise Volcano Observatory (Observatoire Volcanologique du Piton de la Fournaise, OVPF) has been progressively implemented since 2002 (refer to Peltier et al. (2015a) for detailed chronogram). By the year of the March-April 2007 eruption, 12 continuous GNSS stations had been installed on the Central Cone of Piton de la Fournaise. The network did not extend to the Eastern Flank until the end of 2009 / beginning of 2010. By the end of 2014, there were 24 permanent GNSS stations, including 16 stations inside the Enclos Fouqué caldera (10 on the Central Cone and 6 on the Eastern Flank, see map in Figure 4.1c for locations) and 8 outside (not shown here). The increased density of the GNSS network provides greater insight into the sophisticated processes going on in the volcanic edifice, with a sufficient space and time resolution (Got et al., 2013; Rivet et al., 2014; Peltier et al., 2015a).

In the present study, we paid particular attention to the displacements measured at the 6 GNSS stations installed on the Eastern Flank (GPSG, GPNG, HDLG, GBNG, CRAG and GBSG marked by red triangles in **Figure 4.1c**). The receivers record one measurement every 30 s. The daily GNSS solutions were processed using the GAMIT/GLOBK software (Herring et al., 2010) following Peltier et al. (2015a). The 1σ accuracies of the daily positions are ~ 5 mm and ~ 10 mm for horizontal and vertical components, respectively. The precise ground displacement time series in three dimensions (up-down, U-D; east-west, E-W; north-south, N-S) at each GNSS station were then obtained after having been corrected for plate motion using the data recorded at the REUN IGS station (**Figure 4.1b**). This IGS station is located about 15 km west of the volcanic summit and the ground displacement observed at this station is considered to be mainly affected by plate motion.

4.3 InSAR processing

4.3.1 InSAR time series generation

First, we used the DORIS software to generate all the interferograms with small baselines (perpendicular baselines < 500 m and temporal baselines < 365 days) in order to construct four initial SB subsets for both TSX and CSK ascending and descending orbit datasets. No multilooking was applied before forming the interferograms in order to retain the highest spatial resolution. Filtering of the range and azimuth was applied prior to the generation of interferograms in order to reduce geometric decorrelation and to discard non-overlapping Doppler frequencies (Hooper, 2008). An IGN (French National Geographic Institut) Lidar Digital Elevation Model (DEM), with 5 m resolution, was used to simulate and subtract the topographic contribution, and to georeference the interferograms. We then added interferograms with larger baselines but good coherence to our SB dataset to ensure the soundness of the network. Taking the CSK ascending orbit as an example, due to the lack of SAR acquisitions during the period between March 2012 and June 2013, we added several interferograms with larger temporal baselines but good coherence (see orange lines in **Figure 4.2**) to ensure no isolated clusters remained in the network. Finally, interferograms with clear strong, turbulent atmospheric artifacts were rejected. We eventually obtained 4 independent subsets of 325, 196,

257, and 244 SB interferograms from ascending and descending orbits of TSX and CSK, respectively (Table 4.1; Figure 4.2). The coherent pixels referred to as slowly-decorrelating filtered phase (SDFP) pixels were next selected based on a statistical analysis of the amplitude difference dispersion and the phase stability (Hooper et al., 2007; Hooper, 2008). We chose a 3D unwrapping algorithm (Pepe & Lanari, 2006; Hooper & Zebker, 2007) that takes ‘time’ into account (as the third dimension) to unwrap the phases of the SDFP pixels. To further refine the SDFP pixels, we searched for unwrapping errors using the redundancy of SB networks and manually removed them. In order to reduce the amount of data for further processing, we subsampled all the SB interferograms to a 20 m resolution. Ultimately, 172598, 176806, 145289 and 163627 refined SDFP pixels were retained for TSX ascending, TSX descending, CSK ascending and CSK descending subsets, respectively.

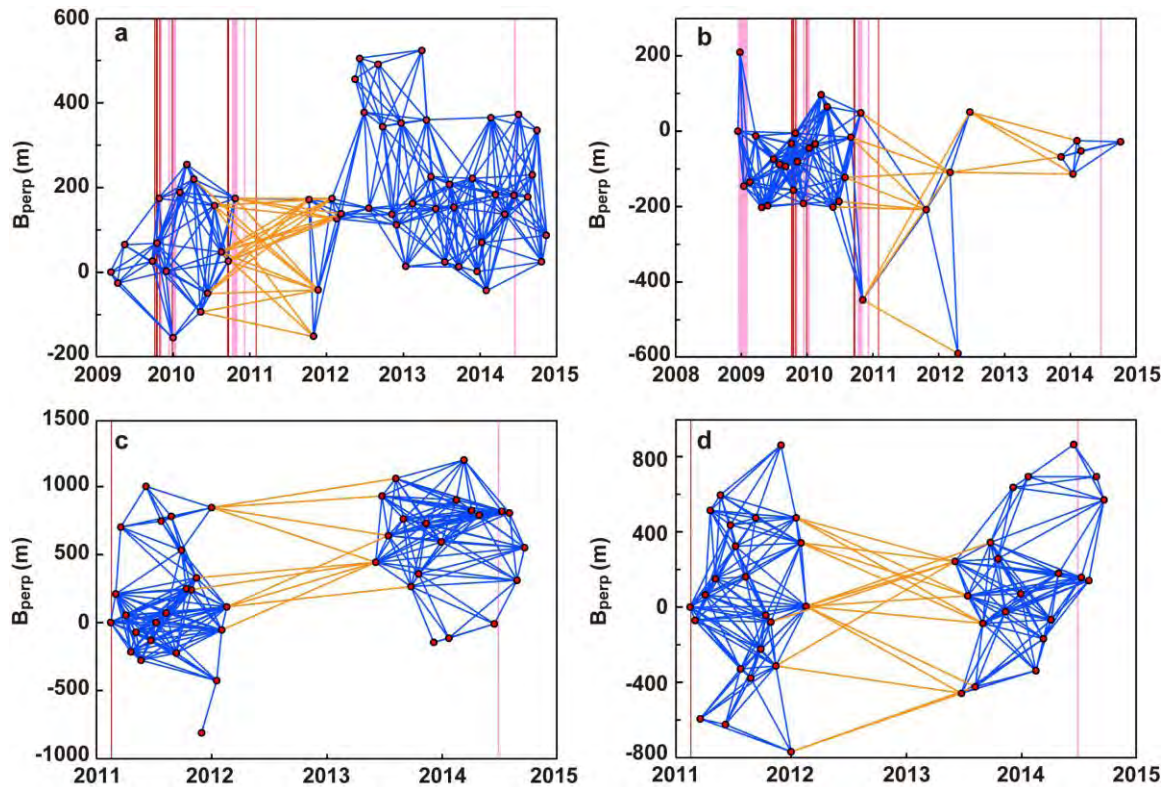


Figure 4.2 Perpendicular baselines (in meters) as a function of time for: (a) TSX ascending orbit; (b) TSX descending orbit; (c) CSK ascending orbit; (d) CSK descending orbit. Black-edged, red-filled circles represent individual SAR acquisitions, and the lines connecting them indicate the small baseline interferograms formed by two SAR images. Orange lines represent the interferograms with relatively larger baselines but good coherence. Pink areas and dark red vertical lines represent times of eruptions and intrusions, respectively, which occurred during the study period.

The generation of InSAR time series is a process of inversion from the space of an SB subset to the space of single master subset (where all the maps are chronologically ordered relative to one single map from one particular epoch) based on the redundant information of the SB subset. We performed a least squares adjustment independently on each SB subset, on a pixel-by-pixel basis, to obtain the time series corresponding to each SAR acquisition. The inversion is expressed by [Equation \(4.1\)](#):

$$\phi_{sb} = G\phi_{ts} \quad (4.1)$$

where ϕ_{sb} are the interferometric phases from the SB subset, ϕ_{ts} the time series to be inverted and G the design matrix with zeros, plus and minus ones ([Usai, 2003](#)).

Subsets of the inverted InSAR time series for the four acquisition geometries (ascending and descending orbits of the TSX and CSK datasets) are shown in [Figure 4.3](#). The maps were referenced spatially to the average of a small zone (indicated by a black circle in [Figure 4.3a](#)) that is located ~ 10 km away from the volcanic craters and is not expected to be affected by volcanic displacement, and temporally to the map for the first acquisition of the orbit. The time series maps reveal that the X band InSAR data exhibit excellent coherence in most areas of the volcanic edifice where recent lava flows cover the ground surface. The areas lacking coherence correspond either to vegetated areas (e.g. the Grand Brûlé, see [Figure 4.1c](#) for location) or to areas affected by transient eruptive activity (e.g. the Central Cone, see [Figure 4.1c](#) for location). During the period spanned by our study, from December 2008 to November 2014, seven eruptions occurred at Piton de la Fournaise, with vents located either in the summit craters or on the slopes and/or at the base of the Central Cone ([Table 2.2](#); [Roult et al., 2012](#); [Bato et al., 2016](#)). Most of the displacement patterns associated with these eruptions do not extend beyond the base of Central Cone. Only the October 2010 eruption produced a larger displacement field that extended eastwards to the top of the Upper Eastern Flank (UEF, see [Figure 4.1c](#) for location; [Bato et al., 2016](#)), which is visible in [Figure 4.3a-b](#) (map 2011/10/24 and onward).

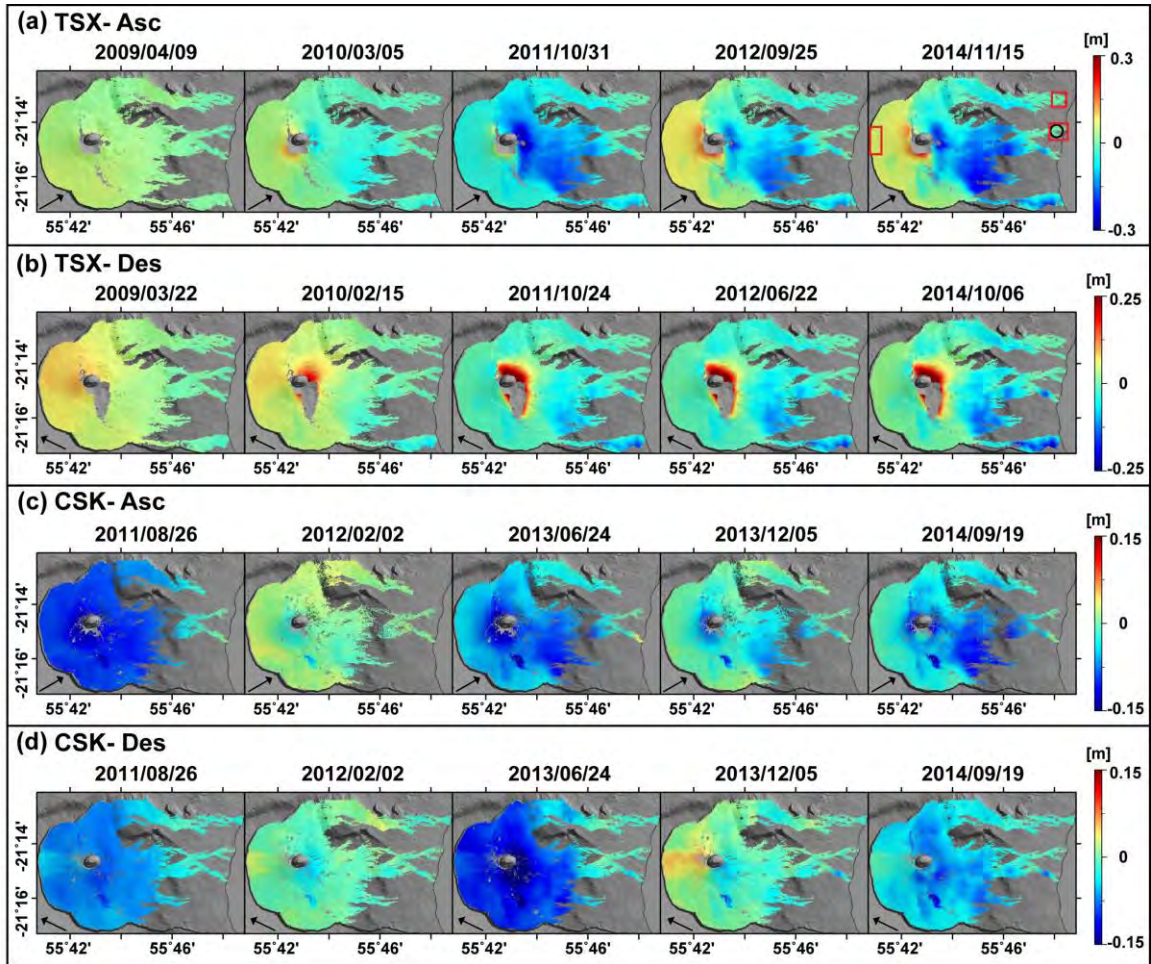


Figure 4.3 Subset of uncorrected InSAR time series maps from (a) TSX ascending, (b) TSX descending, (c) CSK ascending, and (d) CSK descending data. The maps are spatially referenced to a non-displacement zone (indicated by a black circle in **Figure 4.3a**) that is located ~ 10 km away from volcanic craters. TSX ascending maps are temporally referenced to the map of 7 March 2009, with TSX descending maps being temporally referenced to map of 12 December 2008, and both CSK ascending and descending maps are temporally referenced to map of 15 February 2011. Positive values represent decreases in earth-satellite distance, while negative values represent increases in earth-satellite distance. Areas in grey correspond to low coherence areas or to areas characterized by unwrapping errors detected in TSX and CSK interferograms. Red rectangles indicate the areas where no displacement is expected to occur. Black arrows indicate the LOS directions. Maps are draped on a shaded DEM and projected in Geographic Lat/Lon referenced to WGS-84 Datum.

Name	Date of Beginning	Date of end	Location
------	-------------------	-------------	----------

PITON DE LA FOURNAISE
CHAPTER 4: LONG-TERM GROUND DISPLACEMENT BETWEEN 2009 AND 2014

June 2014	2014/06/20	2014/06/21	Near summit, South-Southeastern (S-SE) slope of the Central Cone
February 2011	2011/02/20	2011/02/20	Seismic crisis without eruption
December 2010	2010/12/09	2010/12/10	N-NW Flank of the Central Cone
October 2010	2010/10/14	2010/10/31	SE Base of the Central Cone
September 2010	2010/09/23	2010/09/23	Seismic crisis without eruption
January 2010	2010/01/05	2010/01/12	Summit, inside of the Dolomieu crater
December 2009	2009/12/14	2009/12/15	Near summit, S-SW slope of the Central Cone
November 2009	2009/11/05	2009/11/06	Near summit, S-SE slope of the Central Cone
October 2009	2009/10/18	2009/10/18	Seismic crisis without eruption
October 2009	2009/10/07	2009/10/07	Seismic crisis without eruption
December 2008	2008/12/14	2009/02/03	Summit, inside of the Dolomieu crater

Table 4.2 Eruptions and intrusions at Piton de la Fournaise during the study period (OVPF observation). The locations of eruptive fissures are also indicated in **Figure 4.1c**.

4.3.2 InSAR artifact analysis

Even though large InSAR datasets were used, a close inspection of the inverted time series (**Figure 4.3**) revealed that non-negligible long-wavelength artifacts are present in some maps. These artifacts mainly explain the high values of the standard deviation (from 16.6 to 26.2 mm) computed in areas where no displacement is expected (Got et al., 2013; Peltier et al., 2015; outlined by red rectangles in **Figure 4.3a**; **Table 4.3**). Therefore, it is necessary to identify and correct these artifacts continuing with the analysis.

	TSX-Asc	TSX-Des	CSK-Asc	CSK-Des
Uncorrected	17.7	16.6	21.2	26.2
Corrected	5.5	6.0	7.0	6.7

Table 4.3 Comparison of average standard deviations without and with correction in non-displacement areas ($\times 10^{-3}$ m)

It is well known that the accuracy of InSAR analysis is mainly affected by two sources of artifacts: residual orbital errors and atmospheric delays (Bürgmann et al., 2000; Hanssen, 2001). Fattahi and Amelung (2014) have noted that InSAR uncertainty is dominated by atmospheric delays rather than orbital errors. They estimated an uncertainty in velocity gradients due to the orbital errors ranging from $\sim 0.2 - 0.5 \text{ mm yr}^{-1} 100 \text{ km}^{-1}$ for TerraSAR-X and Sentinel-1 satellites, indicating that for modern satellites with precise orbits (such as TSX and CSK), precise InSAR time series results can be derived without orbital correction if other sources of artifacts are identified and properly corrected for (Fattahi & Amelung, 2014). This is particularly true when, as in our case, the study area is small ($\sim 13 \times 10 \text{ km}$).

Hence, we focused more on investigating atmospheric delays induced by variations of the refraction index in the troposphere. Different methods for estimating tropospheric delays have been investigated in previous studies. Some of them are based on using external data such as the Precipitable Water Vapor (PWV) estimation using MERIS and MODIS near infrared products or GNSS data (e.g. Li et al., 2005; Froger et al., 2007; Remy et al., 2011, 2015) or a high resolution weather model (Foster et al., 2006), or Global Atmospheric Models (GAMs; Jolivet et al., 2011, 2014). We examined the potential of MODIS and MERIS data for InSAR atmospheric corrections at Piton de la Fournaise. The main limitation is that the collection of both data relies heavily on the time and on the cloud conditions. MERIS data were acquired at $\sim 9:30$ am local time while MODIS data were acquired at $\sim 10:30$ am/ $1:30$ pm local time, which do not unfortunately match the acquisition times of our processed SAR data (Table 4.1). The specific tropical and oceanic climate of La Réunion Island induces water vapor that can be highly variable in time and space and have a short life span. *These climatic conditions and the time lag between PWV and SAR image acquisitions make it impossible to use MODIS and MERIS data to mitigate tropospheric effects on InSAR measurements.* Moreover, the MERIS data are only available up to the end of the ENVISAT mission in 2012. The main limitation for using GNSS data to estimate the tropospheric delays at Piton de la Fournaise is the network density. The stations were mainly concentrated in the Central Cone area, until three stations (HDLG, CRAG, and GBSG; see Figure 4.1c for location) were installed on the Eastern Flank in late 2009. The implementation of the other three stations on the Eastern Flank was even later, in 2010 (GPNG and GPSG) and

2011 (GBNG). Given that the processed TSX data begins from late 2008 and that we preferred to use a consistent approach for all interferogram corrections in order to reduce uncertainty and ensure the compatibility, we did not use GNSS data for the tropospheric correction in this study. We also attempted to correct interferograms for tropospheric delays using the ERA-Interim analysis implemented in PyAPS (Jolivet et al., 2011). However, this technique did not work satisfactorily either due to the coarse resolution of ERA-Interim meteorological parameters (~ 75 km) or the acquisition time difference between SAR data and ERA-Interim data (about 90 min).

Without a reliable solution to correctly mitigate atmospheric errors in our series of InSAR data, we adopted the following approach. We first assumed that turbulent tropospheric delays were randomly distributed and independent of one another (Ferretti et al., 2001; Berardino et al., 2002; Cavalié et al., 2007, 2008). Thus in this study, the turbulent tropospheric delays were efficiently removed by the least square adjustment using the redundant information of the large time series of interferograms. Contrary to turbulent delays, vertically stratified tropospheric components correlated with elevation exhibit long-wavelength phase delays that are generally seasonal, with similar spatial patterns that can bias the long-wavelength ground displacements recorded by InSAR (Doin et al., 2009). Due to their periodicity, these delays can significantly blur subtle signals related to long-term deformation, such as those expected on the Piton de la Fournaise. Different methods have been proposed to estimate tropospheric delays using the interferograms themselves based on empirical functions (Remy et al., 2003; Cavalié et al., 2008; Bekaert et al., 2015). These methods can estimate the tropospheric artifact from the correlation between the interferometric phase and the topography. Nevertheless, the ground displacement signal may bias the estimation and be mistaken for an artifact, especially when the ground displacement also correlates with the elevation, as found for our InSAR dataset (see Section 4.8.1 in supplementary materials). One possible solution is to mask all displacements affecting areas in the interferogram and estimate the relationship between the interferometric tropospheric phase and the topography in the non-displacement areas. However, investigation into the InSAR time series (**Table 4.3**) prevented us from implementing this solution, as most parts of the volcanic edifice (the Central Cone, the Eastern Flank, and the northern and southern parts of Enclos Fouqué) are expected to be affected by varying degrees of long-term displacement. In this case, a classical approach is to use empirical corrections in conjunction with a long-term deformation model. However, we did not have a reliable long-term

deformation model that could explain the complex ground deformation patterns observed at Piton de la Fournaise. So, we decided to use the following method using empirical corrections in conjunction with a statistically-based approach to estimate the temporal behavior of the long-term ground deformation.

4.3.3 InSAR artifact correction approach

We applied a principal component decomposition, implemented in Principal Component Analysis-based Inversion Method package (PCAIM; [Kositsky and Avouac, 2010](#)) to the InSAR time series obtained in [Section 4.3.1](#), in order to search for a Long-Term Displacement Model (LTDM) and then remove it prior to artifact estimation. (see [Lin et al., 2010](#), [Remy et al., 2014](#) for application to volcanic deformation studies).

4.3.3.1 *Estimation of Long-Term Displacement Model*

It is necessary to take precautions when applying the principal component decomposition. In particular, several maps in the InSAR time series are characterized by large-amplitude transient signals, such as those produced by strong large-wavelength tropospheric artifacts or by short-wavelength ground displacements related to dyke intrusion (mainly in the Central Cone). These transient signals could produce large variance signals which are higher than the variance related to the long-term displacement signal recorded in the whole InSAR time series and prevent the long-term displacement signal from being captured in the decomposition analysis. Thus we eliminated some time series maps which recorded large strong wavelength tropospheric signals. We also searched out and masked the pixels (about 10 % and 2% for TSX and CSK data, respectively) which are affected by strong deformation peak (greater than 6 cm) caused by the eruptive activity during the study period. Furthermore, in order to increase the signal-to-noise ratio, the ascending and descending time series of TSX and CSK were combined into a large data matrix respectively. Then we interpolated the values at missing epochs over the overlapped period. Eventually, we obtained a TSX data matrix with 338889 lines (total pixel number) and 80 rows (epochs), and a CSK data matrix with 304123 lines and 40 rows as the inputs for the decomposition. The input data matrices were decomposed into a linear combination of principal components, each of them individually associated with a spatial

function or pattern (U), a significance value (S) and a temporal function (V), where the spatial function presents the spatial distribution of signals, the significance value indicates the importance of the relative component, and the temporal function describes the temporal behavior of signals (Kositsky and Avouac, 2010) (see Section 4.8.2 in supplementary materials).

Figure 4.4 summarizes the first three components with their significance values, which are one order of magnitude larger than the other components obtained from the TSX and CSK datasets. The non-data zone in the Central Cone area in **Figure 4.4b, d** differs from that in **Figure 4.3** because we masked the coherent pixels that were affected by large transient displacements associated with eruptive activity, as described above. The first component of the TSX dataset and the third component of the CSK dataset show a similar spatial pattern observed for the Eastern Flank (**Figure 4.4b, d**) with an amplitude that decreases gradually with time (**Figure 4.4a, c**). Nevertheless, although this signal clearly dominates the TSX time series, it does not have the same effect on the CSK time series. It is thus questionable whether the third component of the decomposition of the CSK data is reliable to estimate long-term displacement. To assess this question, the decomposition of the TSX data was carried out using only the measurements acquired from 2012 to 2014, and the result was compared to the one obtained from the decomposition of the CSK data. The result is very similar both in space and time. Furthermore, the spatial pattern of this signal correlates well with the ground displacement pattern observed soon after the 2007 eruption. This led us to consider this signal as being mainly related to ground displacements affecting the volcano edifice during the study period. On the contrary, the other components (2nd and 3rd for TSX, 1st and 2nd for CSK) are mostly related to stratified tropospheric delays which explains the strong correlation observed between the spatial components and the topography (see scatter plots in **Figure 4.4b, d**). The temporal behavior of the second and the third components for TSX data appears to show some seasonal variations (mainly positive in winter/ negative in summer) but a similar behavior is not observed in the first and the second components of the CSK data. These results highlight the need to mitigate the stratified tropospheric delays in order to be able to accurately measure subtle long-term displacements by InSAR at Piton de la Fournaise.

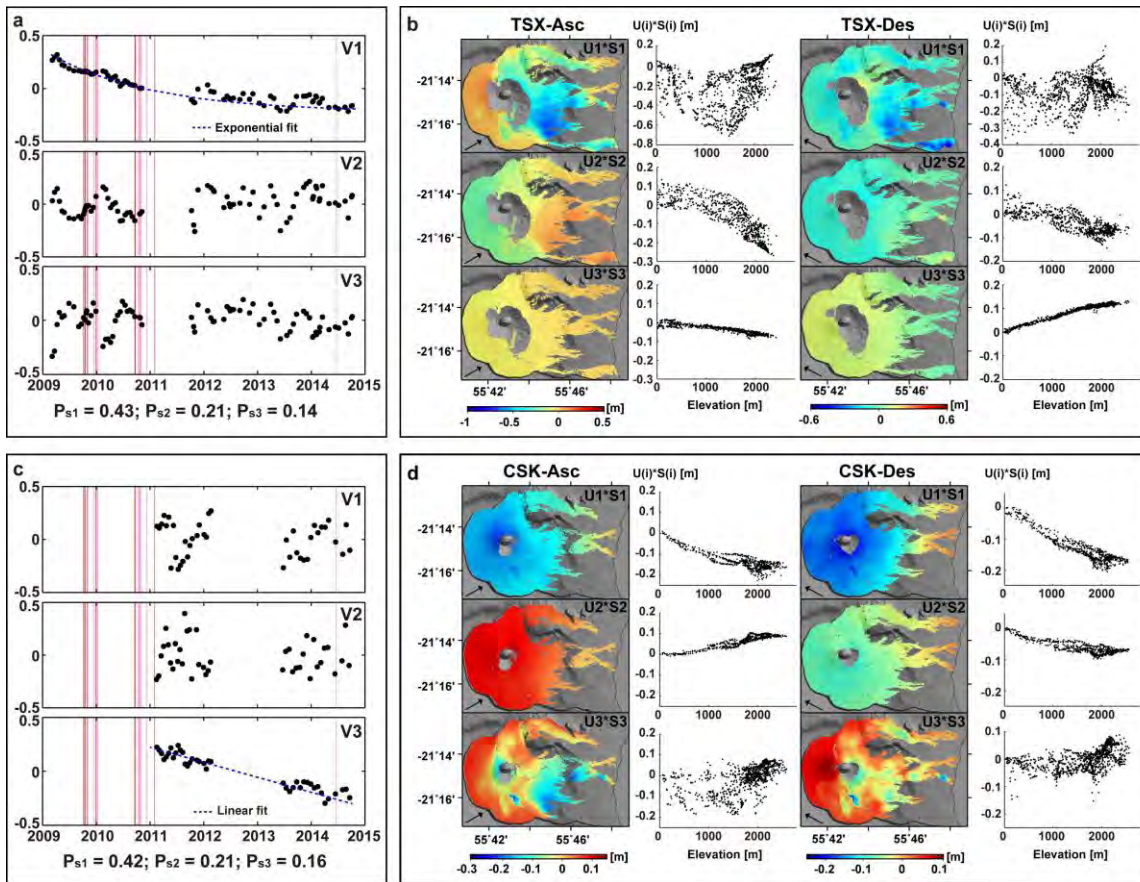


Figure 4.4 Results from the principal component decomposition applied to TSX and CSK InSAR time series inverted from the SB interferograms, with no correction applied. (a) and (c), Normalized temporal functions (V1 to V3) of the first three principal components with corresponding proportions (P_{S1} to P_{S3}) of significance values for (a) TSX and (c) CSK datasets respectively. The first temporal function (V1) in (a) evolves exponentially (blue dashed curve) with time and is associated with long-term ground displacement during the observed period (2009-2014) of TSX. The third temporal function (V3) in (c) evolves linearly (blue dashed line) with time and is associated with long-term ground displacement during the observed period (2011-2014) of CSK. Pink areas and dark red vertical lines represent times of eruptions and intrusions, respectively, which occurred during the study period. (b) and (d), The spatial functions weighted by significance values ($U1*S1$ to $U3*S3$) of the first three principal components for TSX and CSK datasets respectively. The scatter plots indicate the correlations between the principal components and the elevation. Areas in grey correspond to area with low coherence or affected by unwrapping errors or strong transient motions. Black arrows on the maps indicate the LOS directions. Maps are draped on a shaded DEM and projected in Geographic Lat/Lon referenced to WGS-84 Datum.

Figure 4.4a (V1) and c (V3) indicate that an exponential decay and a linear function provides a good fit for the temporal functions of the displacement-related components for TSX

(2009-2014) and CSK (2011-2014), respectively. The LTDM in TSX is estimated by reconstructing the data using U1, S1 and the best-fit single-term exponential model (**Figure 4.4a-b**). In the same way the LTDM observed in CSK is estimated by reconstructing the data using U3, S3 and the best-fit linear model (**Figure 4.4c-d**).

4.3.3.2 Stratified Delay Mitigation

Once the LTDM time series has been created, the LTDM components within the SB interferograms are then accessible by differential operations. We can extract the LTDM component from each SB interferogram and put it aside for later use. Next we deal with the residual signals in each SB interferogram. We approximated the phase ramps induced by long-wavelength artifacts (mainly stratified tropospheric delays and a small proportion of possible residual orbital errors), on an interferogram-by-interferogram basis, using 3 different empirical functions: a). S-trop_orb, a spline function estimating the tropospheric and residual orbital phase ramp solved by a genetic algorithm; b). Q-trop_orb: a quadratic function (**Equation (4.2)**);

$$\phi_i = ax_i + by_i + cx_iy_i + dx_i^2 + ey_i^2 + fz_i + gz_i^2 + h \quad (4.2)$$

where for pixel i in an interferogram, ϕ_i is the interferometric phase without the LTDM component; x_i, y_i represent the pixel coordinates; z_i is the elevation from the Lidar DEM; a, b, \dots, h are fitting parameters;

c). Q- trop_orb_dem: the same as b) except that it takes into account a DEM error estimation (**Equation (4.3)**; [Hooper et al., 2007](#); [Fattahi & Amelung, 2013](#)) that estimates the baseline-dependent residuals in the interferograms induced by the errors in the DEM;

$$\phi_i = ax_i + by_i + cx_iy_i + dx_i^2 + ey_i^2 + fz_i + gz_i^2 + h + \phi_i^{dem} \quad (4.3)$$

where ϕ_i^{dem} represents the phase residual produced by DEM error. This kind of phase residual is estimated based on its dependency on a spatial baseline (refer to [Hooper et al., 2007](#); [Fattahi & Amelung, 2013](#) for details).

Next, for each interferogram, we removed independently the 3 approximated phase ramps and then added back the corresponding LTDM component. The phase ramp that maximally reduced the variance in the interferogram was selected for correcting that

interferogram. On the contrary, if all 3 phase ramps increased the variance of a given interferogram, we did not apply any correction to it. As shown in **Table 4.4**, the different approximation functions can generally reduce more than half the variance of interferograms. The quadratic functions (with and without DEM error estimation) are more effective than the spline function in most cases (variance reduction [VR]: ~ 63% versus ~50%). The additional DEM error term in the quadratic function improves the correction by a few tenths of a percentage point but does not make a significant difference to the results because of the high precision of the Lidar DEM and the short spatial baselines of the interferograms (see also [section 4.8.1](#) in the Supplementary Material for correction examples).

ID	Time span (day)	Uncorrected SD ($\times 10^{-3}$ m)	S-trop_orb		Q-trop_orb		Q-trop_orb_dem	
			SD ($\times 10^{-3}$ m)	VR (%)	SD ($\times 10^{-3}$ m)	VR (%)	SD ($\times 10^{-3}$ m)	VR (%)
1	22	5.9669	4.7278	20.77	3.7845	36.58	3.56	40.34
2	22	12.0994	7.7184	36.21	8.2974	31.42	8.2187	32.07
3	33	11.5069	5.3519	53.49	3.7112	67.75	3.709	67.77
4	33	13.1269	8.7397	33.42	5.3162	59.50	5.3904	58.94
5	44	6.1347	3.4246	44.18	3.015	50.85	3.1342	48.91
6	44	32.9519	8.1353	75.31	7.7431	76.50	7.5485	77.09
7	66	28.0356	2.3894	91.48	2.9055	89.64	3.0595	89.09
8	66	6.4152	3.6574	42.99	2.7121	57.72	2.6971	57.96
9	66	15.4389	5.7839	62.54	4.3906	71.56	4.3691	71.70
10	88	11.6115	2.6758	76.96	2.2925	80.26	2.2656	80.49
11	88	16.6632	4.5805	72.51	3.4712	79.17	3.4534	79.28
12	99	10.2492	7.9326	22.60	6.5785	35.81	6.5844	35.76
13	110	7.4594	4.2372	43.20	3.2536	56.38	3.1337	57.99
14	132	3.9821	3.0987	22.18	2.9731	25.34	3.0698	22.91
15	132	32.9519	4.9755	84.90	4.8914	85.16	4.5828	86.09
16	154	13.0539	3.2566	75.05	3.1532	75.84	3.277	74.90
17	198	15.2916	5.6161	63.27	4.5199	70.44	4.4944	70.61
18	242	10.0132	7.0795	29.30	6.7645	32.44	6.7625	32.46
19	253	18.6436	8.2811	55.58	6.4527	65.39	6.4524	65.39
20	286	16.083	10.6597	33.72	7.512	53.29	7.4811	53.48
Average (overall)				50.20		62.46		63.05

Table 4.4 Standard deviations (SD) and variance reductions (VR) of selected interferograms. (The average values in the last row refer to the average of all the interferograms)

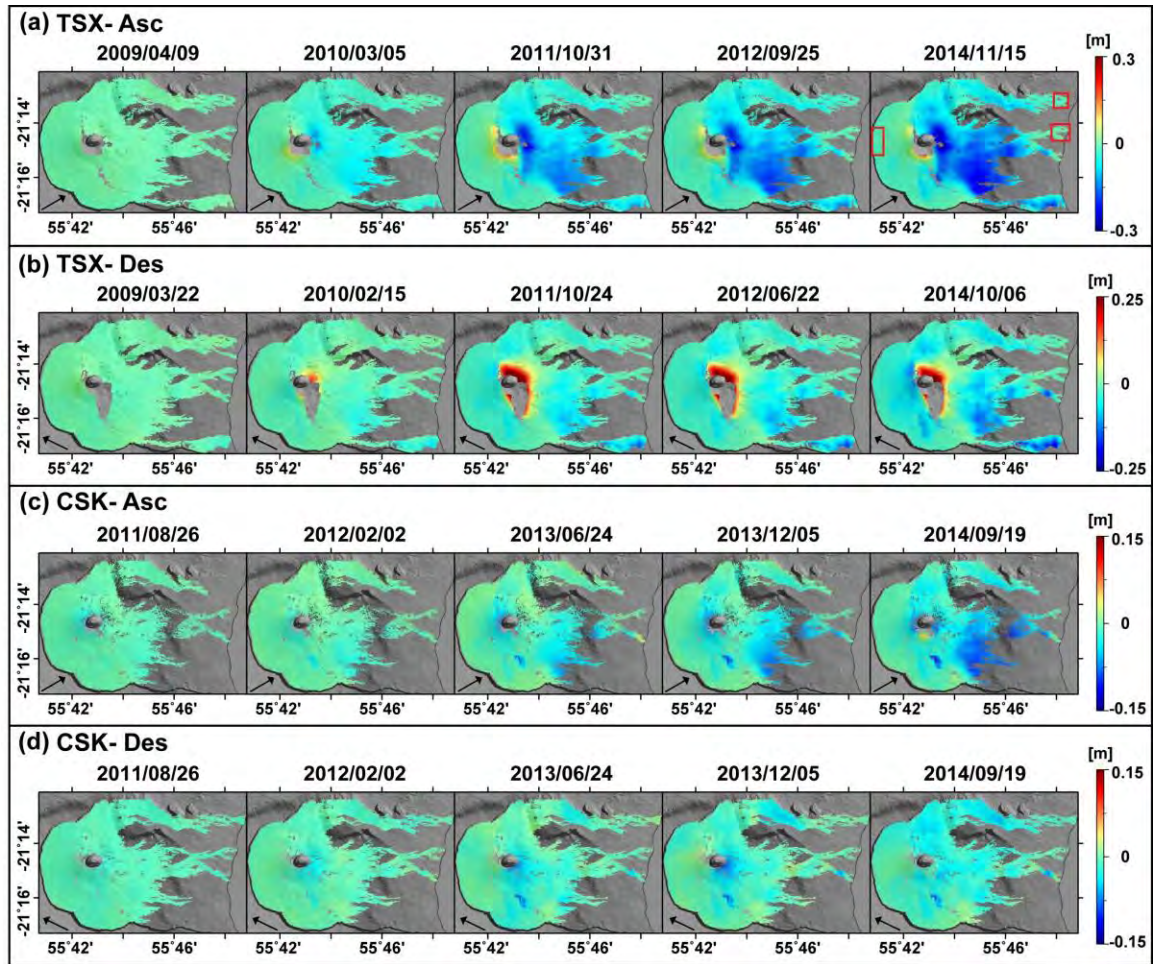


Figure 4.5 Subset of corrected InSAR time series maps, corresponding to **Figure 4.3**, from (a) TSX ascending, (b) TSX descending, (c) CSK ascending, and (d) CSK descending data. The maps conventions are as in **Figure 4.3**.

The corrected InSAR time series for each acquisition geometry were inverted using **Equation (4.1)** once the SB interfergrams had been corrected. No temporal or spatial filtering was applied in order to avoid losing any interesting signals, in particular those related to transient events. **Figure 4.5** shows the resulting corrected InSAR time series that correspond to the uncorrected ones in **Figure 4.3**. It demonstrates that the proposed correction approach has apparently succeeded in mitigating the long-wavelength artifact in the InSAR time series. This is quantitatively confirmed by the significant reduction in the variance for 3 non-displacement areas (**Figure 4.5a**, **Table 4.3**).

4.3.4 InSAR 2-dimensional (2D) ground displacement

Our InSAR dataset provides ambiguous measurement of the ground surface displacement as it depends on the incidence and heading angles of the TSX and CSK satellites. Furthermore, there are some temporal gaps in our InSAR datasets (**Figure 4.2**) which can make it difficult to accurately characterize the complex temporal evolution of the ground displacement affecting the volcano edifice. In order to overcome these difficulties, we decided to jointly analyze the observations provided by the four datasets. We first merged the corrected InSAR LOS time series from the TSX and CSK datasets (four time series in total) into two large ascending and descending time series. The merging process is explained in supplementary materials ([Section 4.8.3](#)). We then used these two large time series for mapping the surface displacement in two dimensions (U-D and E-W components). A subset of the resulting merged InSAR 2D displacement maps is shown in **Figure 4.6**. We did not resolve the N-S component due to its large error resulting from the near-polar orbits and the availability of only right-looking images (see [Section 4.8.4](#) in supplementary materials).

PITON DE LA FOURNAISE
CHAPTER 4: LONG-TERM GROUND DISPLACEMENT BETWEEN 2009 AND 2014

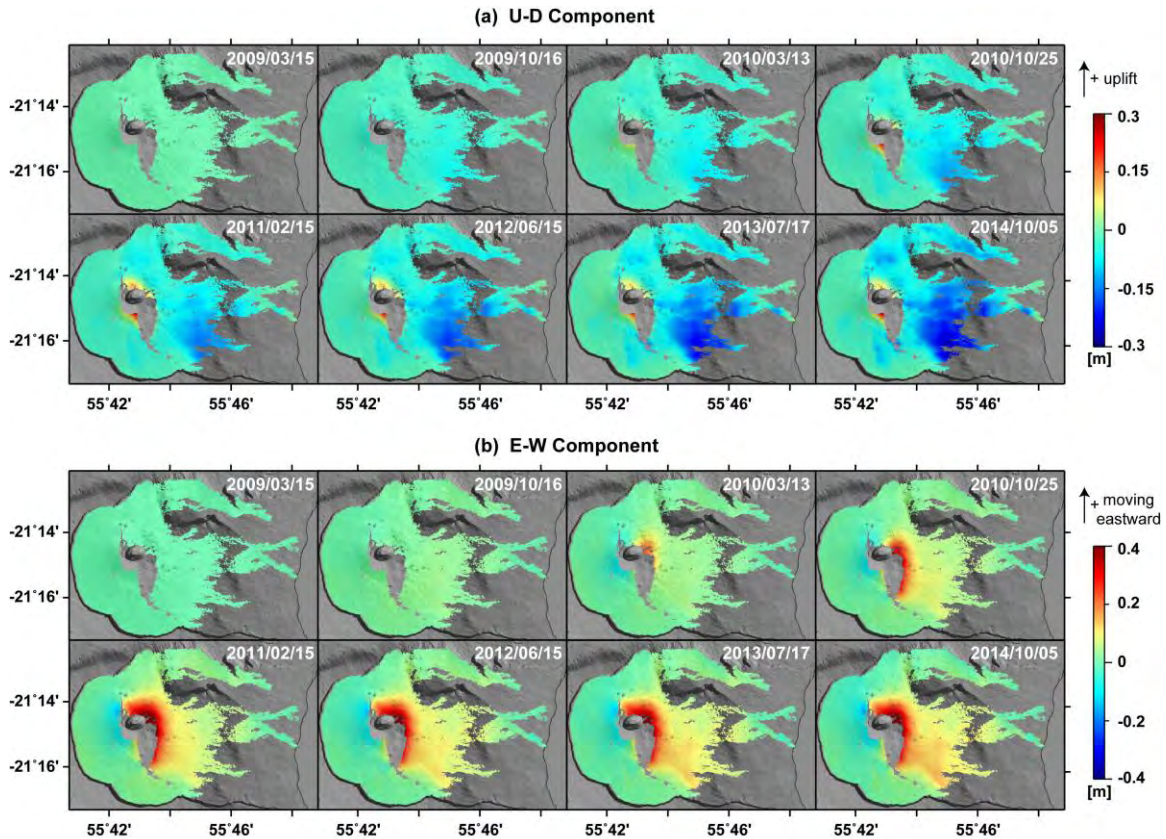


Figure 4.6 Subset of (a) U-D and (b) E-W components of ground displacement for the merged InSAR time series. All the maps are spatially referenced to a non-displacement zone (indicated by a black circle in **Figure 4.3a**) that is located ~ 10 km away from the volcanic craters, and temporally referenced to the first map in the merged time series (15 March 2009). Positive values represent upward displacement on U-D maps and eastward displacement on E-W maps, while negative values represent downward displacement on U-D maps and westward displacement on E-W maps. The signals visible on the Central Cone from maps 2010/03/13, 2010/12/25, and 2011/02/15 (and all those following) correspond to the cumulative displacements caused by the November 2009 – January 2010 eruptions, the November 2009 – October 2010 eruptions, and the November 2009 – December 2010 eruptions, respectively. Areas in grey correspond to area with low coherence or affected by unwrapping errors. Maps are draped on a shaded DEM and projected in Geographic Lat/Lon referenced to WGS-84 Datum.

PITON DE LA FOURNAISE
CHAPTER 4: LONG-TERM GROUND DISPLACEMENT BETWEEN 2009 AND 2014

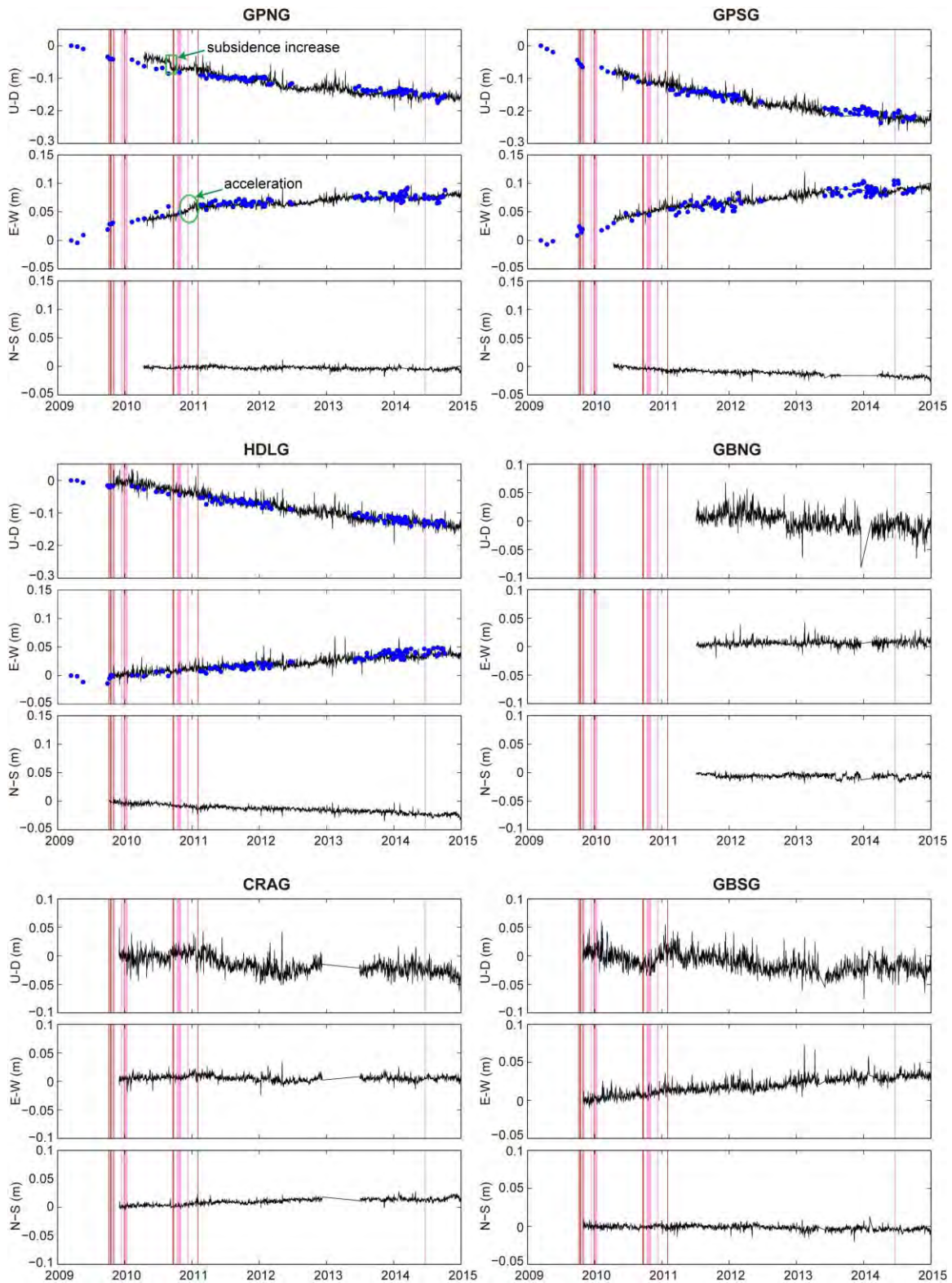


Figure 4.7 Cumulative displacements (U-D, E-W and N-S components) recorded at stations GPNG, GPSG, HDLG, GBNG, CRAG, and GBSG installed on the Eastern Flank of Piton de la Fournaise (see **Figure 4.1c** for

location). The plate motion was previously removed using the data recorded at the REUN IGS station located 15 km away from the volcano (**Figure 4.1b**) where only plate motion is considered to take place. The InSAR-derived ground displacements (U-D and E-W) at stations GPNG, GPSG, and HDLG are superimposed on the GNSS time series (blue points). The GNSS time series at these three stations are shifted to reduce the root mean square between InSAR and GNSS observations in order to make different geodetic data comparable in time. The subsidence increase and the acceleration of eastward motion are indicated by a green rectangle and ellipse, respectively. Pink areas and dark red vertical lines represent times of eruptions and intrusions, respectively, which occurred during the study period.

We have been able to evaluate the accuracy of the 2D InSAR displacements and the ability of our approach to mitigate the stratified tropospheric phase delay in the interferograms thanks to the time series of daily positions recorded at the GNSS stations. Of the six stations on the Eastern Flank, InSAR measurements can only be compared with those recorded at GPNG, GPSG and HDLG, since stations CRAG, GBSG and GNBG are located in areas where the InSAR data are incoherent. Comparison of the InSAR-derived results with the GNSS time series shows a good agreement, confirming the reliability of our InSAR results (**Figure 4.7**). The root mean square (RMS) of the differences between the two datasets is ~ 0.8 cm and ~ 1.5 cm for the E-W and the vertical components of the ground displacement, respectively. We think that these differences are mainly induced by uncorrected atmospheric effects in the InSAR data and the larger uncertainties in the vertical GNSS calculations. In some cases InSAR failed to detect subtle signals which were visible with continuous GNSS time series. For example, the increase in subsidence of the GNSS signal (green rectangular in **Figure 4.7**) observed at GPNG in 2010 is not clearly recorded by InSAR. This could be due to the fact that this signal, observed at only one GNSS station, was very localized and was below the spatial and/or the temporal resolution of InSAR data, which could also explain why it was not observed at other stations of the GNSS network. Continuous eastward motions recorded by GNSS signals at GPNG also reveal a subtle trend increase in displacement occurring during the unrest period from October 2010 to January 2011 (green ellipse in **Figure 4.7**). Such short duration signal is not observed with InSAR due to the low temporal resolution of SAR data during this period, as well as the lack of coherence.

4.4 Ground displacement analysis

GNSS and InSAR time series can now be jointly analyzed. The main advantages of the InSAR time series analysis technique is that it provides a high measurement density making it possible to investigate the large scale spatial pattern of ground motion, while GNSS provides a higher temporal resolution, providing insight into the dynamics of phenomena. During the entire study period, several ground displacement patterns affecting the major part of the volcanic edifice are clearly visible in **Figure 4.6**, including on the Central Cone, the Eastern Flank, and the northern and southern parts of the Enclos Fouqué.

4.4.1 Displacement of the Central Cone

The Central Cone experienced strong and transient displacement induced by volcanic events (7 eruptions and 4 intrusions; **Table 4.2**) during the study period. Time series maps (**Figure 4.6**) indicate that the strongest displacements of the Central Cone recorded by InSAR were during the November 2009 – December 2010 eruptions (up to 0.20 m eastward displacement, and 0.10 m uplift), and the October – December 2010 eruptions (up to 0.40 m eastward displacement, and 0.25 m uplift). Among all these eruptive events, the October 2010 eruption (16.4 day duration; [Roult et al., 2012](#); [Bato et al., 2016](#)) induced the largest transient displacement that involved the widest area of ground surface ($\sim 4 \times 2$ km). The E-W component of the ground displacement induced by this eruption appears clearly on the eastern Cone Flank (CF, location in **Figure 4.1c**) and even extends to the Upper Eastern Flank (UEF, location in **Figure 4.1c**; **Figure 4.6**).

PITON DE LA FOURNAISE
CHAPTER 4: LONG-TERM GROUND DISPLACEMENT BETWEEN 2009 AND 2014

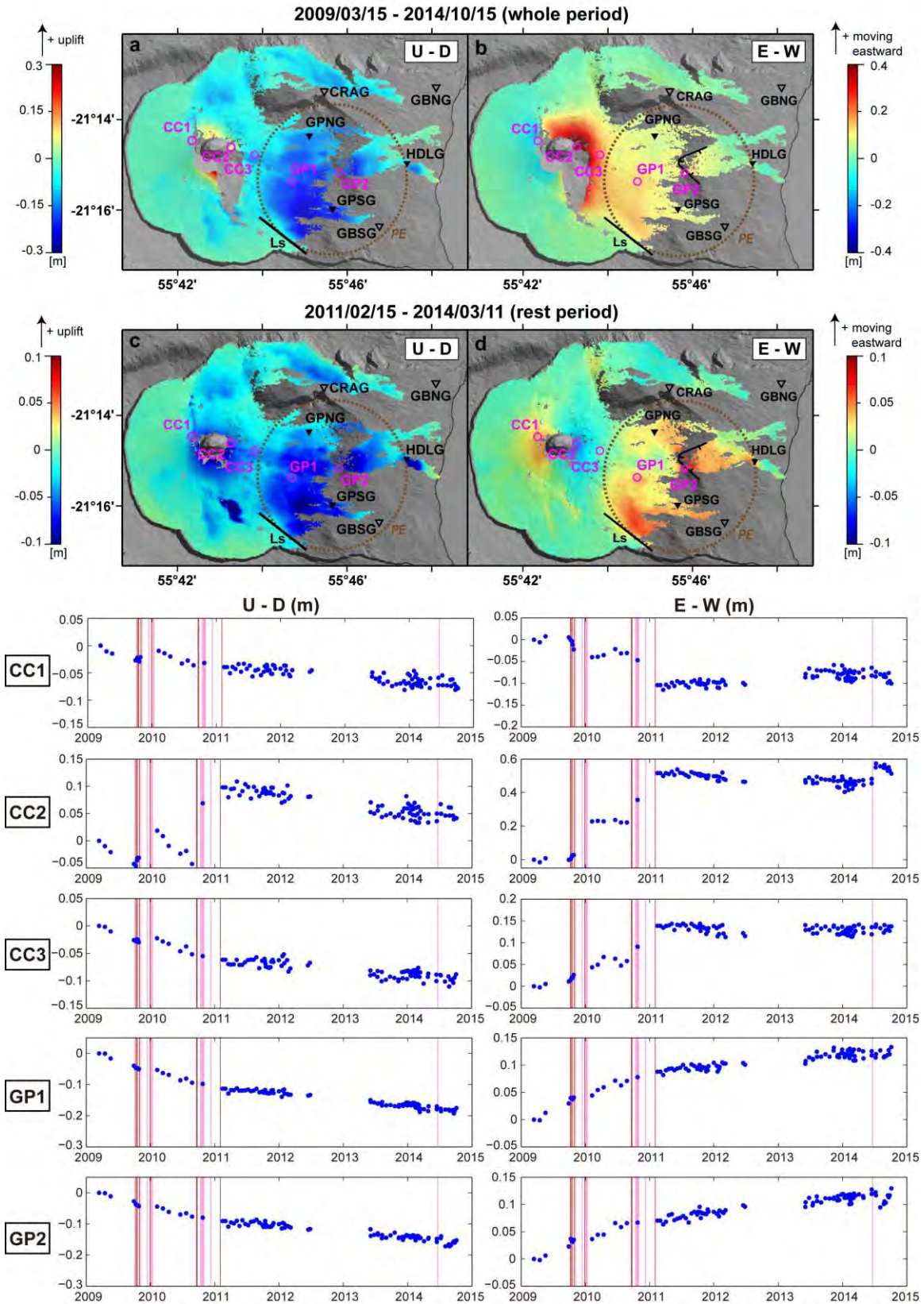


Figure 4.8 Spatial pattern and temporal evolution of the ground displacement of the Central Cone and the Eastern Flank at Piton de la Fournaise during the whole study period (a and b) and during the rest period (c and d). a) Cumulative U-D and b) cumulative E-W displacement maps of the merged InSAR data (15 March 2009 – 5 October 2014). c) Cumulative U-D and d) cumulative E-W displacement maps calculated from CSK data (15 February 2011 – 11 March 2014). Brown dashed ellipse PE indicates the large area of time-dependent displacement on the Eastern Flank. Black line Ls indicates the southern limit of PE, as inferred from InSAR results. The black line with hatch marks indicates the V-shaped structure that was interpreted as the scar of a small-scale landslide by Bachèlery (1981). Locations of the six GNSS stations (GPNG, GPSG, HDLG, GBNG, CRAG, and GBSG) on the Eastern Flank are marked with black triangles, with InSAR coherence maintained at three stations (GPNG, GPSG, and HDLG) marked by filled black triangles. The maps conventions are as in **Figure 4.6**. Time series derived from the merged data at points CC1 – CC3 (for the Central Cone, marked by magenta circles), and GP1 – GP2 (for the Eastern Flank, marked by magenta circles) are illustrated below. Pink areas and dark red vertical lines represent times of eruptions and intrusions, respectively, which occurred during the study period.

During the whole period covered by this study, the temporal evolution of the Central Cone displacement varies from area to area (**Figure 4.8a-b**). The point CC1, located on the western CF, subsides linearly, interrupted by a weak uplift (~ 0.03 m) in late 2009 during the eruptive period (**Figure 4.8**, CC1). Similarly, a linear subsidence is observed at point CC2, located on the eastern CF, during rest periods. However, during eruptive periods it is interrupted by uplift in late 2009 (~ 0.06 m), and again between late 2010 and early 2011 (~ 0.15 m) (**Figure 4.8**, CC2). Simultaneous with this linear subsidence, the western CF (see **Figure 4.8**, CC1) displays slight eastward displacement while the eastern CF (see **Figure 4.8**, CC2) displays slight westward displacement during the rest periods. In order to better highlight the spatial pattern of this long-term displacement affecting the Central Cone, we computed vertical (U-D) and horizontal (E-W) displacement maps spanning the longest rest period of the considered time window at Piton de la Fournaise, which started in February 2011 and ended in June 2014 (**Figure 4.8c-d**). The vertical displacement map highlights the limited spatial extent of the subsidence pattern. The maximum subsidence is about 0.09 m over the 3.5-year period (**Figure 4.8c**). The E-W map shows significant eastward displacement observed on the western CF (up to 0.07 m) (**Figure 4.8d**). It also shows a weaker westward displacement on the eastern CF (up to 0.03 m) (**Figure 4.8d**). Both vertical and horizontal displacement patterns are very similar to those obtained by Froger et al. (2015) using InSAR data spanning a one-year period just after the March-April 2007

eruption and to those recorded by the permanent GNSS stations during this period (e.g. [Staudacher and Peltier, 2015](#)).

4.4.2 Displacement of the Eastern Flank

On both vertical and E-W displacement maps, a similarly large area on the central and southern part of the Eastern Flank (pattern *PE*, roughly outlined by the brown dashed ellipse in **Figure 4.8**) is affected by downward and eastward long-term displacement. This sector covers ~ 20 km², extending from Grandes Pentes to the upper-middle part of Grand Brûlé, ranging in elevation from 1800 to 300 m. The maximum cumulative downward and eastward displacement in the sector are up to 0.26 m and 0.15 m, respectively, during the study period (**Figure 4.8a-b**). The cumulative eastward displacement is in general lower than the downward displacement in magnitude. Similar results are obtained from continuous GNSS observations recorded at stations GPNG, GPSG and HDLG where cumulative subsidences of 0.12 m, 0.15 m and 0.13 m were recorded, accompanied by an eastward motion (cumulative displacements of 0.05 m, 0.06 m and 0.04 m) over the entire period of GNSS acquisition for these three stations respectively (**Figure 4.7**; [Peltier et al., 2015a](#)). InSAR results show that no eastward displacement appears to the east of the HDLG station (**Figure 4.8b**), which suggests that HDLG might lie on, or close to, the eastern limit of the mobile sector, although the eastward motion could also possibly extend further eastwards given that the InSAR coherence is only remained in a narrow region along the coast. GBSG station, installed on the upper part of Grand Brûlé, shows only eastward displacement (0.04 m over 5 years) without clear downward displacement (**Figure 4.7**), suggesting eastward motion actually affects larger areas than downward motion. The eastern limit of the eastward motion is inferred to be somewhere to the east of GBSG. Its upper limit is inferred to be situated just to the west of GPNG, as revealed by the lack of eastward displacement at CC3 and in the upper part of UEF during the rest period (**Figure 4.8d**). This suggests that the area involving the lower eastern CF and the upper part of UEF could be stable and decoupled from the lower part to the east. The time-dependent eastward motion affecting the Upper – Middle Eastern Flank (UEF and MEF) (see points GP1 and GP2 in **Figure 4.8** for example) can be divided in two distinctive stages. The first stage spans the period from March 2009 to February 2011 where the eastward displacement rate decreases exponentially with

time. After February 2011, this rate decreases rather linearly with time suggesting a change in the displacement regime.

The observed displacement pattern (*PE*) affecting the Eastern Flank during the 2009-2014 period shows a good agreement with the trapezoidal pattern observed from May 2007 to July 2008 (the post-eruptive period of the March-April 2007 eruption) in previous studies (Augier, 2011; Froger et al., 2015; see also Section 3.3). Before being able to assess whether the former is the continuation of the latter, we have to characterize possible short wavelength contributions such as those related to recent lava flows.

4.4.3 Displacement on recent lava flows

The cumulative vertical displacement map shows several subsidence patterns affecting the volcano flanks (**Figure 4.9a**, localized patterns *P1 – P6* and large patterns *PE1 – PE4* on the Eastern Flank). Visual comparison between the vertical displacement (**Figure 4.9a**) and recent lava flows map (lava flows emplaced after 1998; **Figure 4.9b**) reveals that these long-term subsidence patterns correlate well spatially with the location of recent lava flows. Among these subsidence patterns, *P6* corresponds to the lava flow emitted during the October 2010 eruption (the eruptive fissure and the lava contour are marked with dark red and black lines respectively in **Figure 4.9**). The other subsidence patterns are located in the field of relatively older lava flows (**Table 4.5**). As previously observed at Etna and Okmok volcano (Briole et al., 1997; Stevens et al., 2001a; Lu et al., 2005) the subsidence affects not only the area covered by the lava flow but also a margin extending some tens to hundreds of meters beyond the lava flow. This suggests (as already proposed by Stevens et al. (2001a) and Lu et al. (2005)) that these margins are affected by substrate subsidence due to lava-flow gravity load. All the localized patterns (*P1 – P6*) present mainly vertical subsidence decreasing in time with nearly no long-term eastward motion (**Figure 4.8b** and **Figure 4.9a**). Contrary to the vertical displacement, the horizontal displacement patterns on the Eastern Flank (*PE1 – PE4*) do not spatially correlate with lava flow fields (**Figure 4.8b** and **Figure 4.9a-b**). This confirms, as on other active volcanoes (e.g. Griffiths & Fink, 1993; Stevens et al., 2001a, 2001b; Ebmeier et al., 2012; Chaussard, 2016), that post-lava flow emplacement motion at Piton de la Fournaise occurring on and adjacent to lava flow fields is mostly vertical and negligibly horizontal.

PITON DE LA FOURNAISE
CHAPTER 4: LONG-TERM GROUND DISPLACEMENT BETWEEN 2009 AND 2014

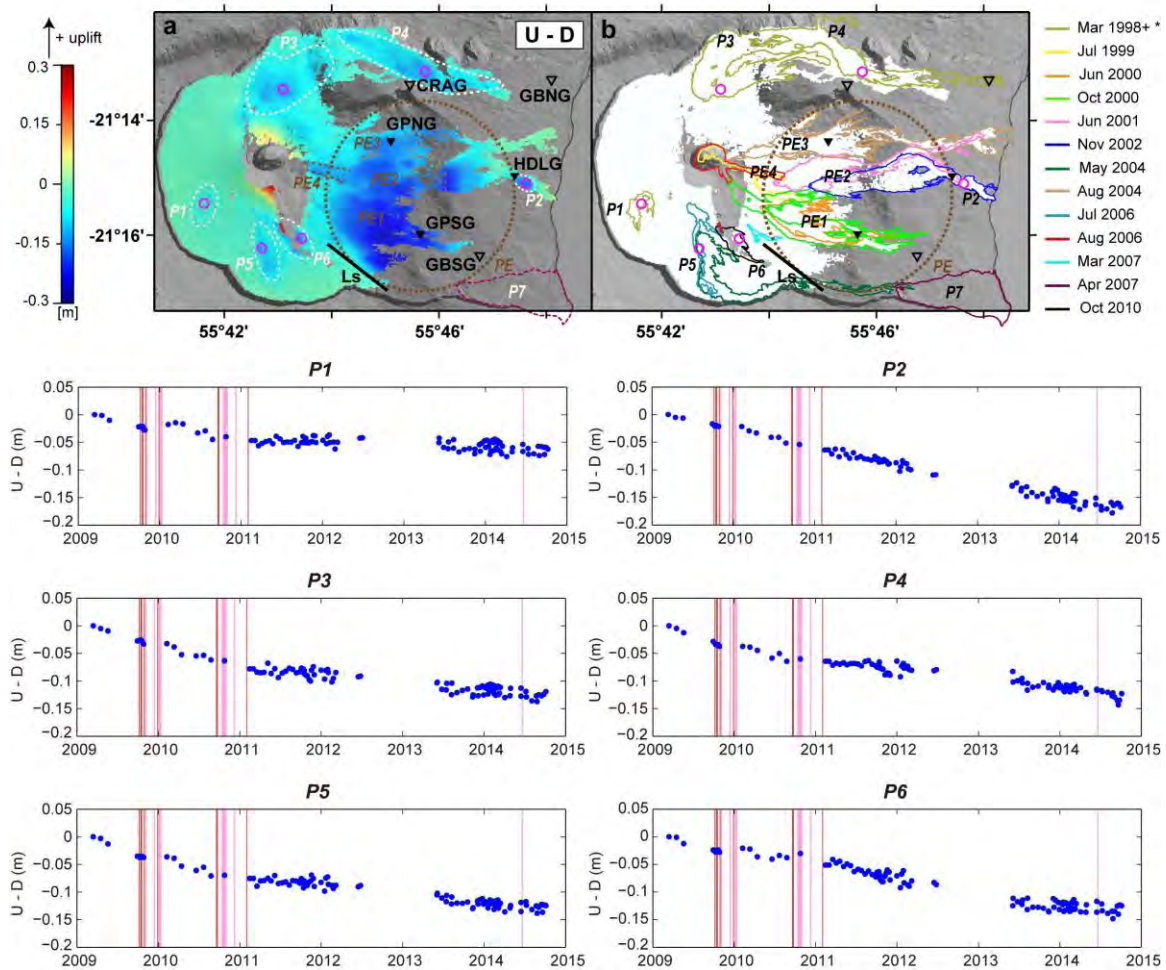


Figure 4.9 Spatial pattern and temporal evolution of the subsidence in recent lava flow fields at Piton de la Fournaise during the whole study period. (a) Cumulative U-D displacement map of the merged InSAR data (15 March 2009 – 5 October 2014). The maps conventions are as in Figure 4.6. (b) Sketch map of recent lava flows emplaced since 1998 on the flanks of Piton de la Fournaise superimposed on the white areas corresponding to the coherent areas in map a). Note: Seven lava flows emplaced within or overlapping the 1998 lava flow field (on the northern part and northeastern part of Enclos Fouqué) between 2000 and 2005 are not plotted here for the sake of clarity, including the February 2000, the January 2002, the August 2003, the January 2004, the February 2005, the November 2005, and the December 2005 lava flows. White dashed lines (in Figure 4.9a) indicate the location of localized subsidence patterns P1 – P6. PE1 – PE4 indicate the subsidence patterns on the Eastern Flank associated respectively with the June and October 2000 lava flows (PE1), June 2001 and November 2002 lava flows (PE2), August 2004 lava flow (PE3), and July 1999 and August 2006 lava flows (PE4). P7 indicates the pattern of the April 2007 lava flow, which lost coherence in the merged InSAR data. Location of the October 2010 eruptive fissure is indicated by a dark red line. The brown dashed ellipse PE, the black line Ls, and the black triangles are as indicated in

Figure 4.8. Time series derived from the merged U-D component for the localized subsidence patterns P1 – P6 are illustrated at the bottom. Pink areas and dark red vertical lines represent times of eruptions and intrusions, respectively, which occurred during the study period.

	Location	Year of emplacement	Mean thickness (m) ^a	Mean subsidence rate (m/yr) ^b
Localized Subsidence Patterns	P1*	1998-03	5.4 ± 3.53	-0.00315
	P2	2001-06, 2002-11	6.27 ± 2.76	-0.01092
	P3	1998-03, 2000-02, 2003-08	11.17 ± 8.21	-0.00809
	P4	1998-03, 2002-01, 2005-02, 2005-12	10.72 ± 4.91	-0.01033
	P5	2004-05, 2006-07	8.15 ± 4.40	-0.0105
	P6*	2010-10	5.85 ± 1.38	-0.0184
	P7*	2007-04	12.9 ± 6.58	-0.01853
Subsidence patterns on the Eastern Flank	PE1	2000-06, 2000-10	8.83 ± 5.54	-0.01264
	PE2	2001-06, 2002-11	10.74 ± 6.36	-0.01217
	PE3*	2004-08	4.94 ± 3.13	-0.0104
	PE4	1999-07, 2006-09	8.94 ± 3.77	-0.01613

Table 4.5 Year of emplacement, mean thickness (with their standard deviations) and mean subsidence rate for lava flows from 2009-2014 affected by localized subsidence patterns (P1 – P7) and large subsidence patterns on the Eastern Flank (PE1 – PE4)

^a For P6, the thickness was derived from the study of Bato et al. (2016). For the others, the thicknesses were measured using the vertical difference between two available DEMs acquired respectively in 1997 and 2008. Only pixels coherent in TSX-CSK merged data (**Figure 4.8a-b**) were used for calculating the thickness, except for the thickness of P7 which was measured using pixels coherent in TSX dataset (**Figure 4.5a-b**).

^b For P6, the mean subsidence rate was obtained using coherent pixels in CSK dataset (**Figure 4.8c-d**). For P7 the displacement was measured using coherent pixels in TSX dataset (**Figure 4.5a-b**). For the rest, the mean subsidence rates were evaluated using pixels coherent in TSX-CSK merged data (**Figure 4.8a-b**).

* represents single lava flow emplacement (no other flow emplacement in the same area) since 1998.

The amplitude of the post-lava flow emplacement subsidence affecting a given lava flow is generally proportional to its thickness and is also in relation to the age of the lava flow (Griffths & Fink, 1993; Stevens et al., 2001a; Lu et al. 2005; Dieterich et al., 2012; Albino et al., 2015; Chaussard, 2016). We carried out our primary investigation on the relationship between subsidence in lava fields and the lava thickness and age based on the results of our study. The thickness of the lava flows emplaced between March 1998 and April 2007 (corresponding to

patterns *P1 – P5*, *P7*, and *PE1 – PE4*) were estimated by differentiating two available DEMs. One is a 25 m resolution DEM from an aerial photogrammetry campaign carried out by IGN in 1997 and the other one is a 7.5 m DEM calculated from data acquired during an airborne LiDAR survey carried out in 2008-2009 by IGN. The thickness of the October 2010 lava flow (corresponding to pattern *P6*) was derived from the study of Bato et al. (2016). We summarized the observations (including the year of emplacement, mean thickness, and mean subsidence rate) of each subsidence pattern in **Table 4.5**. The mean lava subsidence rate normalized to mean lava thickness is plotted according to the lava age in **Figure 4.10**. **Figure 4.10** and **Table 4.5** show two important features. Firstly, there is a clear relationship between normalized subsidence rate and lava age for lava flows located outside the large area of the Eastern Flank affected by long-term displacement (*P1- P7*). However, a notable exception concerns the localized pattern *P2*. This specific point-like subsidence pattern is characterized by a strong subsidence rate even though it is located at the convergence of two relatively old, locally thin lava flows. This suggests that, in addition to lava cooling, there could be another source accounting for the observed subsidence in *P2* (for example, a collapsed lava tunnel in an older flow). Secondly, the amplitudes of the normalized subsidence rates for lava flows located inside the large displacement sector on the Eastern Flank affected by long-term displacement (*PE1 – PE4*) are clearly greater than those located outside. This indicates that the observed downward motion in this area cannot be explained only by post-emplacement lava flow subsidence; a global downslope movement of the Eastern Flank must also contribute to the observed downward displacement. Supposing that the mechanical properties of the substrate are similar beneath the whole volcano edifice, an exponential decay curve fits the correlation between the normalized subsidence rate and the age of lava fields to first order, based on measurements obtained from the group of lava flows located outside the large displacement sector (blue line in **Figure 4.10**). From this empirical observation we estimate that the contribution of post-emplacement lava flow subsidence might contribute up to 66 % of the downward motion observed inside the large mobile sector on the Eastern Flank. And, as a consequence, we estimate that the remaining 34 % of downward displacement and most of the eastward displacement may correspond to a widespread seaward motion that affects most of the Eastern Flank.

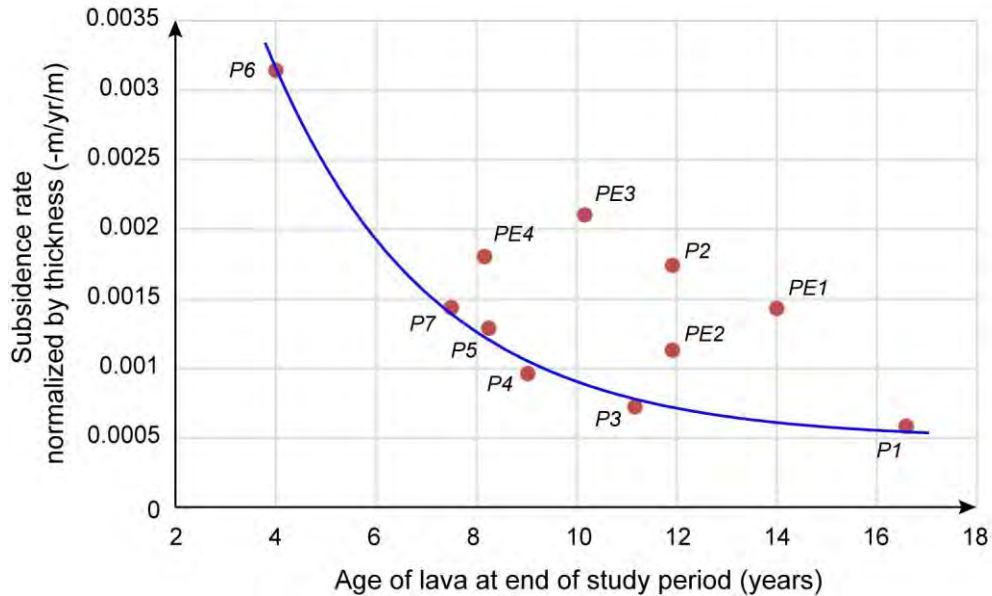


Figure 4.10 Mean subsidence rate in lava flow fields (P1 – P7, and PE1 – PE4) normalized to lava thickness with respect to the age of the lava. For a pattern with overlapping lava flows, the most recent emplacement time is used to obtain the age of the lava. As already indicated in **Table 4.5**, the displacement of P7 was measured using coherent pixels in TSX dataset. The blue line indicates the exponential decay relationship between the normalized subsidence rate and the age of the lava, estimated by using data from patterns (P1, P3 – P7) located outside the large mobile sector on the Eastern Flank.

4.5 Discussion

One of the most significant results in this study is the characterization of the widespread long-term seaward motion affecting the Eastern Flank of Piton de la Fournaise volcano during the period of 2009-2014. Similar time-dependent motions have been described previously for the eastern flank of Mount Etna (e.g. Froger et al., 2001; Palano et al., 2009) and the southern flank of the Kīlauea (e.g. Swanson et al., 1976; Denlinger & Okubo, 1995; Plattner et al., 2013). The main difference of the seaward motion between Piton de la Fournaise and those volcanoes is that the motion at Etna and Kīlauea extends and increases to the coast, while results show that the seaward motion at Piton de la Fournaise is mainly inland of the coast and appears to be very small along the coast. But even so, these seaward motions are direct evidence of large flank

destabilizations that could potentially result in catastrophic hazards, which emphasizes the need for understanding their behavior and investigating their origins.

4.5.1 Ongoing post-eruptive displacement

The widespread motion affecting the Eastern Flank was first observed during the March-April 2007 distal eruption (Augier, 2011; Clarke et al., 2013; Froger et al., 2015; see also Section 3.2). To explain the sudden eastward displacement and the limited displacement of the Western Flank observed during this eruption, Got et al. (2013) proposed a deformation model of the volcanic edifice using elasto-plastic rheology. From this model, the authors reached the conclusion that the deformation could have exceeded the rock elastic limit resulting in a large seaward plastic displacement of the Eastern Flank. Furthermore, the sudden occurrence of strain weakening in the Eastern Flank and some ground observations led Got et al. (2013) to propose that the plastic deformation could have been concentrated along a sub-horizontal pressurized structure, such as a sheet intrusion of magma (e.g., a sill). Froger et al. (2015) reached a similar conclusion by interpreting the large-scale downslope displacement as slip along a pre-existing structural discontinuity such as a low-angle normal fault or a detachment surface which was reactivated during the eruption by the intrusion of a sill.

All these interpretations favor the idea of the existence of a structural discontinuity in the Eastern Flank of Piton de la Fournaise, such as a décollement or a detachment. Even though a detachment has been proposed to explain the recurrent collapse of the Eastern Flank in the past (Duffield et al., 1982; Lénat et al., 1989), the existence of this structural discontinuity is still a matter of debate. This is mainly due to the absence of clear shallow seismicity below the Eastern Flank during rest periods of the Piton de la Fournaise (Clarke et al., 2013; Peltier et al., 2015a). Nevertheless, this hypothesis is supported by the work of Famin and Michon (2010) who reported the discovery of a sliding surface in the interior of Piton des Neiges (the second and oldest volcano on La Réunion Island). These authors demonstrate the potential role of hydrothermal alteration sustained by the cooling sills to induce slow displacement, and of frequent sill injections along the sliding surface to trigger rapid and significant sliding of the slope (Famin & Michon, 2010). Another argument in favor of a structural discontinuity in the Eastern Flank of Piton de la Fournaise is the altered argillaceous hyaloclastic breccia identified at

556 m to 616 m and 890 m to 1010 m below the ground surface at the Grand Brûlé boreholes (see **Figure 4.1c** for location, [Rançon et al., 1989](#)). However, the lateral extension of this breccia is not known.

Our InSAR-derived results reveal that the Eastern Flank experienced a large-wavelength time-dependent displacement whereas there is no clear displacement, observed on the Western Flank during the study period except for the slight localized subsidence on the 1998 lava flow (**Figure 4.9**, pattern *P1*). This confirms the strong asymmetry in the displacement of the volcano edifice not only within the volcanically active periods ([Got et al., 2013](#)) but also during the rest ones. The spatial pattern and temporal evolution of the displacement on the Eastern Flank observed in this study (2009-2014) is very similar to that observed in previous studies during the one-year post-eruptive period (2007-2008; [Augier, 2011](#); [Froger et al., 2015](#); see also [Section 3.3](#)). As in these studies, the InSAR displacement maps and GNSS measurements at CRAG and GBNG in our study (**Figure 4.6** and **Figure 4.7**) reveal that the time-dependent displacement affecting the Eastern Flank does not concern the northern part (i.e. the Plaine des Osmondes) indicating that this area is decoupled from the southern part of the Eastern Flank ([Peltier et al., 2015a](#)). The upper part of the Plaine des Osmondes (**Figure 4.1c**) was interpreted by [Bachelery \(1981\)](#) as the most recent collapse structure of the Enclos Fouqué Caldera. The lack of horizontal displacement observed in this area could indicate that this particular structure could play a role in the displacement behavior at Piton de la Fournaise. The vertical and horizontal displacement maps also reveal that the large mobile sector on the Eastern Flank is limited to the south by a sharp N120-130°E boundary (Ls, indicated by black lines in **Figure 4.8**). This boundary coincides in location with one identified by [Froger et al. \(2015\)](#) from the analysis of InSAR data spanning the one-year post-eruptive period following the March-April 2007 eruption. The authors of that study suggested that this sharp feature might correspond to a normal fault that has been reactivated by the EW extensional stress field produced by the co-eruptive displacement (during the March-April 2007 eruption) of the Eastern Flank. As mentioned in [Section 4.4](#), the eastern limit of the mobile sector might be somewhere close to the GNSS station HDLG, and the continuous extension of the UEF and MEF is accompanied by a contraction of the LEF (Lower Eastern Flank, see **Figure 4.1c** for location). This suggests that the LEF (at least the middle-lower part of the Grand Brûlé according to our InSAR-derived results) acts as barrier to eastward

motion. Nevertheless, it is worth mentioning that there is no structural evidence for compression in the area along the coast (le Friant et al., 2011).

From a one-year post-eruptive InSAR dataset, Augier (2011) and Froger et al. (2015) showed that the co-eruptive displacement of the Eastern Flank was followed by a transient stage during which the strain increased with time at a decreasing rate leading to a cumulative eastward displacement up to 0.18 m. InSAR time series of displacements retrieved from our study (**Figure 4.8**, GP1 and GP2) and continuous GNSS observations at GPNG and GPSG (**Figure 4.7**) reveal that the stage of transient creep, which began right after the strong instantaneous displacement of the March-April 2007 eruptive period, continued until February 2011. During this stage of transient creep, a subtle trend increase is observed in GNSS time series during the unrest period from October 2010 to January 2011 (**Figure 4.7**) suggesting a slight acceleration in the Eastern Flank motion associated with volcanic activity, similar to the acceleration observed in mid-April 2015, albeit with a considerably smaller amplitude (Peltier et al., 2016a). This stage appears to have been followed by an apparent steady-state stage in the UEF and MEF (**Figure 4.8**, GP1 and GP2), where the strain rate remained nearly constant until late 2014. These strong spatial and temporal similarities confirm that the observed time-dependent displacement in this study is mainly the continuation of creep triggered by the historical eruption of March-April 2007.

4.5.2 Possible origins of eastward motion

Got et al. (2013) and Peltier et al. (2015a) proposed an elegant hypothesis in which the eastward motion of the Eastern Flank and the summit motion (combining an integral subsidence and eastward displacement on the western CF and westward displacement on the eastern CF) can be regarded as two different sides of the same process. Such a model provides an interesting framework for understanding ground deformation mechanisms at Piton de la Fournaise. According to these authors, the eastward motion of the Eastern Flank relaxes the summit horizontal stress that induces summit subsidence driven by gravity and the reservoir depressurization located between 0 and 1000 m above sea level. In such a context, the strain-time relation observed on the Eastern Flank during a stage of transient strain (i.e. exponential decrease of displacement rate with time; **Figure 4.8**, GP1 and GP2) followed by a stage of

steady-state strain (i.e. linear decrease of displacement rate with time; **Figure 4.8**, GP1 and GP2) would be the return to equilibrium of the dynamic system formed by reservoir pressure, cone weight and flank strength (Peltier et al., 2015a). Eastward displacement affecting the Eastern Flank would thus be the main mechanism to reduce the stress applied to the system during the distal eruption of March-April 2007, and the constant strain rate observed from February 2011 to late 2014 would be evidence of steady displacement occurring at constant stress during plastic or viscoplastic deformation. InSAR results confirm the ongoing subsidence affecting the Central Cone observed in previous studies by InSAR during the one-year period following the March-April 2007 eruption (Froger et al., 2015; see also Section 3.3) and by GNSS measurements in the 6.5-year period after the March-April 2007 eruption (Peltier et al., 2015a; Staudacher & Peltier, 2015). During the time interval of this study, this subsidence exhibits a linear time dependency obviously affected by strong and sudden motions during different eruptive events, but with a clear restart of the slow-rate summit deflation after each event (**Figure 4.8**, CC1 and CC2). Such behavior appears to support the hypothesis that summit subsidence would be favored by eastward motion of the Eastern Flank (Peltier et al., 2015a). Nevertheless, spatial and temporal behavior of the ground displacements observed in this study clearly indicate that eastward motion and summit deflation cannot be driven by one process alone during the study period. Indeed the time-dependent displacement of the slow-rate summit deflation and the eastward motion of the Eastern Flank exhibit different temporal behaviors (**Figure 4.8**, CC1, CC2, GP1 and GP2). The summit deflation reached a steady state regime in the year following the March-April 2007 eruption (Augier, 2011; Peltier et al., 2015a; Froger et al., 2015) while the change in regime for the eastward motion of the Eastern Flank observed in this study occurred about 4 years after this event. Both vertical and horizontal components of the displacement pattern captured by InSAR affecting the Central Cone (**Figure 4.8c-d**) are clearly close to those observed, with lower amplitude, in the one-year post-eruptive displacement maps (Froger et al., 2015; see also Section 3.3). The short-scale pattern and the inversion of the post-eruptive displacements carried out by Froger et al. (2015) show that the Central Cone is deformed by stress relaxation processes occurring in a very shallow source. These results suggest that the main relaxation mechanism, which drove the summit deflation during the study period, could be related to the 300 m collapse that affected the Dolomieu crater during the March-April 2007 eruption.

Time-dependent deformations similar to that observed on the Eastern Flank of Piton de la Fournaise are classically interpreted as the deformation of a ductile material or slippage along a fault surface in a stable sliding regime (Palano et al., 2009; Lundgren et al., 2003; Froger et al., 2015). The absence of clear shallow seismicity below the Eastern Flank during rest periods of Piton de la Fournaise (Clarke et al., 2013; Peltier et al., 2015a) clearly indicates that either the material behavior of the mobile sector yields without any apparent loss of continuity or that the occurrence of slip is not sufficient for resultant faults to be highly seismic. The long-term displacement affecting the Eastern Flank could result from deformation on a frictional or ductile structural discontinuity suspected to have played a major role in the strong widespread motion of the Eastern Flank during the April 2007 eruption (Got et al., 2013, Froger et al., 2015). The gravitational force and ductile behavior of material could have driven the long-term displacement. Geophysical investigations show that the Eastern Flank is covered by lava flows to a thickness of about 100 m (Lénat et al., 2012). The applied stress during the March-April 2007 eruption could have induced this deposit layer to yield, resulting in long-term viscous deformation. Spatial heterogeneity of the ground displacement pattern could be due to spatial variation in the viscosity or the topographic slope. However, it is worth mentioning that there is no evidence of spatial heterogeneity in rheological properties of the 100 m- thick lava flow layer covering the Eastern Flank and no clear correlation between displacement and topographic slope gradient is observed (see Section 4.8.5 in supplementary materials). Another possibility is that the long-term displacement could reflect a variation in frictional strength of the structural discontinuity over time. To be able to explain the temporal behavior of the displacement, the frictional behavior of this structural discontinuity could have enabled a transition from a stick-slip mode observed during the eruption to a stable sliding mode observed after the eruption. Such behavior could be related to an increase in confining pressure that tended to stabilize the fault after the March-April 2007 eruption (Hyndman et al., 1997). An explanation may be strong decompression of a pressurized hydrothermal system related to the eruption followed by recompression which induced an increase in pore pressure in the system.

Regardless of the assumptions, it seems difficult to explain the spatial variation in eastward displacement pattern observed on the Eastern Flank by InSAR (Figure 4.8b, d) as suggested that deformation is not driven by a unique frictional or ductile structural discontinuity. Eastward long-term displacements up to 0.1 m are effectively concentrated in two principal

regions during the rest period (**Figure 4.8d**). The easternmost of these two regions is limited to the west and to the north by a V-shaped structure visible in the topography (**Figure 4.1** and **Figure 4.8**) and classically interpreted as the scar of a small-scale landslide (Bachèlery, 1981, Michon & Saint Ange, 2008). The westernmost is limited to the southwest by the sharp N120-130°E lineament mentioned previously (Ls in **Figure 4.8**). Although this lineament does not coincide with any clear topographic feature it is likely related to a buried structural discontinuity. These observations suggest that complex structural mechanisms could play a significant role. Bachèlery (1981) proposed a polyphase caldera collapse model to explain the formation of the large Enclos - Grandes Pentes - Grand Brûlé structure. In this model, Grandes Pentes would be the headwall of a large landslide extending seawards and the Grand Brûlé would be the scar of several lateral landslides. Based on this model, a possible scenario is that slip on a main structural discontinuity, driven by the ascent of magma, could load secondary faults and the observed displacement could then be induced by release of the excess stress on these secondary faults. The lack of shallow seismicity on this flank would indicate that the sliding mode of these secondary faults is stable, and instability does not occur during this post-eruptive relaxation phase, suggesting a velocity strengthening behavior.

4.6 Conclusions

This study provides, for the first time, precise InSAR time series maps describing the spatial pattern and temporal evolution of ground displacements during the 2009-2014 period at Piton de la Fournaise volcano. Joint use of X band InSAR data acquired by two different SAR constellations (TSX/TDX and CSK), and combined analysis of InSAR data with GNSS data has been shown to be a useful way to characterize ground displacement. Using SAR data acquired both in ascending and descending orbits offers great advantages, making it possible to properly determine the U-D and E-W components of displacement and to provide greater insight and understanding into their origins. The following conclusions can be drawn from this study:

1. The powerful potential of the principal component decomposition method to obtain a priori knowledge of the long-term ground displacements has been demonstrated, and this method allows us to properly estimate InSAR artifacts without worrying about the long-wavelength displacement signal being mistaken for an artifact. The

proposed InSAR artifact correction strategy based on the principal component decomposition has been proven to be a very efficient method for the purposes of this study. It could also be applied elsewhere, especially to volcanoes with significant topography.

2. Slight summit deflations, captured by InSAR, which affect the Central Cone during the rest periods of Piton de la Fournaise, are separated by sudden and intense motions during eruptive periods. The short-scale pattern and low amplitude of this displacement lead us to suggest that the deformation is caused by stress relaxation in a shallow source.
3. Recent lava flow fields (since 1998) have predominantly vertical subsidence with negligible horizontal displacement. The amplitudes of the localized subsidence show clear correlation with lava thickness and age. Lava flow subsidence is clearly not the only contribution to the observed large-scale downward displacement on the Eastern Flank.
4. A widespread active seaward motion affecting the Eastern Flank of Piton de la Fournaise during the 2009-2014 period is demonstrated by our InSAR and GNSS observations and confirmed to be mainly due to the ongoing post-eruptive displacement of the March-April 2007 eruption. As the physical origin of the mechanisms driving the instability of the Eastern Flank of Piton de la Fournaise remains somewhat uncertain, we considered different alternative hypotheses to explain the observed self-sustaining displacement.
5. Our results and interpretations provide major indications of the potential instability of the Eastern Flank of Piton de la Fournaise. Regular and large scale monitoring is urgently required to assess all possible related hazards.

4.7 Acknowledgements

The authors would like to thank for the Agence Nationale de la Recherche (ANR) through the framework of GEOSUD, ANR-10-EQPX-20 project, ASI through the CSK 2080 project for our CSK images, and DLR for TSX/TDX images through the LAN 0237 project, and CNES (TOSCA) and INSU (SNO1) for supporting InSAR data acquisition at Piton de la Fournaise. The GNSS data used

in this paper was collected by Observatoire Volcanologique du Piton de la Fournaise/ Institut de Physique du Globe de Paris (OVPF/IPGP). This is IPGP contribution number XXXX and Labex Clervolc contribution number YYYY. Yu CHEN would like to especially thank the Chinese Scholarship Council (CSC) for her PhD scholarship. The authors wish to extend a special acknowledgment to Fran Van Wyk de Vries for proofreading an early version of this manuscript, and M. Rabinowicz and M. Gerbault for helpful discussions. Thanks to two anonymous reviewers who made constructive reviews of the manuscript. Many thanks to Dr. Mike Poland for his useful reviews and very constructive remarks that greatly improve this paper.

4.8 Supplementary Material

4.8.1 Presentation of the stratified tropospheric artifact

Figure 4.11a shows an example of SB interferogram. It spans 16 days during a quiet volcanic period when no ground displacement is expected to occur. The stratified tropospheric signal can be simply estimated by a linear function (**Figure 4.11b**) expressing the phase-elevation correlation.

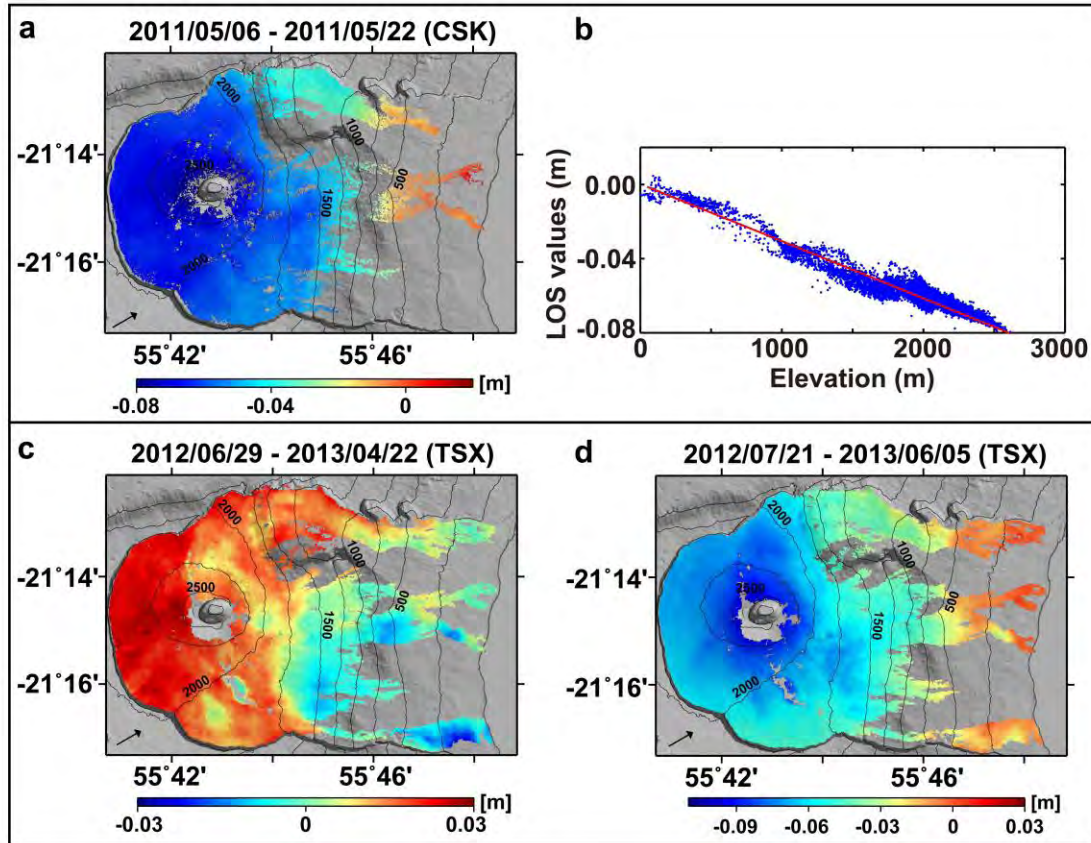


Figure 4.11 Stratified tropospheric artifact present in the interferograms. (a) A CSK interferogram spanning from 6 to 22 May 2011 and (b) its phase-elevation correlation. (c) A TSX interferogram spanning from 29 June 2012 to 22 April 2013. (d) A TSX interferogram spanning from 21 July 2012 to 5 June 2013. Positive values represent decreases in earth-satellite distance, while negative values represent increases in earth-satellite distance. Black arrows indicate the LOS directions. Maps are draped on a shaded DEM and projected in Geographic Lat/Lon referenced to WGS-84 Datum, with contours every 250m.

However, many interferograms spanning longer period of time contain not only stratified tropospheric but also ground displacement signals. For example, **Figure 4.11c-d** illustrates different long-wavelength signals (tropospheric artifact and ground displacement) with distinct spatial patterns and distinct ranges of amplitude in two interferograms spanning the same period of time (about 1 year duration), during which long-term displacement is expected to take place. In spite of being contaminated by long-wavelength artifacts, a clear spatial pattern of displacement signal covering almost the whole Grandes Pentes and the upper-middle part of the Grand Brûlé of the Eastern Flank is still recognizable from the interferogram in **Figure 4.11c**. Nevertheless, no similar displacement pattern is found in the same time-

spanning interferogram in **Figure 4.11d**, because it is totally overlapped by the long-wavelength tropospheric artifact that has similar spatial pattern, same signs and comparable order of amplitude. In this case, it will be highly risky using empirical functions to mitigate the stratified tropospheric artifact.

Section 4.3.3 describes in detail the approach used to mitigate the vertically stratified tropospheric contributions correlated with elevation in the interferograms and **Figure 4.12** shows some examples of the efficiency of the mitigation according to the phase ramp used.

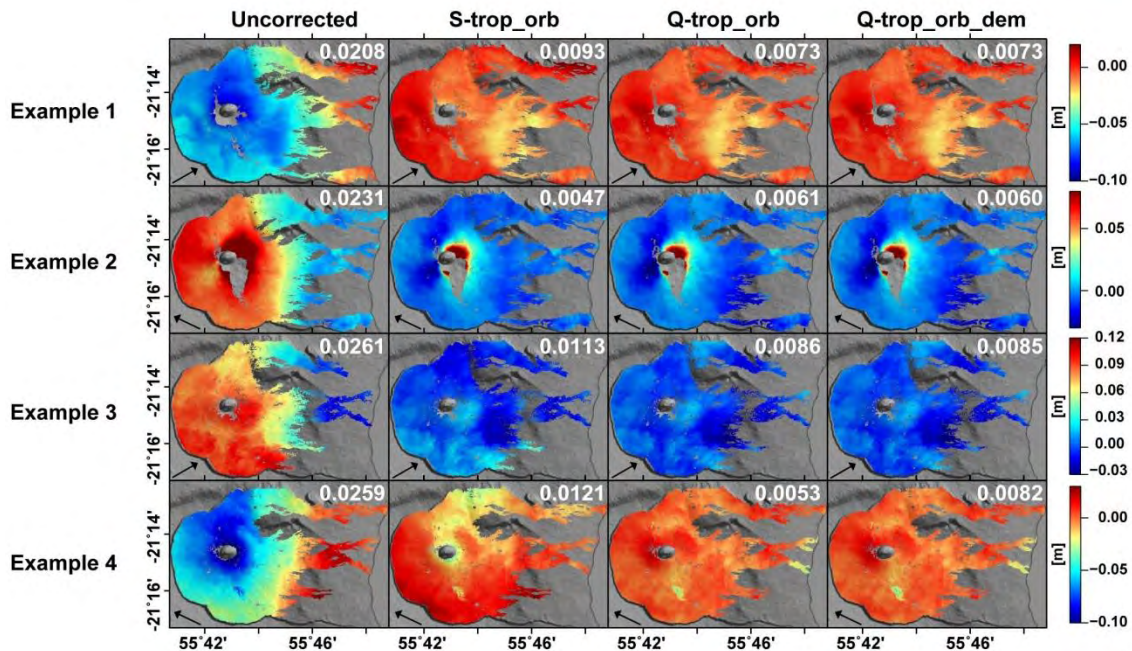


Figure 4.12 Examples showing the correction results using different empirical functions. The values in white are the standard deviations (m). Example 1: TSX ascending interferogram spanning 253 days; Example 2: TSX descending interferogram spanning 99 days; Example 3: CSK ascending interferogram spanning 208 days; Example 4: CSK descending interferogram spanning 128 days.

4.8.2 PCAIM decomposition

PCAIM decomposition is an effective and practical inversion method to investigate and extract the dominated information involved in large and/or heterogeneous datasets, such as

InSAR time series data and GPS measurements. It not only can significantly reduce the data redundancy, but also takes the data uncertainties into account, as the latter is not often the case of classic PCA decompositions (Kositsky & Avouac, 2010). The InSAR ground displacements time series, as input to PCAIM in this study, are decomposed into a linear combination of several principal components, each of whom is individually associated with a spatial function, a significance value and a temporal function, where the spatial function presents the spatial distribution of displacements, the significance value indicates the importance of the relative component, and the temporal function describes the temporal behaviors of displacements (Kositsky & Avouac, 2010). We demonstrate here the main principle of PCAIM decomposition, while readers can refer to (Kositsky & Avouac, 2010; Lin et al., 2010b; Perfettini et al., 2010; Remy et al., 2014) for more detailed theories and examples of applications.

Let us consider the original InSAR time series as a matrix X_0 ($m \times n$), where m is the number of observations (pixels) and n corresponds to the number of epochs. X_0 is centered along its rows to make sure each time series has a mean value of zero. The centered matrix X ($m \times n$) is then decomposed into three matrix, expressed as **Equation (4.4)**:

$$X_{m \times n} = U_{m \times m} \cdot S_{m \times n} \cdot V_{n \times n}^T \quad (4.4)$$

where $U_{m \times m}$, $V_{n \times n}$ are both square matrixes representing the spatial function and temporal function of components respectively. $S_{m \times n}$ is a diagonal matrix whose values signify the significance of each component. $V_{n \times n}^T$ donates the transpose of $V_{n \times n}$.

In order to approximate and reconstruct the original data X , the first k components with maximum deformation signals are selected,

$$X \cong X_k = U_k \cdot S_k \cdot V_k^T \quad (4.5)$$

where U_k , V_k correspond to first k columns of $U_{m \times m}$ and $V_{n \times n}$ respectively, S_k is a diagonal matrix of k square.

The number of components k for reconstruction can be determined by statistics of the reduced Chi-Square χ^2 , **Equation (4.6)**, a measure of the fitness between the original data and the reconstructed data. We chose the k value that makes Chi-Square the most approximate to 1

so that the misfits are on average of the same order of magnitude with that of measurement uncertainties.

$$\chi^2 = \frac{1}{N - k(n + m + 1)} \sum_{i=1}^m \sum_{j=1}^n \frac{(X(i, j) - X_k(i, j))^2}{\sigma(i, j)^2} \quad (4.6)$$

Where N is the total number of the data, and $\sigma(i, j)^2$ is the 1-sigma uncertainty of the (i, j) data point.

4.8.3 Merging of TSX and CSK time series

In order to calculate the time series of the ground displacement in two dimensions, both ascending and descending LOS time series with acquisition dates as close as possible are required. As shown in **Figure 4.2** and described in [Section 4.3.4](#), there exist one or several large time gaps in each acquisition geometry. A simple linear interpolation at missing epochs in time gaps would introduce extra noise into the LOS time series, and further bias the time series of the 2D component of ground displacement. Therefore, we tactfully merged the TSX and CSK corrected time series in order to achieve the most complementary and fill in the time gaps as much as possible.

We separated the acquisition dates of the four time series into two subsets: ascending date subset (including TSX_Asc and CSK_Asc), and descending date subset (including TSX_Des and CSK_Des). The Euclidean distance of the two subsets was then computed. Any ascending and descending combination with time interval less than 15 days were selected. Furthermore, for insurance purposes, we inspected each selected combination and deleted those with time intervals happening to overlap any eruptive event. Then the corresponding date was set to be the mean of the two dates of the combination. The date repetitions were searched for and weeded out. In this way, a new ascending and a new descending displacement time series were formed according to all the selected combinations. The time series of the 2D components of the ground displacement can be finally inverted based the vectors pointing from the ground to the satellite LOS.

4.8.4 Relative error in components of the ground displacement

We calculated the relative measurement errors (equivalent to the dilution of precision of GNSS measurements) in the estimates of the vertical (U-D) and horizontal components (E-W and N-S) of the ground displacement referring to the formulation of Wright et al. (2004) (Table 4.6). Five possible combinations of ascending (Asc) and descending (Des) passes were tested. We assumed that errors in LOS are independent and their standard deviations equal to 1.

	Case 1			Case 2			Case 3			Case 4			Case 5
	TSX_Asc/TSX_Des			TSX_Asc/CSK_Des			CSK_Asc/TSX_Des			CSK_Asc/CSK_Des			ALL
Azimuth(°)	-12/-168			-12/-164			-16/-168			-16/-164			ALL
Incidence(°)	33.5/36.5			33.5/52.2			48.8/36.5			48.8/52.2			ALL
E-W	1.26	1.27	-	1.07	1.19	-	1.08	1.14	-	0.95	0.95	-	0.76
U-D	0.86	-	14.71	0.97	-	2.32	0.96	-	2.83	1.11	-	38.38	1.80
N-S	-	5.96	101.28	-	4.73	10.28	-	4.42	12.20	-	3.43	118.56	7.87

Table 4.6 Relative errors in vector components of ground displacement estimated from LOS displacement

It can be seen from Table 4.6 that the error in the N-S component of the ground displacement is much (about one order of amplitude) larger than in E-W and U-D components. The main reason results in the difficulty in resolving the N-S displacement component is the near-polar orbits of the satellites (both TSX and CSK) and the small angular distance of the different LOS measurement (both satellite azimuth angle and incidence angle) (Wright et al., 2004). When three or more viewing geometries are available, all of the three components of the ground displacement are possible to be estimated, as shown in Case 5. However, more satellite passes cannot significantly reduce the error of N-S component (that is several times larger than other components in Case 5) if the view geometry lacks diversity. If the SAR data are acquired by both left- and right- looking antenna, the error in N-S component could be further improved (Wright et al., 2004). Both TSX and CSK data in this study are collected by right-looking radar, leading to unsatisfying precision of N-S component of the ground displacement.

4.8.5 Correlation between E-W displacement and slope

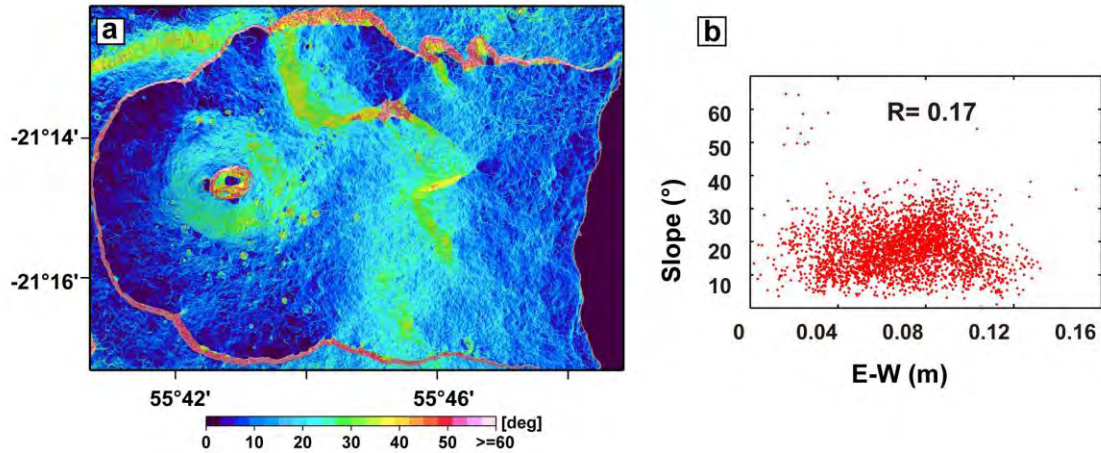


Figure 4.13 (a) Slope map (in degrees) of Piton de la Fournaise. (b) Scatter plot of the correlation between the cumulative E-W displacement (in meters, 2009 – 2014) and the slope in the Eastern Flank area. R indicates the correlation coefficient. According to the $R = 0.17$, no clear relationship between E-W displacement and slope is found.

4.9 Effectiveness tests

4.9.1 Effectiveness of GAMs for mitigating atmospheric artifact

The InSAR has been widely and successfully applied to measure large scale deformations of the ground surface related to, such as, volcano eruptive activities (e.g., Remy et al., 2015; Froger et al., 2015) or co-seismic displacement fields (e.g., Massonnet et al., 1993; Lasserre et al., 2005; Simons et al., 2002). However, the measuring of low-amplitude and long-wavelength deformation such as those due to long-term post-eruptive and post-seismic motions remains challenging due in particular to atmospheric propagation delays (e.g., Jolivet et al., 2012). The phase delay introduced by spatio-temporal variations of the refractivity of air can reach tens of centimeters and often overlaps the deformation signal of interest (Hanssen, 2001). The patterns of the stratified tropospheric delay result from stratification of the low troposphere typically mimic the topography, making it particularly difficult to discriminate between atmospheric and

deformation signals in areas where topography is strong and correlated with deformation (Beauducel et al., 2000).

The Global Atmospheric Models (hereafter GAMs) have been recently used in several studies to correct for the stratified tropospheric delays in SAR interferograms (Doin et al., 2009; Jolivet et al., 2011, 2014). Doin et al. (2009) compared quantitatively the GAMs outputs with empirical corrections, and then validated the potential of GAMs. Jolivet et al. (2011) developed a predictive, systematic correction tool using GAMs. Jolivet et al. (2014) explored and validated the effectiveness of three GAMs, ERA-Interim (European Center for Medium-Range Weather Forecasts, ECMWF), the North American Regional Reanalysis (NARR), and the Modern Er5a-Retrospective Analysis for Research and Applications (MERRA), in several geographic and tectonic settings on both single interferograms and time series products. Here in this study, the ERA-Interim model is used to derive atmospheric delays for correcting SAR interferograms obtained from TSX/TDX data over Piton de la Fournaise volcano. The effectiveness of this GAMs is then tested by comparing with the outputs of proposed atmospheric correction method.

ERA-Interim is the latest atmospheric reanalysis of the ECMWF. It is computed based on a 4D-Var assimilation of global surface and satellite meteorological data (Dee et al., 2011). It provides estimates of several meteorological parameters including temperature, water vapor partial pressure, and geopotential height on a global ~ 75 km grid along 37 pressure levels, at 0:00, 6:00, 12:00, and 18:00 UTC daily from 1989 to present (Jolivet et al., 2011).

In order to model the atmospheric phase delay at one SAR acquisition time, we extract the temperature, water vapor partial pressure, and geopotential height at each pressure level on each grid point in the vicinity of the SAR scene, from the ERA-Interim output at the closest time to the acquisition time. Then the geopotential height is converted to a regular vertical metric grid. Based on these estimates and **Equations (2.20) – (2.21)**, the tropospheric phase delay comprising hydrostatic and wet delay contributions on each grid point is computed. Then, a bilinear interpolation in the horizontal direction and a spline interpolation in the vertical direction along the altitude is applied to generate a map of the predicted phase delay for this SAR acquisition. The predicted interferometric stratified tropospheric delay corresponding to an interferogram is finally derived by differentiating delay maps at each time of acquisition (Jolivet et al., 2011, 2014). This whole process described above is implemented as an open-source and

Python-based package tool, called PyAPS (Python-based Atmospheric Phase Screen), which is available at <http://www.earthdef.caltech.edu> (Agram et al., 2013). This package allows one to automatically download atmospheric reanalysis products and to compute maps of stratified tropospheric delays in both radar and geocoded geometries using a DEM used in InSAR processing.

In this thesis, in order to explore the effectiveness of GAMs in the case of Piton de la Fournaise, I selected five interferograms with strong atmospheric artifact spanning short periods (Table 4.7, maps for cases 1 – 2 are shown in Figure 4.14 – Figure 4.15 and maps for cases 3 – 5 are shown in Appendix 8). Because of the short temporal baselines, no ground displacement is expected to occur. The reference elevation is set to 30 km as it is the top of the atmospheric layer modeled in ERA-Interim (Jolivet et al., 2014). Above this reference elevation, the effects due to spatio-temporal variations in atmospheric stratification is assumed to be negligible.

Interferogram	1	2	3	4	5
Time span	2010/03/05	2013/12/20	2012/06/07	2012/09/03	2011/10/31
	– 2010/04/07	– 2014/01/11	– 2012/06/29	– 2012/09/25	– 2011/11/22
SD_0 (m)	0.0137	0.0157	0.01	0.0137	0.0345
SD_1 (m)	0.0108	0.011	0.0054	0.0094	0.0097
VR_1 (%)	21.2	29.9	46.0	31.4	71.9
SD_2 (m)	0.0038	0.0038	0.0027	0.0035	0.0038
VR_2 (%)	73.0	75.8	73.0	74.5	89.0

Table 4.7 Standard deviations (m) and variance reductions (%) of selected interferograms. (SD_0, SD_1, and SD_2 represent standard deviations of original interferogram, atmospheric artifact corrected interferogram using GAMs, and interferogram corrected using proposed correction method, respectively. VR_1 and VR_2 donate the percentages of the variance reduction corresponding to SD_1 and SD_2.)

Figure 4.14 – Figure 4.15 show that the predicted atmospheric delays, based on ERA-Interim, display clear relationship with topography corresponding to the long-wavelength stratified tropospheric delays. However, the predictions seem to have not well fitted the original interferograms. They are either over predicted (Figure 4.14) or under predicted (Figure 4.15). The residual interferograms (Figure 4.14 – Figure 4.15e) and the corresponding phase/elevation plots (Figure 4.14 – Figure 4.15g) show that large long-wavelength residuals are remained in the interferograms after correction with ERA-Interim predictions in all cases, indicating that this method cannot satisfactorily mitigate the stratified atmospheric delay in the case of this study.

PITON DE LA FOURNAISE
CHAPTER 4: LONG-TERM GROUND DISPLACEMENT BETWEEN 2009 AND 2014

Except for the case 5, the ERA-Interim reanalysis reduces the variance of interferogram no more than a half, with a minimum variance reduction of 21.2 % (Table 4.7).

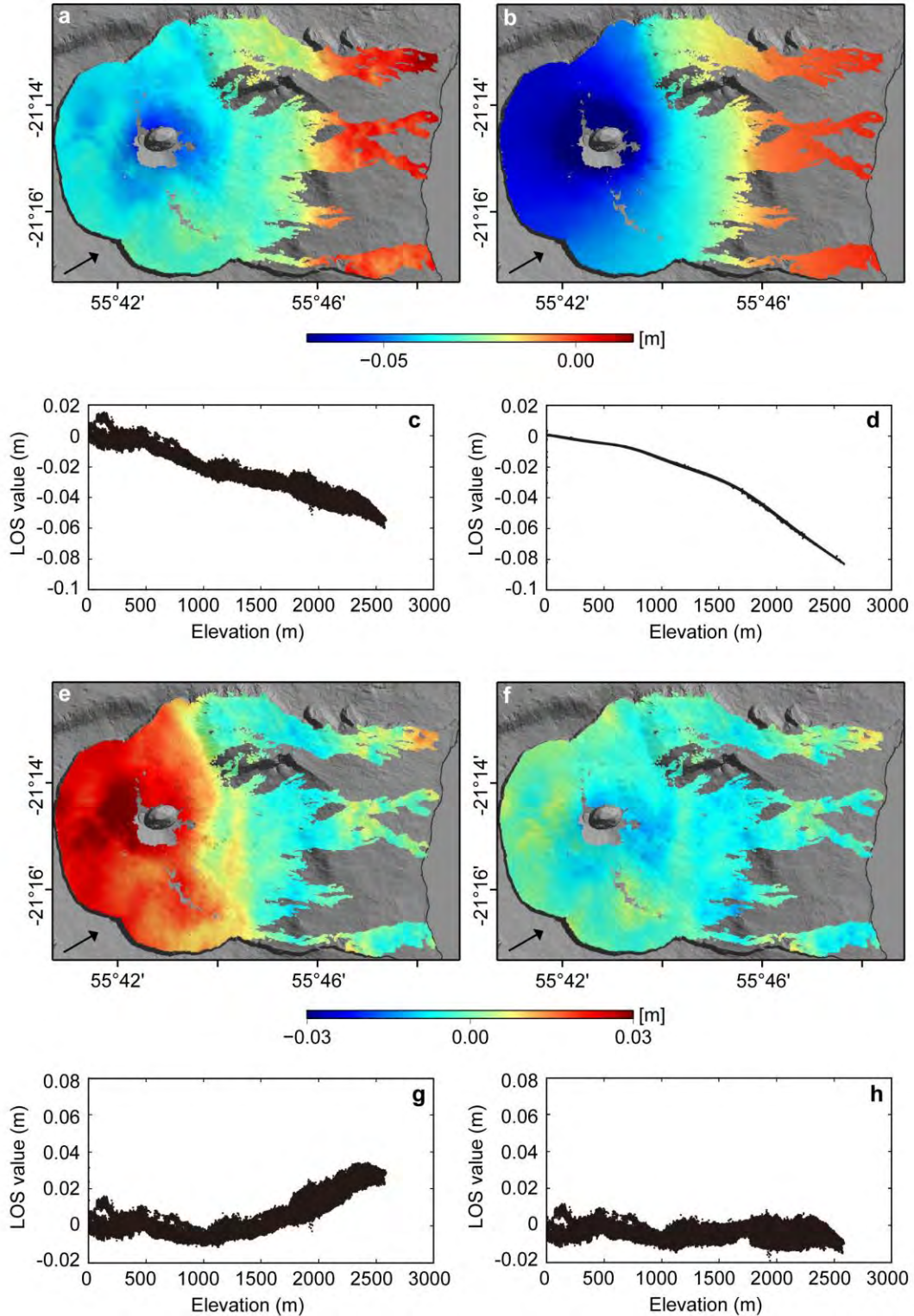


Figure 4.14 (a) An interferogram over Piton de la Fournaise from TSX/TDX SAR acquisitions on 5 March 2010 and 7 April 2010. (b) Stratified tropospheric delay predicted using ERA-Interim. (c) and (d) are the corresponding phase/elevation plots to (a) and (b). (e) Residuals after correction with the ERA-Interim prediction. (f) Residuals after correction with proposed method. (g) and (h) are the corresponding phase/elevation plots to (e) and (f). Maps are draped on a shaded DEM and projected in Geographic Lat/Lon referenced to WGS-84 Datum. Black arrows indicate the LOS directions.

PITON DE LA FOURNAISE
CHAPTER 4: LONG-TERM GROUND DISPLACEMENT BETWEEN 2009 AND 2014

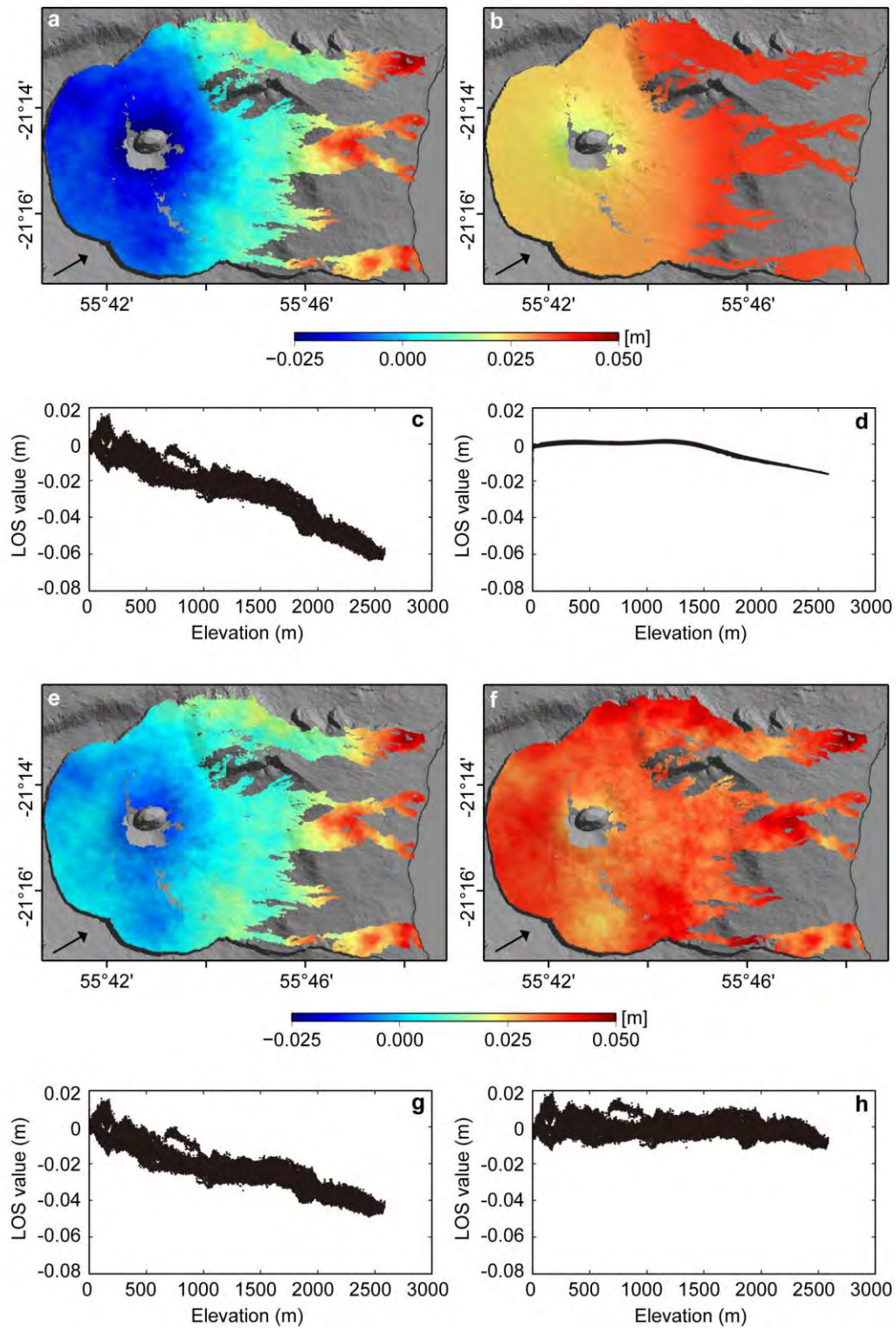


Figure 4.15 (a) An interferogram over Piton de la Fournaise from TSX/TDX SAR acquisitions on 20 December 2013 and 1 January 2014. (b) Stratified tropospheric delay predicted using ERA-Interim. (c) and

(d) are the corresponding phase/elevation plots to (a) and (b). (e) Residuals after correction with the ERA-Interim prediction. (f) Residuals after correction with proposed method. (g) and (h) are the corresponding phase/elevation plots to (e) and (f). Maps are draped on a shaded DEM and projected in Geographic Lat/Lon referenced to WGS-84 Datum. Black arrows indicate the LOS directions.

In comparison with corrections based on ERA-Interim predictions, the proposed correction method have made more favorable performances in mitigating the long-wavelength atmospheric delays (**Figure 4.14 – Figure 4.15f, h, and Table 4.7**). Rare long-wavelength signal is remained across the entire interferogram (**Figure 4.14 – Figure 4.15f**) and phase/elevation trends are extremely diminished with values fluctuating around zero in residuals after correction according to the phase/elevation plots (**Figure 4.14 – Figure 4.15h**). More than 70 % of variances have been reduced by the proposed correction method in all cases, with a maximum variance reduction of 89 % in the second case (**Table 4.7**).

Besides of the stratified long-wavelength tropospheric delay, varying levels of turbulent tropospheric delays are also visible in the interferograms (**Figure 4.14 – Figure 4.15a**). These short-wavelength patterns show no clear correlation with topography and distributed randomly in space and time. The turbulent delays are a difficulties to both correction methods since visible turbulent patterns are still remained in the both residual interferograms (**Figure 4.14 – Figure 4.15e and f**). In order to mitigate turbulent atmospheric signals, time series analysis or interferogram stacking are usually required (e.g., Ferretti et al., 2001; Berardino et al., 2002; Cavalie et al., 2007; Hooper et al., 2007; Hetland et al., 2012).

Overall, the GAMs method based on ERA-Interim reanalysis has not been competent to satisfactorily mitigate the atmospheric artifact in the interferograms over Piton de la Fournaise volcano. Through analysis of the reasons leading to poor predictions, I attribute it to: 1) the coarse spatial resolution of ERA-Interim meteorological parameters (~ 75 km) with respect to the study area ($\sim 13 \times 10$ km²), which is not adequate for an accurate analysis; 2) the acquisition time difference between SAR data and ERA-Interim data (~ 90 mins minimum), which is long enough with respect to variations of water vapor. Although the examples are derived from one track of TSX/TDX data, the other tracks (TSX/TDX and CSK) share similar situations. Consequently, the GAMs was not adopted for correcting the atmospheric artifact in this study, even though it is free, automatic, independent, and always available.

4.9.2 Effectiveness of the proposed artifact correction method

While performing the StaMPS/MTI-SB treatment, neither the ready-made orbital correction nor the ready-made linear empirical atmospheric correction were adopted. It is because: first of all, both of them do not take the possible correlation between the orbital residual/atmospheric delay and the displacement into account; second, the orbital residual is expected to be small due to the use of the modern satellites images and the small area of the study zone; third, the simple linear model of the atmospheric correction does not suitable for all the interferograms. More detailed necessity for developing a new correction method has been demonstrated in [Section 4.3.3](#). In order to test the effectiveness of our proposed correction method, we analyzed the results derived directly from StaMPS/MTI-SB and the results after applying our correction method by comparing them with GNSS data. The first dataset selected for comparison is the uncorrected InSAR time series derived from StaMPS/MTI-SB (no orbital and atmospheric correction). The second is the InSAR time series filtered by a spatio-temporal filter provided by StaMPS/MTI-SB. The last is the InSAR time series corrected by our proposed correction method. For all the datasets, the TSX and CSK LOS data were merged (after filtering or correction steps) and decomposed into 2D components of ground displacement using the method shown in [Section 4.3.4](#).

4.9.2.1 Three sets of InSAR time series

- **Uncorrected InSAR time series**

It is worth noting that for this dataset and the dataset 2) below, the DEM error is removed alongside the process of StaMPS/MTI-SB using the ready-made module (see [Section 2.4.2](#)). The term “uncorrected” refers to no orbital and atmospheric correction applied.

- **Spatio-temporally filtered InSAR time series**

The StaMPS/MTI-SB provides a spatio-temporal filter module for reducing the residual orbital and atmospheric contribution and the noise remained in the data. It assumes that the orbital and atmospheric contribution are correlated in space and uncorrelated in time, and that the noise term is correlated neither in space nor in time, while the displacement term is

correlated both in space and in time. Therefore, the displacement term can be separated from other contributions by applying a high-pass filter in time and then a low-pass filter in space.

The application of the spatio-temporal filter relies on a prerequisite, which is that the residual orbital and atmospheric contribution are uncorrelated in time. However in practice, it is possible that they are also correlated temporally, in which case they will not be accurately estimated by this filter procedure. The study area in this thesis is located in coastal areas where the tropospheric moisture content is likely to vary seasonally. Therefore, this method of reducing the artifact may not be adequate enough. Furthermore, the result of filter depends highly on the parameters concerning the size of the temporal and spatial length. Shorter will keep or introduce more artifact in the deformation result (see **Figure 4.16c**) and larger will increase the risk of losing deformation signal and/or deformation signal behavior being changed (**Figure 4.16d-e**). Repeated time consuming tests are required to seek out the suitable parameters. Additionally, the filter fails easily in areas where short-wavelength or transient displacement (such as volcano summit) occurs.

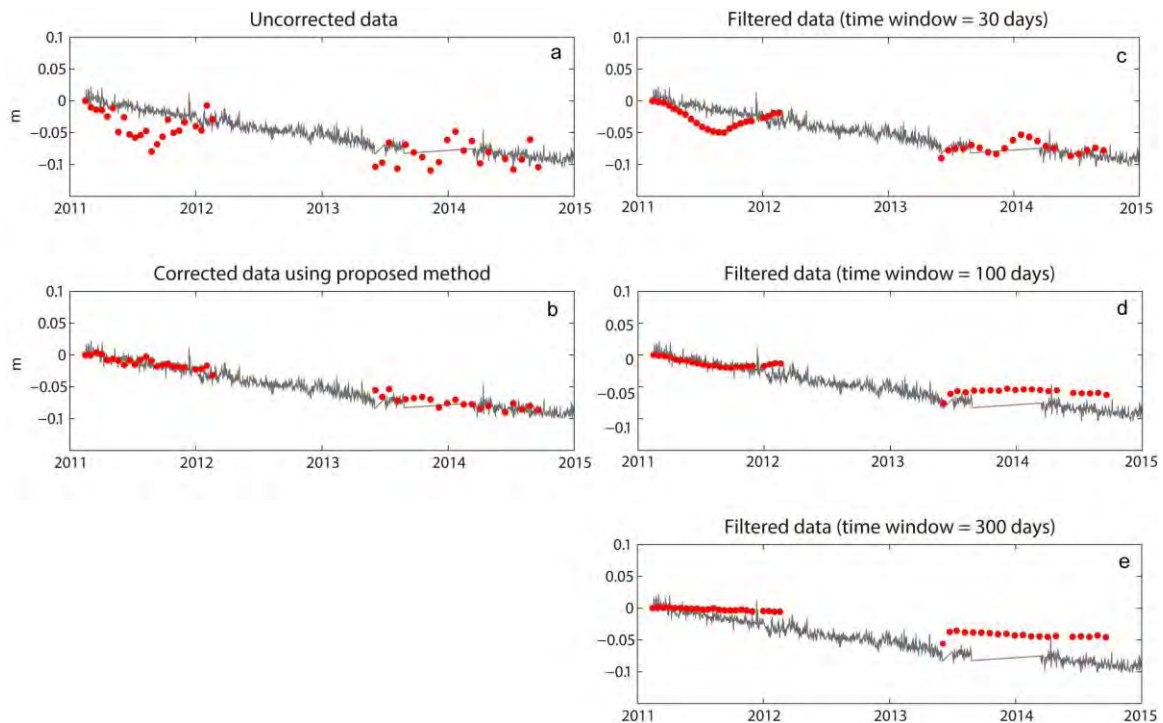


Figure 4.16 Comparison of time series (CSK ascending orbit) filtered using different parameters. The point is located at GPSG GNSS station (see **Figure 4.1** for location) with absence of transient displacement. (a) the uncorrected time series. (b) the corrected time series using the proposed method. (c), (d) and (e) the

filtered time series using 30, 100 and 300 days as temporal window size. The time series are superimposed on the GNSS measurement (grey lines) in LOS projection at GPSG station.

- **Corrected InSAR time series using proposed method**

The detailed description of the proposed artifact correction method is elaborated in [Section 4.3.3](#).

As mentioned in [Section 2.4.3](#), the DEM error correction approach implemented in StaMPS/MTI-SB is based on an assumption that the expected displacement evolves linearly in time. However in practice, a variety of temporal revolutions of ground displacement are possible, such as linear, exponential, or complex, irregular time-variable displacements. In this study, since an a priori long term displacement model (LTDM, exponential behavior for TSX and linear for CSK, see [Section 4.3.3](#)) is investigated, the DEM error estimation (for TSX data) differs from that applied on dataset 1) and 2). The exponential LTDM is previously removed while estimating the DEM error for TSX data.

4.9.2.2 Comparison between two methods

- **Time series at three GNSS stations**

The InSAR time series at location of GPSG, GPNG and HDLG GNSS stations from the three datasets are plotted with GNSS time series in **Figure 4.17**, **Figure 4.18**, and **Figure 4.19**, and the Root-Mean-Squares (RMS) between InSAR and GNSS time series are listed in **Table 4.8**.

PITON DE LA FOURNAISE
CHAPTER 4: LONG-TERM GROUND DISPLACEMENT BETWEEN 2009 AND 2014

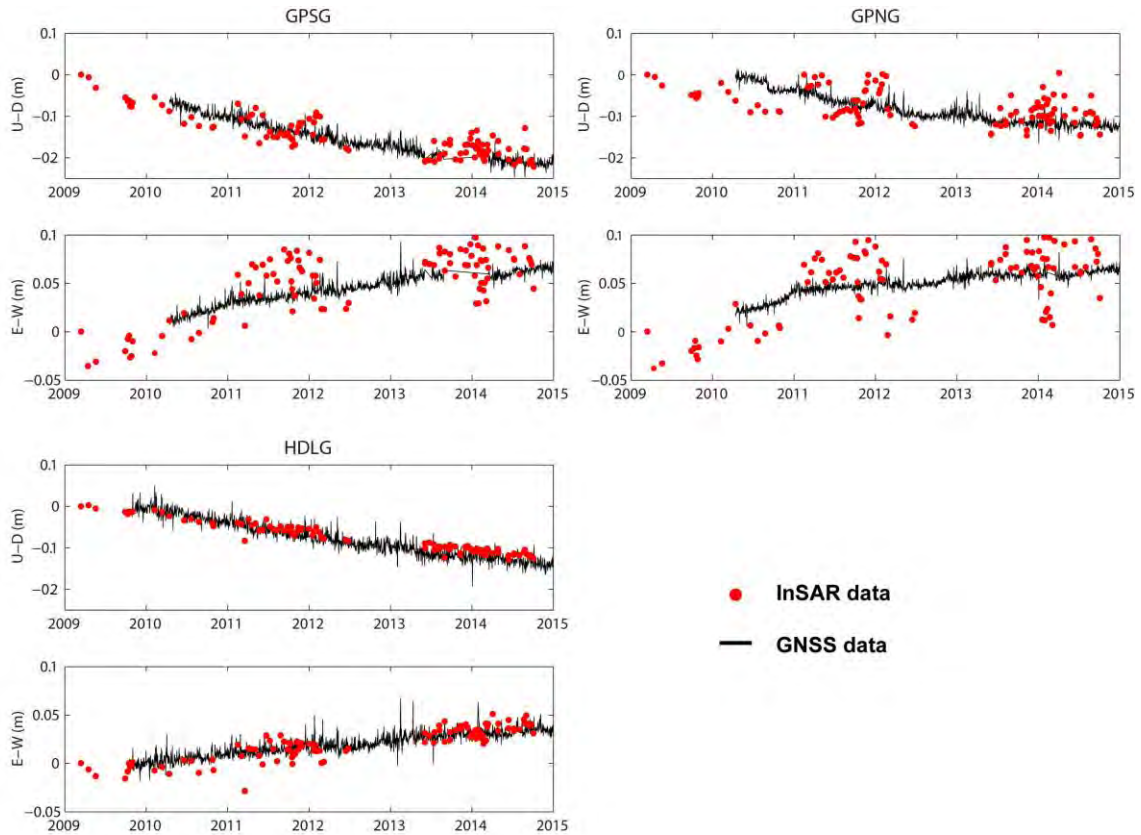


Figure 4.17 Uncorrected InSAR time series superimposed on the GNSS time series. The GNSS time series are shifted in order to search for the minimum RMS.

The original InSAR time series at GPSG and GPNG stations (**Figure 4.17**) are seriously contaminated by artifacts and noise. The displacement signal is hardly able to be recognized due to the significant variations. On the contrary, the InSAR data at HDLG station displays a clear linear deformation trend which fits well the GNSS data (see also RMS values in **Table 4.8**).

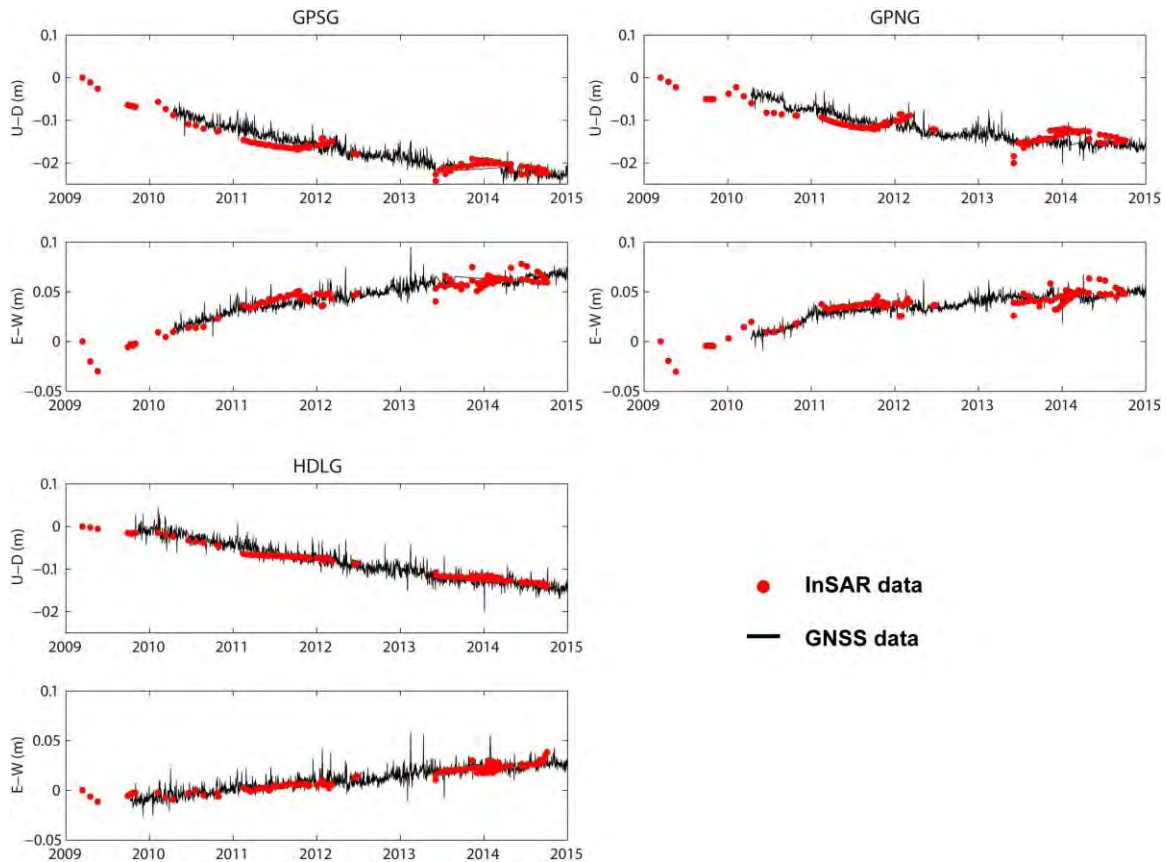


Figure 4.18 Spatio-temporally filtered InSAR time series superimposed on the GNSS time series. The time window for filtering was set as 100 days. No transient displacement occurred at these three stations. The GNSS time series are shifted in order to search for the minimum RMS.

As shown in **Figure 4.18**, the spatio-temporal filtering has greatly reduced the artifact and noise level of the InSAR time series at all those three stations. It improves the agreement between InSAR and GNSS datasets (**Table 4.8**). However, additional effects were introduced while filtering. For example in the U-D components of GPSG and GPNG stations, the time series between 2011-2012 and 2013-2014 are distorted in **Figure 4.18**, similar to the case in **Figure 4.16c**. To the contrary, the filter works satisfactorily in the case of HDLG station where displacement signal plays a more significant role than artifact and noise. And the filter procedure has not been misled and distorted because of the clear linear displacement behavior. Therefore, the performance of the spatio-temporal filter mitigating InSAR artifact and noise depends highly on the level of artifact and noise, and the complexity of the displacement behavior.

PITON DE LA FOURNAISE
CHAPTER 4: LONG-TERM GROUND DISPLACEMENT BETWEEN 2009 AND 2014

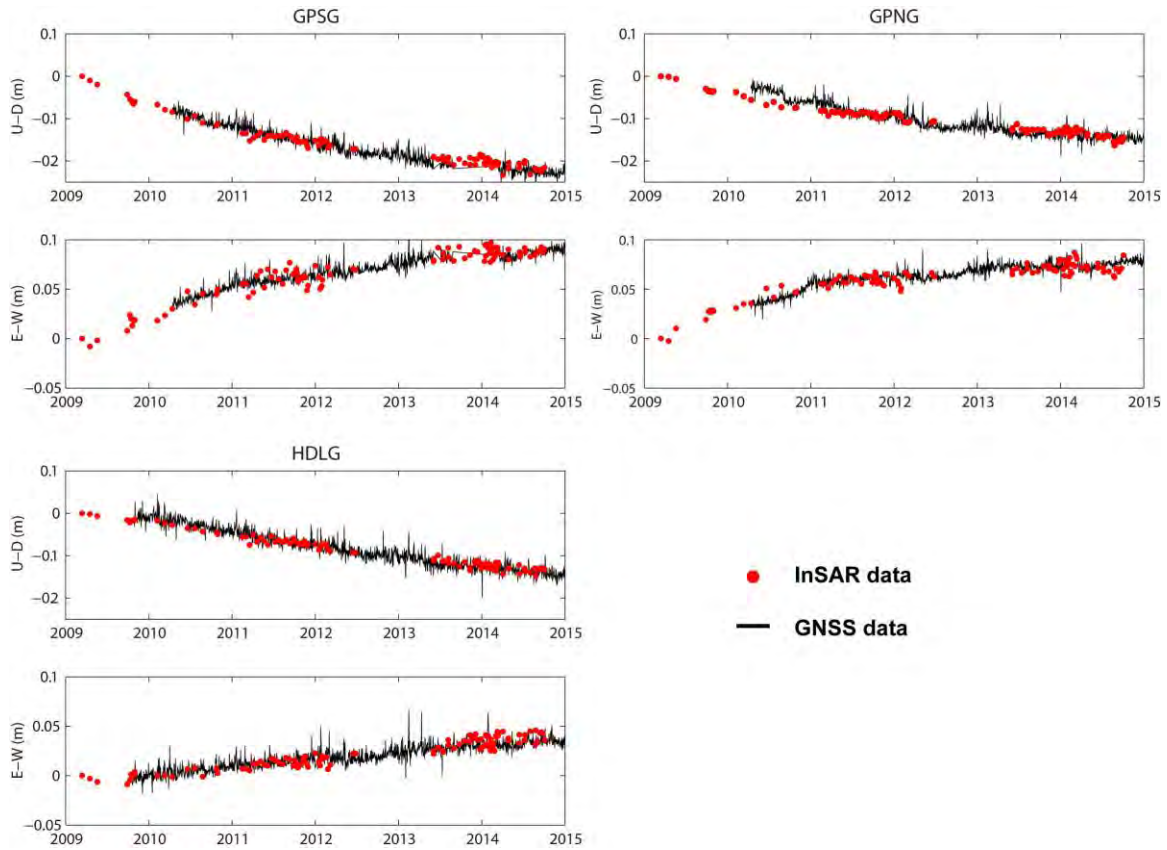


Figure 4.19 Corrected InSAR time series superimposed on the GNSS time series. The GNSS time series are shifted in order to search for the minimum RMS.

Datasets	GPSG		GPNG		HDLG	
	U-D	E-W	U-D	E-W	U-D	E-W
Uncorrected data & GNSS	30.8	23.4	70.3	27.8	17.0	9.7
Spatio-temporal filtered data & GNSS	18	7.9	27.1	8.1	12.8	7.6
Corrected data & GNSS	15.8	9.4	15.8	8.0	14.2	8.2

Table 4.8 RMS (mm) between three InSAR datasets and GNSS data at location of GPSG, GPNG, HDLG stations

Figure 4.19 indicates that our proposed correction method works extremely well at all the stations. Compared with the original data (**Figure 4.17**), the variation has been significantly reduced. At the same time, the displacement trend becomes clearly visible. Compared with the filter, the proposed correction method has comparable performance in terms of RMS (**Table 4.8**),

and the filter seems even better sometimes (at GPSG E-W, HDLG U-D and E-W). The filtered time series at HDLG (**Figure 4.18**) are evidently smoother than the corrected time series (**Figure 4.19**). If the original data was not badly contaminated by artifact and noise, and the temporal deformation behavior was simple everywhere in the study area, the spatio-temporal filter would be the most adequate and efficient method. However, it is unfortunately not the case of this study. The artifact and noise have comparable magnitude with deformation signal. The deformation evolves variously from area to area and cannot be simply pre-assumed. Furthermore, the distortion of displacement behavior as described in preceding paragraph is unacceptable in an accurate analysis. Therefore, the filter method is not qualified for this study.

- **Displacement maps**

The effectiveness of a correction method cannot be sufficiently demonstrated by the performance at few points. The spatio-temporal filter method is way behind when inspecting each displacement map in time series. **Figure 4.20** presents three examples showing the performance of the two methods. The major part of the Western Flank of Piton de la Fournaise where no displacement is expected to occur can be considered as an area of reference while inspecting the maps. The uncorrected maps (upper row) are contaminated by varying degrees of long-wavelength artifact which overlaps the deformation signal. The filtering hasn't worked well enough in any case. It has either over-mitigated (left column), insufficiently mitigated (middle column) the artifact, or introduced extra artifact (right column), indicating the instability and inapplicability of the filter procedure. On the contrary, the proposed correction method has performed just appropriately (lower row). The deformation signal evidently shows up after correction. The expected non-deformation areas (the major Western Flank, the coastal area) are nearly free of displacement in all corrected maps.

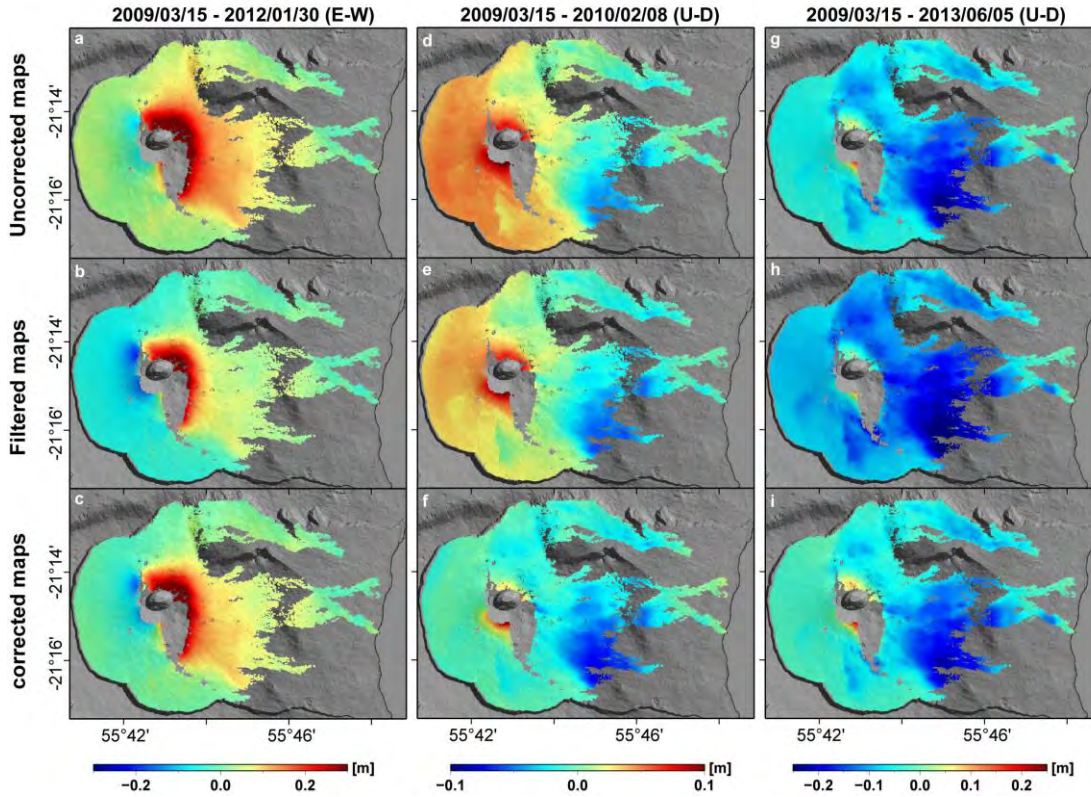


Figure 4.20 Displacement maps from three InSAR datasets. (a), (b) and (c) are the uncorrected, spatio-temporal filtered, and corrected (by the proposed method) displacement maps spanning from 15 March 2009 to 30 January 2012. (d), (e), and (f) are the uncorrected, spatio-temporal filtered, and corrected displacement maps spanning from 15 March 2009 to 8 February 2010. (g), (h), and (i) are the uncorrected, spatio-temporal filtered, and corrected displacement maps spanning from 15 March 2009 to 5 June 2013.

Datasets	Uncorrected data	Spatio-temporal filtered data	Corrected data
U-D	51.9	19.9	8.0
E-W	42.7	10.4	7.6

Table 4.9 Average RMS (mm) of three InSAR datasets in non-deformation areas.

The RMS values in non-deformation areas are calculated for each InSAR time series (see **Table 4.9**) in order to estimate the artifact/noise level of the whole dataset. One zone on the Western Flank, one zone in the coastal area are expected to be affected by neither time-dependent nor eruption-related displacement. Indeed, the spatio-temporal filter has reduced the artifact/noise level by about 70%. The proposed correction method has reduced the

artifact/noise level by almost one order of magnitude, implementing a millimeter-accuracy InSAR analysis.

In brief, the proposed correction method has shown its powerful capacity and effectiveness in all respects. It could be applied and improved in applications of other volcano areas.

**CHAPTER 5 : COMPARISON OF DISPLACEMENT
BETWEEN 2007 – 2008 AND 2009 – 2014**

By analyzing the large amount of InSAR data during the period of 2009-2014 over the Piton de la Fournaise, we observed a widespread displacement pattern on the Eastern Flank affected by an overall downward and eastward motion (see [Chapter 4](#)), similar with that during 2007-2008 (one year rest period right after the March-April 2007 eruption, see [Chapter 3](#)). It leads us to consider if the displacement observed during 2009-2014 is in relation with that observed during 2007-2008. Investigating the correlation of the displacement between these two periods can provide useful insights for understanding the deformation mechanism and possible origins. In this chapter, we compare the displacement behavior of the Central Cone and the Eastern Flank of Piton de la Fournaise volcano between 2007 – 2008 and 2009 – 2014 periods by combining the studies carried out in [Chapter 3](#) and [4](#). To complete the knowledge of displacement of the Central Cone that was mainly affected by transient events, we first describe in detail the five eruptions occurred between 2009 and 2014 in terms of deformation pattern and magnitude.

5.1 Displacement of the Central Cone

5.1.1 Eruptions between 2009 and 2004

Imaging transient deformation of volcano using InSAR allows us to study the impact area and the impact level of volcanic activity and provide useful insights concerning the eruptive cycles of the volcano. In this section, we process SAR images acquired before and after eruptions to generate interferograms showing the ground surface displacements during the transient events.

The **Table 5.1** lists the information of the eruptions that occurred at Piton de la Fournaise between 2009 and 2014. Their eruptive fissures are illustrated in **Figure 5.1**. Due to the absence of coherence inside of the craters, the December 2008 and the January 2010 eruptions were not able to be observed by InSAR data. Five eruptions occurred during the study period recorded by InSAR data (TSX/TDX) are presented in the following subsections. The interferograms are calculated using software DORIS based on single-look SAR images. A Lidar Digital Elevation Model (DEM) over La Réunion Island with 5 m resolution was used for

geocoding and for simulation and subtraction of topographic contribution. The software SNAPHU (Chen & Zebker, 2002) is adopted to unwarp the inteterferograms. 2D components (E-W and U-D) of displacement maps spanning the each eruption period were calculated (based on the equations in Section 2.3.6) using an ascending and a descending interferogram under an assumption that the displacement in the North-South direction is weak. The interferograms and 2D components of displacement maps shown in the following subsections are resampled in 30 m.

Name	Date of Beginning	Date of end	Location
June 2014	2014/06/21	2014/06/22	Summit, South-Southeastern (S-SE) slop of the Central Cone
December 2010	2010/12/09	2010/12/10	N-NW Flank of the Central Cone
October 2010	2010/10/14	2010/10/31	SE base of the Central Cone
January 2010	2010/01/05	2010/01/12	Summit, inside of the Dolomieu crater
December 2009	2009/12/14	2009/12/15	Summit, S slop of the Central Cone
November 2009	2009/11/05	2009/11/06	Summit, E-SE slop of the Central Cone
December 2008	2008/12/14	2009/02/03	Summit, inside of the Dolomieu crater

Table 5.1 Summary of the eruptions that occurred at Piton de la Fournaise between 2009 and 2014 (OVPF observation).

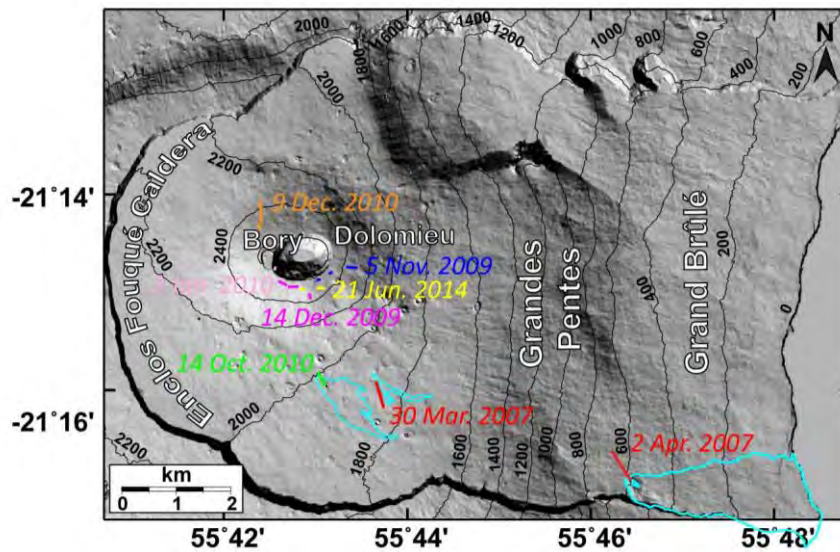


Figure 5.1 Locations of eruptive fissures from 2009 to 2014 indicated by colored lines and labels overlapping on the topography map of Piton de la Fournaise with 200 m elevation contours. The location of the 30 March 2007, 2 April 2007 and 14 October 2010 lava flow contours are indicated by cyan lines. Map is projected in Geographic Lat/Lon referenced to WGS-84 Datum.

5.1.1.1 The November 2009 eruption

The November 2009 eruption is the first eruption that can be observed by the available InSAR data. The lava flowed outside the crater for the first time since 2007. It was a short-lived eruption that began on 5 November and ended the next day after 13 hours. Four eruptive fissures have opened up during the eruption. Three fissures were located on the south-to-southeast near the rim of Dolomieu crater. The fourth was located on the eastern slope of the summit cone between 2310 and 2390 m elevation (**Figure 5.1**). The ascending and descending interferograms over the Central Cone area and the corresponding unwrapped interferograms, spanning the December 2009 eruption, are displayed respectively in **Figure 5.2** and **Figure 5.3**.

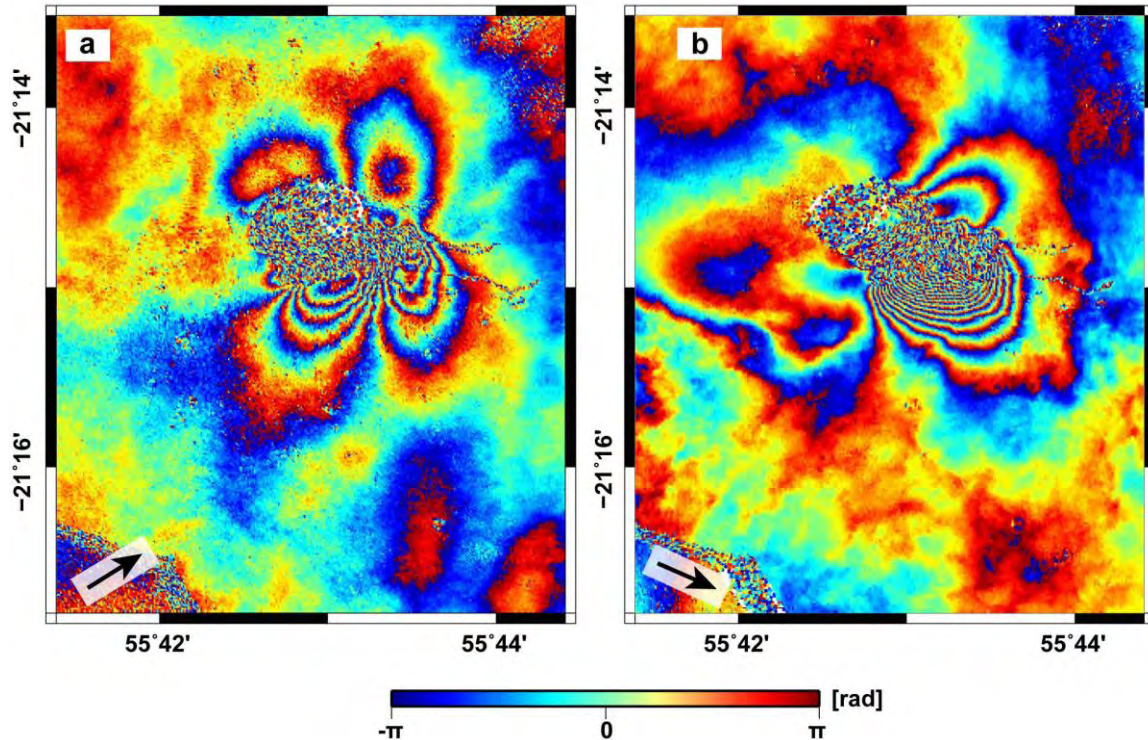


Figure 5.2 (a) Interferogram calculated over the Central Cone area by combining two TSX/TDX ascending images acquired on 24 October and 26 November 2009. (b) Interferogram calculated over the Central Cone area by combining two TSX/TDX descending images acquired on 28 October and 08 November 2009. Each fringe corresponds to movement in LOS direction of the satellite of 1.5 cm. The black arrows indicate the LOS direction of the satellite. Maps are in Geographic Lat/Lon referenced to WGS-84 Datum.

The ascending interferogram shows a four-leaf clover pattern centered approximately on the eastern edge of the Dolomieu crater (**Figure 5.2a**). There are 5 concentric fringes in the southwestern “leaf” and 5 in the southeastern “leaf” as well indicating respectively a decrease and an increase in the ground-satellite distance of about 7.5 cm. 1 and 2 fringes are shown in the northwestern and southeastern “leaves” corresponding respectively to a slight decrease and an slight increase in the ground-satellite distance of about 1.5 cm and 3 cm (**Figure 5.2a** and **Figure 5.3a**). Similarly, in the descending interferogram (**Figure 5.2b** and **Figure 5.3b**), about 4.5 cm and 24 cm of maximum increases in the ground-satellite distance can be observed respectively in the northeastern and southeastern part of the Central Cone.

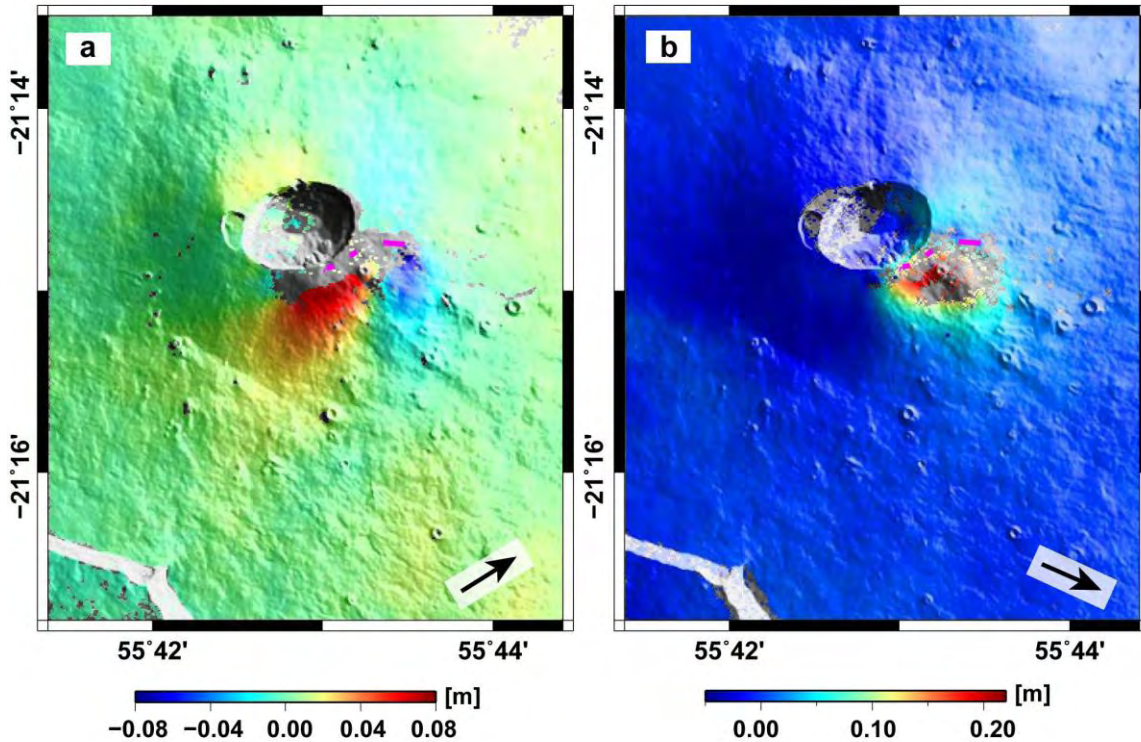


Figure 5.3 Unwrapped interferogram of **Figure 5.2**. (a) Ascending Interferogram: 24 October 2009 - 26 November 2009. (b) Descending Interferogram: 28 October 2009 - 08 November 2009. The eruptive fissures are indicated by magenta lines. Positive signs indicate movement towards the satellite. The black arrows indicate the LOS direction of the satellite. Maps are in Geographic Lat/Lon referenced to WGS-84 Datum.

As shown in **Figure 5.4**, the southeastern part of the Central Cone was affected by both eastward displacement (up to 15 cm, **Figure 5.4a**) and uplift (up to 10 cm, **Figure 5.4b**). The eastern part of the Central Cone was affected by eastward displacement up to 10 cm. The displacement maps show a larger area affected by horizontal displacement including south-southeast-east slope of the Central Cone than that affected by vertical displacement concentrating on the south-southeast part. This eruption did not involve area farther than 2 km to the summit.

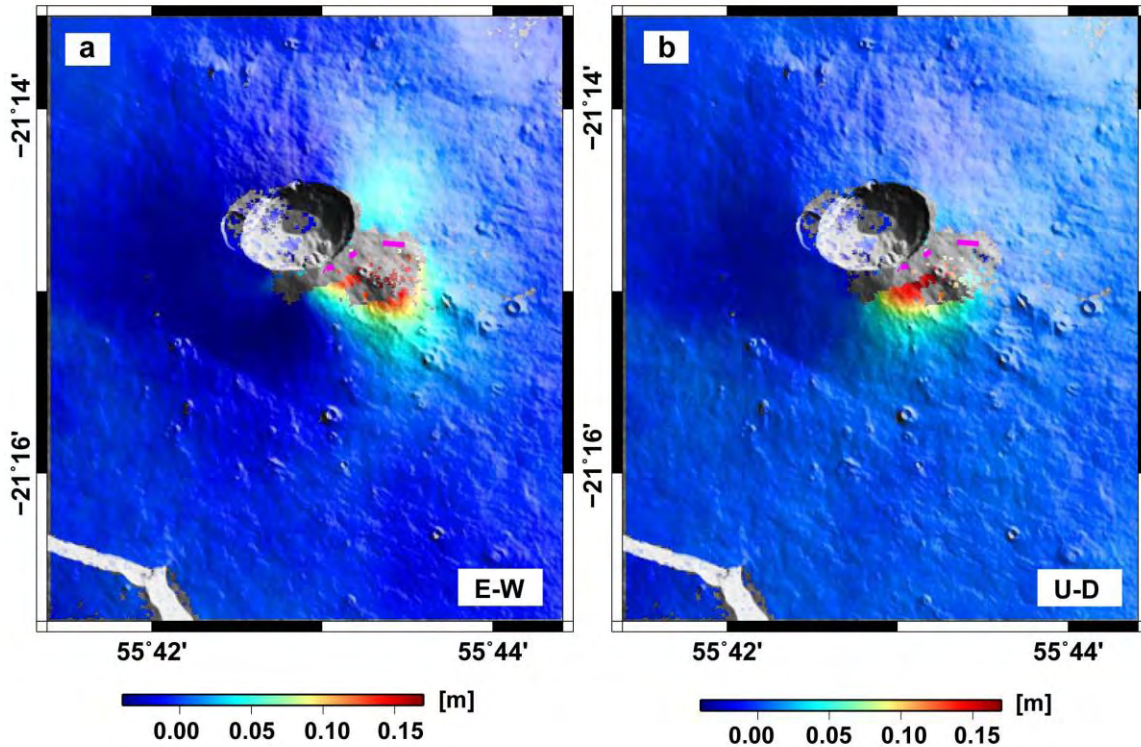


Figure 5.4 (a) Vertical (U-D) and (b) East-West (E-W) displacement maps showing the displacement during the November 2009 eruption. The maps are calculated with a TSX/TDX ascending interferogram spanning from 24 October to 26 November 2009 and a TSX/TDX descending interferogram spanning from 28 October to 8 November 2009 in **Figure 5.3**. Positive signs represent eastward displacement in the E-W map and uplift in the U-D map. The eruptive fissures are indicated by magenta lines. Maps are draped on a shaded DEM and in Geographic Lat/Lon referenced to WGS-84 Datum.

5.1.1.2 The December 2009 eruption

On 14 December 2009, a summit eruption began again at Piton de la Fournaise volcano on the southern edge of Dolomieu crater when the eruptive fissures opened up (**Figure 5.1**).

The ascending and descending interferograms over the Central Cone area and the corresponding unwrapped interferograms, spanning the December 2009 eruption, are displayed respectively in **Figure 5.5** and **Figure 5.6**. Fringes induced by long-wavelength tropospheric artifact are visible in both ascending and descending interferograms. We did not remove the tropospheric artifact before calculating the 2D components of ground displacement maps by

considering its order of magnitude over the zoomed area ($\sim 4 \times 5 \text{ m}^2$) is insignificant to the ground displacement induced by eruptive activity.

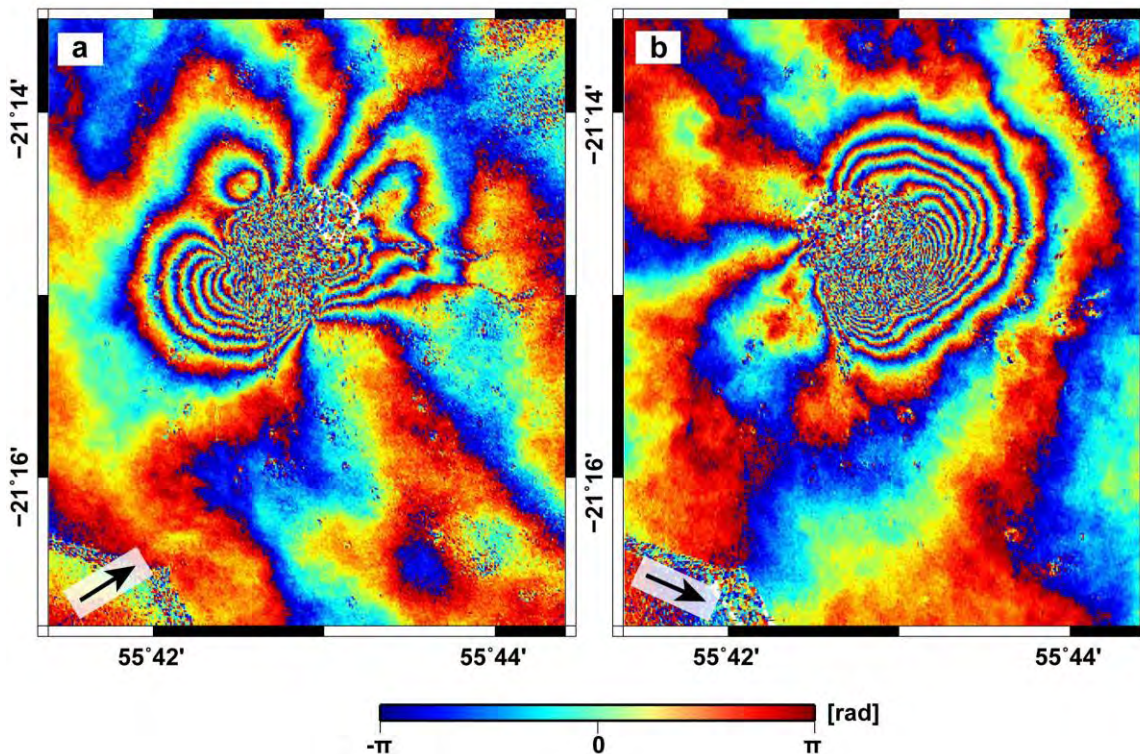


Figure 5.5 (a) Interferogram calculated over the Central Cone area by combining two TSX/TDX ascending images acquired on 26 November 2009 and 31 January 2010. (b) Interferogram calculated over the Central Cone area by combining two TSX/TDX descending images acquired on 11 December 2009 and 13 January 2010. Each fringe corresponds to movement in LOS direction of the satellite of 1.5 cm. The black arrows indicate the LOS direction of the satellite. Maps are projected in Geographic Lat/Lon referenced to WGS-84 Datum.

The ascending interferogram shows a butterfly-shape displacement pattern with an NS axis crossing through the center of Dolomieur crater (**Figure 5.5a** and **Figure 5.6a**). Up to ~ 13.5 cm of decrease in ground-satellite distance is observed to the west of the axis and up to ~ 10.5 cm of increase in ground-satellite distance is observed to the east. A maximum decrease of ~ 20.5 cm in ground-satellite distance can be observed from the ear-shape displacement pattern in the descending interferogram (**Figure 5.5b** and **Figure 5.6b**).

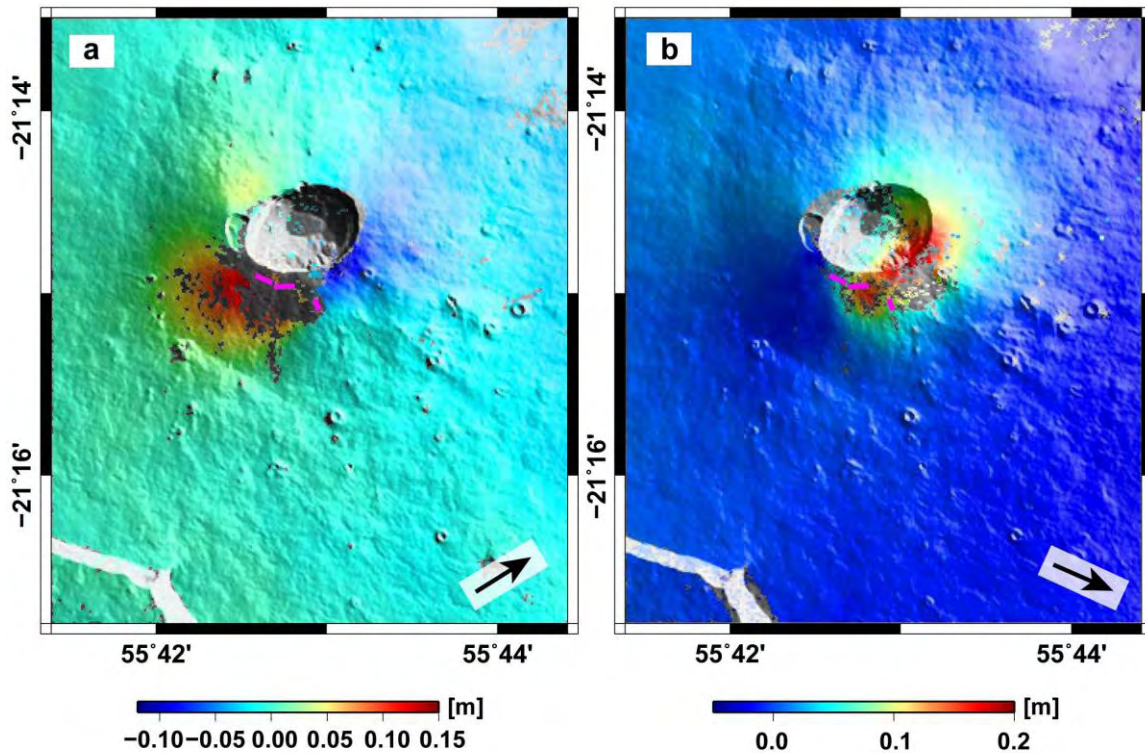


Figure 5.6 Unwrapped interferogram of **Figure 5.5**. (a) Ascending Interferogram: 26 November 2009 - 31 January 2010. (b) Descending Interferogram: 11 December 2009 - 13 January 2010. The eruptive fissures are indicated by magenta lines. Positive signs indicate movement towards the satellite. The black arrows indicate the LOS direction of the satellite. Maps are projected in Geographic Lat/Lon referenced to WGS-84 Datum.

The whole summit area was affected by varying degrees of displacement, shown in **Figure 5.7**. The horizontal displacement is characterized by a NS-trending axis crossing the Dolomieu crater (**Figure 5.7a**). The horizontal displacement is oriented eastward on the eastern side of the axis and westward on the western side. The eastward displacement reached a maximum of 18 cm at the east rim of the Dolomieu crater, and the westward displacement was up to 12 cm. The whole area within ~ 1 km distance to the crater rim showed an uplift reaching a maximum of 11 cm on the southwestern part.

The duration of the December 2009 eruption was only six hours, which was one of the shortest in recent decades at Piton de la Fournaise.

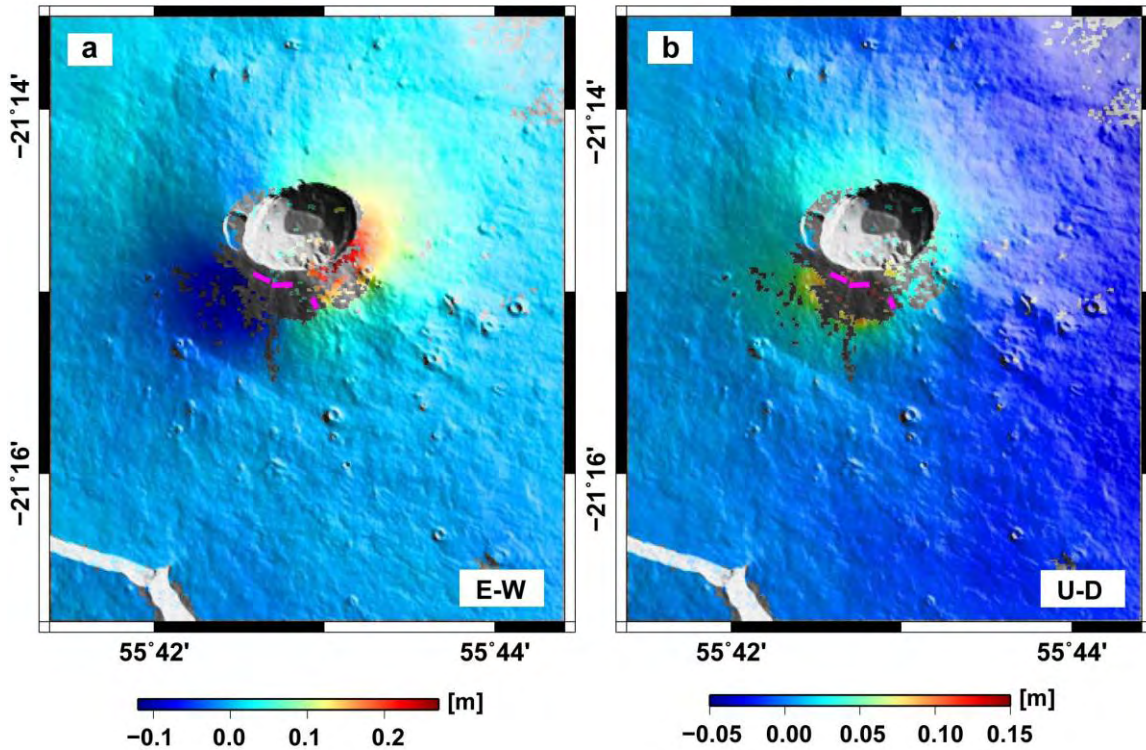


Figure 5.7 (a) Vertical (U-D) and (b) East-West (E-W) displacement maps showing the displacement during the December 2009 eruption. The maps are calculated with a TSX/TDX ascending interferogram spanning from 26 November to 29 December 2009 and a TSX/TDX descending interferogram spanning from 11 December 2009 to 13 January 2010 in **Figure 5.6**. Positive signs represent eastward displacement in the E-W map and uplift in the U-D map. The eruptive fissures are indicated by magenta lines. Maps are draped on a shaded DEM and projected in Geographic Lat/Lon referenced to WGS-84 Datum.

5.1.1.3 The October 2010 eruption

The October 2010 eruption began at 7:10 pm (local time) on the 14 October 2010. The eruption site was located at an elevation of 2000 m, at the southeastern base of the Central Cone, ~ 1.5 km away from the Dolomieu crater (see the eruptive fissure in **Figure 5.1**). An aphyric basalt type lava flow (**Figure 5.1**) was progressively emitted until the eruption ceased on 31 October. This effusive eruption lasted 16.4 days in total (Roult et al., 2012).

The ascending and descending interferograms over the Central Cone area and the corresponding unwrapped interferograms, spanning the October 2010 eruption, are displayed respectively in **Figure 5.8** and **Figure 5.9**.

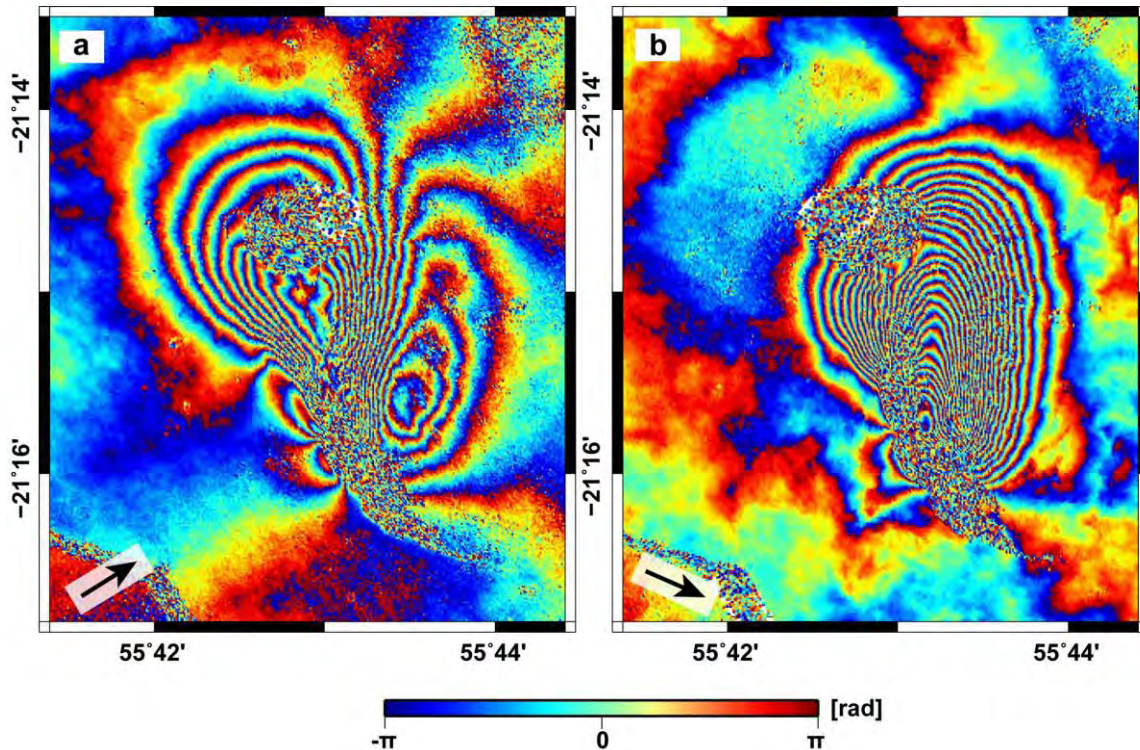


Figure 5.8 (a) Interferogram calculated over the Central Cone area by combining two TSX/TDX ascending images acquired on 19 September 2010 and 22 October 2010. (b) Interferogram calculated over the Central Cone area by combining two TSX/TDX descending images acquired on 1 September 2010 and 26 October 2010. Each fringe corresponds to movement in LOS direction of the satellite of 1.5 cm. The black arrows indicate the LOS direction of the satellite. Maps are projected in Geographic Lat/Lon referenced to WGS-84 Datum.

The ascending interferograms (**Figure 5.8a** and **Figure 5.9a**) show two main displacement patterns. The western pattern elongates along a NNW-SSE axis joining the Dolomieu crater with the site of the October eruption. There are 9 concentric fringes indicating a maximum decrease in the ground-satellite distance of about 13.5 cm (**Figure 5.8a**). The oriental pattern is lying along a NNE-SSW axis. There are about 5 concentric fringes indicating a maximum increase in the ground-satellite distance about 8 cm. This pattern seems to extend over the entire upper part of the Grandes Pentes. Two less important small patterns are visible to the west of the eruption site (**Figure 5.8a** and **Figure 5.9a**). In the north, a 2 fringes pattern corresponds to a slight increase (3 cm) in ground-satellite distance. In the south, a pattern of about 1.5 fringes corresponds to a reduction of the ground-satellite distance of 2.25 cm.

The descending interferograms (Figure 5.8b and Figure 5.9b) show a main interferometric pattern, the maximum of which is located slightly to the east of the eruption site. This pattern is elongated in the NS direction on the southeast and east slopes of the Central Cone. There are between 27 and 28 concentric fringes corresponding to a decrease in the ground-satellite distance of about 42 cm (maximum). This pattern seems to extend to the upper part of the Grandes Pentes as well. To the west of the eruption site, a second much smaller expanded pattern is visible. There are between 2 and 3 fringes corresponding to an elongation of the ground-satellite distance of 4 cm (maximum).

The interferograms are almost completely incoherent in the area of October 2010 eruption site and the area covered by the lava flow of October 2010 (Figure 5.1, Figure 5.8 and Figure 5.9). This is due to radical changes of the ground surface structure induced by the emplacement of the lava flow. The unwrapped interferogram lost coherence in the area to the north of the eruption site as well, which is due to the densification of interferometric fringes resulting in unwrapping errors.

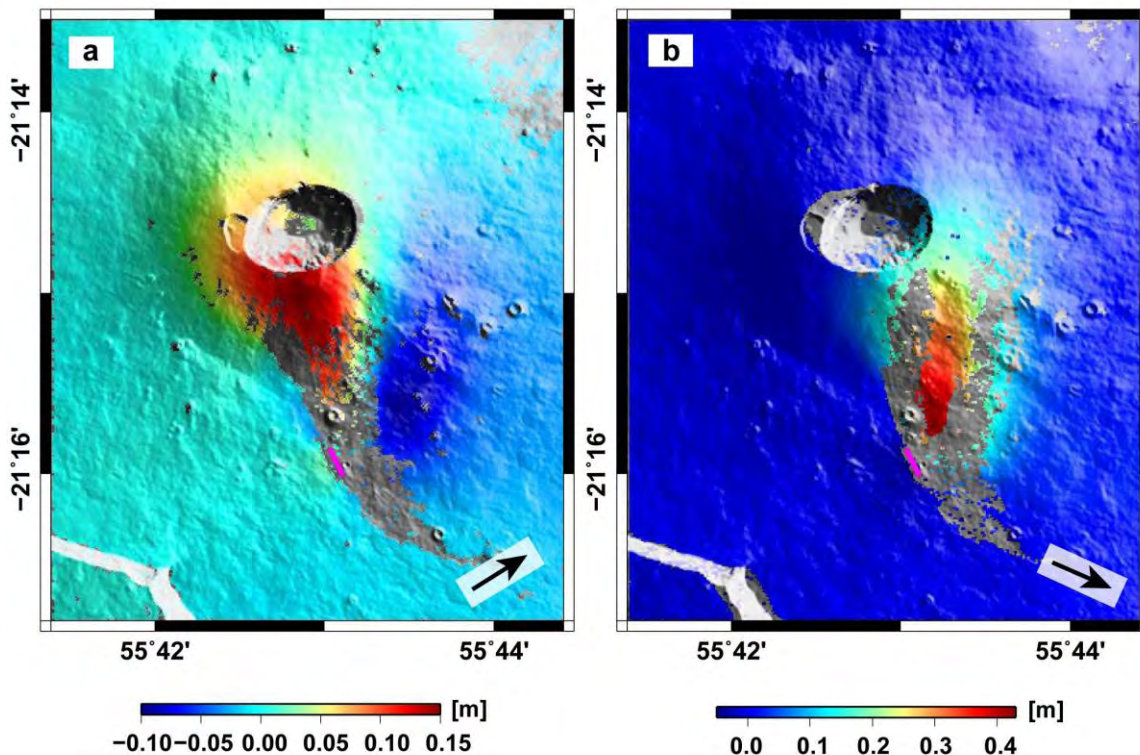


Figure 5.9 Unwrapped interferogram of **Figure 5.8**. (a) Ascending Interferogram: 19 September 2010 - 22 October 2010. (b) Descending Interferogram: 01 September 2010 - 26 October 2010. The eruptive fissures are indicated by magenta lines. Positive signs indicate movement towards the satellite. The black arrows indicate the LOS direction of the satellite. Maps are projected in Geographic Lat/Lon referenced to WGS-84 Datum.

The 2D component of displacement maps are shown in **Figure 5.10**. The E-W displacement shows an asymmetric pattern that separated by a NS-trending axis joining the eruption site and the Dolomieu crater (**Figure 5.10a**). To the east of the axis, the south-southeast-east slope of the Central Cone was affected by eastward displacement reaching to a maximum of 30 cm to the east of the eruption site. The eastward displacement had even extended to the upper Grandes Pentes where the average amplitude was 3 to 5 cm. To the west of the axis, the western half of the Central Cone moved to the west with a maximum displacement of 7 cm. Furthermore, a small zone near the west of the eruption site was affected by westward displacement as well with a maximum displacement of 6 cm. The vertical displacement map (**Figure 5.10b**) displays a large uplift area extending from the eruption site to the entire summit zone. The maximum uplift reached up to ~ 20 cm between the eruption site and the south rim of the Dolomieu crater. A small zone to the northwest of the eruption site displayed a slight subsidence up to 4 cm. The overall displacement during the October 2010 eruption is compatible with a dyke injection oriented ~ NS dipping eastward which is rooted under the Dolomieu crater and reach the ground surface during the October 2010 event.

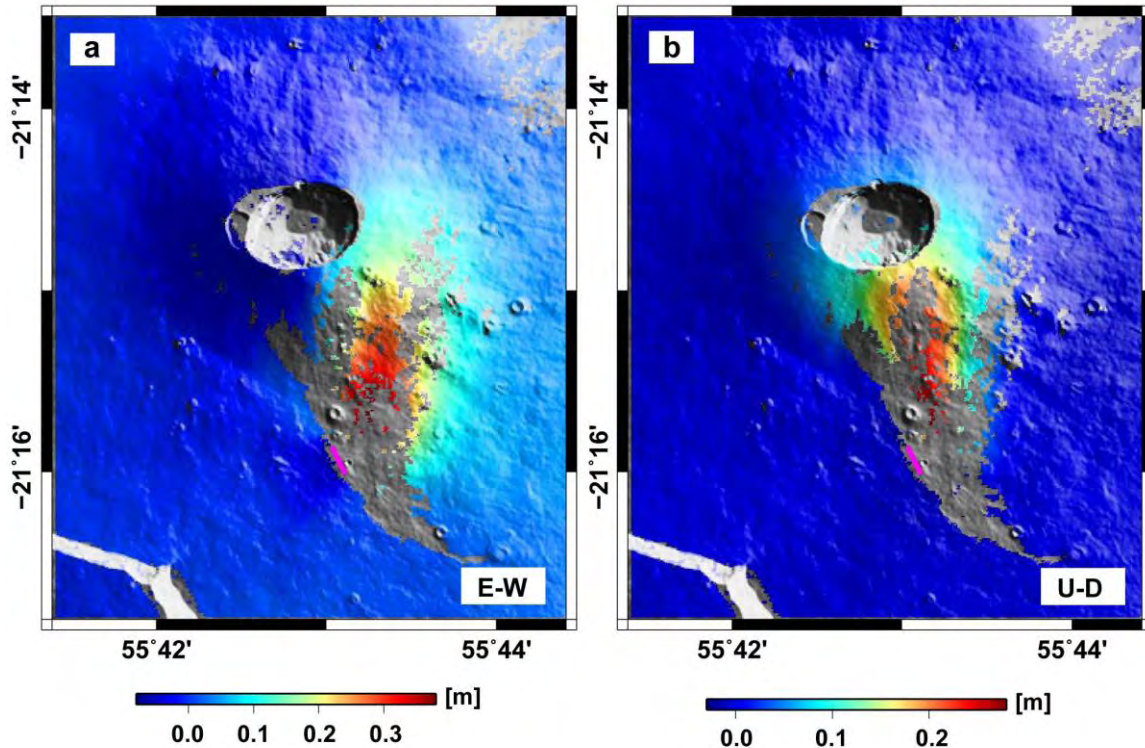


Figure 5.10 (a) Vertical (U-D) and (b) East-West (E-W) displacement maps showing the displacement during the October 2010 eruption. The maps are calculated with a TSX/TDX ascending interferogram spanning from 19 September to 22 October 2010 and a TSX/TDX descending interferogram spanning from 1 September to 26 October 2010 in **Figure 5.9**. Positive signs represent eastward displacement in the E-W map and uplift in the U-D map. The eruptive fissures are indicated by magenta lines. The grey area indicates the emitted lava flow. Maps are draped on a shaded DEM and projected in Geographic Lat/Lon referenced to WGS-84 Datum.

5.1.1.4 The December 2010 eruption

Again, on 9 December 2010, the volcano turned to be active after about one month rest. It lasted 15 hours and ceased on 10 December. Two eruptive fissures oriented NS opened up on the northwestern slope of the Central Cone during the eruption (**Figure 5.1**). The end of the December 2010 eruption began a new period of rest for about 4 years until June 2014.

The ascending and descending interferograms the Central Cone area and the corresponding unwrapped interferograms, spanning the December 2010 eruption, are displayed respectively in **Figure 5.11** and **Figure 5.12**.

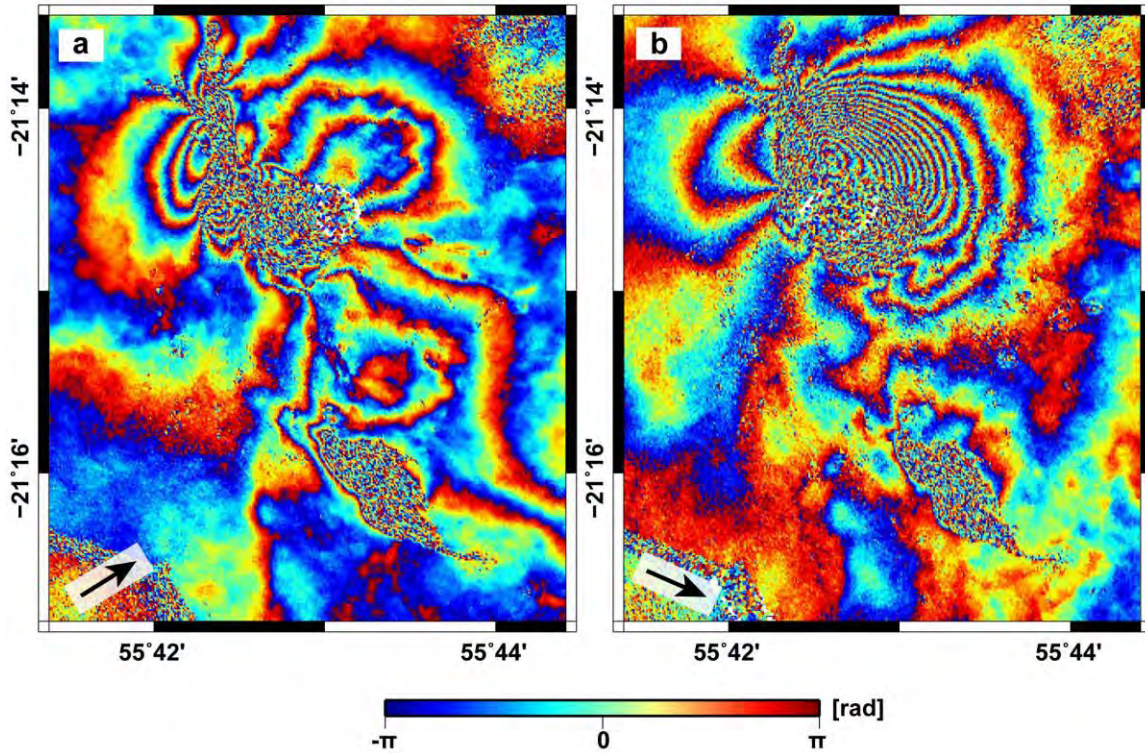


Figure 5.11 (a) Interferogram calculated over the Central Cone area by combining two TSX/TDX ascending images acquired on 22 October 2010 and 9 October 2011. (b) Interferogram calculated over the Central Cone area by combining two TSX/TDX descending images acquired on 6 November 2010 and 24 October 2011. Each fringe corresponds to movement in LOS direction of the satellite of 1.5 cm. The black arrows indicate the LOS direction of the satellite. Maps are projected in Geographic Lat/Lon referenced to WGS-84 Datum.

The ascending interferogram (**Figure 5.11a** and **Figure 5.12a**) shows two main displacement patterns located to either side of the eruption site, lying along two parallel NNE-SSW axis. A maximum of ~ 9 cm (about 6 fringes) decrease in ground-satellite distance presents in the western pattern and a maximum of ~ 6 cm (about 4 fringes) increase in ground-satellite distance is observed in the eastern pattern (**Figure 5.11a** and **Figure 5.12a**). In the descending interferogram (**Figure 5.11b** and **Figure 5.12b**), two distinct patterns distribute to either side of the eruptive site. To the east, there are about 17 fringes corresponding to a maximum decrease in ground-satellite distance of ~ 25.5 cm. To the west, on the contrary, only 3 fringes indicating a slight increase in ground-satellite distance of ~ 4.5 cm (maximum).

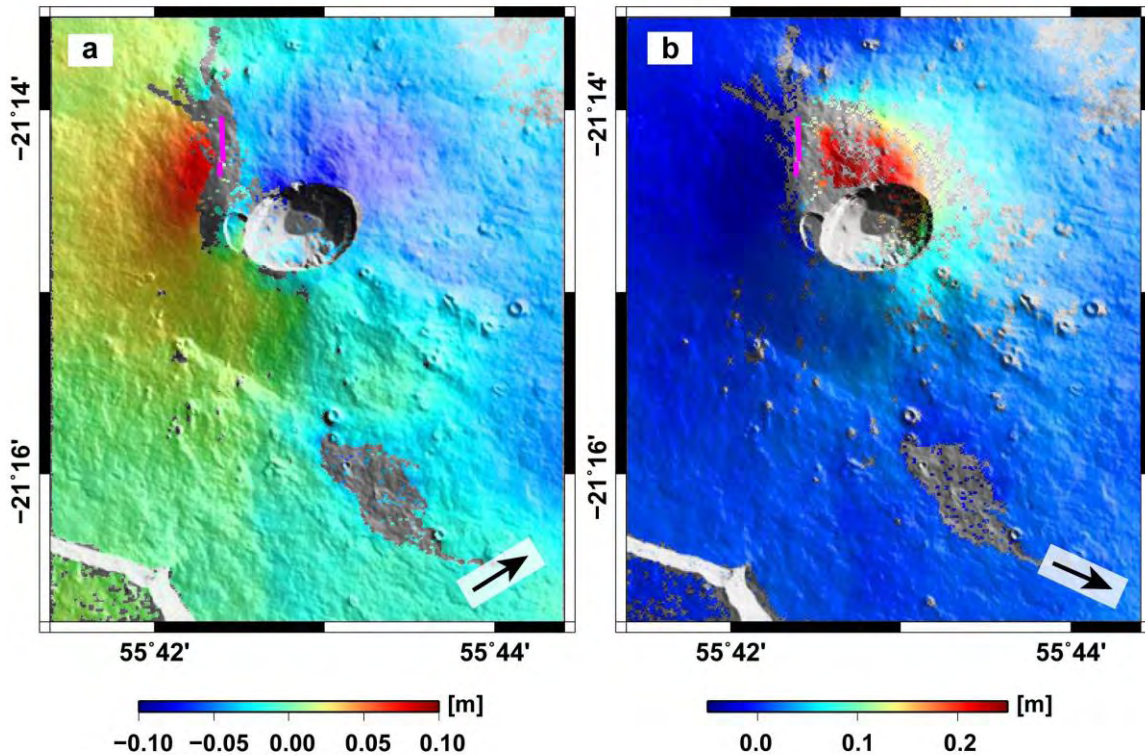


Figure 5.12 Unwrapped interferogram of **Figure 5.11**. (a) Ascending Interferogram: 22 October 2010 - 9 October 2011. (b) Descending Interferogram: 6 November 2010 - 24 October 2011. The eruptive fissures are indicated by magenta lines. Positive signs indicate movement towards the satellite. The black arrows indicate the LOS direction of the satellite. Maps are projected in Geographic Lat/Lon referenced to WGS-84 Datum.

The E-W displacement map (**Figure 5.13a**) shows that to the east of the eruptive site, the north-northeast Central Cone was affected by eastward displacement with a maximum of ~ 27 cm, and that to west, westward displacement up to ~ 12 cm was affecting the northwest-west Central Cone. The northern slope of the Central Cone was affected by an uplift reach ~ 10 cm (**Figure 5.13b**). The maps present not only the displacement induced by the December 2010 eruption, but also the eastward and downward displacement affecting the upper part of the Eastern Flank due to the long-time span of the interferograms.

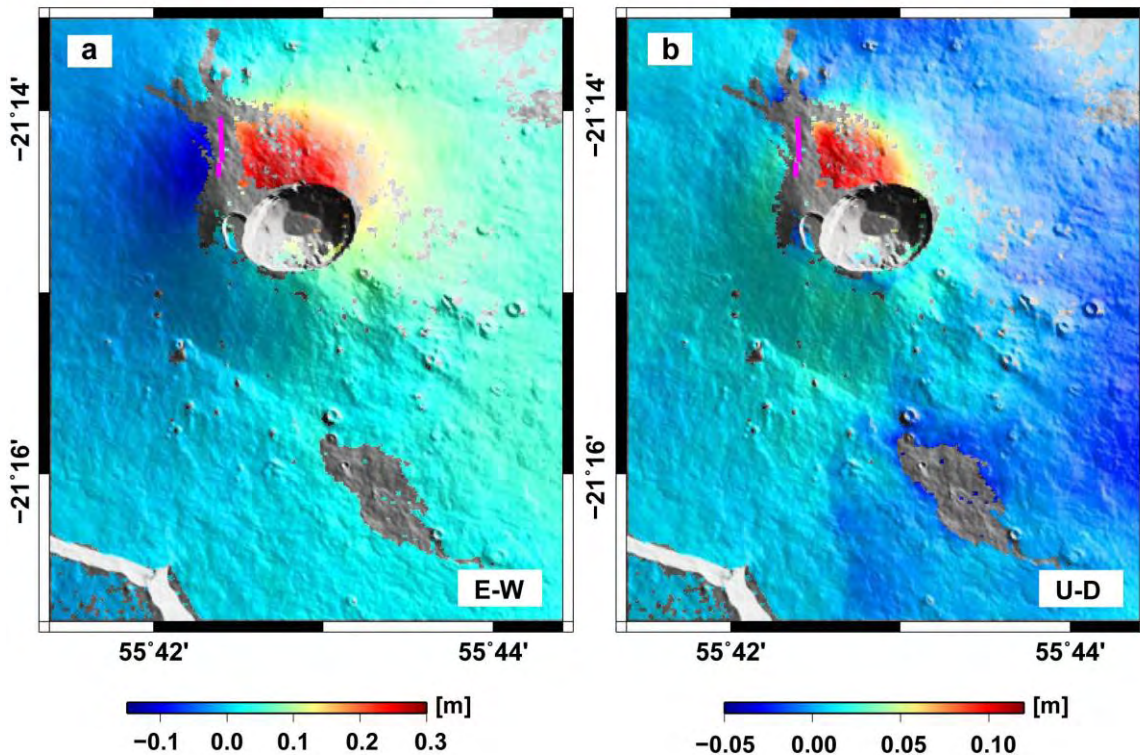


Figure 5.13 (a) Vertical (U-D) and (b) East-West (E-W) displacement maps showing the displacement during the December 2010 eruption. The maps are calculated with a TSX/TDX ascending interferogram spanning from 22 October 2010 to 9 October 2011 and a TSX/TDX descending interferogram spanning from 6 November 2010 to 24 October 2011 in **Figure 5.12**. Positive signs represent eastward displacement in the E-W map and uplift in the U-D map. The eruptive fissures are indicated by magenta lines. Maps are draped on a shaded DEM and projected in Geographic Lat/Lon referenced to WGS-84 Datum.

5.1.1.5 The June 2014 eruption

Piton de la Fournaise experienced an eruption on 21 June 2014 after 4 years silence. It was a short eruption that ended on 22 June after 30 hours of activity.

The ascending and descending interferograms over the Central Cone area and the corresponding unwrapped interferograms, spanning the June 2014 eruption, are displayed respectively in **Figure 5.14** and **Figure 5.15**.

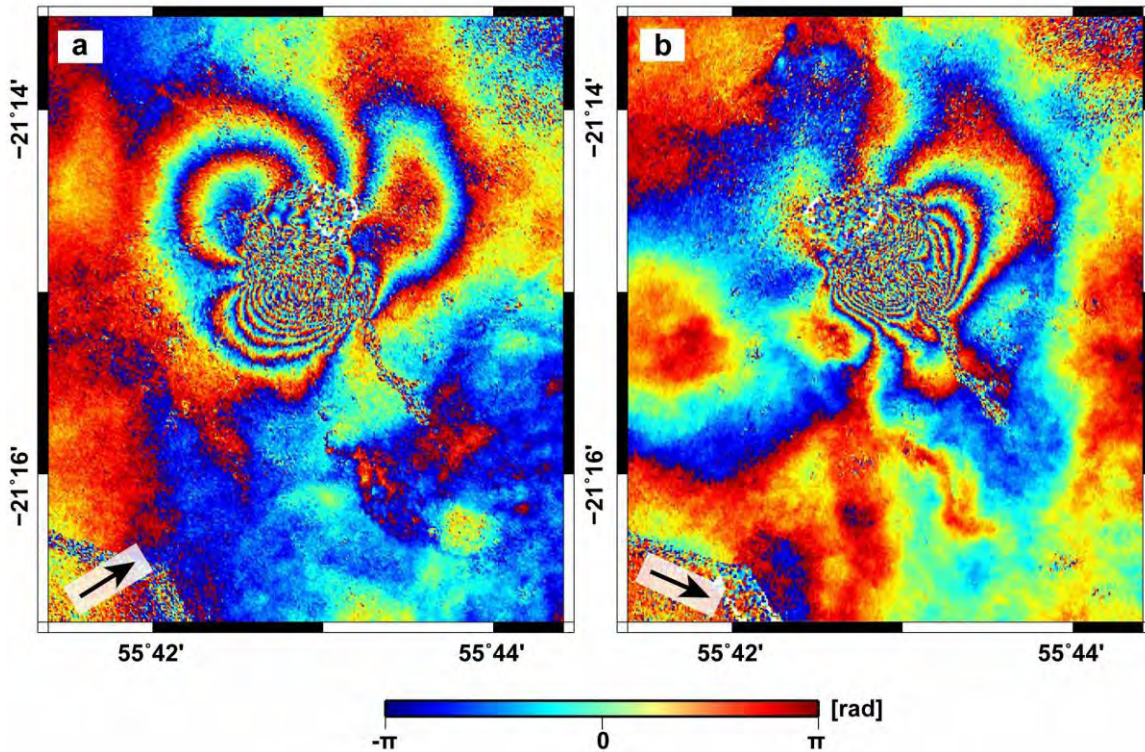


Figure 5.14 (a) Interferogram calculated over the Central Cone area by combining two TSX/TDX ascending images acquired on 14 June 2014 and 6 July 2014. (b) Interferogram calculated over the Central Cone area by combining two TSX/TDX descending images acquired on 28 February 2014 and 6 October 2014. Each fringe corresponds to movement in LOS direction of the satellite of 1.5 cm. The black arrows indicate the LOS direction of the satellite. Maps are projected in Geographic Lat/Lon referenced to WGS-84 Datum.

The eruption site is located on the southern slope of the summit. The ascending interferogram (**Figure 5.14a** and **Figure 5.15a**) shows three interferometric patterns respectively located on the northwestern, southern and southeastern slope of the summit. Up to ~ 10 cm of movement towards the satellite is observed from the coherent pixels on the southern slope of the summit. A slight movement of ~ 3 cm (maximum) towards the satellite is observed on the northwestern slope. About 4.5 cm (maximum) of increase in ground-satellite distance shows on the southeastern slope of the summit (**Figure 5.15a**). A maximum of ~ 10.5 cm of decrease in ground-satellite distance is observed from the displacement pattern that concentrates on the southeastern slope of the summit in the descending interferogram (**Figure 5.14b** and **Figure 5.15b**).

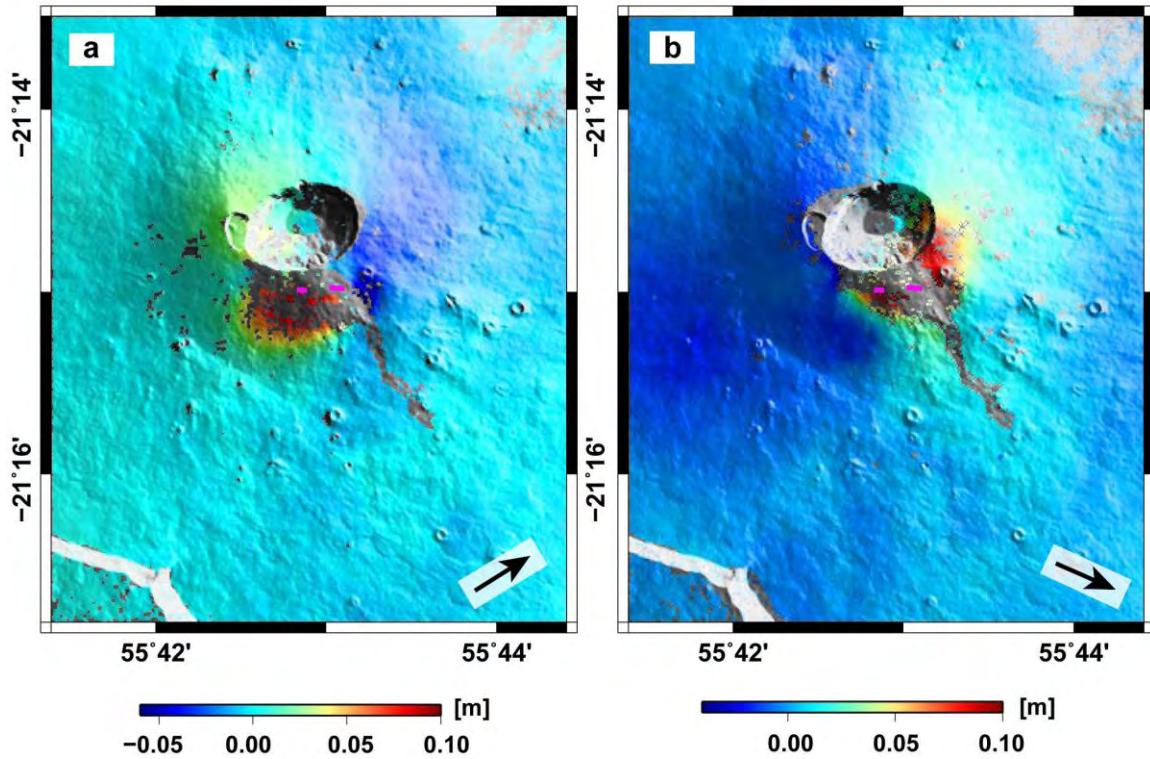


Figure 5.15 Unwrapped interferogram of **Figure 5.14**. (a) Ascending Interferogram: 14 June 2014 - 6 July 2014. (b) Descending Interferogram: 28 February 2014 - 6 October 2014. The eruptive fissures are indicated by magenta lines. Positive signs indicate movement towards the satellite. The black arrows indicate the LOS direction of the satellite. Maps are projected in Geographic Lat/Lon referenced to WGS-84 Datum.

The displacement maps (**Figure 5.16**) show that the western slope of the summit moved to the west with a maximum of ~ 10 cm. The southern slope simultaneously experienced an uplift up to ~ 15 cm. The southeastern-eastern slope of the summit experienced an eastward motion reaching ~ 13 cm maximum.

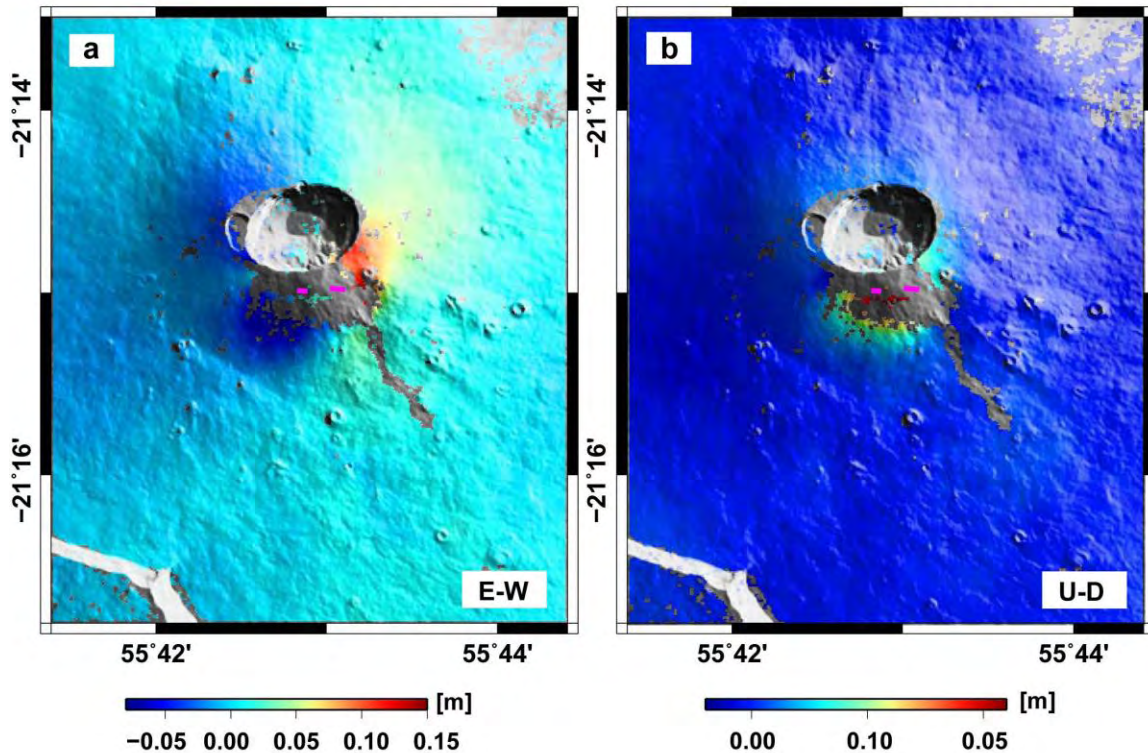


Figure 5.16 (a) Vertical (U-D) and (b) East-West (E-W) displacement maps showing the displacement during the June 2014 eruption. The maps are calculated with a TSX/TDX ascending interferogram spanning from 14 June to 6 July 2011 and a TSX/TDX descending interferogram spanning from 28 February to 6 October 2014 in **Figure 5.15**. Positive signs represent eastward displacement in the E-W map and uplift in the U-D map. The eruptive fissures are indicated by magenta lines. Maps are draped on a shaded DEM and projected in Geographic Lat/Lon referenced to WGS-84 Datum.

5.1.1.6 Discussion

Peltier et al. (2009a) defined five eruptive cycles with a sequence of summit/near-summit, proximal eruptions, and distal, low-altitude eruptions between 2000 and 2007 at Piton de la Fournaise. The March-April 2007 eruption ended the last cycle with eruptive fissures opening up at low altitude of the Eastern Flank. Although different studies (e.g. Peltier et al., 2008, 2009b; Froger et al., 2015; Fontaine et al., 2014; Di Muro et al., 2014) suggest deformation sources at different depths below the Central Cone, all together, they are consistent with the injection of deep magma into the shallow plumbing system. After the major eruption of March-April 2007, the volcano experienced a sequence of short lived, small volume

eruptions and intrusions (Peltier et al., 2010b; Rault et al., 2012), which suggests a change in cyclicity with respect to the 2000 – 2007 period (Peltier et al., 2016a). As imaged with InSAR data (Section 5.1.1), these eruptions occurred mostly inside or around the summit craters, within the Central Cone area (with an exception of the October 2010 eruption which extended to the upper part of the Eastern Flank). The short spatial scale of the displacement patterns of these eruptions produced by shallow dyke intrusions supports the hypothesis that these dykes were started from the shallower part of the plumbing system of the volcano beneath the Central Cone, as discussed by Peltier et al. (2010) and Di Muro et al. (2015).

5.1.2 Long-term displacement

5.1.2.1 *Spatial pattern*

In order to better compare the spatial pattern of displacement during different periods, the cumulative 2D components of displacement maps are displayed in the same color scale (Figure 5.17 and Figure 5.18).

As the cumulative displacement maps during 2009 – 2014 period (Figure 5.17b and Figure 5.18b) integrate all the transient signals induced by eruptions, they do not allow analysis of the spatial pattern of the long-term displacement at the Central Cone. By comparing the two maps spanning the 2007 – 2008 (Figure 5.17a and Figure 5.18a) and the 2011 – 2014 (Figure 5.17c and Figure 5.18c) volcanic rest periods, we find a strong similarity in terms of the spatial pattern of the displacement in the Central Cone area. Both of them exhibit a centripetal subsidence pattern with similar extent of affecting area, suggesting that the summit long-term deflations during these two periods are linked to very close sources or the same source that located in a shallow level according to the short spatial scale of the displacement.

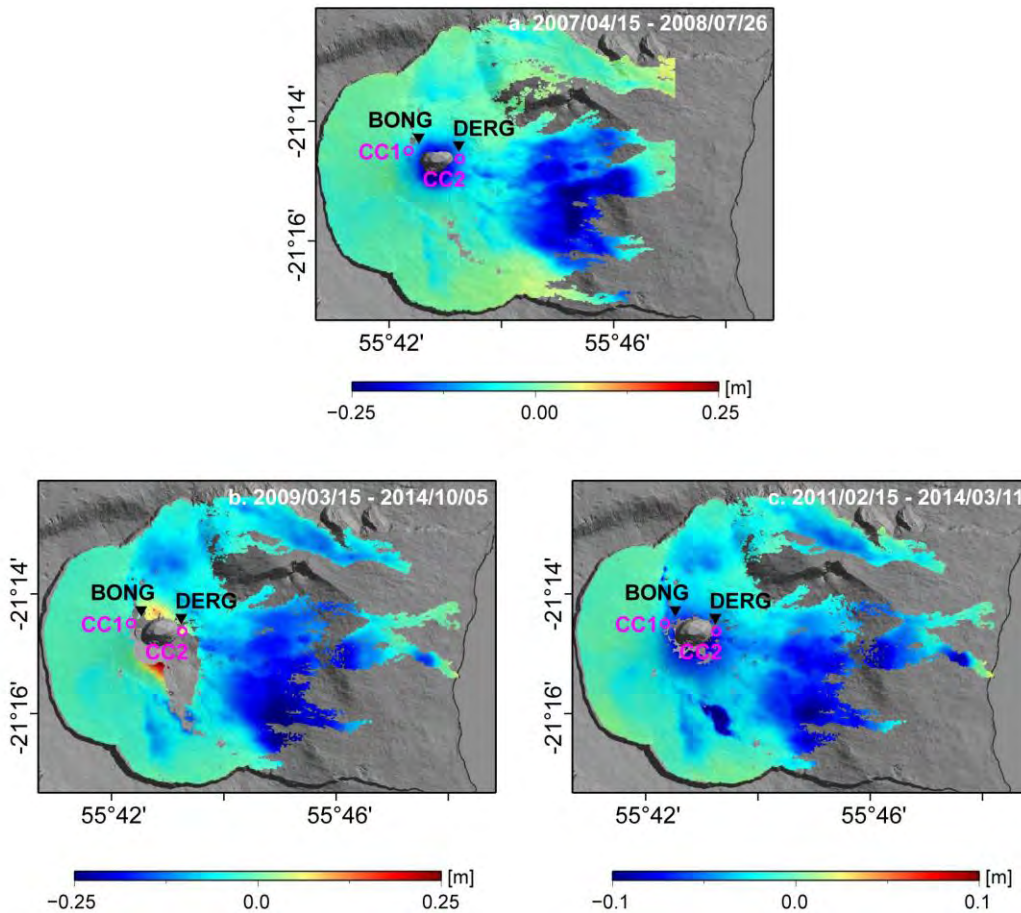


Figure 5.17 Comparison of cumulative U-D displacement of the Central Cone area during (a) 2007-2008 (rest period), (b) 2009-2014, and (c) 2011-2014 (rest period) periods. Positive values represent upward displacement, while negative values represent downward displacement. Location of four GNSS stations (BONG, DERG) on the Central Cone are marked with black triangles. Maps are draped on a shaded DEM and projected in Geographic Lat/Lon referenced to WGS-84 Datum.

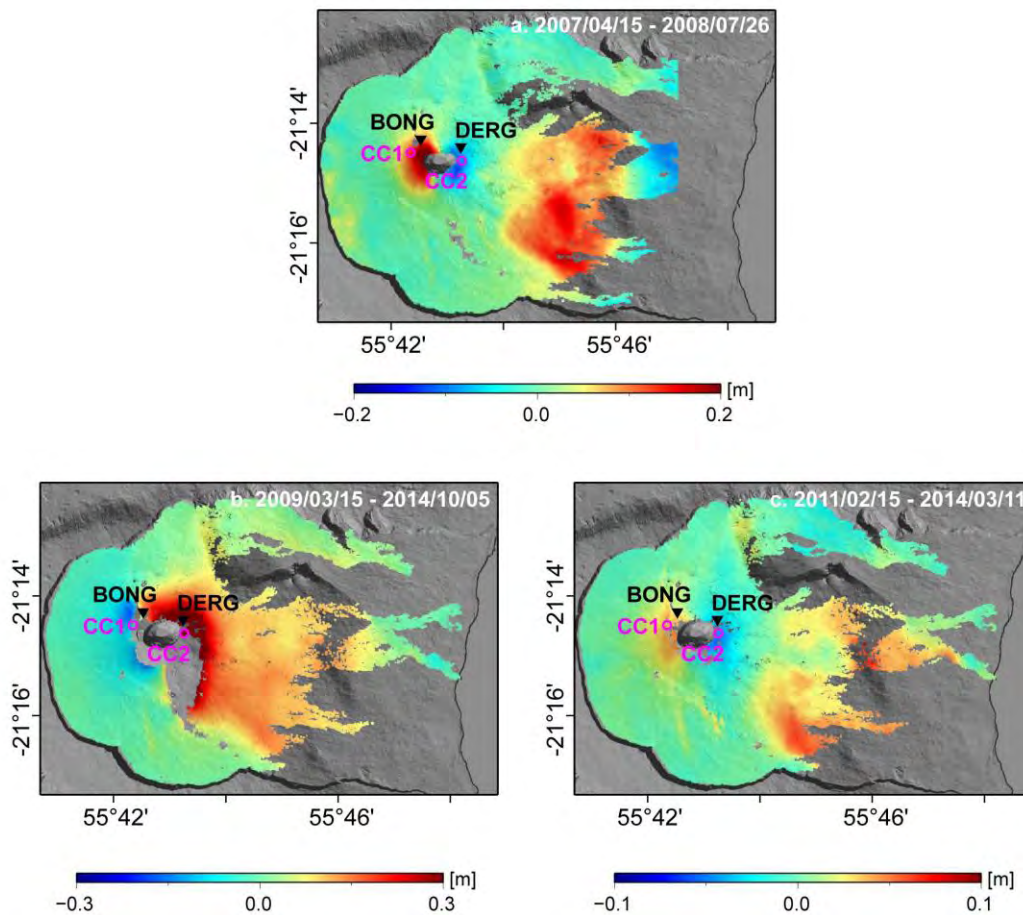


Figure 5.18 Comparison of cumulative E-W displacement of the Central Cone area during (a) 2007-2008 (rest period), (b) 2009-2014, and (c) 2011-2014 (rest period) periods. Positive values represent upward displacement, while negative values represent downward displacement. Location of four GNSS stations (BONG, DERG) on the Central Cone are marked with black triangles. Maps are draped on a shaded DEM and projected in Geographic Lat/Lon referenced to WGS-84 Datum.

5.1.2.2 Temporal behavior

In order to make the two periods comparable, we choose to plot the displacement time series at two points, CC1 and CC2 (see **Figure 5.17** and **Figure 5.18** for location; consistent with the study in **Chapter 4**), located on the western and eastern flank of the Central Cone respectively (**Figure 5.19** and **Figure 5.20**). The InSAR time series clearly show that the Central Cone is characterized by transient displacements during eruptive periods (late 2009 and late 2010 to early 2011) and long-term deflations during post-eruptive or rest periods, which is one

of the typical volcano deformation regimes. This observation coincides the GNSS measurements at Central Cone stations, BONG and DERG, in the study of Peltier et al. (2015a). In 2007-2008, the rate of the summit deflation was estimated by InSAR at ~ 0.45 m/yr (U-D) and ~ 0.48 m/yr (E-W) at point CC1 during the first month right after the March-April 2007 events and it then decreased exponentially to ~ 0.05 m/yr (U-D) and ~ 0.04 m/yr (E-W) in mid-2008 (Figure 5.19). This summit deflation is linked to the renewal of the edifice contraction/relaxation following the April 2007 Dolomieu crater collapse (Peltier et al., 2010b; Staudacher & Peltier, 2015; Froger et al., 2015). Different from the exponential behavior during 2007-2008, the summit deflations which occurred in 2009, 2010, and 2011 – 2014 display quite stable and linear deformation trends (Figure 5.19 and Figure 5.20). The rate of the displacement is nearly constant at ~ 0.015 m/yr (U-D) and ~ 0.025 m/yr (E-W) on the east rim of Dolomieu crater during the long phase of quiescence of 41 months that started after the February 2011 intrusion until June 2014 before a reawakening in June 2014 (Figure 5.20; Peltier et al., 2015a). This phenomenon suggests the deformation of the Central Cone may have changed the regime during the end of the post-eruptive period of the March-April 2007 eruption.

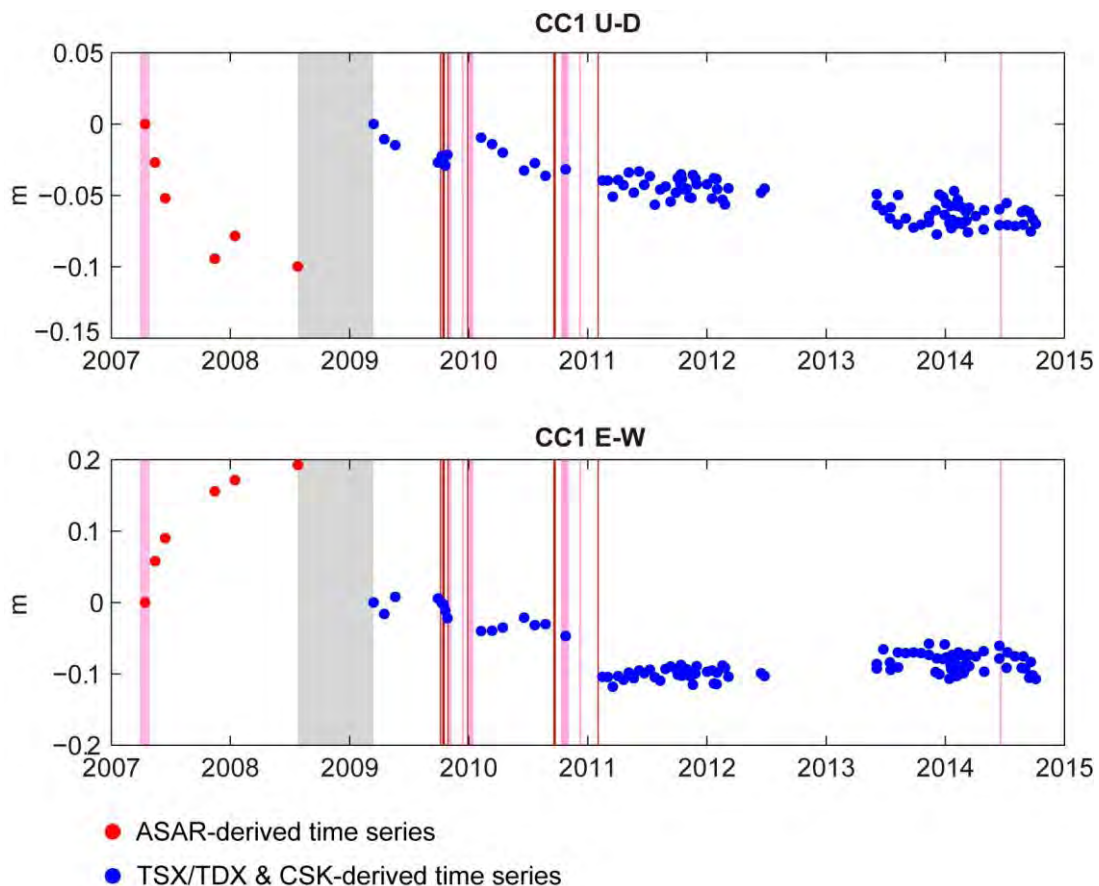


Figure 5.19 InSAR time series at point CC1 during 2007 – 2008 (red cycles) and 2009 – 2014 (blue cycles) periods. It is worth noting that the two time series are not connected and each of them is referenced to its first date. The grey area indicates the period during which no data is acquired. Pink areas and dark red vertical lines represent times of eruptions and intrusions, respectively, which occurred in the study period.

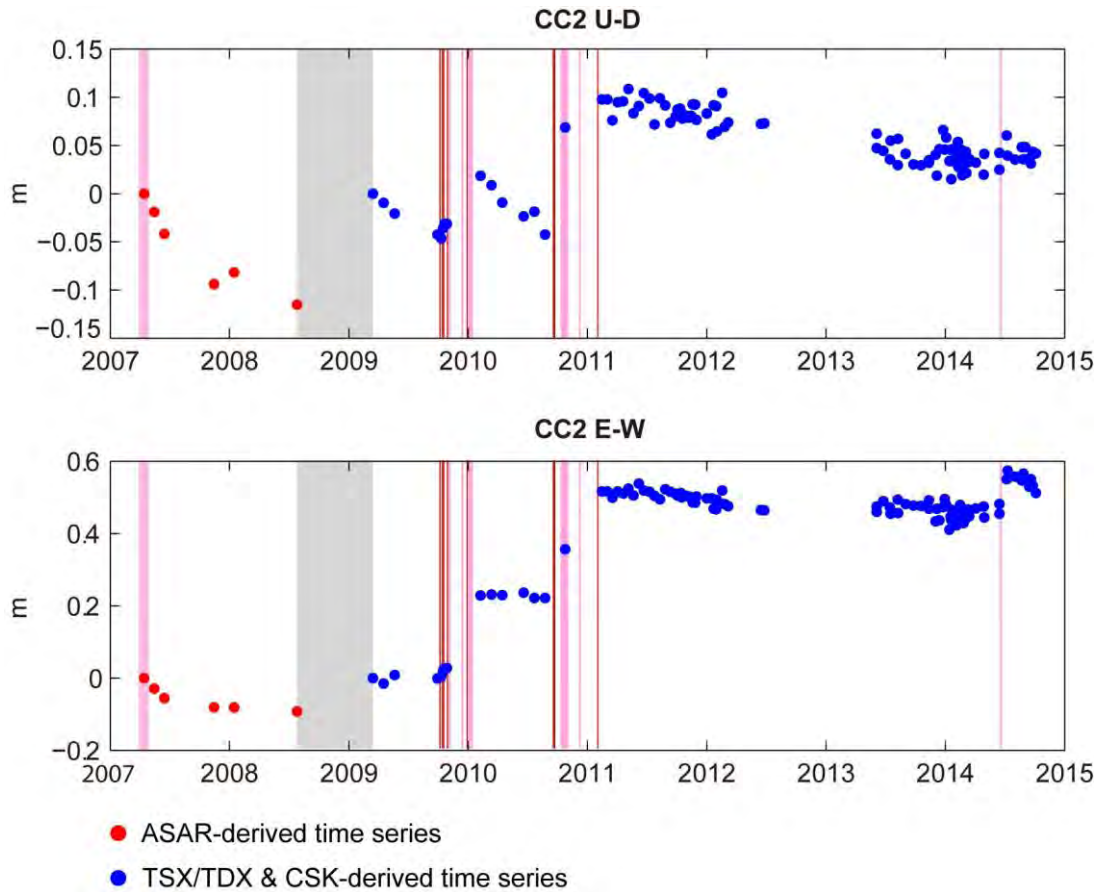


Figure 5.20 InSAR time series at point CC2 during 2007 – 2008 (red cycles) and 2009 – 2014 (blue cycles) periods. It is worth noting that the two time series are not connected and each of them is referenced to its first date. The grey area indicates the period during which no data is acquired. Pink areas and dark red vertical lines represent times of eruptions and intrusions, respectively, which occurred in the study period.

5.2 Displacement of the Eastern Flank

5.2.1 Spatial pattern

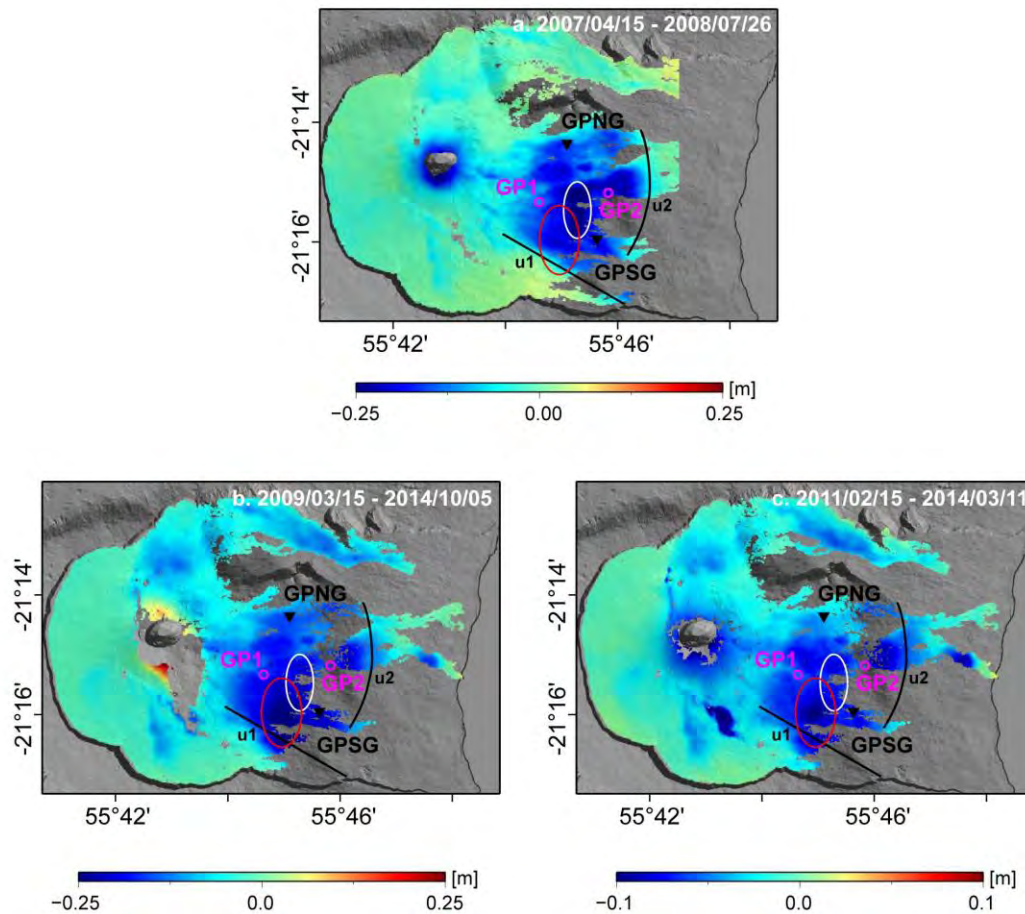


Figure 5.21 Comparison of cumulative U-D displacement maps of the Eastern Flank during (a) 2007-2008 (rest period), (b) 2009-2014, and (c) 2011-2014 (rest period) periods. Positive values represent upward displacement, while negative values represent downward displacement. Location of four GNSS stations (GPNG and GPSG) on the Eastern Flank are marked with black triangles. u1 and u2 indicate respectively the southern and eastern limits of the large scale displacement pattern on the Eastern Flank during 2007-2008 period. The white and red ellipses outline the areas affected by the most significant downward displacement during 2007-2008 and 2009-2014 periods, respectively. Maps are draped on a shaded DEM and in Geographic Lat/Lon referenced to WGS-84 Datum.

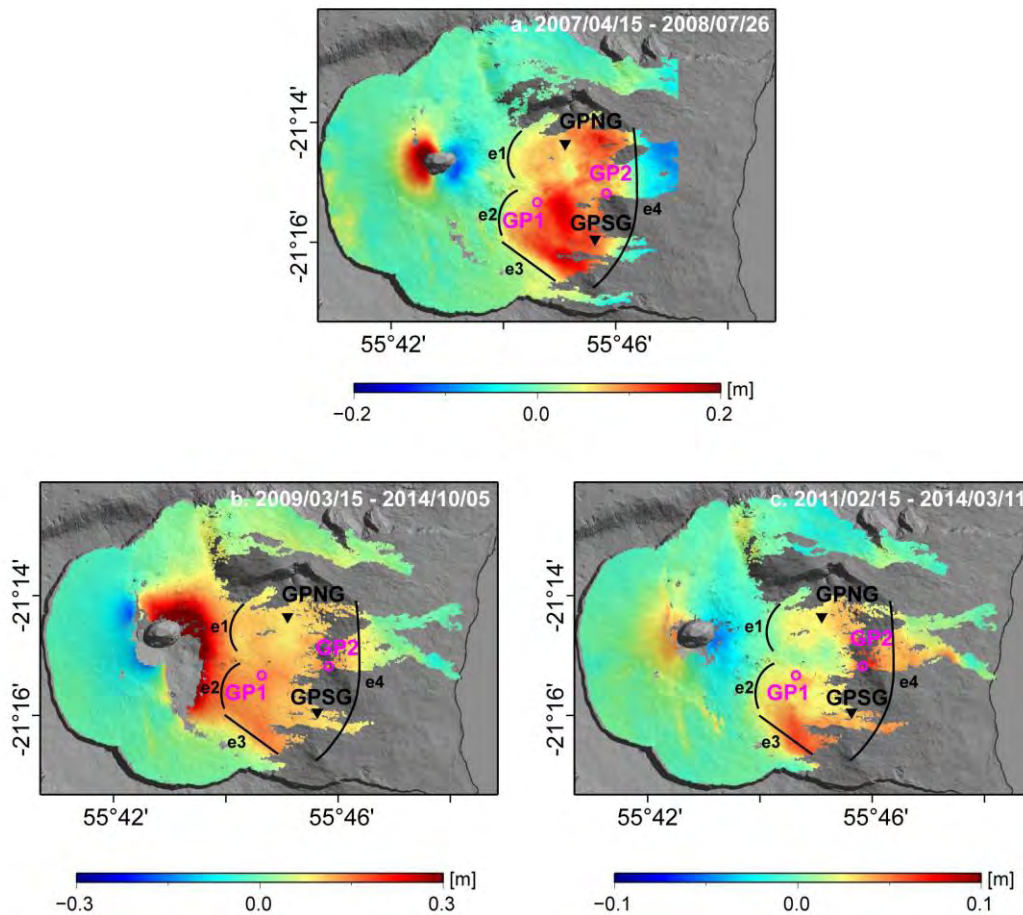


Figure 5.22 Comparison of cumulative E-W displacement maps of the Eastern Flank during (a) 2007-2008 (rest period), (b) 2009-2014, and (c) 2011-2014 (rest period) periods. Positive values represent eastward displacement, while negative values represent westward displacement. Location of four GNSS stations (BONG, DERG, GPNG and GPSG) on the Central Cone and on the Eastern Flank are marked with black triangles. e1-e2, e3, and e4 indicate respectively the western, southern and eastern limits of the large scale pattern on the Eastern Flank during 2007-2008 period. Maps are draped on a shaded DEM and in Geographic Lat/Lon referenced to WGS-84 Datum.

The U-D displacement affecting areas on the Eastern Flank in 2007-2008 and 2009-2014 display a very similar geometrical shape, except that the limit of the latter extends outwards (the eastern limit extends to the east and the southern limit extends to the southwest) (**Figure 5.21**, u1-u2). Within the deformation sector, location of the area affected by the most significant subsidence (white ellipse in **Figure 5.21**) in 2007-2008 differs from that in 2009-2014 (red ellipse in **Figure 5.21**), although the distributions of U-D displacement magnitude are in good agreement in most areas during these two periods.

The E-W displacement contributed by the October 2010 eruption affected a large area that even extended to the Upper Eastern Flank and interfered with the long-term eastward displacement of the Eastern Flank, making it difficult to distinguish the boundary between each other (**Figure 5.22b**). However western limits of the large scale eastward moving sector can be easily recognized in both 2007-2008 and 2011-2014 rest periods, and they are extremely identical (**Figure 5.22a** and **c**, e1-e2). Similarly to the U-D displacement pattern, the eastern limit of the E-W displacement moves to the east and the southern limit moves to the southwest, revealing that the displacement affecting sector spreads from 2007-2008 to 2009-2014 (**Figure 5.22**, e3-e4). Contrast to the U-D displacement, the distributions of E-W displacement magnitude during these three periods coincide with each other. The relatively large displacement zones during the three periods share the same or at least overlapped locations (**Figure 5.22**).

5.2.2 Temporal behavior

The ASAR time series (2007-2008) and TSX/TDX & CSK merged time series (2009-2014) are two independent datasets that span different time periods without overlap. Since the Eastern Flank is affected by continuous long-term displacement during the whole period, it is possible to approximately link the two time series by assuming a temporal law. Here we shifted and adjusted them using an exponential function (**Equation 5.1**) at points located on stations GPNG and GPSG, and points GP1 and GP2 that are selected in the study of [Chapter 4](#) (see **Figure 5.21** and **Figure 5.22** for location). The best fits were obtained when the residuals reached the minimum.

$$d = ae^{-\frac{t}{\tau}} = ae^{-\frac{\ln 2}{t_{1/2}}t} \quad (5.1)$$

where d represents the displacement vector and t is the acquisition dates. τ corresponds to the mean lifetime (or exponential time constant), and it is related to the decay rate, λ , in the way of $\tau = 1/\lambda$. $t_{1/2}$ represents the half-life which is the time required for the decaying quantity (the displacement) to fall to one half of its initial value. The mean lifetime τ is equal to the half-time divided by the natural log of 2, thus $\tau = \frac{t_{1/2}}{\ln 2} \approx 1.44 \cdot t_{1/2}$.

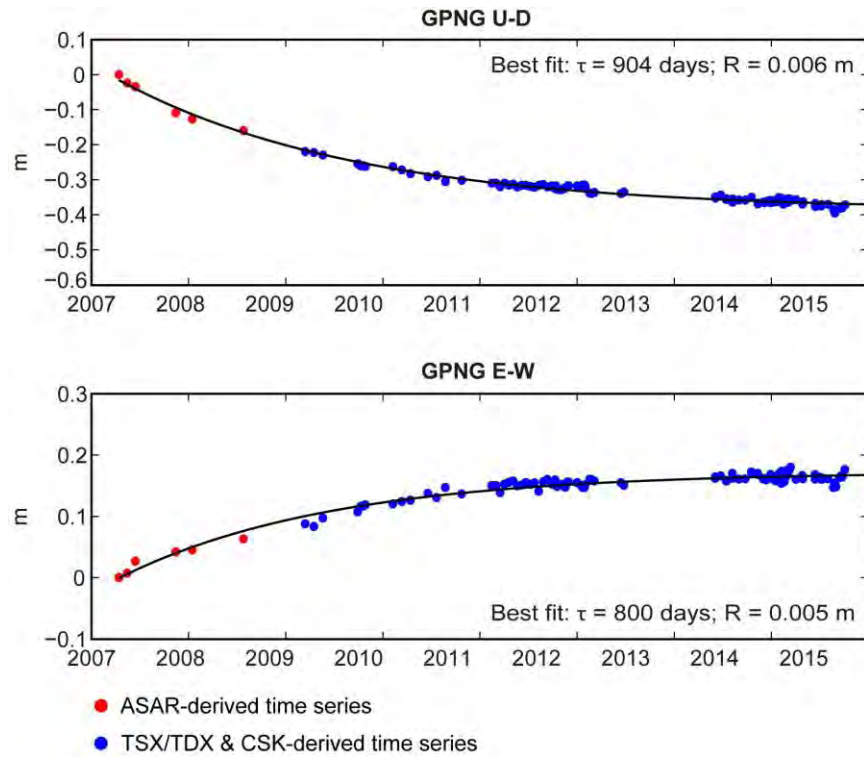


Figure 5.23 Connected InSAR time series in 2007-2014 at station GPNG located on the Eastern Flank, adjusted by exponential function. τ indicates the mean lifetime of the decay, and R represents the minimum residual between data and function.

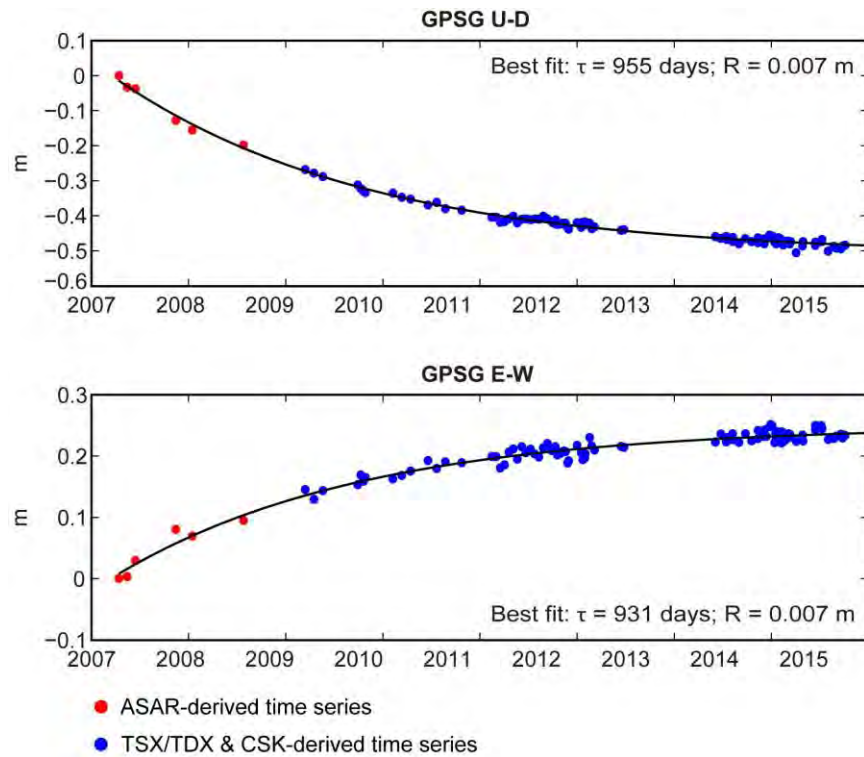


Figure 5.24 Connected InSAR time series in 2007-2014 at station GPSG located on the Eastern Flank, adjusted by exponential function. τ indicates the mean lifetime of the decay, and R represents the minimum residual between data and function.

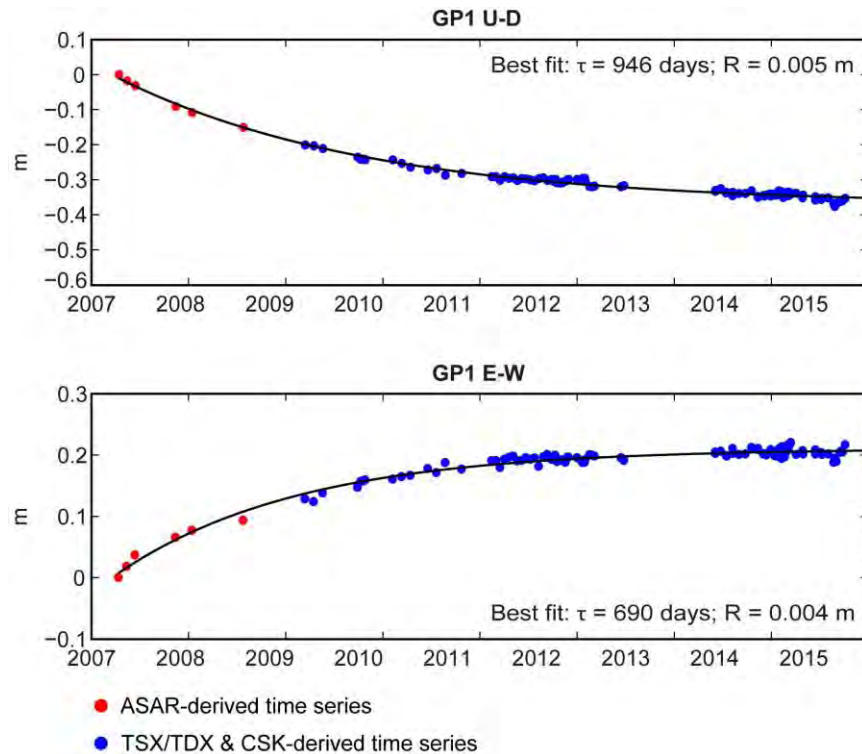


Figure 5.25 Connected InSAR time series in 2007-2014 at point GP1 located on the Eastern Flank, adjusted by exponential function. τ indicates the mean lifetime of the decay, and R represents the minimum residual between data and function.

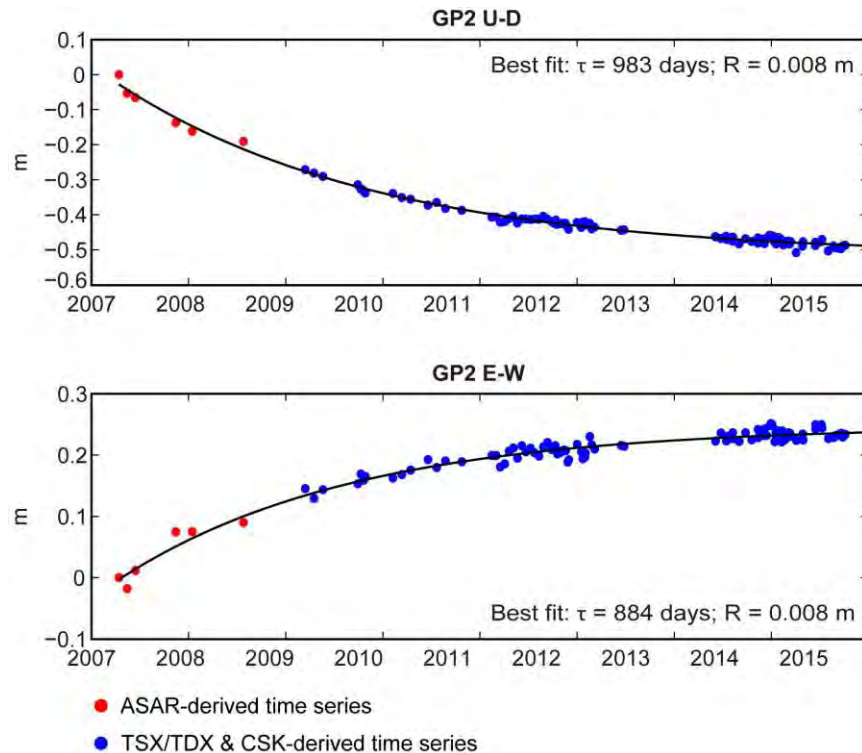


Figure 5.26 Connected InSAR time series in 2007-2014 at point GP2 located on the Eastern Flank, adjusted by exponential function. τ indicates the mean lifetime of the decay, and R represents the minimum residual between data and function.

Figure 5.23 – Figure 5.26 show the obtained curves at the four points. The good connectivity between the ASAR and TSX/TDX & CSK time series and the small residuals between data and the estimated function in both U-D and E-W components indicate that an exponential function could satisfyingly explain the temporal displacement behavior of the large mobile sector on the Eastern Flank between 2007 and 2014. It suggests that the large scale long-term seaward motion of the Eastern Flank which began after the end of the March-April 2007 eruption could have been persisting for at least 7 years, with amplitude following a likely exponentially decreasing law. This interpretation supports the conclusion made in [Chapter 4](#) that the widespread seaward flank motion of Piton de la Fournaise during the 2009-2014 period is mainly due to the ongoing post-eruptive displacement of the March-April 2007 eruption.

Compared with the mean lifetime of the Eastern Flank motion observed by Augier ([2011](#)) (160 days at a point on the Eastern Flank), the mean lifetimes obtained here are about 6 times larger. This is mainly due to that Augier ([2011](#)) had only the InSAR data in 2007-2008 to model

the exponential decay. Very close mean lifetimes between the U-D displacements at four points (904 days for GPNG, 955 days for GPSG, 946 days for GP1 and 983 days for GP2) suggest a common process or processes playing a role in the U-D displacement at and/or adjacent to these locations. The mean lifetimes of the E-W displacement vary more importantly than those of the U-D displacement from 690 to 930 days, which suggests the underlying processes responsible for the eastward motion of the Eastern Flank may vary spatially.

5.3 Discussion and conclusions

In this chapter, we compared the ground displacement at Piton de la Fournaise between 2007 – 2008 and 2009 – 2011 periods in terms of spatial pattern and temporal evolution. Differing from the distal March-April 2007 eruption, the eruptions that occurred during the subsequent 7 years are mainly small-scale eruptions affecting only the Central Cone area. This suggests a shallow deformation source under the summit craters. Summit slow-rate long-term deflation during rest periods is one of the typical volcano deformation regimes. The similar spatial pattern of the subsidences between 2007 – 2008 and 2009 – 2014 suggests close sources or the same source were/was playing a role. The exponentially decreasing subsidence in 2007 – 2008 and the linear subsidence in 2009 – 2014 suggest a change in deformation regime may have occurred in late 2008. The downslope displacement affecting area of the Eastern Flank extended to the east and to the south from 2007 – 2008 to 2009 – 2014. Similar spatial displacement patterns are observed between the two periods, although the most significant area of the U-D displacement moved slightly to the south. Good connectivity between two time series at four point on the Eastern Flank suggests the widespread seaward motion of the Eastern Flank could have kept deforming since the end of the March-April 2007 eruption for at least 7 years, with an exponentially decreasing amplitude. The estimates of mean lifetimes suggest the U-D displacement adjacent to the four points could be caused by a common process or processes, while different processes could play a role in the E-W displacement of those locations.

CHAPTER 6 : CHARACTERIZATION OF DISPLACEMENT IN LAVA FIELDS

Lava flows can continue to deform for years after their emplacements generating measureable ground deformation on and adjacent to lava flow fields (Briole et al., 1997; Stevens et al., 2001a, 2001b). This deformation is mainly driven by processes such as (Stevens et al., 2001a, 2001b): (1) thermal contraction associated with cooling and consolidation, (2) compaction of vesicles and void space within the lava body, (3) depression of flow substrate in response to surface load. Being one of the most active basaltic volcanoes in the world, Piton de la Fournaise (La Réunion Island, Indian Ocean; **Figure 6.1 inset**) erupts frequently and produces significant lava flows, for instance, it erupted 34 times and emitted nearly 500 Mm³ of magma to the surface between March 1998 and April 2007, preceded by a six years of quiescence (Roult et al., 2012; Peltier et al., 2015a; Staudacher et al., 2015). The lava fields emplaced between March 1998 and April 2007 are illustrated in **Figure 6.1**. They have mainly covered the north-eastern, eastern and south-eastern flanks of the volcano. Characteristics of these lava flows including the geometric parameter (surface, volume, and flux), location and elevation etc. have been investigated and listed by Roult et al. (2012). Continuous ground deformations recorded at the GNSS stations located in these lava fields (**Figure 6.1**) have also been reported by Staudacher & Peltier (2015) and Peltier et al. (2015a). Nevertheless no analysis focusing on the long-term post-emplacment deformation in lava fields in large spatial extent has yet been performed. This kind of analysis, however, is indispensable to correctly estimate the ground deformation field of the volcano.

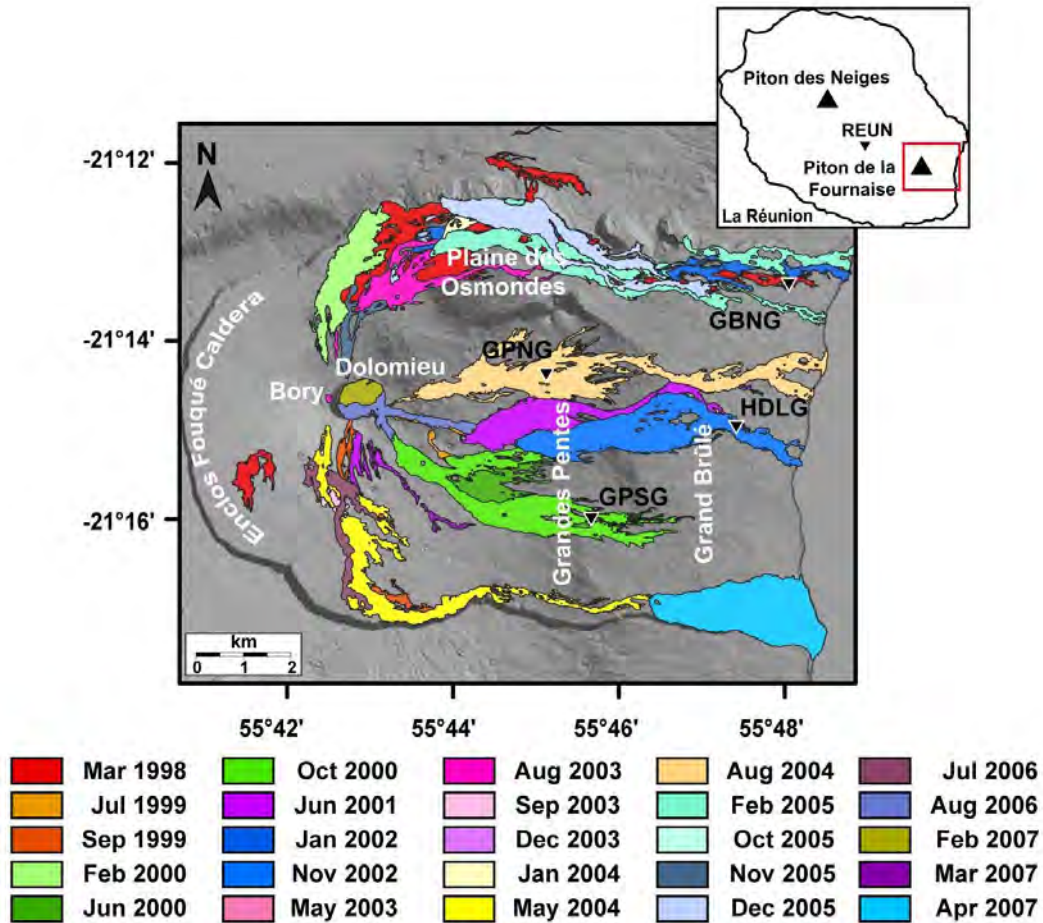


Figure 6.1 Location of lava flow fields emplaced between 1998 and 2007 at Piton de la Fournaise, superimposed on a shaded relief map with the main areas mentioned in the paper: the Enclos Fouqué caldera, the Dolomieu and Bory caters, the Plaine des Osmondes, the Grandes Pentès and the Grand Brûlé areas. Location of flank GNSS stations, GPNG, GPSG, HDLG and GBNG, installed on these lava fields is indicated by black triangles. The inset shows the location of the Piton des Neiges and Piton de la Fournaise volcanoes in La Réunion Island. Coordinates in Geographic Lat/Lon WGS84.

Here we use Interferometric Synthetic Aperture Radar (InSAR), a technique that can provide large scale displacement maps, to characterize the long-term deformation associated with lava fields emplaced between March 1998 and April 2007 at Piton de la Fournaise. Indeed, InSAR has been widely and successfully applied to monitor the surface deformations at worldwide volcanoes such as the Etna, Kilauea and Piton de la Fournaise etc. (e.g. Lundgren & Rosen, 2003; Lundgren et al., 2003, 2013; Hooper et al., 2007; Fukushima et al., 2010; Solaro et al., 2010; Bagnardi & Amelung, 2012; Baker & Amelung, 2012; Plattner et al., 2013; Froger et al.,

2015; Remy et al., 2015). However, the number of InSAR studies focusing on the deformation due to the post-lava emplacement processes is very limited with respect to those focusing on deformation associated with magmatic processes (Chaussard, 2016). Furthermore, among those few InSAR studies detecting lava deformation after emplacement (e.g. Briole et al., 1997; Stevens et al., 1999, 2001a, 2001b; Lu et al., 2005; Ebmeier et al., 2012; Bato et al., 2016; Chaussard, 2016), the studies carried out at Piton de la Fournaise are yet scanty (Tinard, 2007; Peltier et al., 2010a; Bato et al., 2016) and none of them provides detailed analysis and comparison on the long-term post-emplacement deformation for multiple lava fields. In this study, we used the TSX time series spanning between 2009 and 2014 (acquired in Chapter 4) to retrieve the long-term deformation occurred in lava fields at Piton de la Fournaise. The spatial pattern and temporal behavior of displacement are presented, and the relationship between displacement, lava thickness and age is investigated. Results derived by InSAR data between show a significant difference of deformation behavior between lava fields in the Eastern Flank area and those outside.

6.1 Data processing

6.1.1 InSAR time series

Here we use the TSX time series that acquired in Chapter 4 instead of the TSX-CSK merged time series because it remained coherence in the Apr 2007 lava flow area. **Figure 6.2** shows the U-D and E-W components of the cumulative displacement maps observed from InSAR data. It is worth noting that the summit area is affected by large transient displacement associated with eruptive activities (Nov 2009, Dec 2009, Jan 2010, Oct 2010 and Dec 2010) during the study period. The cumulative displacement in the summit area is evident in **Figure 6.2b**. Since this study focuses on mainly long-term displacement in lava fields on volcano flanks, the transient deformation in the summit area will not be discussed afterwards and the color scales were adjusted to the visualization of long-term displacement.

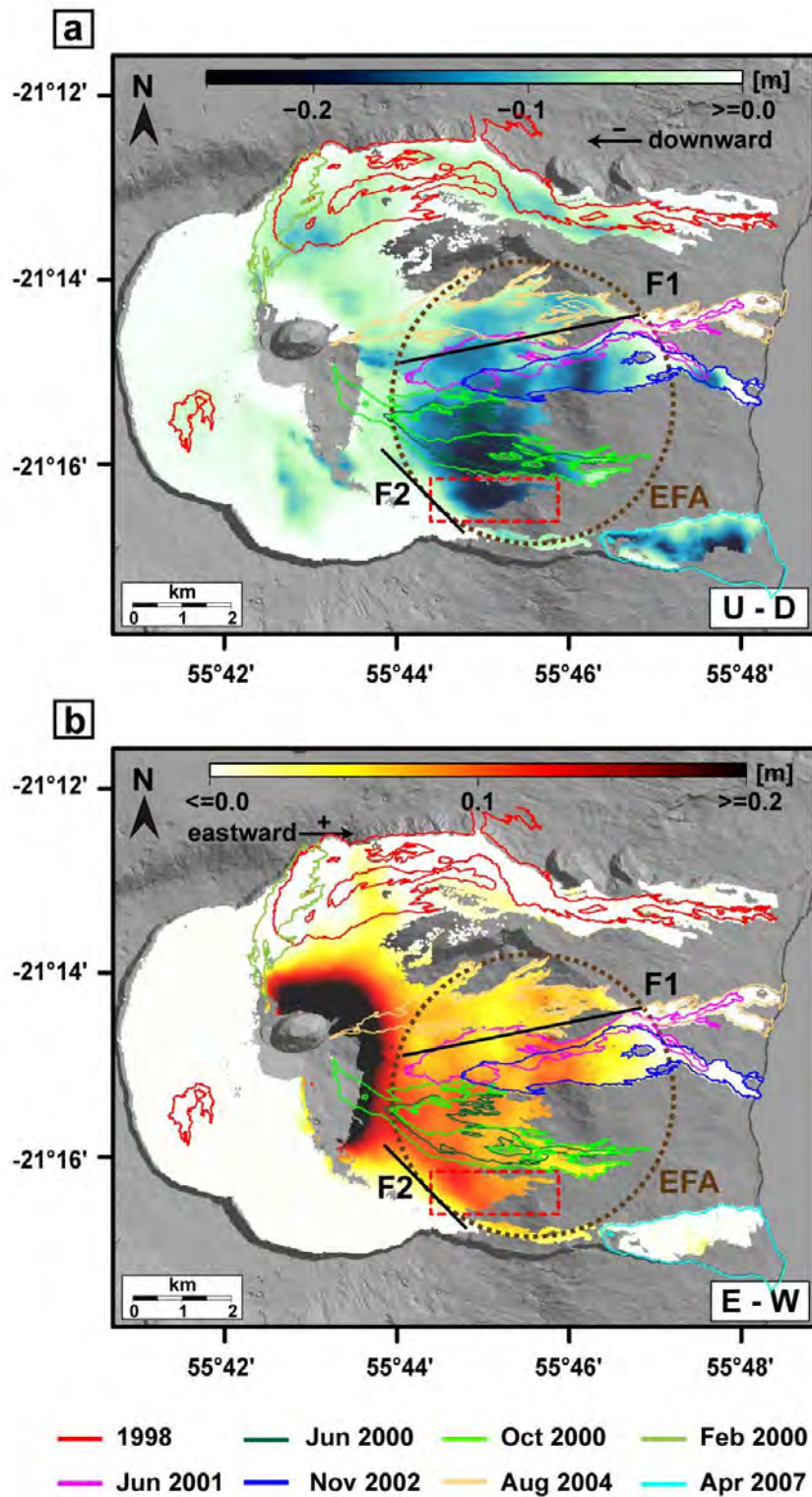


Figure 6.2 Cumulative displacement map, (a) U-D component and (b) E-W component, spanning from 7 March 2009 to 6 October 2014 derived from TSX data (Coordinates in Geographic Lat/Lon WGS84). The

map is spatially referenced to a non-displacement zone that is located ~ 10 km away from volcanic craters. Nine lava flow contours are superimposed on the maps. The dashed brown ellipse indicates the Eastern Flank Area (EFA) that is affected by both downward and eastward displacement during the study period. The red rectangle denotes southern part of the EFA where no lava fields emplaced between 1998 and 2007 but significant displacement occurred. F1 and F2 (black lines) represent the rough location of two structures inferred from this study.

6.1.2 Extracting single lava fields between March 1998 and April 2007

At Piton de la Fournaise, lava flows are often superimposed on those emitted during earlier eruptions (**Figure 6.1**). Such superimposition of two or multiple lava flows can induce more complex processes such as, compaction in the rough interface between two flows, subsequent thermal contraction of the whole composite lava, and the acceleration of creep in the substrate resulting from the heat transfer from the above to the underlying flow ([Stevens et al., 2001a](#)). In this study, we therefore only consider the displacement restricted to single lava flow fields (**Figure 6.3**) attempting to avoid the considerations of interactions between lava flows. The selection of lava flow fields followed three principles:

- 1) No superimposition. Only single lava flow (emplaced between March 1998 and April 2007) covering areas are selected by spatial analysis.
- 2) Emplacements on volcano flanks. We extracted the lava fields situated away from the summit cone and affected by long-term displacement rather than transient eruptive displacement.
- 3) InSAR coherent area. The selected areas are required to be coherent in InSAR data. Some flow areas where significant displacement is supposed to occur, however, are not remained coherent in InSAR data. These areas are not taken into account in the analysis.

Nine lava flow fields were eventually extracted including the Mar 1998a-b, the Feb 2000, the Jun 2000, the Oct 2000, the Jun 2001, the Nov 2002, the Aug 2004 and the Apr 2007 lava fields (named after their dates of emplacement; **Figure 6.3**).

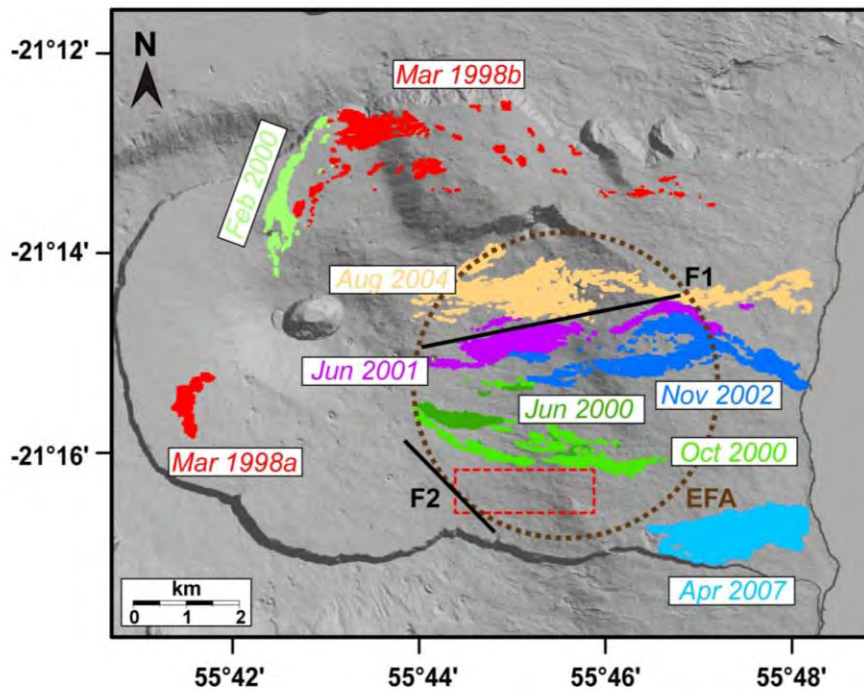


Figure 6.3 Nine extracted single lava fields coverage emplaced between March 1998 and April 2007. The dashed brown ellipse indicates the EFA that is affected by both downward and eastward displacement during the study period. The red rectangle denotes southern part of the EFA where no lava fields emplaced between 1998 and 2007 but significant displacement occurred. F1 and F2 (black lines) represent the rough location of two structures inferred from this study.

6.1.3 Estimating lava thickness

To evaluate the thickness of lava flows emplaced between 1998 and 2007 at Piton de la Fournaise, we used two available Digital Elevation Models (DEMs). One is a 25 m resolution DEM from aerial photogrammetry in 1997 and the other is measured via airborne LiDAR surveying in 2008 with 7.5 m resolution. It is worth noting that no eruptive events generating surface displacement occurred between the acquisition time of the 1997 DEM and March 1998, and between April 2007 and the acquisition time of the 2008 DEM. The two DEMs were first downsampled to a same grid posting. We then used the vertical difference between the two DEMs to estimate topographic height change, which reflects the thickness of total deposits. Given that lava is main production of Hawaii style eruptions composing the deposits, as at Piton

de la Fournaise, and no independent data providing information about the discrepancies between the total deposit thickness and the lava thickness is available, we used the difference between the two DEMs to approximately represent the thickness of lava flows (**Figure 6.4**). It is reasonable to some extent according to previous studies carried out by Bato et al. (2016) and Chaussard (2016). The former used the difference of DEMs to estimate the thickness of October 2010 lava flow at Piton de la Fournaise. The latter also used the height change represent the lava thickness at Paricutin volcano, where, even though ash and pyroclastic are expected to account for up to 30 % of total deposit thickness. Additionally, the effects of erosion and redistribution of the less consolidated materials are not considered in this study. We used finally the extracted lava flow fields (**Figure 6.3**) as a mask to obtain the thickness of each lava field.

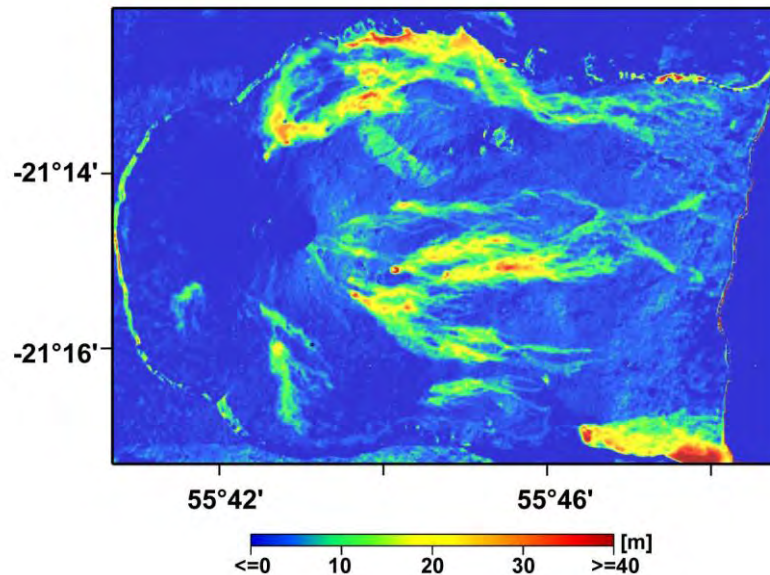


Figure 6.4 Estimated thickness of lava flows that emplaced at Piton de la Fournaise between 1998 and 2007.

6.2 Results

Griffiths and Fink (1993) and Griffiths (2000) showed that after the emplacement of lava flows, a solid crust quickly forms and grows at their surface; the flow spreads only in depth from a certain thickness. The strength in the plane parallel to lava flow surface is far larger than that

in the plane perpendicular to its surface. Thus, the displacement due to post-lava emplacement processes should be largely vertical and negligibly horizontal. **Figure 6.2** show that the areas corresponding to the Mar 1998a-b, the Feb 2000 and the Apr 2007 lava fields (**Figure 6.3**) are mainly affected by downward displacement. But a large scale pattern on the Eastern Flank of Piton de la Fournaise (indicated using dashed brown ellipse in **Figure 6.2 – Figure 6.3**, hereafter called the Eastern Flank Area, EFA) involving the Jun 2000, the Oct 2000, the Jun 2001, the Nov 2002 and the Aug 2004 lava fields is affected by not only downward but also eastward displacement. Even so, the eastward displacement patterns do not show any clear correlation in space with lava flow fields, contrary to the vertical displacement (**Figure 6.1 – Figure 6.2**). It allows us to assume that the horizontal displacement induced by post-emplacement of lava fields is negligible. Since an evident regional difference in deformation arises, we divide the lava fields into two groups (inside and outside the EFA) to further analysis.

6.2.1 Subsidence in lava fields outside the EFA

The cumulative vertical displacement during the 2009 – 2014 period and the lava thickness for each selected lava flow emplaced outside the EFA are shown in **Figure 6.5**. All lava flow fields outside the EFA show a trend of downward movement with varying degrees of magnitudes. From a visual inspection, large subsidence occurs generally in and adjacent to thick areas (**Figure 6.5**). To quantitatively characterize the relationship between subsidence and thickness of lava flow fields, we divided coherent pixels into several small bins along thickness (1 m unit). Displacements in each bin are statistically analyzed and plotted in function with thickness in **Figure 6.6**, on the background of the population distribution histogram. The Mar 1998a lava thickness ranges from meters to fifteen meters giving slight cumulative subsidence of ~ 0.03 to ~ 0.06 m during the ~ 5.5 years period. The Mar 1998b lava field (up to 30 m thick) subsides cumulatively ~ 0.02 to ~ 0.12 m. The Feb 2000 lava (up to 20 m thick) subsides ~ 0.02 to ~ 0.1 m in total. The Apr 2007 lava field (thickness up to 25 m) shows overall downward displacement of ~ 0.02 to ~ 0.25 m. **Figure 6.6** shows that the subsidence magnitude increases with the raising of flow thickness (a positive correlation) following clear linear laws in all cases. We fitted the correlation using linear functions and the best fits are presented in red lines with norm of residuals, marked alongside, indicating the goodness of linear fits (**Figure 6.6**). The low values of norms of residuals (~ 1 cm, ~ 7 cm, ~ 3 cm and ~ 12 cm for the Mar 1998a, Mar 1998b,

Feb 2000 and Apr 2007 lava fields, respectively) confirm the linear relationship between subsidence and thickness in the selected lava fields outside the EFA, though one order of magnitude larger norm of residuals was obtained from the Apr 2007 lava field. It is worth noting that the origins of the linear fits are not zeros, which indicates that part of displacement could be due to the substrate loading process. This process can induce subsidence in areas beyond the lava flow margin, for instance the Mar 1998a and the Feb 2000 lava flows (**Figure 6.2**). The absolute subsidence – thickness (m/m) slopes of four lava flow fields (0.0014, 0.0013, 0.0016 and 0.0028 for the Mar 1998a, Mar 1998b, Feb 2000 and Apr 2007 lava fields, respectively) show that the magnitude of subsidence occurring in one meter thick lava increases with the decrease of lava age. The younger Apr 2007 lava subsides ~ 0.0028 m per meter (thickness) during the 2009 – 2014 period (**Figure 6.6d**), which is about twice larger than the magnitude of subsidence occurring in the 10 years older lava flow fields (the Mar 1988a-b lava fields; **Figure 6.6a-b**). The Mar 1998a lava field (**Figure 6.6a**) exhibits an absolute subsidence – thickness slope of 0.0014, approximate to that of the Mar 1998b lava field that emplaced in the same year (0.0013; **Figure 6.6b**) and a little smaller than that of Feb 2000 lava field that emplaced 2 years later (0.0016; **Figure 6.6c**).

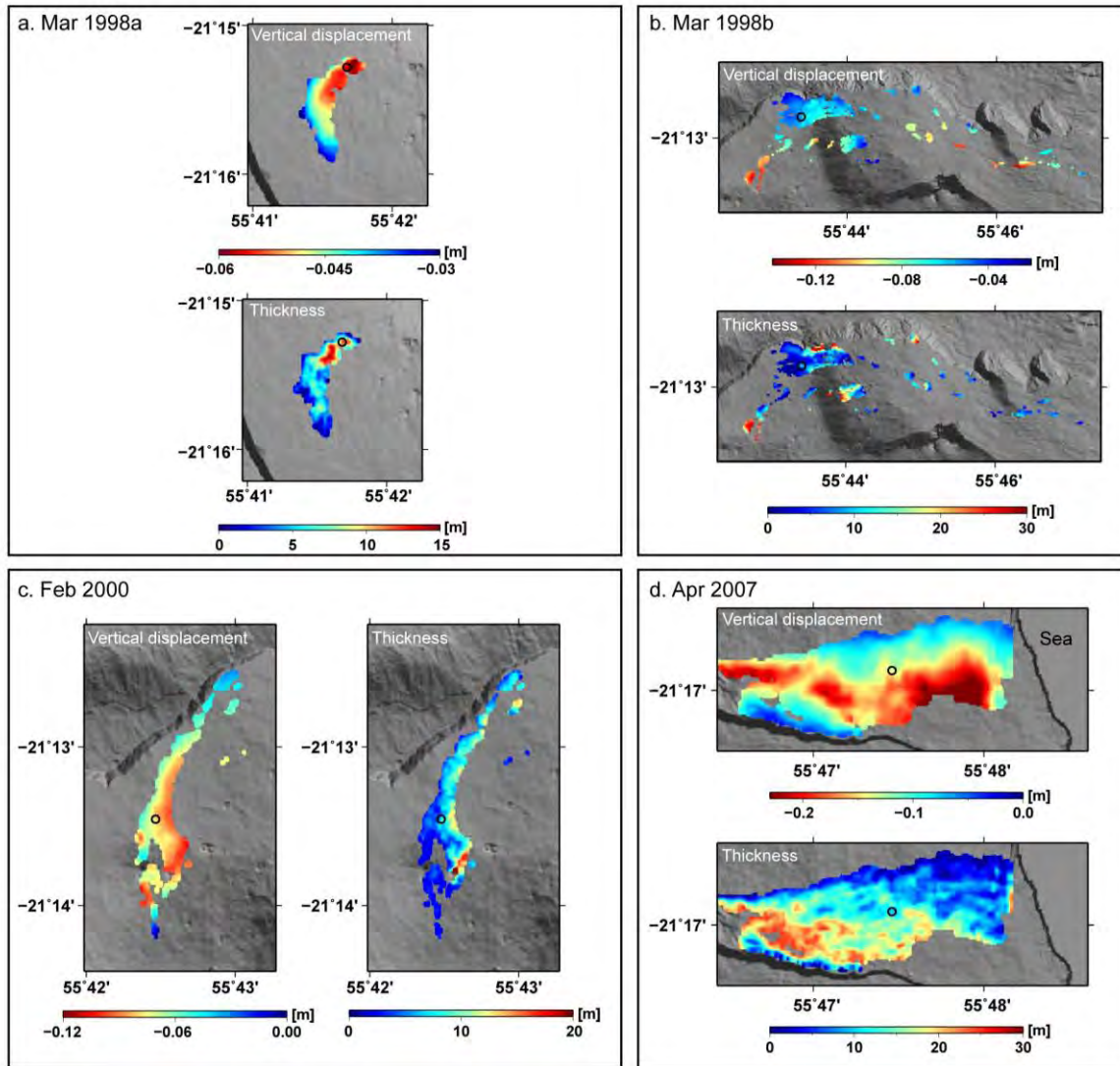


Figure 6.5 Cumulative U-D displacement and thickness maps for four lava fields located outside the EFA. (a) Mar 1998a lava field, (b) Mar 1998b lava field, (c) Feb 2000 lava field, and (d) Apr 2007 lava field. Black circles indicates the selected points with 10 m of thickness for time series plots in **Figure 6.7**.

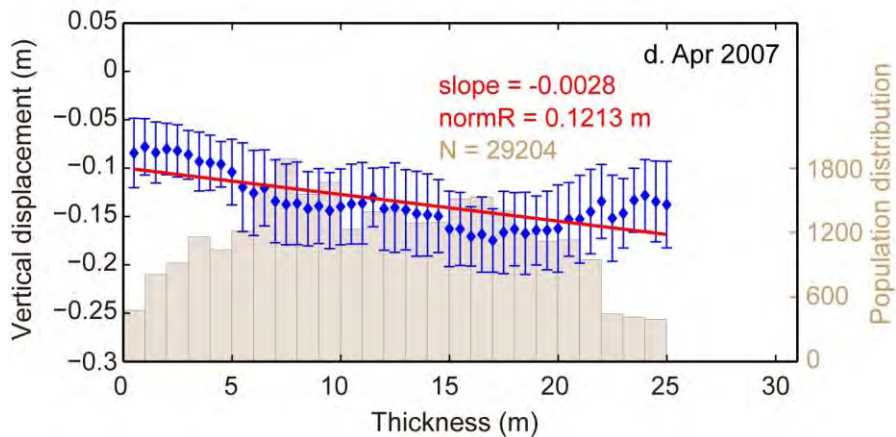
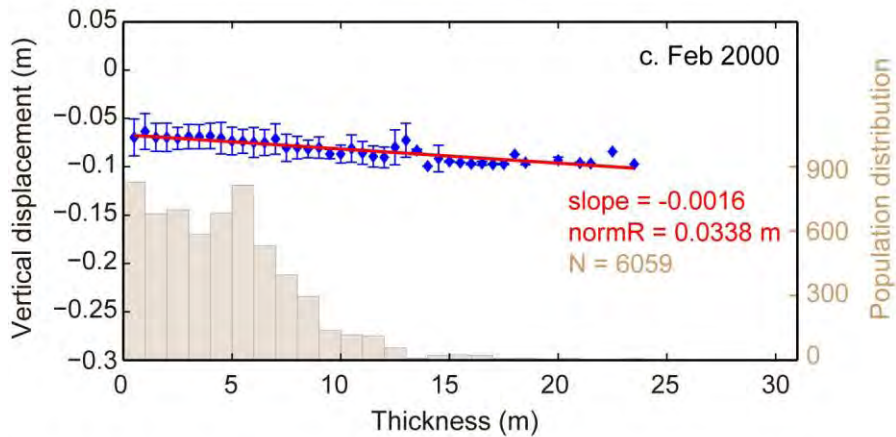
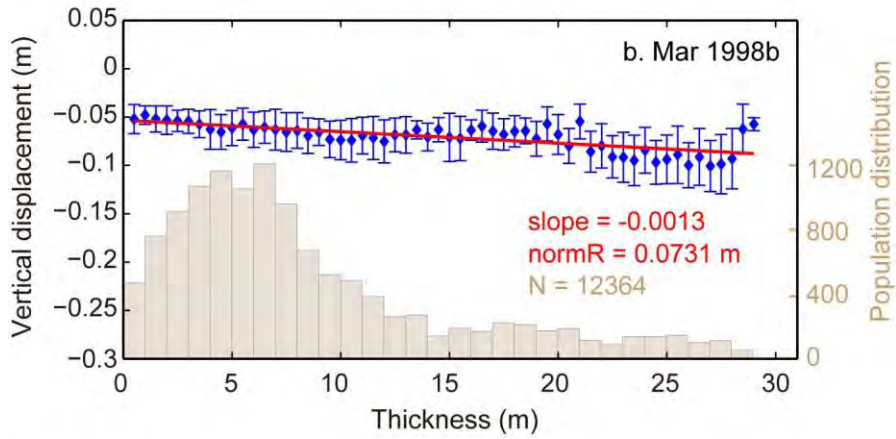
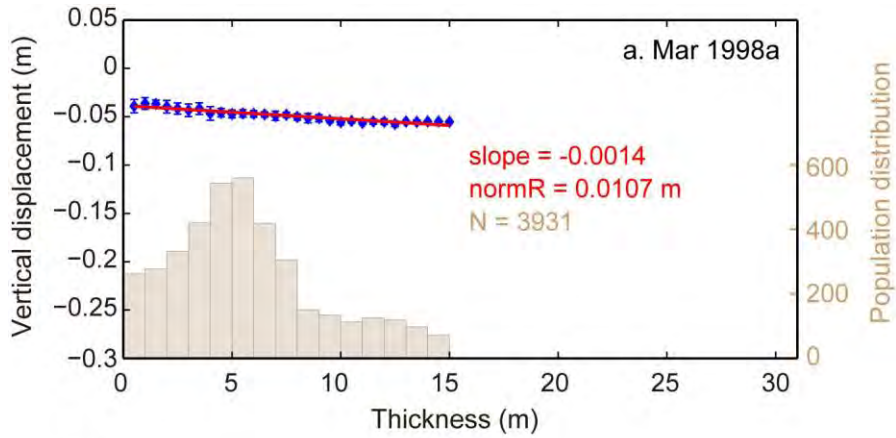


Figure 6.6 Vertical displacement with their standard deviations and histogram of population distribution in function with lava thickness, for four lava fields located outside the EFA. (a) Mar 1998a lava field, (b) Mar 1998b lava field, (c) Feb 2000 lava field, and (d) Apr 2007 lava field.

To investigate the temporal behavior of subsidence, we select one point of 10 m thick in each lava field outside the EFA (see Figure 4 for location of points) as representatives and plot the displacement time series in **Figure 6.7a**. Four time series display a similar trend, revealing the four lava fields subside following a similar temporal behavior between 2009 and 2014 – continuous subsidence without being clearly interrupted by volcano eruptive phases and subsidence rate decaying with time. For the lava field that emplaced in Feb 2000 (green triangles in **Figure 6.7a**), the magnitude of subsidence rate (at the 10 m thick point) decays from ~ 0.04 m/yr at the beginning of study period (9 years after it emplaced) to ~ 0.01 m/yr about 5 years later, reduction by three quarters.

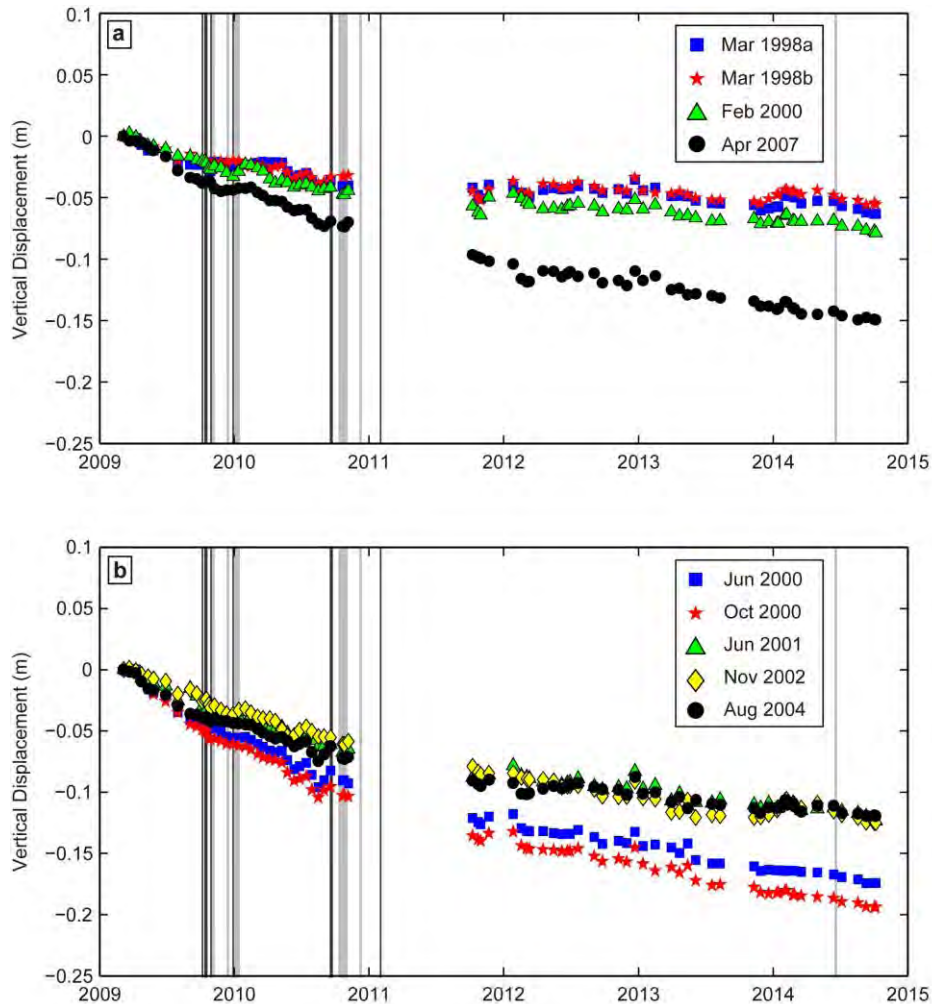


Figure 6.7 Temporal behavior of vertical displacement in lava field located (a) in and (b) outside the EFA. Light grey areas and black vertical lines represent timing of eruptions and intrusions, respectively, which occurred in the study period (refer to caption of **Figure 6.2** for timing).

6.2.2 Subsidence in lava fields inside the EFA

Same analysis was performed on the lava fields inside the EFA (result figures: **Figure 6.8**, **Figure 6.9** and **Figure 6.7b**). Similar to the lava fields located outside the EFA, the inside lava fields show a trend of downward displacement all over the area during the study period (**Figure 6.8** and **Figure 6.9**). However, the subsidence pattern and behavior in the EFA display huge variability contrast with the uniformity shown outside the EFA. First, the magnitude of subsidence are generally large in lava fields inside the EFA than those outside. A majority of pixels falls into the cumulative subsidence interval 0.1 – 0.2 m regardless of lava thickness and

age (**Figure 6.8** and **Figure 6.9**). Four of five lava fields (the Jun 2000, Oct 2000, Jun 2001 and Nov 2002 lava fields) give maximum subsidence over 0.2 m (**Figure 6.8** and **Figure 6.9**). Second, the subsidence – thickness relationship behaves differently among five lava fields. The Jun 2000 and Oct 2000 lava fields will be two remarkable exceptions since their subsidence magnitudes decrease with the increase of lava thickness (**Figure 6.9a-b**). They both display a linear trend, and the decreasing rate of the Jun 2000 (0.0042; **Figure 6.9a**), however, is significantly larger than that of the Oct 2000 lava field (0.0007; **Figure 6.9b**). Third, the subsidence – thickness slope and the age do not show any clear correlation. Indeed, the absolute subsidence – thickness slope of the Nov 2002 lava field (0.0052; **Figure 6.9d**) is larger than that of a one year older lava field (Jun 2001, 0.0034; **Figure 6.9c**). Nevertheless, the youngest lava field (Aug 2004) has the lowest slope among these three (**Figure 6.9c-e**). Furthermore, the Jun 2001 and Nov 2002 lava fields subside (m/m of thickness) about twice and three times more significantly than the lava that emplaced just one and two years ago in Feb 2000 outside the EFA (**Figure 6.9c-d** and **Figure 6.6c**). More remarkably, the absolute subsidence – thickness slope of the Jun 2001 and Nov 2002 lava fields (0.0034 and 0.0052; **Figure 6.9c-d**) are even much greater than the 6 years younger lava field that emplaced outside the EFA (**Figure 6.6d**). Last, relatively large norms of residuals for the Jun 2001 and Nov 2002 lava fields indicate that linear fits seem unable to satisfactorily explain the relationship between the subsidence and thickness for them.

PITON DE LA FOURNAISE
CHAPTER 6: CHARACTERIZATION OF DISPLACEMENT IN LAVA FIELDS

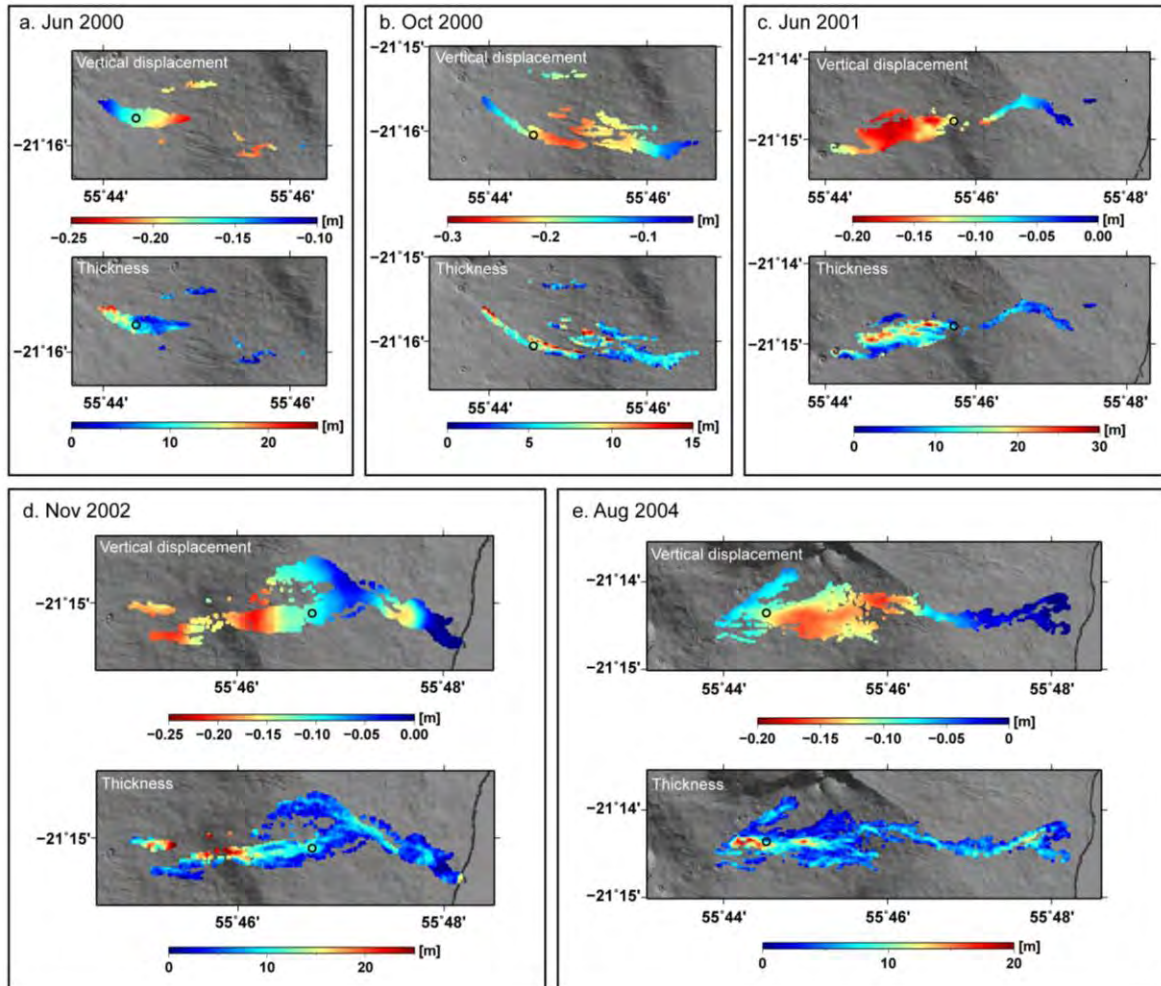
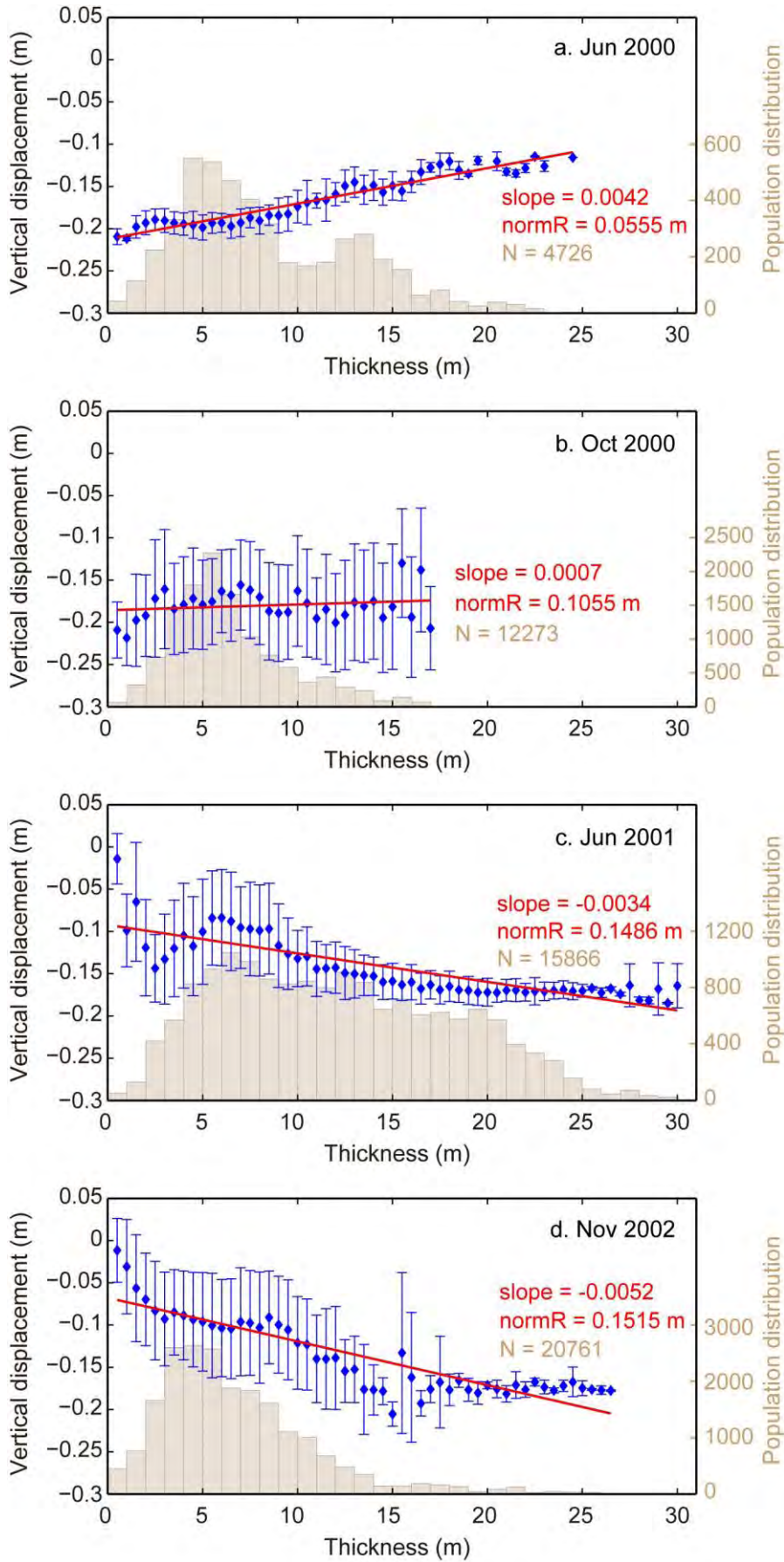


Figure 6.8 Cumulative U-D displacement and thickness maps for five lava fields located in the EFA. (a) Jun 2000 lava field, (b) Oct 2000 lava field, (c) Jun 2001 lava field, (d) Nov 2002 lava field, and (e) Aug 2004 lava field. Black circles indicates the selected points with 10 m of thickness for time series plots in **Figure 6.7**.



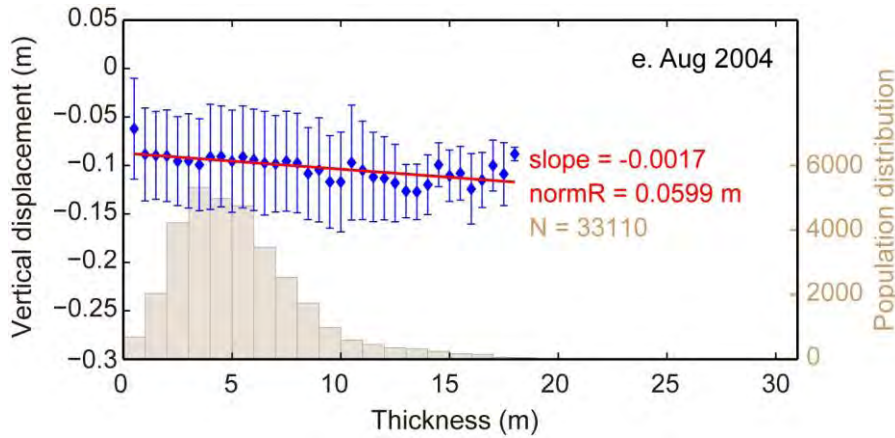


Figure 6.9 Vertical displacement with their standard deviations and histogram of population distribution in function with lava thickness, for five lava fields located in the EFA. (a) Jun 2000 lava field, (b) Oct 2000 lava field, (c) Jun 2001 lava field, (d) Nov 2002 lava field, and (e) Aug 2004 lava field.

Despite of all the differences, the time series of lava fields inside the EFA show a similar displacement behavior in time (continuous subsidence with rate decreasing in time) to those lava fields outside (**Figure 6.7a-b**). For a lava field that emplace in Jun 2000 (blue squares in **Figure 6.7b**), almost the same time with the Feb 2000 lava emplacement, however, the magnitude of subsidence rate is more important (up to ~ 0.07 m/yr at the beginning of study period and ~ 0.02 m/yr at the end). As already mentioned before, the subsidence at a certain timing does not exhibit clear correlation with the lava age.

Complexities of displacement in lava fields located inside the EFA are evident comparing with the lava subsidence outside the EFA, indicating that the post-emplacement subsidence of lava fields may not be the single component contributing to the downward displacement observed in the EFA.

6.3 Discussion

The vertical displacement (2009-2014) affecting the lava fields that emplaced between 1998 and 2007 at Piton de la Fournaise has been derived and analyzed in this study. Results show that the cumulative subsidence in lava fields outside the EFA increase with the increase of lava thickness, presenting a positive linear correlation (**Figure 6.6**). Similar correlations have been previously observed from lava fields at other volcanoes, such as Etna, Okmok, Santiaguito

and Paricutin volcanoes (Stevens et al., 2001a; Lu et al., 2005; Ebmeier et al., 2012; Chaussard, 2016). For every meter of lava, the magnitude of subsidence increases as the lava age decrease; for a certain lava field, the subsidence rate decays in time (**Figure 6.6** and **Figure 6.7a**). These observed subsidence behaviors are expected to be the results of post-lava emplacement processes such as thermal contraction, void space compaction and substrate loading (Stevens et al., 2001a). However, the subsidence behaviors in lava fields inside the EFA differ significantly from those outside the EFA and previous studies (**Figure 6.7b**, **Figure 6.8** and **Figure 6.9**). The correlations between subsidence and thickness vary from one to another. Subsidence in the Jun and Oct 2000 lava fields even display negative correlations with thicknesses. The subsidence per meter of thickness does not correlate with lava age (**Figure 6.9**). This irregularity is further illustrated in **Figure 6.10** in which an exponential curve is fitted using values observed in lava fields outside the EFA to roughly explain the expected correlation between the subsidence (per meter of thickness) induced by post-lava emplacement processes and the lava age. The markers correspond to lava fields inside the EFA deviate broadly (in particular the Jun 2000, Oct 2000, Jun 2001, Nov 2002 lava fields) in both directions from the simulated curve, which evidences that the observed subsidence cannot be entirely explained only by post-lava emplacement processes. Other process/processes must have played a significant role in provoking resultant subsidence behaviors, for instance, older lava fields (the Jun 2001 and Nov 2002 lava fields) exhibit larger subsidence (per meter of thickness) than younger ones (the Aug 2004 and Apr 2007 lava fields); signs of subsidence – thickness correlations for the Jun and Oct 2000 lava fields are even inversed (**Figure 6.6**, **Figure 6.9** and **Figure 6.10**).

The portion of subsidence (per meter of thickness) due to post-lava emplacement processes in lava fields inside the EFA is expected to drop on the fitted curve (as shown by transparent blue squares with approximated subsidence – thickness slopes in brackets in **Figure 6.10**). The magnitude of discrepancies between the observed (blue squares) and the approximated (transparent blue squares) values reveal the level of effects produced by other potential processes on lava fields inside the EFA that vary spatially from north to south. The significant discrepancies of the Jun 2000, Oct 2000, Jun 2001 and Nov 2002 lava fields suggest that the potential processes might have accounted for larger portion of observed than post-lava emplacement processes. The two lava fields of 2000 located in south, especially, display inversed subsidence – thickness slopes (subsidence decreasing with increase of thickness) with

respect to others. This suggests the role potential processes played on 2000 lava fields could dominantly affect the pattern of observed deformation. In particular, the areas covered by relatively thinner lava show a higher sensitivity in the accumulation of deformation in response to such potential processes. The Aug 2004 lava field located in north, however, presenting a less discrepancy (close to the fitted curve; **Figure 6.10**) reveal a relatively slighter effect from the potential processes. Based on this exponential law, we estimated that the contribution of post-emplacment lava flow subsidence might contribute 22 % (in Jun 2000 lava field) – 79 % (in Aug 2004 lava field) of the subsidence observed inside the EFA. Thus the other processes could contribute up to 78 % of the subsidence. This estimation differs from that in [Section 4.4.3](#), which is mainly because in [Section 4.4.3](#) we use only the mean values of displacement and thickness while here we take into account their correlation by statistic analysis (**Figure 6.6** and **Figure 6.9**).

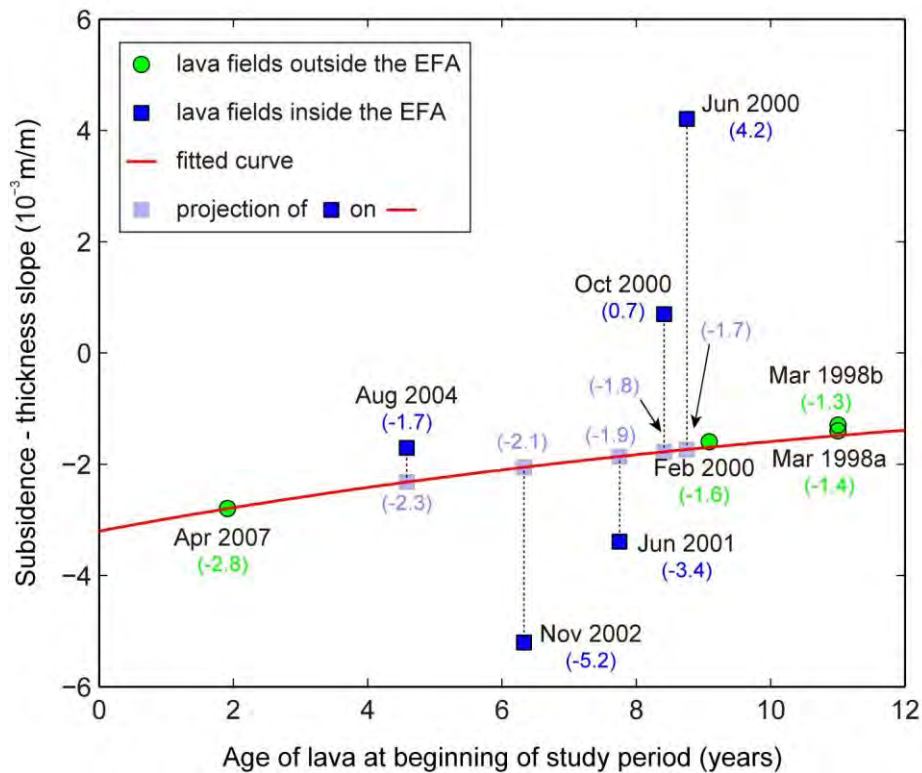


Figure 6.10 Cumulative subsidence in lava fields normalized by lava thickness (i.e. subsidence – thickness slope) in relation with the age of lava. The red curve indicates the fitted exponential relationship, estimated by using data derived from the lava fields outside the EFA (the green circles).

As already discussed in [Chapter 4](#), several possible origins such as pre-existing structural discontinuity, summit stress associated with magmatism, and activated fault movement have been proposed to explain the Eastern Flank motion of Piton de la Fournaise. However, the precise origin remains undetermined. According to the spatial variation of the displacement of lava fields, we suggest that some potential structures (e.g. normal faults) could exist. Such potential structures (dip and strike) could make an important contribution to influencing the spatial distribution of strain accommodation. Significant difference in observed deformation between the Aug 2004 lava field and the other four in the EFA (**Figure 6.10**) suggests one inclined structure/fault could underlie between the Aug 2004 and the Jun 2001 lava fields (as indicated in **Figure 6.2** and **Figure 6.3**, F1). Taking into account the red rectangle deformation area, another structure could be located along the deformed boundary as indicated by F2 in **Figure 6.2** and **Figure 6.3**. The geographical location of the northern structure (F1) suggested by this study is approximately coincident with a previously recognized normal fault ([Michon & Saint-Ange, 2008](#)). The location of structure F2 coincides generally with a sharp feature observed by [Froger et al. \(2015\)](#), who proposed it could be also related to a normal fault that was activated during the March-April 2007 eruption. The two structures make the area covered by the 2000-2002 lava fields as a mobile hanging wall, which indicates that the internal rocks (as well as their overlying lava fields) between the two structures would significantly slide along a plane beneath the Eastern Flank, contrast to the external rocks (Aug 2004 lava field). This interpretation could explain the significant discrepancies of the Jun 2000, Oct 2000, Jun 2001 and Nov 2002 lava fields and the small discrepancy of the Aug 2004 lava fields in **Figure 6.10**. However, the existence of the interface beneath the Eastern Flank is still a subject of debate, which is mainly due to rareness of clear shallow seismicity below the Eastern Flank and that the earthquakes below the mobile flank are not aligned along a plane ([Clarke et al., 2013](#); [Peltier et al., 2015a, 2015b](#)). Thus, according to available data and the results retrieved in this study, the deep mechanism driving the flank motion at Piton de la Fournaise is always a valuable issue to investigate.

6.4 Conclusions

We measured the long-term deformation in recent lava fields at Piton de la Fournaise volcano using TSX/TDX InSAR data between 2009 and 2014. InSAR, as a widely used technique for monitoring ground surface deformation, has shown its strength to capture deformation signals in large spatial scale and high resolution that would be unresolvable with techniques based on a few scattered measurement points. The subsidence behavior exhibits a significant difference between the lava fields inside and outside of the EFA (Eastern Flank Area). The former shows a clear linear relationship with lava thickness and it decays with lava age, which is attributed to the post-lava emplacement processes. The latter however displays an irregularity in the subsidence and the relationship between subsidence and thickness and age, which confirms that, besides of the post-lava emplacement processes, other processes must have played a role in the observed subsidence on the Eastern Flank. Detailed analysis of the deformation behavior in lava fields inside the EFA favors the interpretation that two pre-existing normal faults could have been activated during the March-April 2007 eruption and result in a slip along an interface beneath the Eastern Flank, though the existence of the interface is still an issue of debate. We present for the first time a spatial and temporal analysis of ground deformation in multiple lava fields at Piton de la Fournaise, by characterizing the correlations between lava subsidence and lava thickness and age. Although more studies are required to determine the dynamic process driving the instability of the Eastern Flank, the results gained from this study provides essential insights for understanding and monitoring potentially hazardous flank instabilities.

PART II – Llaima

CHAPTER 7 : GROUND DISPLACEMENT AT LLAIMA OBSERVED BY INSAR

7.1 General background of Llaima

Llaima volcano (38.69°S, 71.73°W; **Figure 7.1**), located in the Southern Volcanic Zone of the Andes, about 700 km to the south of Santiago de Chile, is one of the biggest volcanoes in Chile with an area of 500 km², an edifice height of 3125 m, and a volume of about 400 km³ (Naranjo & Moreno, 1991). It is also one of the most historically active volcanoes in South America with a record of around 50 documented eruptions between 1640 and 2009 (Naranjo & Moreno, 2005; Moreno et al., 2009). This complex stratovolcano is built over an 8 km wide Holocene caldera by accumulation of basaltic and andesitic lava flows, andesitic and dacitic pyroclastic flows, pumice falls deposits, and lahar deposits (Naranjo & Moreno, 1991). Llaima has grown since the Late-Pleistocene, characterized mainly by effusive activities. A very explosive period started with a caldera-forming eruption at 13 ka BP and came to an end at 7 ka BP, characterized by several large Plinian eruptions. At least seven eruptions of volcanic explosivity index (VEI) ≥ 3 occurred during the past 7000 years. Its recent activity has been characterized by relatively small eruptions between 1979 and 2003 (11 eruptions with VEI ≤ 2) and by a slight increase in explosivity for the last eruptive cycle, between March 2007 and June 2009 (with $2 \leq \text{VEI} \leq 3$) (Smithsonian Institution Global volcanism report available at <http://www.volcano.si.edu>). During the last eruptive cycle (2007-2009), the Strombolian paroxysmal eruptions in January 2008 and April 2009 are the two largest eruptions with VEI of 3 and 2, respectively (Moreno et al., 2009). Although they are relatively minor eruptions with respect to other volcanoes, they created hazards (for instance, they forced evacuation of local population and caused damage to property) due to the presence of large scale near-summit glaciers, which are highly susceptible to melting and lahar generation during energetic fountaining (Bouvet de Maisonneuve et al., 2012). Activity after these eruptions has been characterized by constant and low seismic activity and fumarole degassing (Mora-Stock et al., 2014).

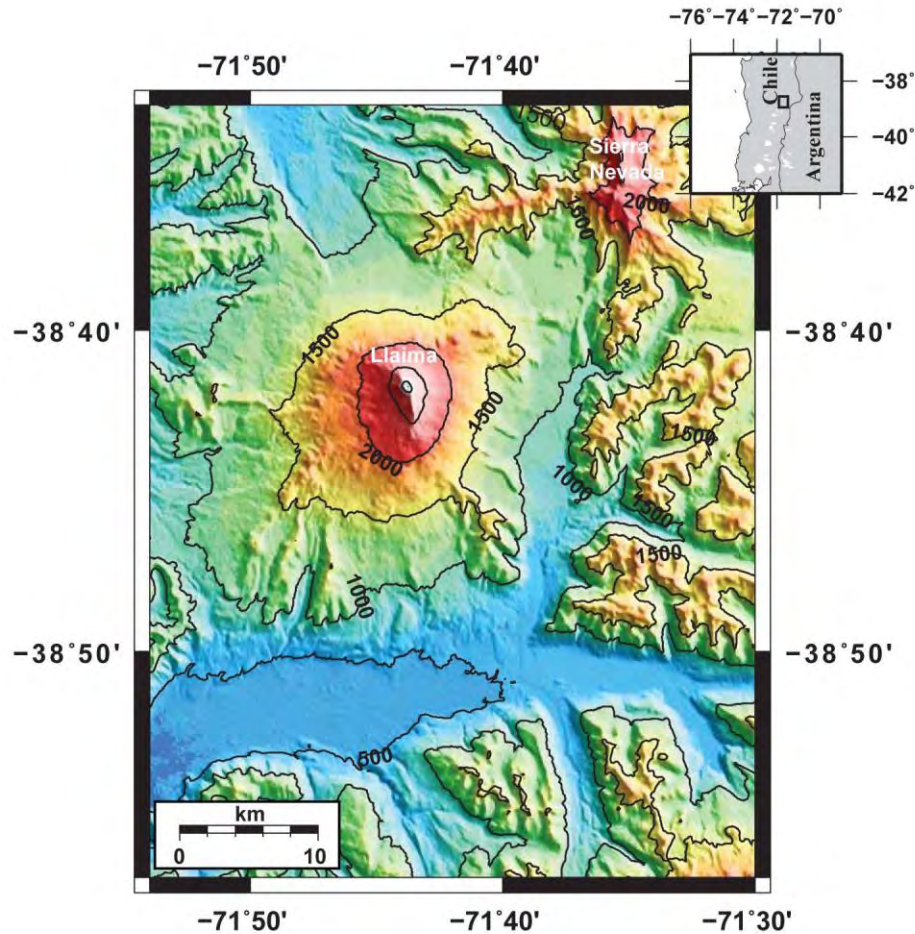


Figure 7.1 Location of Llaima volcano in southern Chile (inset map) and topography of Llaima volcano edifice with contours every 500m.

7.2 InSAR observations at Llaima

Compared with Piton de la Fournaise, the number of InSAR observations at Llaima is limited. Further, the specific environmental conditions (steep slopes, snow-covered summit, dense vegetation cover, and strong tropospheric artifacts) and limited amount of radar data available make it challenging to accurately measure ground surface displacement at Llaima with InSAR.

The 2007-2009 eruptive cycle is the best observed historical activity at Llaima volcano. Besides the sparse seismic monitoring, InSAR was the only other geophysical data that spanned

the whole period. Fournier et al. (2010) combined the L band PALSAR ALOS and the C band ENVISAT data in an attempt to search for deformation in all volcanic arcs of Latin America. They failed to identify any ground displacement associated with deep magmatic sources between 2003 and 2007, which is potentially due to poor temporal or spatial modelling as a result of interferogram decorrelation. But the authors detected a temporally complex combination of uplift and subsidence of up to 11 cm on the eastern flank of the Llaima volcano during December 2007, which is suggested to be related to the January 2008 eruption. They interpreted that the deformation on the eastern flank was the result of sector collapse and creep movement, in agreement with field observations. Bathke et al. (2011) applied a model-assisted phase unwrapping and modelling approach to noisy interferograms in order to characterize deformation sources. They worked on ENVISAT ASAR interferograms spanning the same period as those used by Fournier et al., (2010). But contrary to what was claimed by Fournier et al. (2010), Bathke et al. (2011) discovered two main deformation periods: a summit subsidence of ~ 10 cm from November 2003 to May 2007, followed by uplift of ~ 8 cm from May 2007 to January 2008. Through inverse modeling, the authors proposed that these volcanic deformation episodes were associated with a volume decrease of $10\text{-}46 \times 10^6 \text{ m}^3$, followed by a volume increase of $6\text{-}20 \times 10^6 \text{ m}^3$ of a magma body located beneath Llaima volcano, about 1 km to the southeast of the summit crater at 7 km depth.

To assess if the deformation signals observed by Bathke et al. (2011) were indeed associated with these activity periods, in this dissertation (Chapter 7; Remy et al., 2015), we analyzed ASAR and PALSAR data acquired during several periods of volcanic activity from 2003 to 2011. Our results do not reveal any detectable ground displacement related to a deep magmatic source under Llaima volcano in interferograms spanning the 2008 period of eruptive activity, which strongly differs from that of Bathke et al. (2011), who considered the atmospheric effects as being negligible in their study.

7.3 Revised interpretation of recent InSAR signals observed at Llaima volcano (Chile)

Paper published in **Geophysical Research Letters**

Remy, D., **Y. Chen**, J. L. Froger, S. Bonvalot, L. Cordoba, and J. Fustos (2015), Revised interpretation of recent InSAR signals observed at Llaima volcano (Chile), *Geophys. Res. Lett.*, 42, doi:10.1002/2015GL063872.



RESEARCH LETTER

10.1002/2015GL063872

Key Points:

- The 2008 Llaima eruption was not accompanied by InSAR-detectable displacement
- Tropospheric delay may produce volcano-wide effect up to 2.7 fringes in C band

Supporting Information:

- Figure S1
- Figure S2
- Figure S3
- Figures S1–S3 and Table S4

Correspondence to:

D. Remy,
remy@ird.fr

Citation:

Remy, D., Y. Chen, J. L. Froger, S. Bonvalot, L. Cordoba, and J. Fustos (2015), Revised interpretation of recent InSAR signals observed at Llaima volcano (Chile), *Geophys. Res. Lett.*, 42, 3870–3879, doi:10.1002/2015GL063872.

Received 18 MAR 2015

Accepted 1 MAY 2015

Accepted article online 7 MAY 2015

Published online 29 MAY 2015

Revised interpretation of recent InSAR signals observed at Llaima volcano (Chile)

D. Remy¹, Y. Chen¹, J. L. Froger², S. Bonvalot¹, L. Cordoba³, and J. Fustos^{4,5}

¹GET/UMR5563 (UPS, CNRS, IRD, CNES), Observatoire Midi-Pyrénées, Université P. Sabatier, Toulouse, France, ²LMV/UMR6524 (UBP-CNRS-IRD), Observatoire de Physique du Globe de Clermont-Ferrand, Université B. Pascal, Clermont-Ferrand, France, ³SERNAGEOMIN, Observatorio Volcanológico de Los Andes del Sur, Temuco, Chile, ⁴Department of Geophysics, University of Concepcion, Concepcion, Chile, ⁵School of Environmental Sciences, Catholic University of Temuco, Chile

Abstract We analyzed C band and L band interferometric synthetic aperture radar (InSAR) data acquired from 2003 to 2011 to search for volcanic deformations at Llaima volcano, Southern Andes (38.69°S, 71.73°W). There, specific environmental conditions (steep slopes, snow- or ice-capped summit, dense vegetation cover, and strong tropospheric artifacts) and limited amount of radar data available make it challenging to accurately measure ground surface displacement with InSAR. To overcome these difficulties, we first performed a careful analysis of the water vapor variations using Medium-Resolution Imaging Spectrometer and Moderate Resolution Imaging Spectroradiometer near-infrared water vapor products and then we inverted wrapped interferograms for both topographic correlated phase delays and a simple model source strength. In the light of our results, we conclude that there is no detectable ground displacement related to a deep magmatic source for the 2003–2011 period and that most of the fringes observed in the interferograms were produced by tropospheric delays.

1. Introduction

Since the pioneering study on Mount Etna by *Massonnet et al.* [1995], interferometric synthetic aperture radar (InSAR) data have been widely used to monitor surface displacement related to volcanic activity in various contexts [e.g., *Massonnet and Sigmundsson*, 2000; *Dzurisin*, 2003; *Sparks*, 2003; *Pritchard and Simons*, 2004; *Fournier et al.*, 2010; *Lu and Dzurisin*, 2014; *Pinel et al.*, 2014]. However, for many active volcanoes worldwide, and particularly for explosive andesitic volcanoes, obtaining reliable displacement measurements from InSAR remains a challenge. The main reason is that most of these volcanoes are located in intertropical or temperate areas where the combination of frequent precipitations and fertile soils favors the development of dense vegetation that causes temporal decorrelation of interferometric phases [*Pinel et al.*, 2011; *Ebmeier et al.*, 2013]. Snow cover, summit ice caps, or rapid gullying of loose ground can also contribute to temporal decorrelation [*Lu and Dzurisin*, 2014]. In addition, andesitic volcanoes often have steep slopes, resulting in strong geometric distortions (foreshortening—layover) in SAR images and thus in information loss. A last difficulty arises from changes in the phase delay related to spatial and temporal variations of the physical and chemical properties of the troposphere between successive SAR acquisitions. These changes result in long- and short-wavelength artifacts in the interferograms. Various approaches have been proposed in order to mitigate these tropospheric bias in the interferograms [*Zebker et al.*, 1997; *Beauducel et al.*, 2000; *Remy et al.*, 2003; *Pavez et al.*, 2006; *Puysségur et al.*, 2007; *Doin et al.*, 2009; *Fournier et al.*, 2011; *Pinel et al.*, 2011, 2014]. However, none of them have been entirely successful, and a reliable ready-made solution does not as yet exist. In this situation, discriminating real ground surface displacement from a tropospheric signal can represent a real challenge, and interpreting the interferometric signal in terms of magmatic process requires extreme caution.

Llaima (38.69°S, 71.73°W; 3125 m) is one of the largest Andean volcanoes, with an area of 500 km² and a volume of 400 km³ (Figure 1), and also one of the most active, with more than 48 known eruptions since 1640 [*Moreno et al.*, 2009]. This complex stratovolcano is built over an 8 km wide Holocene caldera by accumulation of basaltic and andesitic lava flows, andesitic and dacitic pyroclastic flows, pumice falls deposits, and lahar deposits [*Naranjo and Moreno*, 1991]. Llaima eruptions are characterized by Strombolian, Hawaiian, and infrequent sub-Plinian eruptions. At least seven eruptions of volcanic explosivity index (VEI) ≥ 3 occurred during the past 7000 years. Its recent activity has been characterized by

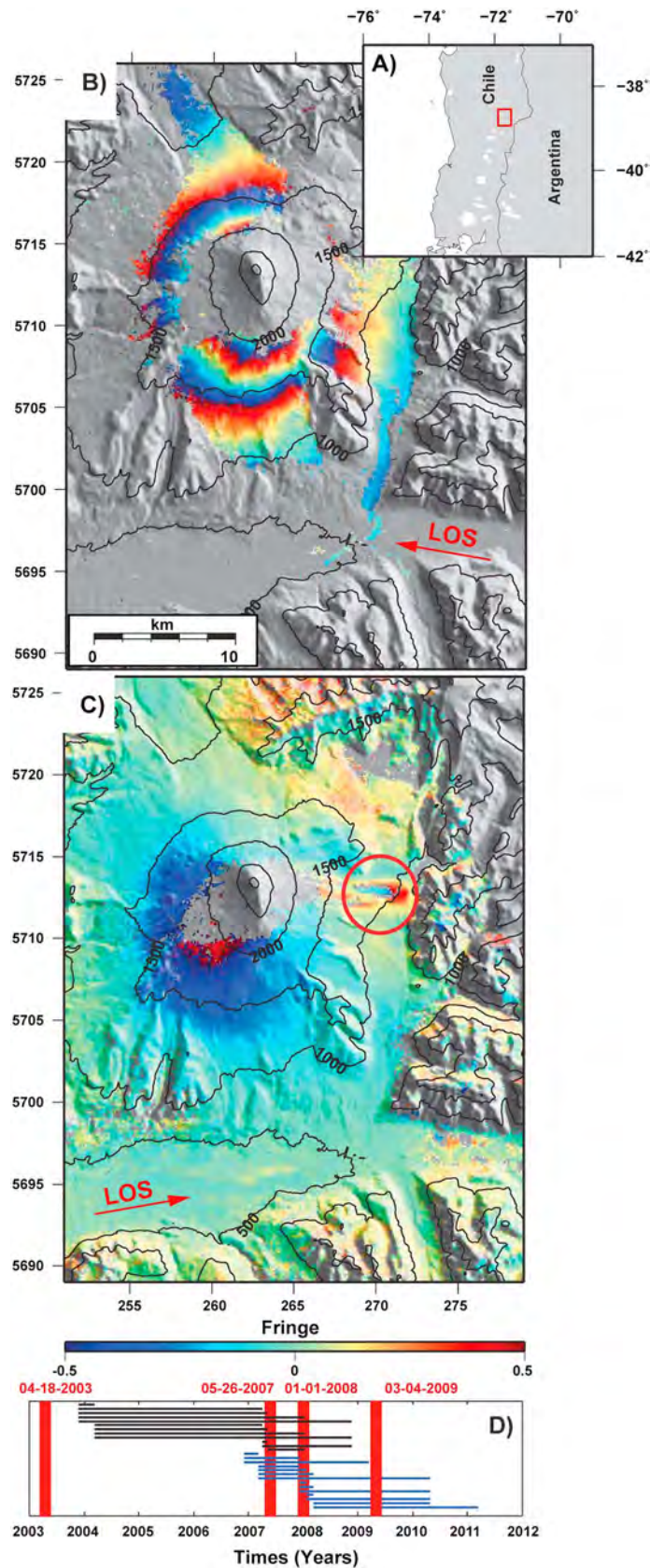


Figure 1

relatively small eruptions between 1979 and 2003 (11 eruptions with $VEI \leq 2$) and by a slight increase in explosivity for the last eruptive cycle, between March 2007 and June 2009 (with $2 \leq VEI \leq 3$) (*Smithsonian Institution Global volcanism report available at <http://www.volcano.si.edu>*). The largest eruption during this period of activity was on 1 January 2008, with a column reaching a height of 11 km accompanied by strong explosions and major seismic activity [Moreno *et al.*, 2009], followed by a second large eruption in 3 April 2009.

Using advanced synthetic aperture radar (ASAR) and Phased Array type L-band Synthetic Aperture Radar (PALSAR) interferograms spanning the 2002–2008 period, Fournier *et al.* [2010] failed to identify any ground displacements related to deep magmatic sources but detected a temporally complex combination of uplift and subsidence of up to 11 cm on the eastern flank of the volcano. The authors interpreted these displacements as being related to a slow landslide, in agreement with field observations. Using ASAR interferograms spanning the same period as those used by Fournier *et al.* [2010], Bathke *et al.* [2011] detected interferometric signals centered on the volcanic edifice. Contrary to what was claimed by Fournier *et al.* [2010], Bathke *et al.* [2011] interpreted these signals in terms of two main displacement episodes: a summit subsidence of ~ 10 cm from November 2003 to May 2007, followed by uplift of ~ 8 cm from May 2007 to January 2008. Through inverse modeling, the authors proposed that these volcanic deformation episodes were associated with a volume decrease of $10\text{--}46 \times 10^6 \text{ m}^3$ followed by a volume increase of $6\text{--}20 \times 10^6 \text{ m}^3$ of a magma body located beneath Llaima volcano.

In this study, we analyzed ASAR and PALSAR data acquired during several periods of volcanic activity from 2003 to 2011, with the objective to assess if ground surface displacements were indeed associated with these activity periods. As a significant proportion of the Llaima flanks' surface is covered by dense broadleaf and coniferous evergreen forest, the ASAR interferograms are generally heavily affected by phase decorrelation. As such decorrelation effects hardly complicate the unwrapping phase operation, we applied the General Inversion for Phase Technique (GIPhT) proposed by Feigl and Thurber [2009] to model the phase data directly without unwrapping. Moreover, given that Llaima volcano is close to the ocean, the atmospheric conditions can be extremely variable both temporally and spatially, leading to possible strong atmospheric artifacts in the interferograms. This is why we paid special attention to the detection of such possible artifacts by performing a close inspection of the Medium-Resolution Imaging Spectrometer (MERIS) and of the Moderate Resolution Imaging Spectroradiometer (MODIS/Terra) images collected over the study area. Indeed, the Level 2 data products of both spaceborne spectrometers include images of precipitable water vapor (PWV) from which it is possible estimating the tropospheric phase delay in InSAR data [Li *et al.*, 2003, 2006].

2. InSAR Observations

We analyzed six images of C band SAR data from the radar ASAR on board the European Space Agency (ESA) satellite Envisat (descending track 10, swath I2) and eight images of L band SAR data from the PALSAR radar on board the Japanese space agency (Japan Aerospace Exploration Agency (JAXA)) satellite ALOS1 (ascending track 117, mode fine beam single polarization) acquired between 2003 and 2011 over the study area (see Figure 1). Differential interferograms were generated with the DIAPASON software ©Centre National d'Etudes Spatiales/Altamira-information, 1996] using the two pass method described by Massonnet and Feigl [1998]. The orbital contribution was removed using precise orbit data from ESA Doppler Orbitography and Radio-positioning Integrated by Satellite (for ASAR interferograms) or orbit state vectors provided in the image header (for PALSAR interferograms). The topographic contribution was removed using the 3 arcsec Shuttle Radar Topographic Mission digital elevation model (DEM). PALSAR and ASAR

Figure 1. Example of ASAR and PALSAR interferograms overlain onto a shaded relief map computed for Llaima in southern Chile. (a) Reference map of the study area. (b) ASAR interferogram (25 November 2003 to 3 April 2007). (c) PALSAR interferogram (6 March 2007 to 11 March 2009). Each fringe (full color cycle) represents 2.83 cm (ASAR) or 11.81 (PALSAR) of range change between the ground and the satellite. Areas where the interferometric coherence is lost or not covered by the track ALOS 117 are shown in grey. Each fringe (full color cycle) represents 2.83 cm (ASAR) or 11.81 (PALSAR) of range change between the ground and the satellite. The black lines show elevation contours every 500 m. Coordinates are expressed in UTM-WGS84 coordinates (19 zone south). The satellite to ground radar line of sight is shown with a red arrow. (d) Time span covered by the 12 ASAR interferograms (in black) and the 14 PALSAR interferograms (in blue) used in this study. The vertical red lines show the timing of the eruptions which occurred during the 2003–2012 period.

interferograms were downsampled during processing to eight looks in azimuth and two looks in range, respectively. We obtained a set of 12 ASAR interferograms produced by data pairs characterized by an altitude of ambiguity (H_a) greater than 30 m (i.e., perpendicular baseline lower than 300 m) suitable for interferometry purpose. At the same time, 14 interferograms were generated by PALSAR pairs having an H_a greater than 40 m, corresponding to a perpendicular baseline lower than 1500 m.

Figure 1 shows a selection of two ASAR and PALSAR interferograms (the full set of interferograms used in this study is shown in Figures S1 and S2 in the supporting information). As expected, the PALSAR interferograms have a higher coherence than the ASAR one over the study area, as the L band wave of PALSAR penetrates more deeply into the vegetation cover and interacts with more stable scatterers [Rosen *et al.*, 1996]. The coherent areas on the C band interferograms are clearly less extended and correspond mainly to recent barren lava flows. On the southern half of the volcano summit, both bands of SAR data are heavily affected by phase decorrelation due to the presence of a glacier.

Most of the calculated interferograms exhibit a concentric pattern of fringes centered on the volcano, as previously observed by Bathke *et al.* [2011] (Figure 1 and Figures S1 and S2 in the supporting information). As the magnitude of the observed phase gradient is not correlated with the H_a in both ASAR and PALSAR interferograms, we concluded that this signal does not result from topography errors in the DEM. On the PALSAR interferogram shown in Figure 1c, we can also see the short-wavelength signal pattern on the eastern flank of the volcano (circled zone) previously identified by Fournier *et al.* [2010]

3. Analysis of Near-Infrared Water Vapor Products

Before making a further detailed analysis of the InSAR data, we analyzed the magnitude and the behavior of the water vapor variation over the study area using MERIS and MODIS PWV estimates [Li *et al.*, 2006, 2012; Remy *et al.*, 2011], as the tropospheric delay (especially that due to water vapor) is considered as a major source of error source in InSAR [Zebker *et al.*, 1997; Hanssen, 2001; Wadge *et al.*, 2002; Li *et al.*, 2012]. Nevertheless, the estimation of atmospheric signal in interferograms using PWV estimates is only possible during the daytime and under cloud-free conditions. Consequently, the analysis of PWV estimates was not possible for PALSAR data as they were acquired during the night (~ 1 A.M. local time). Therefore, we analyzed MERIS near-IR products in reduced resolution mode (nadir pixel of about 1.04 km across track by 1.2 km along track) acquired simultaneously with the ASAR images used in this study. Where possible, we also used the independent information provided by MODIS images acquired less than an hour after the ASAR acquisitions over the study area. We computed the two-way SAR slant path delay (SPD) signal induced by atmospheric water vapor using the relation given by Zebker *et al.* [1997]:

$$\text{SPD} = \frac{\text{PWV}}{\Pi \cos \theta_{\text{inc}}} \quad (1)$$

where the SPD and the PWV are expressed in meter and θ_{inc} is the incidence angle of the ASAR radar beam ($\sim 23^\circ$). Π is an atmospheric parameter that depends on the meteorological profile of pressure, temperature, and moisture along the radar beam path [Bevis *et al.*, 1996]. Since the variability of Π is generally more than an order of magnitude lower than that of the PWV, Π may be treated, in a first approximation, as a constant with a value of about 0.15 [Bevis *et al.*, 1996]. Figure 2a shows the resulting SPD maps estimated from MERIS satellite data acquired over Llaima volcano in the same epochs than the SAR images used to form the interferogram shown in Figure 1b. The whole set of SPD maps is shown in Figure S3 in the supporting information. The two SPD maps presented in Figure 2a show contrasting amplitude and spatial features for the estimated phase delays computed over the study area. They reveal that the amplitude of the atmospheric phase delay due to variability in tropospheric water vapor concentration could be particularly strong (up to 12 cm) and variable in time. The low spatial resolution of MERIS data, with respect to ASAR data, does not reliably mitigate the tropospheric component in ASAR interferograms. Nevertheless, the MERIS-derived SPD maps provide useful indications about the structure and magnitude of phase delays related to vertically stratified water vapor in our subset of ASAR images. Figure 2a also shows the plot of SPD values estimated from MERIS (blue dots) and MODIS (red dot), data versus elevation. In both cases, the estimated SPD values vary strongly with the topography and are clearly related to topography-dependent water vapor variations. The strong dependence between the SPD and the elevation in mountainous regions is the basis for one of the traditional first order approaches used to mitigate atmospheric effects in interferograms. This approach consists of removing a

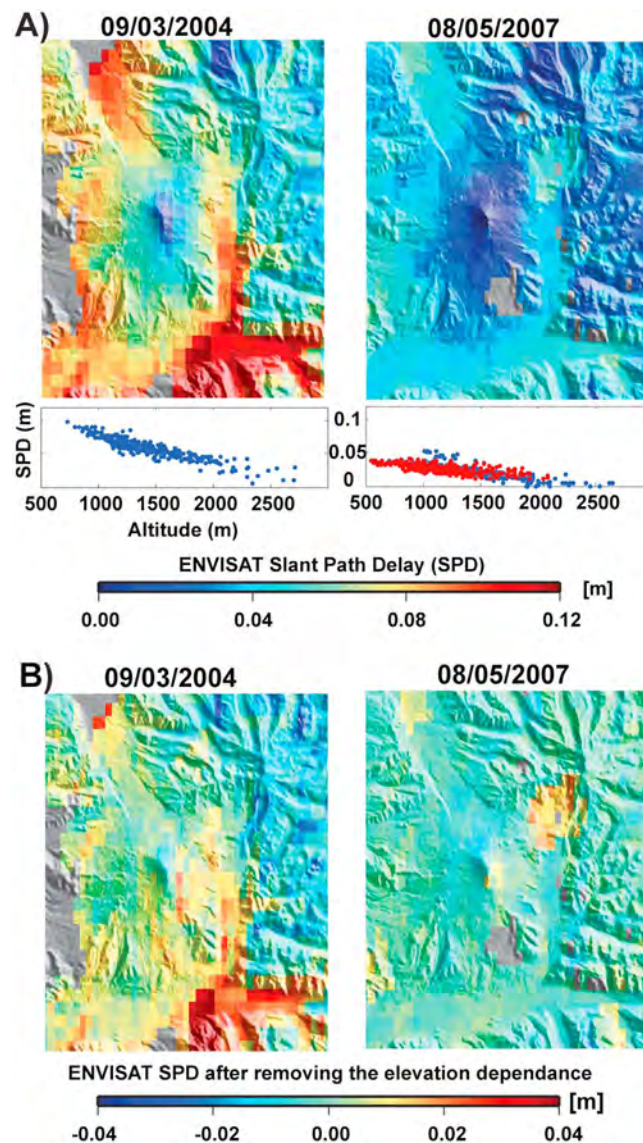


Figure 2. ASAR slant path delay estimated from MERIS satellite data acquired on 9 March 2003 and on 8 May 2007, respectively. (a) The SPD maps (top) and their respective graphs of SPD values versus elevation (bottom). The blue and red dots show values estimated from MERIS and MODIS data, respectively. Note the good agreement between the two PWV products. (b) The same fields as in Figure 2a but after removal of the elevation dependence. SPD maps are shown superimposed on the shaded-relief image, and areas that lack MERIS data are uncolored. The SPD values were interpolated using a nearest neighbor interpolation to improve the graphical quality of the figure. Note that a different color scale is used in order to better contrast the residual SPD maps.

4. Modeling Strategy

Due to the large surface area affected by phase decorrelation in the Llaima region, we did not use the standard approach of unwrapping fringe maps. We chose instead to apply the GIPhT *Feigl and Thurber* [2009] method that allows for a direct comparison between displacement models and wrapped phases and provides a robust determination both of the model misfit and of the model parameter uncertainties. In the absence of constraints on the rheological properties of the crust and on the geometry of the

model of SPD deduced from some linear adjustments of the dependence between elevation and the interferometric phase [Beauducel *et al.*, 2000; Remy *et al.*, 2003; Pinel *et al.*, 2011]. Figure 2b reveals that applying this approach significantly reduces the variance of the observed SPD signals in both SPD maps. Obviously, this simple elevation-dependent model is not able to capture complicated tropospheric moisture patterns. For example, the residual map derived from MERIS data acquired on 3 March 2004 reveals a spatial pattern of underprediction in the model, which extends from the summit of volcano to the southeastern valley. The reason for the presence of this pattern is unknown but it could be related to a local flow of air induced by the strong topography, as in the case of Mount Etna, Italy [Wadge *et al.*, 2002] or Soufrière Hills volcano, Montserrat [Wadge *et al.*, 2006].

According to the amplitude of the topography-dependant delay estimated from MERIS data, our analysis suggests that the set of ASAR data can be divided in two subgroups (see Figure S3 in the supporting information). The first group is composed of the images acquired on 25 November 2003, 9 March 2004, and 18 November 2008, which are characterized by strong negative delay-elevation gradients of about -0.04 m per 1000 m of elevation. On other hand, the images acquired on 3 April 2007 and 8 May 2007 are characterized by lower negative delay-elevation gradients of about -0.02 m per 1000 m of elevation. This leads us to expect that all the interferograms formed using an image belonging to the first group, and those belonging to the second group may have been contaminated by significant vertical stratification effects.

magma chamber, we used a simple point source model embedded in a homogeneous elastic half-space [Mogi, 1958]. In order to reduce the number of parameters and the trade-off between source depth and source strength, we assumed a deformation source located at a fixed position 7 km depth below the summit, consistent with the one proposed by Bathke *et al.* [2011]. We also considered the atmosphere over the study area to be approximately horizontally homogeneous, thus inducing SPD correlated to elevation, at least at the first order [Remy *et al.*, 2003, 2011]. Our previous analysis of spatial and temporal variations of water vapor distribution from MERIS and MODIS data has shown that this correlation can be modeled satisfyingly by a simple linear equation and that the tropospheric contribution to InSAR data can be reduced significantly by removing this model, although some local turbulent effects could remain. The forward model for each interferogram is then defined by two main parameters: one for the displacement source (volume change) and one for the phase-elevation gradient corresponding to atmospheric SPD. Before inverting PALSAR interferograms, we corrected them for a two-dimensional linear ramp, after masking out the region of the Llama volcano, in order to remove the long-wavelength signals related to orbital errors. Due to the large extent of incoherent areas in the ASAR interferograms, this correction was not possible. Even though we used precise orbits that are believed to be accurately determined, our own experience and other studies showed that significant residual orbital contribution can nevertheless remain [Froger *et al.*, 2007; Bahr and Hanssen, 2012; Remy *et al.*, 2014]. So for the ASAR interferograms, we added two additional parameters (horizontal components of residual orbital phase gradient) to the forward model. To invert the model parameters for each interferogram, we selected a set of coherent pixels (i.e., coherency > 0.75) equally distributed in elevation for every 50 m elevation layer (100 pixels per layer). Obviously, as it is not based on continuous spatial sampling, such an approach is valid only because phase variation in the range of 50 m altitude bands is lower than 2π , as confirmed on the interferograms. The displacement vectors computed with the source point approach [Mogi, 1958] at the position of the coherent selected pixels were then converted into phase values by projection along the satellite line of sight and wrapped around the half wavelength. We solved the inverse problem by maximizing the following fitness function given by Vadon and Sigmundsson [1997] and Beauducel *et al.* [2000]:

$$R(m) = \frac{1}{n} \left| \sum_{i=1}^n e^{j2\pi(\phi_{\text{obs}}^i - \phi_{\text{calc}}^i(m))} \right| \quad (2)$$

where ϕ_{obs}^i is the observed phase and $\phi_{\text{calc}}^i(m)$ is the computed phase using a model m for a given pixel i . As this fitness function is highly nonlinear particularly because of the phase ambiguity, we used a genetic algorithm to explore the parameters space. The inversion procedure allows both the determination of the best fitted model parameters and their confidence interval for each interferogram. To determine the uncertainties of the estimated parameters we used the parametrical statistical tests proposed by Mardia and Jupp [2000] and implemented by Feigl and Thurber [2009] in GIPHT. To enhance reliability, we adjusted the model parameters using a weighted least squares method where the weights are inversely proportional to the variance estimated by the inversion procedure [Remy *et al.*, 2003]. Furthermore, this allows us to obtain a value of volume change and of vertical phase gradient for each ASAR image relative to the image acquired on 25 November 2003, and for each PALSAR image relative to the image acquired on 6 March 2007.

5. Results

Figure 3a show the data, model, and residual for the two selected ASAR and PALSAR interferograms spanning the period November 2003 to December 2007, covering the volcanic activity which started in March 2007 (see Figures S1 and S2 in the supporting information for the whole data set). Table S4 in the supporting information also presents the best fitting source characteristics and elevation-dependent path delays for each interferogram and their uncertainties obtained by the least squares adjustment. The RMS of the residual ASAR data ranges from 3 to 7 mm, while the RMS of the residual PALSAR data is about 3 times greater, ranging from 11 to 20 mm. In some residual maps spatial patterns of strong residuals are still present, indicating that the model is not a good fit for the data, due to the simplicity of the adopted tropospheric and displacement models. We think that these spatial patterns are generally related to the complexity of the atmospheric behavior in the study area. A notable exception concerns the temporally complex ground displacement pattern on the eastern flank observed in all PALSAR interferograms encompassing the eruption of January 2008 (location shown by a circle in Figure 1c and Figure S2 in the

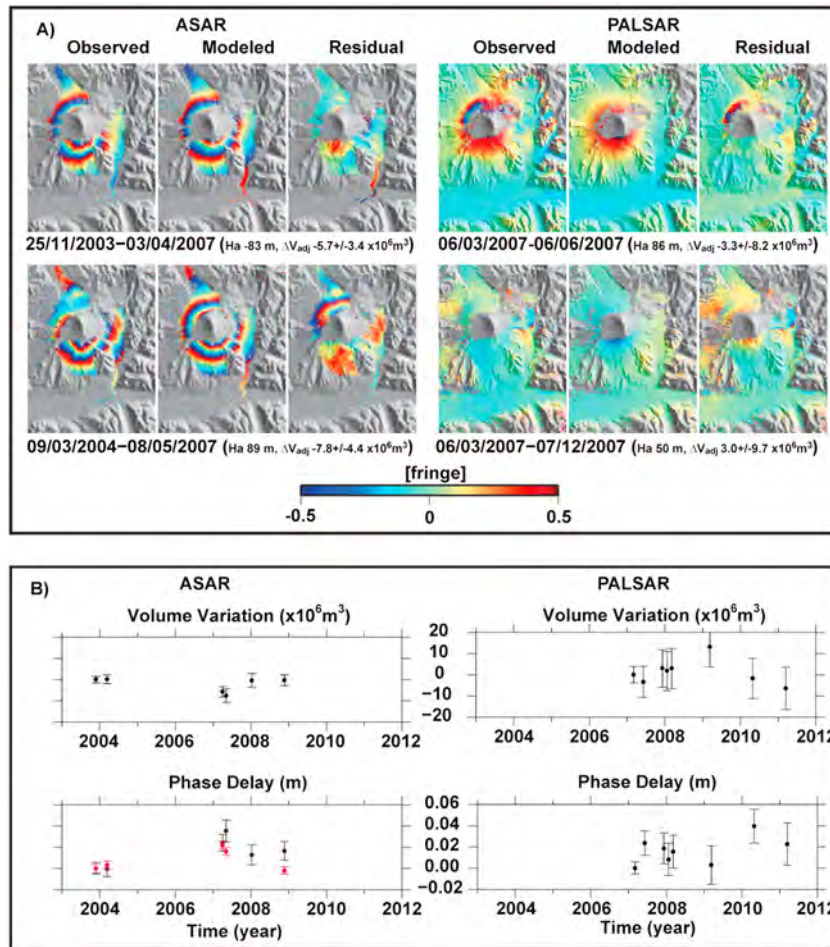


Figure 3. InSAR data and inversion results for Llaima volcano. (a) Observed, modeled, and residual between observed and modeled ground displacements. (left) ASAR interferograms scene pairs 25 November 2003 to 3 April 2007 and 9 November 2004 to 8 May 2007. (right) ALOS interferograms scene pairs 6 March 2007 to 6 June 2007 and 6 March 2007 to 7 December 2007. Each fringe (full color cycle) represents 2.83 cm (ASAR) or 11.81 (PALSAR) of range change between the ground and the satellite. The black lines show elevation contours every 500 m. Areas that lack interferometric coherence are uncolored. Interferometric phase images are shown superimposed on the shaded-relief image. In all these examples, the elevation-dependent model largely explains the observed interferometric signals. The ΔV_{adj} is the adjusted volume change and its standard deviation calculated by global L2 adjustment of the inferred values. In order to improve the quality of the figure, the interferograms were filtered using an adaptive radar interferogram filter [Goldstein and Werner, 1998]. (b) Estimated volume changes (ΔV) and linear contribution of tropospheric effects resulting from the adjustment with respect to the reference image acquired on 25 November 2003 for ASAR and on 6 March 2007 for PALSAR. ASAR slant path delays (SPD) estimated from MERIS data are also shown in red.

supporting information). As already mentioned, *Fournier et al.* [2010] interpreted this deformation to be related to a slow landslide triggered by the 2008 eruption.

Figure 3b shows a synthesis of the results obtained for both the ASAR and PALSAR time series, with the volume change, the elevation-related phase gradient, and their 1 sigma error bars given by the least squares adjustment. The amplitude of the inferred phase delays induced by vertically stratified water vapor in the troposphere is comparable for both the ASAR and PALSAR data sets, with a maximum absolute value of up to about 3.5 cm per 1000 m of elevation, which can produce up to 2.7 C band fringes or 0.6 L band fringes over Llaima volcano. These estimations are consistent with those obtained in the analysis carried out using the MERIS and MODIS data (section 3) and are illustrated clearly in Figure 3b by the good agreement between the ASAR slant path delays estimated from the MERIS data (in red) and those obtained from the inversion of ASAR data. This maximum phase delay of 3.5 cm per 1000 m of

elevation is large, although not exceptional, and such large effects have been documented on various sites: Mount Cameroun [*Heleno et al.*, 2010]; Sakurajima, Japan [*Remy et al.*, 2003]; Soufrière Hills [*Wadge et al.*, 2006], and Colima, Mexico [*Pinel et al.*, 2011]. From these results, we would urge caution in the interpretation of transient ground displacement lower than ± 7 cm on the scale of the whole volcanic edifice, when observed in a single interferogram.

The volume changes inferred by the inversion of interferograms for the volume change are generally small and range from -7.7 to $13 \times 10^6 \text{ m}^3$ during the 2003–2011 period. The uncertainties (1σ) of the adjusted volume changes inferred by the ASAR and PALSAR data are on average about $\pm 3 \times 10^6 \text{ m}^3$ and $\pm 9 \times 10^6 \text{ m}^3$, respectively. The difference in uncertainty in the parameter estimation using L band and C band data is explained by the difference in range precision between both bands [*Sandwell et al.*, 2008]. None of the PALSAR interferograms spanning the December 2006 to March 2011 period shows signals related to a volume change within a deformation source. Through inverse modeling using ASAR data, we estimated that a magma inflation source located at 7 km depth below the summit may be subjected to a volume decrease of 0.7 to $11 \times 10^6 \text{ m}^3$, at a confidence level of 95%, between November 2003 and May 2007. However, due to the limitation of InSAR for surface change detection related to the magnitude of atmospheric perturbations in the Llaima area, as highlighted in this study, the low-volume change inferred by the inversion of SAR data must be interpreted with caution. Furthermore, it is also noteworthy that all the ASAR interferograms, which show a strong interferometric signal, are produced using ASAR images for which the difference of the phase-elevation gradients estimated from MERIS data is significant. This leads us to consider that there is no clear evidence of ground surface displacement caught by InSAR data for the 2003–2011 period and that most of the fringes observed in the interferograms of Llaima volcano are due to tropospheric effects rather than to ground surface displacements.

Different explanations could be invoked for the lack of ground displacement observed by InSAR during eruptive activity at Llaima volcano, including displacement with amplitude below the accuracy of the sensors, related to a deep source, or displacement with extension limited to the incoherent upper part of the edifice, related to a very shallow source such as a magma plug in the upper part of a conduit, or short-lived preeruptive inflation compensated by coeruptive or posteruptive deflation in a single orbital cycle [*Lu and Dzurisin*, 2014].

6. Conclusion

This study demonstrates that the applications of InSAR for detecting transient deformation induced by the activity of andesitic stratovolcanoes remain a challenge. In the Llaima area, the sparsity of the InSAR samples, the reduced surface of the coherent area, and the transient nature of the displacement expected prevented us from using stacking or Small Baseline Subset techniques [*Berardino et al.*, 2003; *Hooper*, 2008], which would make it possible to reduce and enhance the signal-to-noise ratio of the interferometric signal. This led us to carefully analyze the MERIS and MODIS water vapor products in order to assess variable phase delay through the troposphere, which can induce significant uncertainties (in the order of centimeters) in the measured displacements for a single image. This also led us to use the statistical approach proposed by *Feigl and Thurber* [2009] for analyzing wrapped phase data.

Our study does not reveal any detectable ground displacement related to a deep magmatic source under Llaima volcano in interferograms spanning the 2008 period of eruptive activity. It is worth noting that our interpretation strongly differs from that of *Bathke et al.* [2011], who considered the atmospheric effects as being negligible in their study. Our results strengthen those of *Fournier et al.* [2010] because they are now supported by a rigorous analysis of tropospheric phase delay effects related to water vapor variations in SAR interferograms.

Future geodetic studies from InSAR data on Llaima will benefit greatly from the first continuous GPS network on this volcano, set up in 2012 by the Southern Andean Volcano Observatory (Observatorio Volcanológico de Los Andes del Sur). Ground surface displacement and tropospheric delays estimated by InSAR could then be compared with independent measurements provided by the permanent GPS network, significantly improving the potential to monitor volcanic events on Llaima volcano using InSAR.

Acknowledgments

ASAR data were provided by the European Space Agency (ESA) through the project Envisat-AO#857 and Category 1 #2899. PALSAR data from the ALOS satellite mission operated by the Japanese Aerospace Exploration Agency (JAXA) were used under the terms and conditions of the fourth ALOS 2 Research Announcement (project #1142). This work was supported by the Institut de Recherche pour le Développement and the Centre National d'Études Spatiales (CNES). Some of the figures in this paper were made using Generic Mapping Tools [Wessel and Smith, 1991]. Many thanks to M. Pritchard for his useful reviews, comments, and very constructive remarks that greatly improve this paper.

The Editor thanks Matthew Pritchard and an anonymous reviewer for their assistance in evaluating this paper.

References

- Bahr, H., and R. Hanssen (2012), Reliable estimation of orbit errors in spaceborne SAR interferometry, *J. Geod.*, *86*(12), 1147–1164.
- Bathke, H., M. Shirzaei, and T. R. Walter (2011), Inflation and deflation at the steep-sided Llaima stratovolcano (Chile) detected by using InSAR, *Geophys. Res. Lett.*, *38*, L10304, doi:10.1029/2011GL047168.
- Beauducel, F., P. Briole, and J. L. Froger (2000), Volcano wide fringes in ERS synthetic aperture radar interferograms of Etna (1992–1999): Deformation or tropospheric effect?, *J. Geophys. Res.*, *105*, 16,391–16,402, doi:10.1029/2000JB900095.
- Berardino, P., M. Costantini, G. Franceschetti, A. Iodice, L. Pietranera, and V. Rizzo (2003), Use of differential SAR interferometry in monitoring and modelling large slope instability at Maratea (Basilicata, Italy), *Eng. Geol.*, *68*, 31–51.
- Bevis, M., S. Chiswell, S. Businger, T. A. Herring, and Y. Bock (1996), Estimating wet delay using numerical weather analysis and predictions, *Radio Sci.*, *31*, 447–487, doi:10.1029/96RS00008.
- ©CNES/Altamira-information (1996), Philosophie et mode d'emploi de la chaîne logicielle interférométrique DIAPASON, Toulouse, France.
- Doin, M.-P., C. Lasserre, G. Peltzer, O. Cavalié, and C. Doubre (2009), Corrections of stratified tropospheric delays in SAR interferometry: Validation with global atmospheric models, *J. Appl. Geophys.*, *69*(1), 35–50.
- Dzurisin, D. (2003), A comprehensive approach to monitoring volcano deformation as a window on the eruption cycle, *Rev. Geophys.*, *41*(1), 1001, doi:10.1029/2001RG000107.
- Ebmeier, S. K., J. Biggs, T. A. Mather, and F. Amelung (2013), Applicability of InSAR to tropical volcanoes: Insights from Central America, *Geol. Soc. London Spec. Publ.*, *380*, 15–37.
- Feigl, K., and H. Thurber (2009), A method for modelling radar interferograms without phase unwrapping: Application to the *M* 5 Fawnskin, California earthquake of 1992 December 4, *Geophys. J. Int.*, *176*(2), 491–504.
- Fournier, T. J., M. E. Pritchard, and S. N. Riddick (2010), Duration, magnitude, and frequency of subaerial volcano deformation events: New results from Latin America using InSAR and a global synthesis, *Geochem. Geophys. Geosyst.*, *11*, Q01003, doi:10.1029/2009GC002558.
- Fournier, T. J., M. E. Pritchard, and N. Finnegan (2011), Accounting for atmospheric delays in InSAR data in a search for long-wavelength deformation in South America, *IEEE Trans. Geosci. Remote Sens.*, *49*(10), 3856–3867.
- Froger, J. L., D. Remy, S. Bonvalot, and D. Legrand (2007), Two scales of inflation at Lastarria-Cordon del Azufre volcanic complex, central Andes, revealed from ASAR-ENVISAT interferometric data, *Earth Planet. Sci. Lett.*, doi:10.1016/j.epsl.2006.12.012.
- Goldstein, R. M., and C. L. Werner (1998), Radar interferogram filtering for geophysical applications, *Geophys. Res. Lett.*, *25*, 4035–4038, doi:10.1029/1998GL900033.
- Hanssen, R. (2001), *Radar Interferometry Data Interpretation and Errors Analysis*, 308 pp., Kluwer Acad., Dordrecht, Netherlands.
- Heleno, S. I. N., C. Frischknecht, N. d'Oreye, J. N. P. Lima, B. Faria, R. Wall, and F. Kervyn (2010), Seasonal tropospheric influence on SAR interferograms near the ITCZ—The case of Fogo Volcano and Mount Cameroon, *J. Afr. Earth Sci.*, *58*(5), 833–856.
- Hooper, A. (2008), A multi-temporal InSAR method incorporating both persistent scatterer and small baseline approaches, *Geophys. Res. Lett.*, *35*, L16302, doi:10.1029/2008GL034654.
- Li, Z., J. P. Muller, and P. Cross (2003), Comparison of precipitable water vapor derived from radiosonde, GPS and Moderate-Resolution Imaging Spectroradiometer measurements, *J. Geophys. Res.*, *108*(D20), 4651, doi:10.1029/2003JD003372.
- Li, Z., E. Fielding, P. Cross, and J.-P. Muller (2006), Interferometric synthetic aperture radar atmospheric correction: Medium Resolution Imaging Spectrometer and advanced synthetic aperture radar integration, *Geophys. Res. Lett.*, *33*, L06816, doi:10.1029/2005GL025299.
- Li, Z., P. Pasquali, A. Cantone, A. Singleton, G. Funning, and D. Forrest (2012), MERIS atmospheric water vapor correction model for wide swath interferometric synthetic aperture radar, *IEEE Geosci. Remote Sens. Lett.*, *9*(2), 257–261.
- Lu, Z., and D. Dzurisin (2014), *InSAR Imaging of Aleutian Volcanoes: Monitoring a Volcanic Arc From Space*, Springer Praxis Books, *Geophys. Sci.*, 388 pp., Springer, New York.
- Mardia, K. V., and P. E. Jupp (2000), *Directional Statistics*, 429 pp., Wiley, New York.
- Massonnet, D., and K. L. Feigl (1998), Radar interferometry and its application to changes in the Earth's surface, *Rev. Geophys.*, *36*, 441–500, doi:10.1029/97RG03139.
- Massonnet, D., and F. Sigmundsson (2000), Remote sensing of volcano deformation by radar interferometry from various satellites, in *Remote Sensing of Active Volcanism*, *Geophys. Monogr.*, edited by P. Mouginiis-Mark, J. A. Crisp, and J. H. Fink, pp. 207–221, AGU, Washington, D. C.
- Massonnet, D., P. Briole, and A. Arnaud (1995), Deflation of Mount Etna monitored by spaceborne radar interferometry, *Nature*, *375*, 567–570.
- Mogi, K. (1958), Relations between the eruptions of various volcanoes and the deformation of the ground surface around them, *Bull. Earthquake Res. Inst., Univ. Tokyo*, *36*, 99–134.
- Moreno, H., J. A. Naranjo, P. Pena, J. Munoz, D. Basualto, D. Delgado, C. Gallegos, C. Dungan, and C. Bouvet de Maisonneuve (2009), El ciclo eruptivo 2007–2009 del volcan Llaima, Andes del sur, paper presented at XII Congreso geológico Chileno, Santiago, 22–26 Nov.
- Naranjo, J. A., and H. Moreno (1991), Actividad explosiva postglacial en el Volcán Llaima, Andes del Sur (38°45'S), *Rev. Geol. Chile*, *18*(1), 69–80.
- Pavez, A., D. Remy, S. Bonvalot, M. Diament, G. Gabalda, J. L. Froger, P. Julien, D. Legrand, and D. Moisset (2006), Insight into ground deformation at Lascar volcano (Chile) from SAR interferometry, photogrammetry and GPS data: Implication on volcano dynamics and future space monitoring, *Remote Sens. Environ.*, *100*, 307–320.
- Pinel, V., A. Hooper, S. De la Cruz-Reyna, G. Reyes-Davila, M. P. Doin, and P. Bascou (2011), The challenging retrieval of the displacement field from InSAR data for andesitic stratovolcanoes: Case study of Popocatepetl and Colima Volcano, Mexico, *J. Volcanol. Geotherm. Res.*, *200*(1–2), 49–61.
- Pinel, V., M. Poland, and A. Hooper (2014), Volcanology: Lessons learned from synthetic aperture radar imagery, *J. Volcanol. Geotherm. Res.*, doi:10.1016/j.jvolgeores.2014.10.010.
- Pritchard, M. E., and M. Simons (2004), An InSAR-based survey of volcanic deformation in the central Andes, *Geochem. Geophys. Geosyst.*, *5*, Q02002, doi:10.1029/2003GC000610.
- Puysségur, B., R. Michel, and J. P. Avouac (2007), Tropospheric phase delay in interferometric synthetic aperture radar estimated from meteorological model and multispectral imagery, *J. Geophys. Res.*, *112*, B05419, doi:10.1029/2006JB004352.
- Remy, D., S. Bonvalot, P. Briole, and M. Murakami (2003), Accurate measurement of tropospheric effects in volcanic area from SAR interferometry data: Application to Sakurajima volcano (Japan), *Earth Planet. Sci. Lett.*, *213*(3–4), 299–310.
- Remy, D., M. Falvey, S. Bonvalot, M. Chlieh, G. Gabalda, J. L. Froger, and D. Legrand (2011), Variability of atmospheric precipitable water in northern Chile: Impacts on interpretation of InSAR data for earthquake modeling, *J. South Am. Earth Sci.*, *31*(2–3), 214–226.
- Remy, D., J. L. Froger, H. Perfettini, S. Bonvalot, G. Gabalda, F. Albino, V. Cayol, D. Legrand, and M. D. Saint Blanquat (2014), Persistent uplift of the Lazufre volcanic complex (central Andes): New insights from PCAIM inversion of InSAR time series and GPS data, *Geochem. Geophys. Geosyst.*, *15*, 3591–3611, doi:10.1002/2014GC005370.

- Rosen, P., S. Hensley, H. Zebker, F. H. Webb, and E. J. Fielding (1996), Surface deformation and coherence measurements of Kilauea volcano, Hawaii, from SIR-C radar interferometry, *J. Geophys. Res.*, *101*, 23,109–23,125, doi:10.1029/96JE01459.
- Sandwell, D. T., D. Myer, R. Mellors, M. Shimada, B. Brooks, and J. Foster (2008), Accuracy and resolution of ALOS interferometry: Vector deformation maps of the Father's Day intrusion at Kilauea, *IEEE Trans. Geosci. Remote Sens.*, *46*(11), 3524–3534.
- Sparks, R. S. J. (2003), Forecasting volcanic eruptions, *Earth Planet. Sci. Lett.*, *210*, 1–15.
- Vadon, H., and F. Sigmundsson (1997), Crustal deformation from 1992 to 1995 at the Mid-Atlantic Ridge, southwest Iceland mapped by satellite radar interferometry, *Science*, *275*, 193–197.
- Wadge, G., G. S. Mattioli, and R. A. Herd (2006), Ground deformation at Soufriere Hills Volcano, Montserrat during 1998–2000 measured by radar interferometry and GPS, *J. Volcanol. Geotherm. Res.*, *152*(1–2), 157–173.
- Wadge, G., et al. (2002), Atmospheric models, GPS and InSAR measurements of the tropospheric water vapour field over Mount Etna, *Geophys. Res. Lett.*, *29*(19), 1905, doi:10.1029/2002GL015159.
- Wessel, P., and W. H. F. Smith (1991), Free software help map and display data, *Eos Trans. AGU*, *72*(41), 441–446, doi:10.1029/90EO00319.
- Zebker, H. A., P. A. Rosen, and S. Hensley (1997), Atmospheric effects in interferometric synthetic aperture radar surface deformation and topographic maps, *J. Geophys. Res.*, *102*, 7547–7563, doi:10.1029/96JB03804.

Revised interpretation of recent InSAR signal observed at Llaima volcano (Chile)

D. Remy ^(a), Y. Chen ^(a), J.L Froger ^(b), S. Bonvalot ^(a), M. Cordoba ^(c), J. Fustos ^(d)

^(a) GET / UMR5563 (UPS, CNRS, IRD, CNES) ; Obs. Midi-Pyrénées, Université P. Sabatier, Toulouse, France.

^(b) LMV / UMR6524 (UBP-CNRS-IRD), Obs. de Physique du Globe de Clermont-Ferrand, Université B. Pascal, Clermont-Ferrand, France

^(c) *SERNAGEOMIN, Observatorio Volcanológico de Los Andes del Sur (OVDAS), Rudecindo Ortega 03850, Temuco, Chile.*

^(d) Department of Geophysics (DGEO) University of Concepcion, Concepcion, Chile

Contents of this file

Figure S1, S2 S3 and their caption.

Tables S4

Additional Supporting Information (Files uploaded separately)

none

Introduction

Figures 1 and 2 present all the InSAR data used in this study. Figure 3 presents the MERIS images acquired simultaneously with the ASAR images. The MERIS image acquired on 08 January 2008 has not been used in this study because there are lot of missing values in MODIS PWV data due to a cloud.

Table S4 presents the best fitting source characteristics and elevation dependent path delays for each interferogram and their uncertainties obtained by the least square adjustment shown in Figure S1 and S2. The maximum values of the fitness function obtained from ALOS and ASAR data are not comparable due to the dependence of this value with the wavelength of SAR data used. We added so the root mean square (rms) of the final wrapped phase residuals using all the pixels located in the study area with a coherence higher than 0.625, which makes

it possible to compare all the results together. These rms values were computed using the equation of the circular standard deviation given by [Feigl and Thurber, 2009]. We also reported in this table the elevation dependent path delays estimated using MERIS data, which can be compared to the values inferred by ASAR data.

Table 4 also presents ASAR differential Slant Path Delay estimated from MERIS data. As the estimation of atmospheric signal in interferograms using PWV estimates is only possible during the daytime, it is not possible to compare SPD deduced from the inversion of PALSAR data with these independent estimates. We tried to estimate the magnitude and the behavior of tropospheric delays in night-time acquisitions of ascending PALSAR images and we used the ERA-I reanalysis atmospheric model as in PyAPS [Jolivet et al, 2011]. ERA-I numerical model outputs showed that stratified atmospheric could be significant during night-time acquisitions in the study area. Nevertheless, when we attempted to validate the use of ERA-I numerical model outputs by comparing to the independent day-time MERIS estimates we found that this technique did not work satisfactorily for the study area. We think that is likely due to the close proximity of the ocean and highly variable weather system which are not well modeled by ERA-I.

Feigl, K., and H. Thurber (2009), A method for modelling radar interferograms without phase unwrapping: application to the M 5 Fawnskin, California earthquake of 1992 December 4, *Geophysical Journal International*, 176(2), 491-504

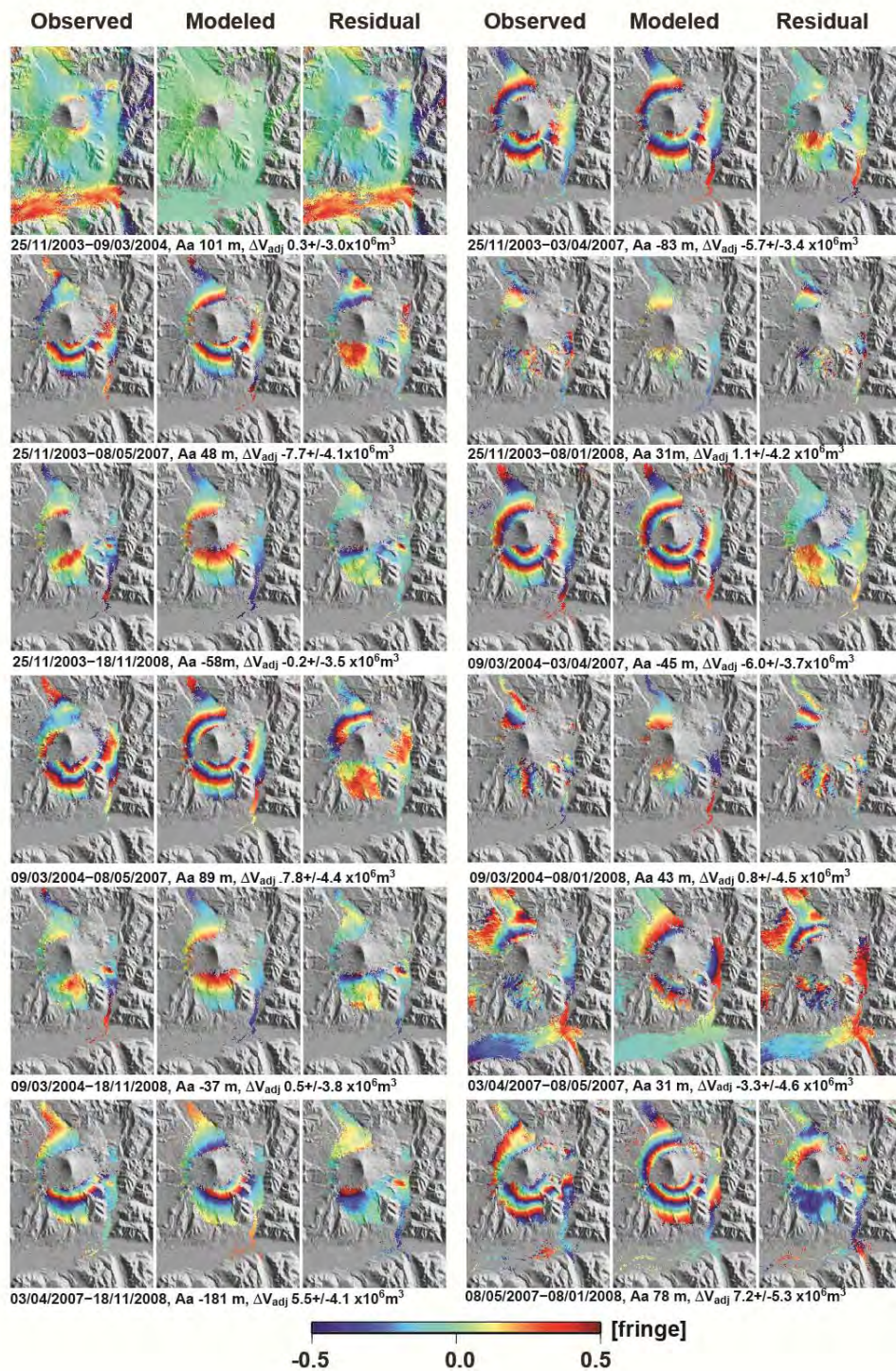


Figure S1. Set of the descending track 10 ASAR interferograms produced by data pairs with an H_a greater than 30 m used in this study overlaid over a shaded relief map. Areas where the interferometric coherence is lost are shown in grey.

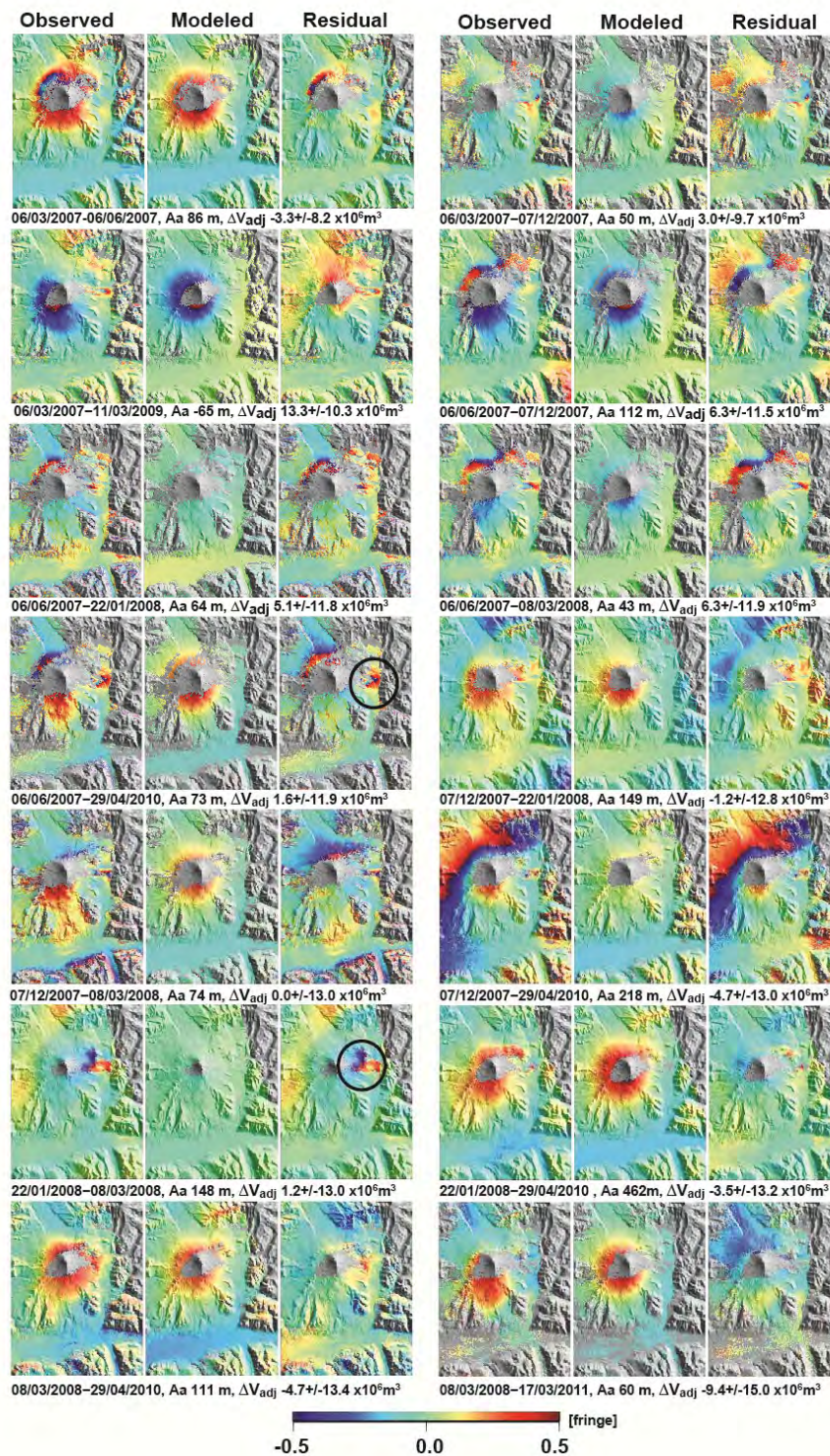


Figure S2. Set of the ascending track ALOS PALSAR interferograms produced by data pairs with an H_a greater than 40 m overlaid over a shaded relief map. Areas where the interferometric coherence is lost are shown in grey. Black circles show the location of the temporally complex deformation observed on the eastern flank of the volcano

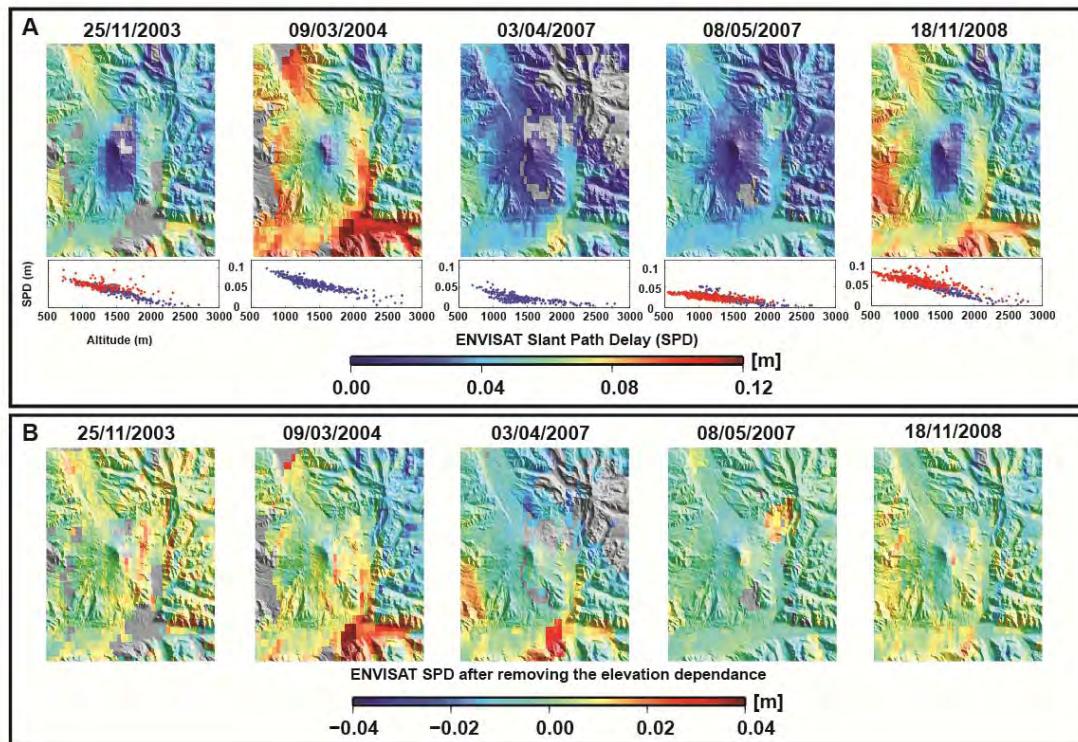


Figure S3. Value of the Slant Path Delay estimated from MERIS images acquired at the same dates than the ASAR images. Due to clouds in the image acquired on 08 January 2008, there are lot of missing values in MODIS PWV data and it has not been used in this study. A) estimated ENVISAT SPD map estimated from MERIS images. Large atmospheric contamination could be particularly large as in the case of the images acquired on 25/11/2003, 09/042004, and 18/11/2008. Graph of SPD values versus elevation are also shown. Blue and Red dots show SPD values estimated from MERIS and MODIS data, respectively. B) The same fields as in A but after removing the elevation dependence of the SPD. By removing the elevation dependence part in the SPD values, the atmospheric contribution is significantly reduced. Nevertheless, large horizontal variability of PWV leads to large residuals (up to 4 cm) in particularly on the southeastern flank of the volcano

Dates	Ha	$\delta\Phi/\delta z_{\text{estb}}$	ΔV_{est} (10^6m^3)	R	RMS (m)	$\delta\Phi/\delta z_{\text{adj}}$ $\pm 1.\sigma$	$\delta\Phi/\delta z_{\text{MERIS}}$ $\pm 1.\sigma$	ΔV_{adj} $\pm 1.\sigma$ (10^6m^3)
ASAR track 10								
25/11/2003-09/03/2004	101	0.002	0.2	0.82	0.003	-0.000 \pm 0.009	0.003 \pm 0.003	0.3 \pm 3.0
25/11/2003-03/04/2007	-83	0.030	-3.5	0.72	0.004	0.024\pm0.010	0.022\pm0.004	-5.7\pm3.4
25/11/2003-08/05/2007	48	0.008	-10.2	0.49	0.006	0.027 \pm 0.011	0.016 \pm 0.003	-7.7 \pm 4.1
25/11/2003-08/01/2008	31	0.010	0.3	0.40	0.007	0.014 \pm 0.011	*	1.1 \pm 4.2
25/11/2003-18/11/2008	-58	0.015	-1.2	0.71	0.004	0.016 \pm 0.011	-0.002 \pm 0.003	-0.2 \pm 3.5
09/03/2004-03/04/2007	-45	0.022	-6.9	0.86	0.003	0.024 \pm 0.011	0.019 \pm 0.004	-6.0 \pm 3.7
09/03/2004-08/05/2007	89	0.029	-7.3	0.44	0.006	0.028\pm0.012	0.013\pm0.003	-7.8\pm4.4
09/03/2004-08/01/2008	43	0.024	2.1	0.42	0.007	0.014 \pm 0.012	*	0.8 \pm 4.5
09/03/2004-18/11/2008	-37	0.012	-1.7	0.66	0.004	0.017 \pm 0.012	-0.005 \pm 0.003	-0.5 \pm 3.8
03/04/2007-08/05/2007	31	-0.002	-9.0	0.36	0.007	0.004 \pm 0.013	-0.006 \pm 0.004	-3.3 \pm 4.6
03/04/2007-18/11/2008	-181	-0.002	6.6	0.72	0.004	-0.007 \pm 0.012	-0.024 \pm 0.003	5.5 \pm 4.1
08/05/2007-08/01/2008	78	-0.032	9.2	0.57	0.005	-0.014 \pm 0.013	*	7.2 \pm 5.3
PALSAR track 117								
06/03/2007-06/06/2007	86	0.023	-5.8	0.86	0.011	0.024\pm0.018		-3.3\pm8.2
06/03/2007-07/12/2007	50	0.019	10.9	0.86	0.012	0.019\pm0.022		3.0\pm9.7
06/03/2007-11/03/2009	-65	0.003	13.3	0.81	0.013	-0.005 \pm 0.027		13.3 \pm 8.9
06/06/2007-07/12/2007	112	-0.003	12.0	0.84	0.013	-0.005 \pm 0.026		6.3 \pm 11.5
06/06/2007-22/01/2008	64	-0.022	-3.4	0.74	0.017	-0.016 \pm 0.027		5.1 \pm 11.8
06/06/2007-08/03/2008	43	-0.002	5.9	0.85	0.013	-0.008 \pm 0.027		6.3 \pm 11.9
06/06/2007-29/04/2010	73	-0.009	-8.4	0.76	0.016	0.016 \pm 0.028		1.6 \pm 11.9
07/12/2007-22/01/2008	149	-0.016	-11.1	0.76	0.015	-0.010 \pm 0.030		-1.2 \pm 12.8
07/12/2007-08/03/2008	74	0.016	-3.6	0.65	0.020	-0.003 \pm 0.030		0.0 \pm 13.0
07/12/2007-29/04/2010	218	0.028	3.5	0.63	0.020	0.021 \pm 0.031		-4.7 \pm 13.0
22/01/2008-08/03/2008	148	0.008	2.3	0.84	0.011	0.007 \pm 0.031		1.2 \pm 13.2
22/01/2008-29/04/2010	462	0.026	-5.6	0.90	0.010	0.031 \pm 0.032		-3.5 \pm 13.2
08/03/2008-29/04/2010	111	0.036	0.2	0.77	0.015	0.024 \pm 0.032		-4.7 \pm 13.4
08/03/2008-17/03/2011	60	0.007	-9.4	0.80	0.014	0.007 \pm 0.035		-9.4 \pm 15.0

Table S4. Parameters associated with the ASAR and ALOS interferograms : Aa Altitude of ambiguity ; $\delta\Phi/\delta z_{\text{est}}$ and ΔV_{est} are the phase-elevation gradient per 1000 m and the volume change inferred from modelled InSAR measurements assuming a Mogi source at 7 km depth. R is the mean resultant length obtained from the pixel-by-pixel difference between data and modelled InSAR measurements from the subset of coherent pixels equally distributed in elevation. rms is the root mean square error of the wrapped phase residuals using the pixels with a coherence higher than 0.625. $\delta\Phi/\delta z_{\text{adj}}$ and ΔV_{adj} are the adjusted phase elevation gradient per 1000 m, the adjusted volume change and their standard deviations calculated by global L2 adjustment of the inferred values. $\delta\Phi/\delta z_{\text{MERIS}}$ is the phase elevation gradient per 1000m and its standard deviations deduced from the MERIS and PWV estimations; * indicate that no MERIS data are available. Data relative to the interferograms displayed in Figure 3 are in bold.

7.4 Analysis of tropospheric artifact in PALSAR interferograms

As mentioned in the study published in GRL, it was not possible to estimate the phase delay using PWV retrieved from MERIS or MODIS for PALSAR images as they were acquired during the night ($\sim 1:00$ am local time) over the study area. Therefore, we attempted to validate the use of ERA-I numerical model outputs for atmospheric correction. We used PyAPS (Jolivet et al., 2011) which estimates differential phase delay maps due to the stratified atmosphere for correcting radar interferograms using inputs from the Global Atmospheric Model (GAM), ERA-Interim (ECMWF). The ERA-Interim atmospheric model provides estimates of 16 meteorological parameters including temperature, relative humidity, and geopotential, at 6 h intervals. Spatially, the outputs are given at grid nodes with 75 km horizontal spacing, and at 37 pressure levels between 0 and 50 km above sea level. Atmospheric delay maps are calculated by producing vertical profiles of total path delay at 75 km resolution based on the atmospheric delay formulations of Baby et al. (1988). These formulations interpolate the parameters horizontally and vertically with bilinear and spline interpolation functions, respectively, and then use a DEM to find the delay at the correct elevation for each point at the surface.

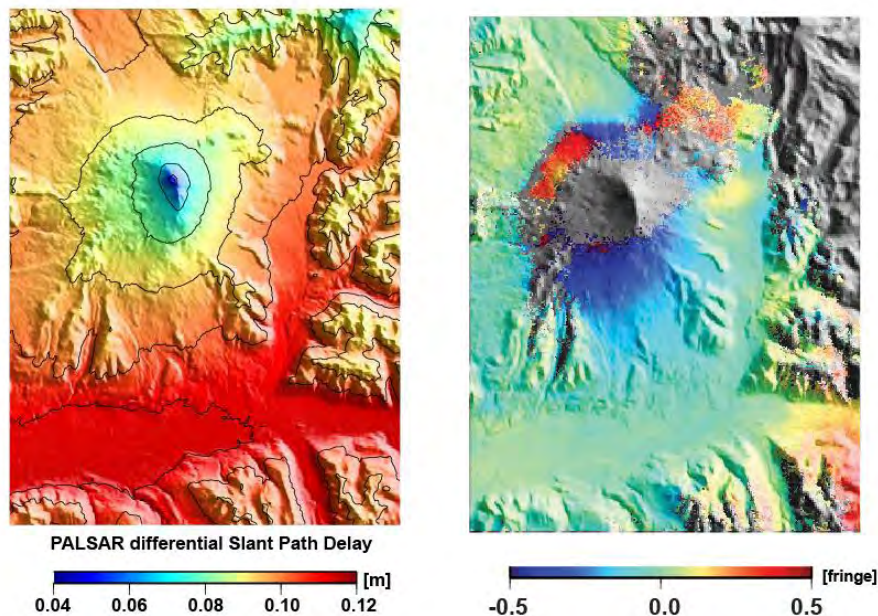


Figure 7.2 Left) Differential Slant Path delay from ERA-interim model using PyAPS between 06/06/2007 and 07/12/2007. **Right)** PALSAR interferogram formed with the images acquired at the same dates. One fringe corresponds to 11.5 cm change of the distance in the Line of Sight of the ALOS satellite.

Figure 7.2 shows one example of differential atmospheric delay maps computed at the same dates with the ALOS PALSAR interferogram produced by data pairs acquired on 6 June 2007 and 7 December 2007, respectively. This figure clearly shows that stratified tropospheric delays exist in the night-time acquisitions of ascending PALSAR images and their amplitudes could be strong (12 cm in this example). Next we compared the result of the wet delay obtained from ERA-Interim with the one obtained from MERIS data. **Figure 7.3** shows two examples of atmospheric delay maps estimated on 9 March 2004 for ASAR acquisition using the different approaches. The amplitude of phase delay induced by vertically stratified water vapor in the troposphere are significantly different: 6.4 cm and 2.7 cm per 1000 m of elevation from ERA-Interim and MERIS, respectively.

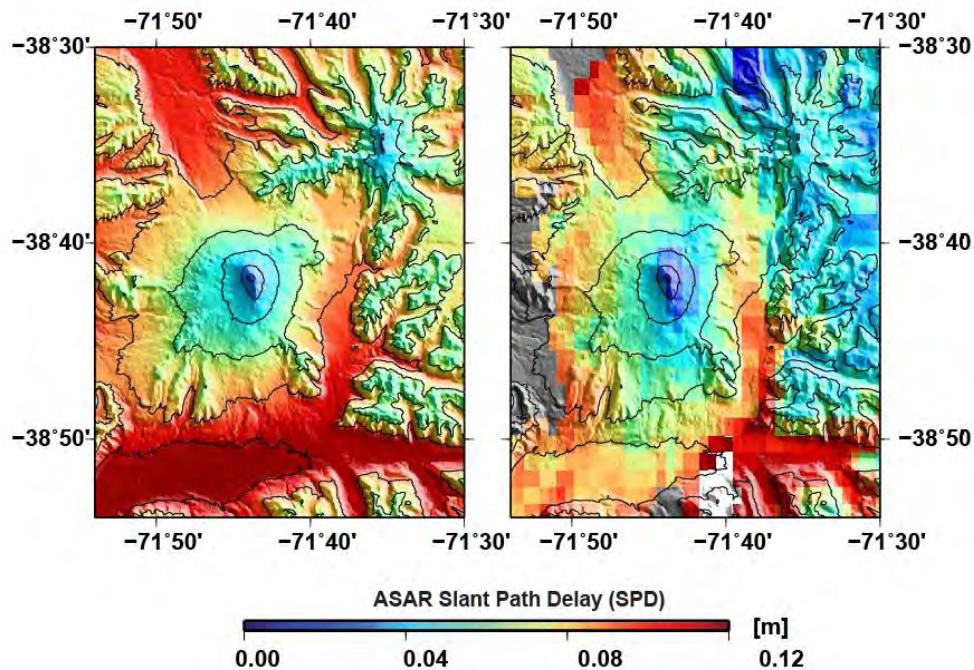


Figure 7.3 ASAR slant path delay for 9 March 2004. **Left)** ASAR slant path delay estimated from ERA-Interim at ~12 h UTC using only the wet component of atmospheric delay. **Right)** ASAR slant path delay estimated from MERIS satellite data acquired at ~14 h UTC.

We think that this discrepancy are likely due to the close proximity of the ocean that induces weather systems that are highly variable in space and time. The low resolution of the ERA-Interim meteorological parameters on ~ 75 km grid, which is several order of magnitude larger than the pixel size of an interferogram makes it impossible to capture small wavelength feature and to well model atmospheric delays at the scale of the volcanic edifice. Furthermore, as water vapor can be *highly variable in time* and have a short life span, the time interval between the acquisition MERIS images (~ 14 h UTC) and the closest ERA-Interim atmospheric meteorological parameters (~ 12 h UTC) is certainly too long. It is also the case between the acquisition of the PALSAR image (~ 4 h UTC) and the ERA-Interim atmospheric meteorological parameters (~ 6 h UTC). All these reasons led us to the conclusion that we could not use estimates from ERA-Interim atmospheric model for estimating the amplitude of the topography-dependant delays in the PALSAR interferograms.

7.5 Pre-eruptive inflation before the April 2009 eruption?

7.5.1 Problem definition

One ascending PALSAR interferogram formed by images acquired on 6 March 2007 and 11 March 2009 reveals a possible burst of uplift prior to the 3 April 2009 eruption (**Figure 7.4**). Even if the volume change inferred by our inversion of about 13.3×10^6 m³ is within the data accuracy (14.5×10^6 m³ at the 95 % confidence level), this estimation is a clear outlier in the time series (**Figure 7.5**; see also **Figure 3b** in the GRL paper in [Section 7.3](#)), especially when the estimated tropospheric phase delay is negligible in this interferogram compared with those in the rest interferograms (see **Table S1** in supporting information in [Section 7.3](#)).

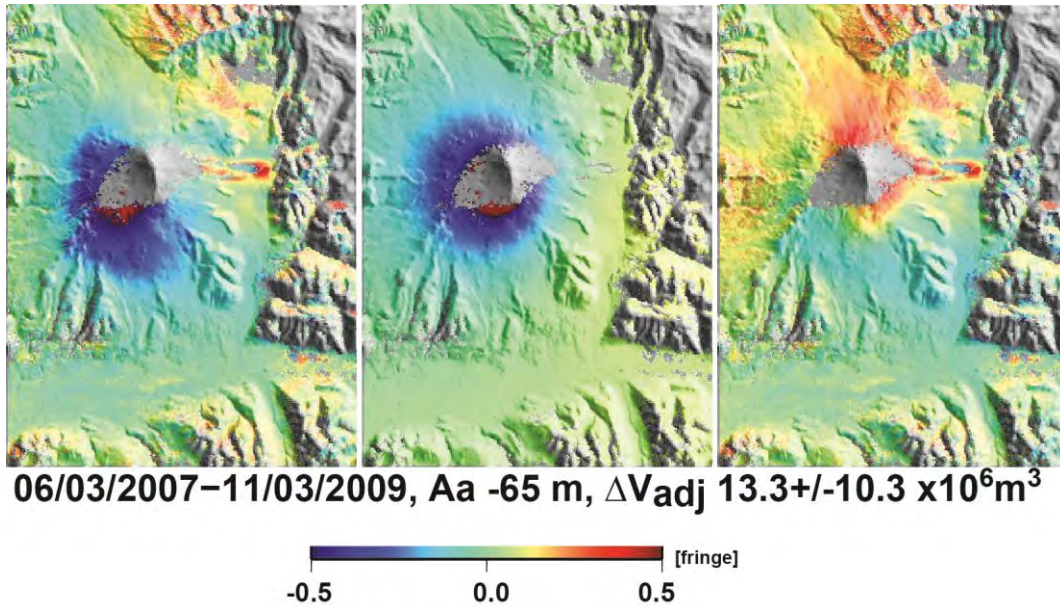


Figure 7.4 PALSAR ascending interferogram (06/03/2007-11/03/2009). **Left)** observed ground displacement. **Middle)** modeled ground displacement. **Right)** residual between observed and modeled ground displacement. Each fringe (full colour cycle) represents 11.81 cm of range change between the ground and the satellite. Areas where the interferometric coherence is lost or not covered by the ALOS ascending track 117 are shown in grey.

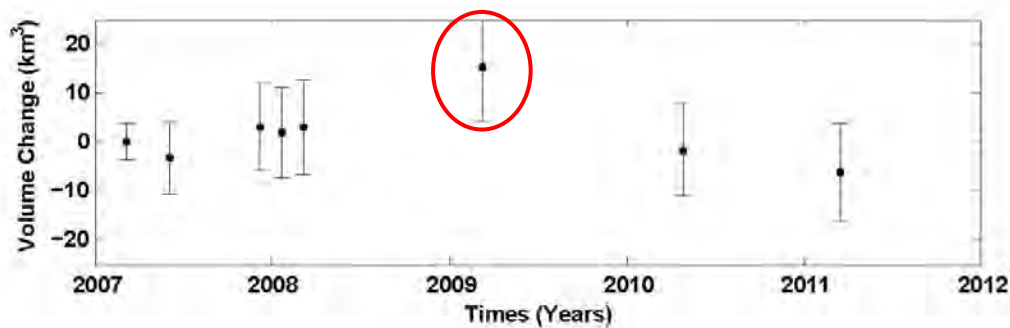


Figure 7.5 Estimated volume changes (ΔV_{adj}) resulting from the adjustment with respect to the reference image acquired on 06/03/2007 for ALOS PALSAR track 117. The red circle indicates the possible burst of uplift prior to the 3 April 2009 eruption.

As in the frame of a single PALSAR time series (ascending track 117), we could not assert that the observed signal was related to volcanic ground deformation prior to the April 2009 eruption. We decided to complement the previous InSAR time series using another set of PALSAR data in attempting to answer this question.

7.5.2 Solving method

We analyzed 7 images from ALOS ascending track 116 in mode FBS (Fine Beam Single) acquired between 2007 and 2011 over the study area. They are acquired on 17 February 2007, 4 April 2007, 20 November 2007, 20 February 2008, 22 February 2009, 13 January 2011, and 28 February 2011. The time span covered by 10 interferograms formed by these 7 images are indicated by green lines in **Figure 7.6**.

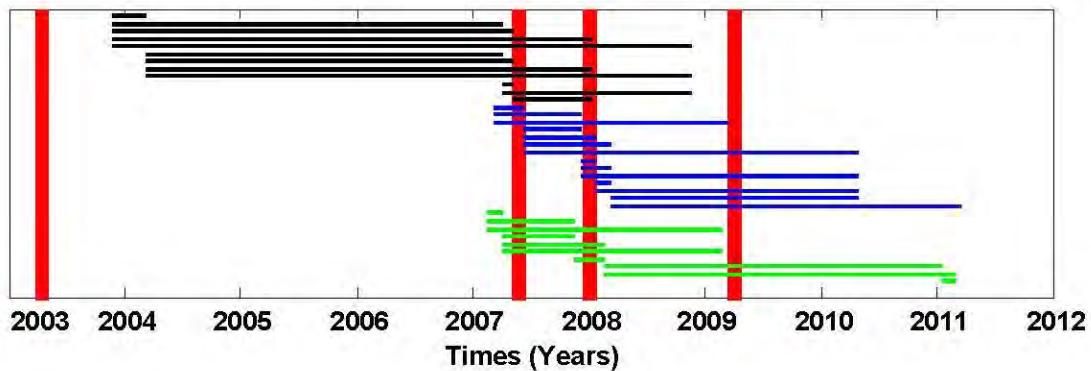


Figure 7.6 Time span covered by the 12 ASAR interferograms (in black) and the 14 PALSAR interferograms (in blue) used in the study published in GRL. Lines in green show the 10 PALSAR interferograms from ascending track 116 used to complement the previous study. The vertical red lines show the timing of the eruptions which occurred during the 2003-2012 period.

Differential interferograms were generated using DIAPASON software ([@CNES/Altamira-information, 1996](#)) using the two pass method described by Massonnet et al. (1998). The orbital contribution was removed using orbit state vectors provided in the image header. The topographic contribution was removed using the the 3 arcsec SRTM DEM. Interferograms were downsampled during processing to eight looks in azimuth and two looks in range, respectively. We considered only interferograms produced by data pairs characterized by an altitude of ambiguity (H_a) greater than 40 m (i.e. perpendicular baseline lower than 1500m) suitable for interferometry purpose (**Figure 7.7**). In order to remove the long-wavelength signals related to orbital errors, we corrected the interferograms for a two-dimensional linear ramp, after masking out the region of the Llaima volcano. The interferograms exhibit generally the same concentric

pattern of fringes centered on the volcanic edifice as observed for interferograms in previous studies.

We adopted the same modelling strategy with the one used in the previous study ([Section 7.3](#)). In order to be consistent with the results obtained from ASAR interferograms, we did not use the standard approach of unwrapping fringe maps. We chose instead to apply the GIPhT ([Feigl & Thurber, 2009](#)) method that allows for a direct comparison between displacement models and wrapped phases and provides a robust determination both of the model misfit and of the model parameter uncertainties. To solve the model parameters (volume change and phase-elevation gradient) that fit the PALSAR interferogram, we used a genetic algorithm (refer to [Section 7.3](#) for detail).

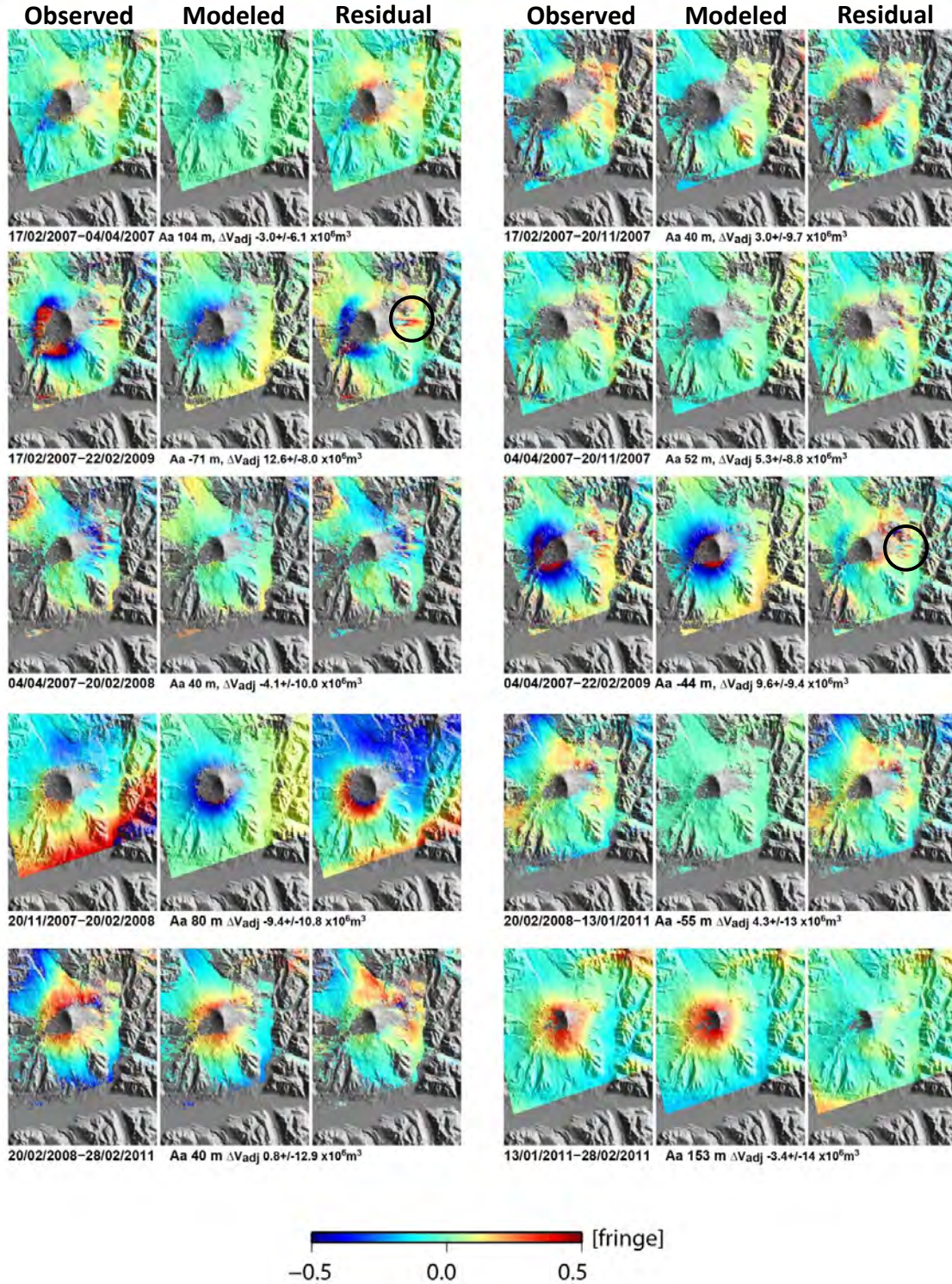


Figure 7.7 Set of the ascending track 116 ALOS PALSAR interferograms produced by data pairs with an *H_a* (*Aa* in the figure) greater than 40 m overlaid over a shaded relief map. Areas where the interferometric coherence is lost are shown in grey. The ΔV_{adj} is the adjusted volume change and its standard deviation

LLAIMA
CHAPTER 7: GROUND DISPLACEMENT AT LLAIMA OBSERVED BY INSAR

calculated by global L2 adjustment of the inferred values. Black circles show the location of the temporally complex deformation observed on the eastern flank of the volcano.

7.5.3 Results

Similarly to the results derived by the ascending track 117 in the GRL paper (Section 7.3), the interferograms obtained here from the ascending track 116 also show strong residual patterns in some residual maps (Figure 7.7). Further, we also observed the temporally complex ground displacement pattern on the eastern flank in the interferograms encompassing the January 2008 eruption (location shown by a circle in Figure 7.7; see also Figure 1c and Figure S2 in Section 7.3), which was interpreted to be related to a slow landslide triggered by this eruption (Fournier et al., 2010).

Dates	Ha	$\delta\Phi/\delta z_{est}$	ΔV_{est} ($10^6 m^3$)	R	RMS (m)	$\delta\Phi/\delta z_{adj}$ $\pm 1.\sigma$	ΔV_{adj} $\pm 1.\sigma$ ($10^6 m^3$)
17/02/2007-04/04/2007	104	0.001	2.5	0.85	0.012	0.005 ± 0.014	3.1 ± 6.1
17/02/2007-20/11/2007	40	0.041	15.9	0.62	0.015	0.021 ± 0.016	8.2 ± 7.4
17/02/2007-22/02/2009	-71	0.015	7.3	0.84	0.014	-0.012 ± 0.018	12.9 ± 8.0
04/04/2007-20/11/2007	52	-0.017	6.1	0.86	0.011	0.016 ± 0.020	5.3 ± 8.8
04/04/2007-20/02/2008	40	-0.041	-7.6	0.86	0.013	-0.018 ± 0.026	-4.1 ± 10.0
04/04/2007-22/02/2009	-44	-0.014	11.6	0.87	0.012	-0.017 ± 0.021	9.8 ± 9.4
20/11/2007-20/02/2008	80	-0.004	13.6	0.55	0.022	-0.033 ± 0.028	-9.4 ± 10.8
20/02/2008-13/01/2011	-55	-0.007	1.8	0.82	0.014	0.018 ± 0.036	4.3 ± 13.0
20/02/2008-28/02/2011	41	0.046	1.9	0.86	0.012	0.041 ± 0.031	0.8 ± 12.9
13/01/2011-28/02/2011	153	0.022	-3.6	0.89	0.010	0.023 ± 0.035	-3.4 ± 14.1

Table 7.1 Parameters associated with the ALOS interferograms (track 116): Ha Altitude of ambiguity; $\delta\Phi/\delta z_{est}$ and ΔV_{est} are the phase-elevation gradient per 1000 m and the volume change inferred from modelled InSAR measurements assuming a Mogi source at 7 km depth. R is the mean resultant length obtained from the pixel-by-pixel difference between data and modelled InSAR measurements from the subset of coherent pixels equally distributed in elevation. RMS is the root mean square error of the wrapped phase residuals using the pixels with a coherence higher than 0.625. $\delta\Phi/\delta z_{adj}$ and ΔV_{adj} are the adjusted phase elevation gradient per 1000 m, the adjusted volume change and their standard deviations calculated by global L2 adjustment of the inferred values. Data relative to the interferograms calculated with the 22 February 2009 acquisition are in bold.

Table 7.1 presents the best fitting source characteristics, the elevation-dependent path delays, and the volume change for each interferogram and their uncertainties obtained by the

least squares adjustment. The amplitudes of the inferred phase delays and volume changes are comparable with those for the other ALOS track (117) used in previous study (**Table S1** in [Section 7.3](#)). The inferred volume changes are generally small ranging from -9.4 to $12.9 \times 10^6 \text{ m}^3$ during the 2007 – 2011 period. The uncertainty (1σ) of the adjusted volume changes is on average about $\pm 10 \times 10^6 \text{ m}^3$. There two interferograms, which are 17/02/2007-22/02/2009 and 04/04/2007-22/02/2009, both calculated with a common acquisition (22 February 2009) show relatively high volume change values ($12.9 \times 10^6 \text{ m}^3$ and $9.8 \times 10^6 \text{ m}^3$, respectively; shown in bold in **Table 7.1**), but with relatively low tropospheric phase delays. These values are very comparable with that obtained from an interferogram of track 117 spanning the same period of time (06/03/2007-11/03/2009; $\Delta V_{\text{adj}} = 13.3 \times 10^6 \text{ m}^3$; **Table S1**). The time series of volume change for the track 116 (**Figure 7.8**) also display a similar behavior with that for track 117 (**Figure 7.5**). The large volume change on 22 February 2009 is a clear outlier in the overall trend, which could be associated with ground deformation prior to the April 2009 eruption.

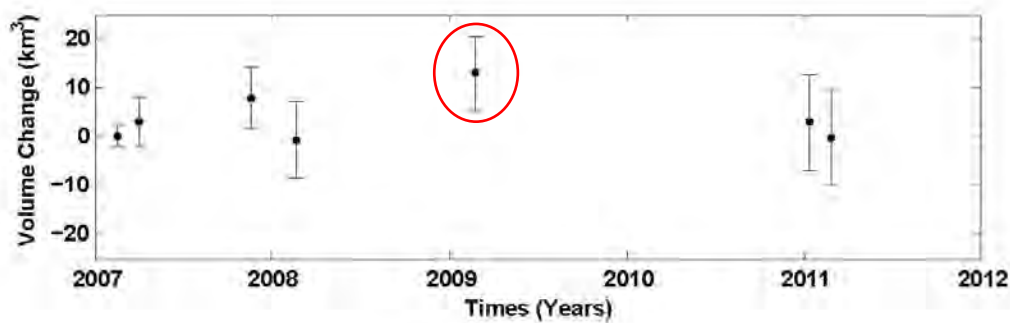


Figure 7.8 Estimated volume changes (ΔV_{adj}) resulting from the adjustment with respect to the reference image acquired on 17/02/2007 for ALOS PALSAR track 116. The red circle indicates the possible burst of uplift prior to the 3 April 2009 eruption.

7.5.4 Discussion and conclusions

The analysis on two independent ascending ALOS PALSAR tracks derives consistent result concerning the exceptional volume change signal in early 2009, which lead us to consider it could be related to a possible burst of uplift induced by magma intrusion just before the April 2009 eruption. However, the volume changes ($13.3 \times 10^6 \text{ m}^3$, $12.9 \times 10^6 \text{ m}^3$ and $9.8 \times 10^6 \text{ m}^3$) are

all within the data uncertainty at 95 % confidence level. Thus in the light of this study, we could not assert with certainty that the observed signal was related to volcanic ground deformation.

This study on ground deformation of Llaima volcano clearly demonstrates that the applications of InSAR for detecting deformation, in particular, the transient deformation induced by the activity of Andean andesitic stratovolcanoes remain a challenge. The sparsity of SAR acquisitions over these volcanoes make it difficult to capture short-term transient deformation. Also, many of these volcanoes are located in intertropical or temperate areas where dense vegetation cover large portion of volcano edifice, which can cause temporal decorrelation of interferometric phases, as in the case of this study. The PALSAR interferograms generally have a higher coherence than ASAR ones as the L band wave penetrates more deeply into the vegetation cover and interacts with more stable scatterers. However, in volcano summit where snow and/or glacier are present, both C and L bands of SAR data fail to maintain good coherence. In addition, andesitic volcanoes often have steep slopes, which can result in strong geometric distortions (foreshortening/layover) in SAR images and thus in information loss. More importantly, spatial and temporal variations of the troposphere can induce strong tropospheric (long- and short-wavelength) artifacts on InSAR products, which blur eventually subtle deformation signals. All these factors reduce or even prevent the ability of InSAR to accurately monitor ground deformation at Andean volcanoes. The use of permanent GNSS network will provide benefits for deformation monitoring, for instance, using GNSS data to validate InSAR-derived results or to independently estimate atmospheric delay and remove it from interferograms. Combined use of GNSS and InSAR will significantly improve the accuracy in ground deformation estimates at these volcanoes.

CHAPTER 8 : CONCLUSIONS & PERSPECTIVES

In this dissertation we used different methods to analyze InSAR time series acquired at Piton de la Fournaise volcano and Llaima volcano. The main objective of this work is to better understand the phenomenon behind the interferometric signals observed on these volcanic edifices. To fulfill this objective, we have analyzed long time series of radar images acquired in different modes and with different wavelengths (bands X, C and L). We have, according to the constraints encountered, implemented different methodological approaches in order to discriminate the different contributions of the observed signals. Thus, we have paid special attention to assess the potential effects and impacts of those signals in the interferograms. Whenever possible, we used all available information to compare our results with other data such as GNSS measurements on Piton de la Fournaise and estimates of the water vapor content from the MERIS or MODIS sensors.

Piton de la Fournaise

We have shown that the classical approach that consists to filter spatially and temporally the InSAR time series does not work in the context of the study where persistent and low-amplitude displacements affect Piton de la Fournaise. We have also shown that the use of a Global Atmospheric Model (GAM) does not allow, in the absence of a suitable spatial and temporal resolution, a good estimation of the tropospheric phase contribution to the InSAR data. So, we have developed an original method to attempt to discriminate the stratified tropospheric effects of the persistent displacements observed on the volcanic edifice. The reliability of the correction method was tested and validated by comparing the InSAR measurements with GNSS measurements.

The InSAR data corrected for tropospheric effects have thus made it possible to demonstrate a complex deformation field emphasizing the diversity of the mechanisms responsible for the displacements observed on this volcanic edifice. The displacements caused by the various phenomenon overlap in space and time, making it difficult to discriminate. Nevertheless, our analysis made it possible to determine three main origins of the signals observed between 2009 and 2014.

The Central Cone is affected by a long-term subsidence only interrupted by intense and brief displacements caused by the magmatic intrusions that occurred during various eruptions.

GNSS observations and InSAR measurements acquired after the historical March-April 2007 eruption showed that this signal began as a result of the Dolomieu collapse. The reduced surface area and low amplitude of this subsidence centered on the cone suggest that this signal is caused by the relaxation of a superficial source but the precise origin remains undetermined.

At Piton de la Fournaise, the main areas that remain coherent with the radar wave are basically lava flows mainly because of the lack of vegetation. However, the emplacement of recent lava flows is accompanied by long-term deformations caused by the thermomechanical compaction of the flows and the flexion of the substratum. These deformations thus make it particularly difficult to detect and to analyze the low-amplitude displacements caused by other processes which are superimposed on them. Therefore, we have focused on characterizing these deformations from an empirical study carried out on lava flows that were not affected by other sources of deformation. We have thus been able to show that the deformations on the recent flows are characterized essentially by subsidence without significant horizontal displacements. The footprint of these subsides is wider than that of lava flows indicating that the flexion of the substratum plays a major role in the deformations. There is a linear relationship between the displacements and the thickness of lava flow and the amplitude of displacements decreases with time. These relationships have allowed us to construct an empirical law for the estimation of the contribution of displacements caused by lava flows over the entire volcanic edifice.

Finally, our study showed that the downslope sliding of the Eastern Flank of Piton de la Fournaise began during the March-April 2007 eruption and continued until November 2014, the date of the last radar image acquisition of our study. To explain this flank motion with an amplitude decaying with time suggesting a phenomenon of relaxation, we studied different hypotheses and proposed different mechanisms. Finally, these results highlight the importance of following the evolution of this sliding given that a potential acceleration of this phenomenon could represent.

Llaima

As at Piton de la Fournaise, our work at Llaima shows that the tropospheric contribution in interferograms remains the main source of error in the interpretation of radar measurements.

At this volcano, the analysis of the MERIS and MODIS data indicates that it is difficult or even impossible to detect a short- and low- amplitude deformation (<7 cm) from a single interferogram. Based on this analysis, we developed a numerical approach that took into account the impact of tropospheric effects to invert the InSAR data acquired between 2003 and 2011. The results of this inversion revealed that no significant deformation was observed during the eruptive period of 2008 and that the majority of the detected interferometric signals were produced by tropospheric delays. This interpretation strongly differs from that proposed by Bathke et al. (2011) who considered the tropospheric effects as negligible in their study and interpreted these signals as the expression of pressure change in a magmatic chamber located 7 km in depth. The analysis of images acquired by the ALOS satellite from two different tracks suggests that an uplift just before the eruption of April 2009 could be the origin of the interferometric signal. Nevertheless, since the volume determined by the inversion is below the margin of error determined by the least square adjustment of this parameter, it is not possible to reject the hypothesis that no deformation was observed by InSAR between 2003 and 2011.

Since the first studies on deformations of the earth's surface carried out by InSAR, the increase of the available images, the improvement of the precision of the orbital vectors and the numerical models of ground made it possible to substantially increase the precision of the interferometric measurements. Nevertheless, the two studies we have carried out have shown that the most important factor limiting the potential InSAR for monitoring deformations in volcanic edifice is the impact of tropospheric contributions in the interferograms. Although the use of Global Atmospheric Models (GAM) to estimate the variations in tropospheric refractive index has shown interest in different studies, the use of this model in our studies has not met expectations. The spatial and temporal resolutions of the estimates produced by the GAM are clearly not in agreement with the spatial and temporal variability of the water vapor content observed in the oceanic climate zones where the two volcanoes studied are located. In the absence of a universal method, we developed specific empirical approaches in order to minimize the impact of tropospheric effects in interferograms for each study case. Our experience highlights that our capability to precisely map the localized deformations on these large volcanic edifices using InSAR relies on the possibility to get with high resolution a good characterization of the spatial and temporal variations of the refractive index of the atmosphere at the radar wave.

With the appearance of the GNSS and InSAR techniques, numerous studies of deformations associated with volcanic activity have been carried out. The main objective of these studies is to quantify the phenomenon of magma transfer that occur in the superficial and deep structures of a volcanic edifice. They provide essential information on the internal structures of volcanoes by making it possible to better understand the ways in which the stresses and deformations are transmitted from the source to the surface of the edifice. The studies carried out in this dissertation are aiming to better understand volcano processes. Nevertheless, many uncertainties generally remain about the nature of the phenomenon responsible for the observed signals emphasizing the understanding of the functioning of volcanic systems remains a major challenge for the earth sciences. The bibliographical analysis of the studies carried out on the edifice showed that many uncertainties still exist on the internal structure and the rheology of the edifice. This led us to explore different possibilities to try to explain the signals that we observed by InSAR and GNSS. The lack of clear phenomenological laws explains why we have not implemented numerical modeling. Given these uncertainties, it was difficult to choose a specific model and rheology.

However, Piton de la Fournaise is one of the best monitored volcanoes in the world with various networks (GNSS, seismic stations, etc.) that are deployed on its flanks. With the implementation of numerous constellations of satellites it will be possible, in the near future, to obtain images acquired every 6 days allowing to image the displacement field at high spatial and temporal resolution. The combined use of different observation techniques will allow better monitoring of the spatial and temporal variations of physical and chemical parameters: seismicity, surface deformation, geochemistry of lava and gases, etc. All these observations will make it possible to improve the fundamental knowledge on the structural scheme and the evolution of Piton de la Fournaise. These advances in the instrumentation of volcanic edifices will also provide important information to better understand the complexity of the functioning mode of large andesitic volcanoes such as Llaima.

Dans ce travail de thèse nous avons utilisé différentes méthodes pour analyser des séries temporelles InSAR acquises sur le Piton de la Fournaise et sur le Llaima. L'objectif principal de ce travail était de tenter de mieux comprendre les phénomènes à l'origine des signaux interférométriques observés sur ces deux édifices volcaniques. Pour remplir cet objectif, nous avons analysé des séries temporelles pluriannuelles d'images radars acquises dans différents modes et différentes longueurs d'ondes (bandes X, C et L). Nous avons, en fonction des contraintes rencontrées, mis en œuvre différentes approches méthodologiques pour tenter de discriminer le plus finement possible les différentes contributions des signaux observés. Ainsi, nous avons prêté une attention toute particulière à l'évaluation fine d'éventuels effets de site et leurs impacts sur ces signaux. Lorsque cela était possible, nous avons utilisé toutes les informations disponibles pour comparer nos résultats à d'autres données *e.g.* les mesures GNSS sur le Piton de la Fournaise ou les estimations du contenu en vapeur d'eau calculées à partir des observations acquises par les capteurs multispectraux MERIS ou MODIS.

Le Piton de la Fournaise

Nous avons montré que l'approche classique qui consiste à filtrer spatialement et temporellement les séries temporelles InSAR est innopérante pour l'étude des déplacements permanents de faibles amplitudes affectant le Piton de la Fournaise. Nous avons également montré que l'utilisation d'un modèle atmosphérique global ne permettait pas, faute d'une résolution spatiale et temporelle adaptées d'estimer correctement la contribution des variations de l'indice de réfraction troposphériques dans les interférogrammes. C'est pour ces raisons que nous avons développé une méthode originale qui permet de discriminer les effets troposphériques stratifiés des déplacements persistants qui sont observés sur l'édifice volcanique. La fiabilité de la méthode de correction a été testée et validée en comparant les mesures InSAR avec celles acquises par des stations GNSS.

Les données InSAR corrigées des effets troposphériques ont ainsi permis de mettre en évidence un champ de déformations complexes soulignant la diversité des mécanismes à l'origine de cette complexité. Les champs de déplacements provoqués par les différents phénomènes se superposent spatialement et temporellement rendant la discrimination de chacun des phénomènes difficile à déterminer. Néanmoins, ce travail a permis de déterminer trois grandes origines des signaux observés entre 2009 et 2014.

Le Cône Central est affecté d'une longue subsidence seulement entrecoupée d'intenses et brefs déplacements provoqués par les intrusions magmatiques survenues lors des différentes éruptions pendant la période de l'étude. Les observations GNSS et les mesures InSAR acquises à la suite de l'éruption historique de 2007 ont montré que ce signal a débuté à la suite de l'effondrement du Dolomieu. La surface réduite et la faible amplitude de cette subsidence centrée autour du cône, suggère que ce signal est provoqué par des phénomènes de relaxation d'une source superficielle mais dont l'origine précise reste indéterminée.

Sur le Piton de la Fournaise, les principales zones qui restent cohérentes sur les différents interférogrammes sont essentiellement les coulées de lave ceci principalement grâce à l'absence de végétations. Or, la mise en place de coulées de laves récentes s'accompagne de déformations à long terme provoquées par la compaction thermomécanique des coulées et la flexion viscoélastique du substratum. Ces déformations rendent ainsi particulièrement difficile la détection et l'analyse des déplacements de faibles amplitudes provoqués par d'autres processus qui se superposent à celles-ci. C'est pour cette raison que nous nous sommes attachés à caractériser le plus finement possible ces déformations à partir d'une étude réalisée sur des coulées qui n'étaient pas affectées par d'autres sources de déformations. Nous avons pu ainsi mettre en évidence que les déformations sur les coulées récentes s'expliquent essentiellement par des phénomènes de subsidence ne s'accompagnant pas de déplacements horizontaux significatifs. L'empreinte de ces subsidences est plus large que celle des coulées indiquant que les déformations sont principalement en relation avec la flexion du substratum. Il existe une relation linéaire entre ces déplacements et l'épaisseur de la coulée et l'amplitude des déplacements décroît avec le temps. Ces relations nous ont permis de construire une loi empirique pour estimer la contribution des déplacements provoqués par la mise en place des coulées de lave sur l'ensemble de l'édifice volcanique.

Enfin, notre étude a montré que le glissement du flanc est qui a débuté durant l'éruption historique de 2007 a continué au moins jusqu'en novembre 2014, date de la dernière acquisition d'image radar de notre étude. Pour expliquer l'existence de ce glissement dont l'amplitude décroît dans le temps suggérant un phénomène de relaxation, nous avons étudié différentes hypothèses et proposé différents mécanismes pouvant expliquer ces déplacements. Enfin, ces résultats soulignent l'importance de suivre l'évolution de ce glissement compte tenu du risque potentiel que pourrait représenter une accélération de ce phénomène.

Le Llaima

Comme sur le Piton de la Fournaise, nos travaux sur le Llaima montrent que la contribution troposphérique dans les interférogrammes est la principale source d'erreurs dans l'interprétation des mesures radars. Sur ce volcan, l'analyse des données multispectrales MERIS et MODIS indique qu'il est difficile, voire impossible de détecter une déformation brève et de faible amplitude ($< 7\text{cm}$) à partir d'un seul interférogramme. En nous appuyant sur cette étude, nous avons développé une approche numérique d'inversion des données InSAR acquises entre 2003 et 2011 qui prend en compte l'impact des effets troposphériques. Les résultats de cette inversion a mis en évidence qu'aucune déformation significative n'est observée durant la période éruptive de 2008 et que la majeure partie des signaux interférométriques détectés était d'origine troposphérique. Cette interprétation va à l'encontre de celle proposée par Bathke et al. (2001) où les auteurs, considérant les effets troposphériques comme négligeables, avaient interprété ces signaux comme l'expression de la mise sous pression d'une chambre magmatique située à 7 km de profondeur. L'analyse de d'images acquises par le satellite ALOS sous deux angles de visée différents suggère qu'un gonflement survenu juste avant l'éruption d'avril 2009 pourrait être à l'origine du signal interférométrique. Néanmoins, comme le volume déterminé par l'inversion est en dessous de la marge d'erreur déterminé par l'ajustement par moindre carré de ce paramètre, il nous est impossible de ne pas rejeter l'hypothèse qu'aucune déformation n'ait été observée par InSAR entre 2003 et 2011.

Depuis les premières études des déformations de la surface terrestre réalisées par interférométrie radar, l'augmentation des images disponibles, l'amélioration de la précision des vecteurs/paramètres orbitaux et des modèles numériques de terrain ont permis d'augmenter sensiblement la précision des mesures interférométriques. Néanmoins, les deux études que nous avons réalisé ont montré que le facteur limitant le plus les potentialités de l'interférométrie radars pour l'étude des déformations des édifices volcaniques est l'impact des contributions troposphériques dans les interférogrammes. Bien que l'utilisation de modèle atmosphérique global pour estimer les variations de l'indice de réfraction de la troposphère ait montré leur intérêt pour différentes études, l'utilisation de ce type de modèle pour nos études n'a pas donné de résultats concluants. Les résolutions spatiales et temporelles des estimations produites par ce modèle global ne sont clairement pas en adéquation avec la variabilité spatiale et temporelle du contenu en vapeur d'eau observée dans les zones au climat océanique où sont

situées les deux édifices volcaniques étudiés. En l'absence d'une méthode universelle, nous avons donc été amenés sur chacun de ces sites à développer des approches empiriques spécifiques pour tenter de minimiser le plus possible l'impact des effets troposphériques dans les interférogrammes. Il est clair que pour pouvoir cartographier précisément les déformations localisées sur ces grands édifices volcaniques, il est indispensable de mieux caractériser/quantifier les variations spacio-temporelles de l'indice de réfraction de l'atmosphère à l'onde radar.

Depuis l'apparition du système GNSS et de l'interférométrie radar, de nombreuses études des déformations en relation avec l'activité volcanique ont été réalisées. L'objectif principal de ces études est de quantifier les phénomènes de transfert de magma qui s'opèrent dans les structures superficielles et profondes d'un édifice volcanique. Elles apportent des indications indispensables sur les structures internes des volcans en permettant notamment de mieux comprendre les modalités selon lesquelles sont transmises les contraintes et les déformations à travers l'encaissant depuis la source jusqu'à la surface de l'édifice. Les études réalisées durant cette thèse s'inscrivent dans cet effort d'une meilleure compréhension de l'objet géologique complexe qu'est un volcan. Néanmoins, de nombreuses incertitudes subsistent généralement sur la nature des phénomènes à l'origine des signaux observés soulignant ainsi que la compréhension du fonctionnement des systèmes volcaniques reste un défi majeur pour les sciences de la terre. L'analyse bibliographique des études réalisées sur l'édifice a montré que de nombreuses incertitudes existaient toujours sur la structure interne de l'édifice et sur sa rhéologie. C'est ce qui nous a amené à explorer différentes possibilités pour tenter d'expliquer les signaux que nous avons observés par InSAR et GNSS. Cette absence de lois phénoménologiques claires explique que nous n'ayons pas mis en œuvre des modélisations numériques, considérant que compte tenu de ces incertitudes, il apparaissait difficile de justifier le choix d'un modèle et d'une rhéologie spécifiques.

Cependant, le Piton de la Fournaise est l'un des volcans les mieux surveillés du monde avec les différents réseaux (GNSS, stations sismiques, etc.) qui sont déployés sur ses flancs. Avec la mise en place de nombreuses constellations de satellites il sera possible, dans un avenir proche, d'obtenir des images acquises tous les 6 jours permettant d'imager le champ de déplacement à haute résolution spatiale et temporelle. L'utilisation combinée des différentes techniques d'observations permettra de mieux suivre les variations des paramètres physiques et

chimiques : sismicité, déformation de surface, géochimie des laves et des gaz, etc. Toutes ces observations conduiront à l'amélioration des connaissances fondamentales sur le schéma structural du Piton de la Fournaise et de son évolution. Ces progrès dans l'instrumentation des édifices volcaniques apporteront également des informations essentielles pour mieux comprendre la complexité du mode de fonctionnement des grands volcans andésitiques comme le Llaima.

REFERENCES

- ©CNES/Altamira-information (1996), Philosophie et mode d'emploi de la chaîne logicielle interférométrique DIAPASON, Toulouse, France.
- Agram, P. S., Jolivet, R., Riel, B., Lin, Y. N., Simons, M., Hetland, E., Doin, M. P., & Lasserre, C. (2013). New radar interferometric time series analysis toolbox released. *Eos, Transactions American Geophysical Union*, 94(7), 69-70.
- Albino, F., Smets, B., d'Oreye, N., & Kervyn, F. (2015). High-resolution TanDEM-X DEM: An accurate method to estimate lava flow volumes at Nyamulagira Volcano (DR Congo). *Journal of Geophysical Research: Solid Earth*, 120(6), 4189-4207.
- Aloisi, M., Bonaccorso, A., Gambino, S., Mattia, M., & Puglisi, G. (2003). Etna 2002 eruption imaged from continuous tilt and GPS data. *Geophysical research letters*, 30(23).
- Amelung, F., Galloway, D. L., Bell, J. W., Zebker, H. A., & Lacznik, R. J. (1999). Sensing the ups and downs of Las Vegas: InSAR reveals structural control of land subsidence and aquifer-system deformation. *Geology*, 27(6), 483-486.
- Anderssohn, J., Motagh, M., Walter, T. R., Rosenau, M., Kaufmann, H., & Oncken, O. (2009). Surface deformation time series and source modeling for a volcanic complex system based on satellite wide swath and image mode interferometry: The Lazufre system, central Andes. *Remote Sensing of Environment*, 113(10), 2062-2075.
- Annen, C., Lénat, J. F., & Provost, A. (2001). The long-term growth of volcanic edifices: numerical modelling of the role of dyke intrusion and lava-flow emplacement. *Journal of Volcanology and Geothermal Research*, 105(4), 263-289.
- Antonello, G., Casagli, N., Farina, P., Leva, D., Nico, G., Sieber, A. J., & Tarchi, D. (2004). Ground-based SAR interferometry for monitoring mass movements. *Landslides*, 1(1), 21-28.
- Augier, A., Froger, J. L., Cayol, V., Fukushima, Y., Tinard, P., Souriot, T., Mora, O., Staudacher, T., Durand, P., Fruneau, B., & Villeneuve, N. (2008). The April 2007 eruption at Piton de la Fournaise, Réunion Island, imaged with ENVISAT-ASAR and ALOS-PALSAR data, *USEReST workshop*, Napoli, Italy.
- Augier, A. (2011). *Etude de l'éruption d'avril 2007 du Piton de la Fournaise (île de la Réunion) à partir de données d'interférométrie RADAR et GPS, développement et application de procédures de modélisation* (Doctoral dissertation, Université Blaise Pascal-Clermont-Ferrand II).

REFERENCES

- Bachèlery, P. (1981). *Le Piton de la Fournaise (Ile de la Reunion). Etude volcanologique, structurale et petrologique. Piton de la Fournaise, Reunion; volcanologic, structural and petrographic study* (Doctoral dissertation, Doctoral Thesis, Univ. of Clermont-Ferrand, Clermont-Ferrand).
- Bachèlery, P., & Mairine, P. (1990). Evolution volcano-structurale du Piton de la Fournaise depuis 0.53 Ma. *Le volcanisme de la Réunion, Monographie. Cent. Rech. Volcanol., Clermont-Ferrand, France*, 213-242.
- Bachèlery, P. (1995). Quelques réflexions à propos de concepts récents sur la structure du Piton de la Fournaise, Réunion. *Rapport Quadriennal 1991-1994*. Comité National Français de Géodésie et de Géophysique, Paris.
- Bachèlery, P., Saint-Ange, F., Villeneuve, N., Savoye, B., Normand, A., Le Drezen, E., Barrère, A., Quod J. P. & Deplus, C. (2010). Huge lava flows into the sea and caldera collapse, April 2007, Piton de la Fournaise volcano. *Geophysical Research Letters*, 34, L21301.
- Bagnardi, M., & Amelung, F. (2012). Space-geodetic evidence for multiple magma reservoirs and subvolcanic lateral intrusions at Fernandina Volcano, Galápagos Islands. *Journal of Geophysical Research: Solid Earth*, 117(B10).
- Bahr, H., & Hanssen, R. (2012). Reliable estimation of orbit errors in spaceborne SAR interferometry. *Journal of Geodesy*, 86(12), 1147-1164.
- Baker, S., & Amelung, F. (2012). Top-down inflation and deflation at the summit of Kīlauea Volcano, Hawai'i observed with InSAR. *Journal of Geophysical Research: Solid Earth*, 117(B12).
- Bathke, H., Shirzaei, M., & Walter, T. R. (2011). Inflation and deflation at the steep-sided Llaima stratovolcano (Chile) detected by using InSAR. *Geophysical Research Letters*, 38(10), L10304.
- Bato, M. G., Froger, J. L., Harris, A. J. L., & Villeneuve, N. (2016). Monitoring an effusive eruption at Piton de la Fournaise using radar and thermal infrared remote sensing data: insights into the October 2010 eruption and its lava flows. *Geological Society, London, Special Publications*, 426, SP426-30.
- Battaglia, J., Ferrazzini, V., Staudacher, T., Aki, K., & Cheminée, J. L. (2005). Pre-eruptive migration of earthquakes at the Piton de la Fournaise volcano (Réunion Island). *Geophysical Journal International*, 161(2), 549-558.
- Battaglia, M., Segall, P., & Roberts, C. (2003). The mechanics of unrest at Long Valley caldera, California. 2. Constraining the nature of the source using geodetic and micro-gravity data. *Journal of Volcanology and Geothermal Research*, 127(3), 219-245.
- Bean, B. R., & Dutton, E. J. (1966). *Radio meteorology*. Dover Publications.

REFERENCES

- Beauducel, F., Briole, P., & Froger, J. L. (2000). Volcano-wide fringes in ERS synthetic aperture radar interferograms of Etna (1992–1998): Deformation or tropospheric effect? *Journal of Geophysical Research: Solid Earth*, *105*(B7), 16391-16402.
- Bechor, N. B., & Zebker, H. A. (2006). Measuring two-dimensional movements using a single InSAR pair. *Geophysical research letters*, *33*(16).
- Bekaert, D. P. S., Hooper, A., & Wright, T. J. (2015). A spatially variable power law tropospheric correction technique for InSAR data. *Journal of Geophysical Research: Solid Earth*, *120*(2), 1345-1356.
- Berardino, P., Fornaro, G., Lanari, R., & Sansosti, E. (2002). A new algorithm for surface deformation monitoring based on small baseline differential SAR interferograms. *Geoscience and Remote Sensing, IEEE Transactions on*, *40*(11), 2375-2383.
- Berardino, P., Costantini, M., Franceschetti, G., Iodice, A., Pietranera, L., & Rizzo, V. (2003). Use of differential SAR interferometry in monitoring and modelling large slope instability at Maratea (Basilicata, Italy). *Engineering Geology*, *68*(1), 31-51.
- Bevis, M., Chiswell, S., Businger, S., Herring, T. A., & Bock, Y. (1996). Estimating wet delay using numerical weather analysis and predictions. *Radio Science*, *31*(3), 447-487.
- Bignami, C., Burrato, P., Cannelli, V., Chini, M., Falcucci, E., Ferretti, A., Gori, S., Kyriakopoulos, C., Melini, D., & Moro, M. (2012). Coseismic deformation pattern of the Emilia 2012 seismic sequence imaged by Radarsat-1 interferometry. *Annals of Geophysics*, *55*(4).
- Bouvet de Maisonneuve, C., Dungan, M. A., Bachmann, O., & Burgisser, A. (2012). Insights into shallow magma storage and crystallization at Volcán Llaima (Andean Southern Volcanic Zone, Chile). *Journal of Volcanology and Geothermal Research*, *211*, 76-91.
- Bovenga, F., Wasowski, J., Nitti, D. O., Nutricato, R., & Chiaradia, M. T. (2012). Using COSMO/SkyMed X-band and ENVISAT C-band SAR interferometry for landslides analysis. *Remote Sensing of Environment*, *119*, 272-285.
- Briole, P., Massonnet, D., & Delacourt, C. (1997). Post-eruptive deformation associated with the 1986–87 and 1989 lava flows of Etna detected by radar interferometry. *Geophysical Research Letters*, *24*(1), 37-40.
- Brooks, B. A., Foster, J., Sandwell, D., Wolfe, C. J., Okubo, P., Poland, M., & Myer, D. (2008). Magmatically triggered slow slip at Kilauea Volcano, Hawaii. *Science*, *321*(5893), 1177-1177.
- Brown, L. G. (1992). A survey of image registration techniques. *ACM computing surveys (CSUR)*, *24*(4), 325-376.

REFERENCES

- Bürgmann, R., Rosen, P. A., & Fielding, E. J. (2000). Synthetic aperture radar interferometry to measure Earth's surface topography and its deformation. *Annual review of earth and planetary sciences, 28*(1), 169-209.
- Carrier, A., Got, J. L., Peltier, A., Ferrazzini, V., Staudacher, T., Kowalski, P., & Boissier, P. (2015). A damage model for volcanic edifices: Implications for edifice strength, magma pressure, and eruptive processes. *Journal of Geophysical Research: Solid Earth, 120*(1), 567-583.
- Cavalié, O., Doin, M. P., Lasserre, C., & Briole, P. (2007). Ground motion measurement in the Lake Mead area, Nevada, by differential synthetic aperture radar interferometry time series analysis: Probing the lithosphere rheological structure. *Journal of Geophysical Research: Solid Earth, 112*(B3).
- Cavalié, O., Lasserre, C., Doin, M. P., Peltzer, G., Sun, J., Xu, X., & Shen, Z. K. (2008). Measurement of interseismic strain across the Haiyuan fault (Gansu, China), by InSAR. *Earth and Planetary Science Letters, 275*(3), 246-257.
- Cayol, V., & Cornet, F. H. (1998). Three-dimensional modeling of the 1983-1984 eruption at Piton de la Fournaise Volcano, Reunion Island. *Journal of Geophysical Research, 103*(B8), 18025-18037.
- Cayol, V., Catry, T., Michon, L., Chaput, M., Famin, V., Bodart, O., Froger, J. L., & Romagnoli, C. (2014). Sheared sheet intrusions as mechanism for lateral flank displacement on basaltic volcanoes: Applications to Réunion Island volcanoes. *Journal of Geophysical Research: Solid Earth, 119*(10), 7607-7635.
- Chadwick, W. W., Geist, D. J., Jónsson, S., Poland, M., Johnson, D. J., & Meertens, C. M. (2006). A volcano bursting at the seams: inflation, faulting, and eruption at Sierra Negra Volcano, Galápagos. *Geology, 34*(12), 1025-1028.
- Chaput, M., Pinel, V., Famin, V., Michon, L., & Froger, J. L. (2014a). Cointrusive shear displacement by sill intrusion in a detachment: A numerical approach. *Geophysical Research Letters, 41*(6), 1937-1943.
- Chaput, M., Famin, V., & Michon, L. (2014b). Deformation of basaltic shield volcanoes under cointrusive stress permutations. *Journal of Geophysical Research: Solid Earth, 119*(1), 274-301.
- Chaussard, E., Wdowinski, S., Cabral-Cano, E., & Amelung, F. (2014). Land subsidence in central Mexico detected by ALOS InSAR time-series. *Remote sensing of environment, 140*, 94-106.
- Chaussard, E. (2016). Subsidence in the Parícutin lava field: Causes and implications for interpretation of deformation fields at volcanoes. *Journal of Volcanology and Geothermal Research, 320*, 1-11.

REFERENCES

- Chen, C. W., & Zebker, H. A. (2000). Network approaches to two-dimensional phase unwrapping: intractability and two new algorithms. *Journal of Optical Society of America A*, 17(3), 401-414.
- Chevallier, L., & Bachèlery, P. (1981). Evolution structurale du volcan actif du Piton de la Fournaise, Ile de la Réunion—Océan indien occidental. *Bulletin volcanologique*, 44(4), 723-741.
- Chouet, B. A., Page, R. A., Stephens, C. D., Lahr, J. C., & Power, J. A. (1994). Precursory swarms of long-period events at Redoubt Volcano (1989–1990), Alaska: Their origin and use as a forecasting tool. *Journal of Volcanology and Geothermal Research*, 62(1-4), 95-135.
- Clarke, D., Brenguier, F., Froger, J. L., Shapiro, N. M., Peltier, A., & Staudacher, T. (2013). Timing of a large volcanic flank movement at Piton de la Fournaise Volcano using noise-based seismic monitoring and ground deformation measurements. *Geophysical Journal International*, 195(2), 1132-1140.
- Costantini, M. (1998). A novel phase unwrapping method based on network programming. *Geoscience and Remote Sensing, IEEE Transactions on*, 36(3), 813-821.
- Curlander J. C. & McDonough R. N. (1991). *Synthetic Aperture Radar: Systems and Signal Processing*. Wiley, New York.
- Cusack, R., & Papadakis, N. (2002). New robust 3-D phase unwrapping algorithms: application to magnetic field mapping and undistorting echoplanar images. *Neuroimage*, 16(3), 754-764.
- Dee, D. P., et al. (2011). The ERA-Interim reanalysis: Configuration and performance of the data assimilation system. *Quarterly Journal of the royal meteorological society*, 137(656), 553-597.
- Delacourt, C., Briole, P., & Achache, J. A. (1998). Tropospheric corrections of SAR interferograms with strong topography. Application to Etna. *Geophysical Research Letters*, 25(15), 2849-2852.
- Denlinger, R. P., & Okubo, P. (1995). Structure of the mobile south flank of Kilauea Volcano, Hawaii. *Journal of Geophysical Research: Solid Earth*, 100(B12), 24499-24507.
- Dhont, D., Chorowicz, J., Collet, B., Barbieri, M., & Lichtenegger, J. (2005). Spaceborne radar applications in Geology: An introduction to imaging radar, and application examples of ERS SAR in Geology and Geomorphology, *ESA publication*, TM-17.
- Dietterich, H. R., Poland, M. P., Schmidt, D. A., Cashman, K. V., Sherrod, D. R., & Espinosa, A. T. (2012). Tracking lava flow emplacement on the east rift zone of Kīlauea, Hawai ‘i, with synthetic aperture radar coherence. *Geochemistry, Geophysics, Geosystems*, 13(5).
- Di Muro, A., Métrich, N., Vergani, D., Rosi, M., Armienti, P., Fougereux, T., Deloule, E., Arienzo, L., & Civetta, L. (2014). The shallow plumbing system of Piton de la Fournaise Volcano (La Reunion

REFERENCES

- Island, Indian Ocean) revealed by the major 2007 caldera-forming eruption. *Journal of Petrology*, 55(7), 1287-1315.
- Di Muro, A., Staudacher, T., Ferrazzini, V., Métrich, N., Besson, P., Garofalo, C., & Villemant, B. (2015). Shallow magma storage at Piton de la Fournaise volcano after 2007 summit caldera collapse tracked in Pele's hairs. In: Carey, R., Cayol, V., Poland, M., Weis, D. (Eds.), *Hawaiian volcanoes: from source to surface. Geophysical monograph series*, 208, 189-212.
- Di Traglia, F., Nolesini, T., Intrieri, E., Mugnai, F., Leva, D., Rosi, M., & Casagli, N. (2014). Review of ten years of volcano deformations recorded by the ground-based InSAR monitoring system at Stromboli volcano: a tool to mitigate volcano flank dynamics and intense volcanic activity. *Earth-Science Reviews*, 139, 317-335.
- Doin, M. P., Lasserre, C., Peltzer, G., Cavalié, O., & Doubre, C. (2009). Corrections of stratified tropospheric delays in SAR interferometry: Validation with global atmospheric models. *Journal of Applied Geophysics*, 69(1), 35-50.
- Ducret, G. (2013). *Mesure de déformation par interférométrie radar: développements méthodologiques et applications à la subduction chilienne* (Doctoral dissertation, Institut de Physique du Globe de Paris; Ecole Normale Supérieure; Sorbonne Paris Cité).
- Duffield, W. A., Stieltjes, L., & Varet, J. (1982). Huge landslide blocks in the growth of Piton de la Fournaise, La Reunion, and Kilauea Volcano, Hawaii. *Journal of Volcanology and Geothermal Research*, 12(1), 147-160.
- Duncan, R. A. (1981). Hotspots in the southern oceans—an absolute frame of reference for motion of the Gondwana continents. *Tectonophysics*, 74(1), 29-42.
- Dzurisin, D. (2003). A comprehensive approach to monitoring volcano deformation as a window on the eruption cycle. *Reviews of Geophysics*, 41(1).
- Ebmeier, S. K., Biggs, J., Mather, T. A., Wadge, G., & Amelung, F. (2010). Steady downslope movement on the western flank of Arenal volcano, Costa Rica. *Geochemistry, Geophysics, Geosystems*, 11(12).
- Ebmeier, S. K., Biggs, J., Mather, T. A., Elliott, J. R., Wadge, G., & Amelung, F. (2012). Measuring large topographic change with InSAR: Lava thicknesses, extrusion rate and subsidence rate at Santiaguito volcano, Guatemala. *Earth and Planetary Science Letters*, 335, 216-225.
- Ebmeier, S. K., Biggs, J., Mather, T. A., & Amelung, F. (2013). Applicability of InSAR to tropical volcanoes: insights from Central America. *Geological Society, London, Special Publications*, 380(1), 15-37.

REFERENCES

- Elliott, J. R., Biggs, J., Parsons, B., & Wright, T. J. (2008). InSAR slip rate determination on the Altyn Tagh Fault, northern Tibet, in the presence of topographically correlated atmospheric delays. *Geophysical Research Letters*, *35*(12).
- Emardson, T. R., Simons, M., & Webb, F. H. (2003). Neutral atmospheric delay in interferometric synthetic aperture radar applications: Statistical description and mitigation. *Journal of Geophysical Research: Solid Earth*, *108*(B5).
- Famin, V., & Michon, L. (2010). Volcano destabilization by magma injections in a detachment. *Geology*, *38*(3), 219-222.
- Farr, T. G., & Kobrick, M. (2000). Shuttle Radar Topography Mission produces a wealth of data. *Eos, Transactions American Geophysical Union*, *81*(48), 583-585.
- Fattahi, H., & Amelung, F. (2013). DEM error correction in InSAR time series. *Geoscience and Remote Sensing, IEEE Transactions on*, *51*(7), 4249-4259.
- Fattahi, H., & Amelung, F. (2014). InSAR uncertainty due to orbital errors. *Geophysical Journal International*, *199*(1), 549-560.
- Feigl, K., & Thurber, H. (2009). A method for modelling radar interferograms without phase unwrapping: application to the M 5 Fawnskin, California earthquake of 1992 December 4. *Geophysical Journal International*, *176*(2), 491-504.
- Ferretti, A., Prati, C., & Rocca, F. (2001). Permanent scatterers in SAR interferometry. *Geoscience and Remote Sensing, IEEE Transactions on*, *39*(1), 8-20.
- Ferretti, A., Monti-Guarnieri, A., Prati, C., Rocca, F., & Massonet, D. (2007). InSAR Principles: Guidelines for SAR Interferometry Processing and Interpretation. ESA TM-19.
- Ferretti, A., Fumagalli, A., Novali, F., Prati, C., Rocca, F., & Rucci, A. (2011). A new algorithm for processing interferometric data-stacks: SqueeSAR. *Geoscience and Remote Sensing, IEEE Transactions on*, *49*(9), 3460-3470.
- Fialko, Y., Sandwell, D., Simons, M., & Rosen, P. (2005). Three-dimensional deformation caused by the Bam, Iran, earthquake and the origin of shallow slip deficit. *Nature*, *435*(7040), 295-299.
- Fontaine, F. R., Roult, G., Michon, L., Barruol, G., & Muro, A. D. (2014). The 2007 eruptions and caldera collapse of the Piton de la Fournaise volcano (La Réunion Island) from tilt analysis at a single very broadband seismic station. *Geophysical Research Letters*, *41*(8), 2803-2811.

REFERENCES

- Foster, J., Brooks, B., Cherubini, T., Shacat, C., Businger, S., & Werner, C. L. (2006). Mitigating atmospheric noise for InSAR using a high resolution weather model. *Geophysical Research Letters*, 33(16).
- Fournier, T. J., Pritchard, M. E., & Riddick, S. N. (2010). Duration, magnitude, and frequency of subaerial volcano deformation events: New results from Latin America using InSAR and a global synthesis. *Geochemistry, Geophysics, Geosystems*, 11(1), Q01003.
- Fournier, T., Pritchard, M. E., & Finnegan, N. (2011). Accounting for atmospheric delays in InSAR data in a search for long-wavelength deformation in South America. *IEEE Transactions on Geoscience and Remote Sensing*, 49(10), 3856-3867.
- Francis PW, Glaze LS, Rothery DA., (1989), Lascar volcano set to erupt, *Nature* 339: 434
- Froger, J. L., Merle, O., & Briole, P. (2001). Active spreading and regional extension at Mount Etna imaged by SAR interferometry. *Earth and Planetary Science Letters*, 187(3), 245-258.
- Froger, J. L., Fukushima, Y., Briole, P., Staudacher, T., Souriot, T., & Villeneuve, N. (2004). The deformation field of the August 2003 eruption at Piton de la Fournaise, Reunion Island, mapped by ASAR interferometry. *Geophysical research letters*, 31(14).
- Froger, J. L., Remy, D., Bonvalot, S., & Legrand, D. (2007). Two Scales of inflation at Lastarria-Cordon del Azufre volcanic complex, central Andes, revealed from ASAR-ENVISAT interferometric data. *Earth and Planetary Science Letters*, 255(1), 148-163.
- Froger, J. L., Bato, M.G., Villeneuve, N., Souriot, T., Rabaute, T., Durand, P., Cayol, V., Di Muro, A., Staudacher, T., Fruneau, B., & Tinel, C. (2011). High-resolution interferometric monitoring of Piton de la Fournaise with TERRASAR-X and COSMO-SKYMED data. *FRINGE 2011 workshop*, 19–23 September 2011. ESRIN, Frascati, Italy.
- Froger, J. L., Famin, V., Cayol, V., Augier, A., Michon, L., & Lénat, J. F. (2015). Time-dependent displacements during and after the April 2007 eruption of Piton de la Fournaise, revealed by interferometric data. *Journal of Volcanology and Geothermal Research*, 296, 55-68.
- Froger, J., V. Cayol, and V. Famin (2016), *Active Volcanoes of the Southwest Indian Ocean, Active Volcanoes of the World*, edited by P. Bachelery, J.-F. Lénat, A. Di Muro, and L. Michon, Springer Berlin Heidelberg, Berlin, Heidelberg.
- Fukushima, Y., Cayol, V., & Durand, P. (2005). Finding realistic dike models from interferometric synthetic aperture radar data: The February 2000 eruption at Piton de la Fournaise. *Journal of Geophysical Research: Solid Earth*, 110(B3).

REFERENCES

- Fukushima, Y., Cayol, V., Durand, P., & Massonnet, D. (2010). Evolution of magma conduits during the 1998–2000 eruptions of Piton de la Fournaise volcano, Réunion Island. *Journal of Geophysical Research: Solid Earth*, 115(B10).
- Gabriel, A. K., & Goldstein, R. M. (1988). Crossed orbit interferometry: theory and experimental results from SIR-B. *International Journal of Remote Sensing*, 9(5), 857-872.
- Gabriel, A. K., Goldstein, R. M., & Zebker, H. A. (1989). Mapping small elevation changes over large areas: differential radar interferometry. *Journal of Geophysical Research: Solid Earth*, 94(B7), 9183-9191.
- Gatelli, F., Monti Guamieri, A., Parizzi, F., Pasquali, P., Prati, C., & Rocca, F. (1994). The wavenumber shift in SAR interferometry. *Geoscience and Remote Sensing, IEEE Transactions on*, 32(4), 855-865.
- Ghiglia, D. C., & Romero, L. A. (1994). Robust two-dimensional weighted and unweighted phase unwrapping that uses fast transforms and iterative methods. *Journal of Optical Society of America A*, 11(1), 107-117.
- Ghiglia, D. C., & Romero, L. A. (1996). Minimum Lp-norm two-dimensional phase unwrapping. *Journal of Optical Society of America A*, 13(10), 1999-2013.
- Giggenbach, W. F., & Le Guern, F. (1976). The chemistry of magmatic gases from Erta'Ale, Ethiopia. *Geochimica et Cosmochimica Acta*, 40(1), 25-30.
- Gillot, P. Y., & Nativel, P. (1989). Eruptive history of the Piton de la Fournaise volcano, Réunion island, Indian Ocean. *Journal of volcanology and geothermal research*, 36(1), 53-65.
- Goldstein, R. M., Zebker, H. A., & Werner, C. L. (1988). Satellite radar interferometry: Two-dimensional phase unwrapping. *Radio science*, 23(4), 713-720.
- Goldstein, R. (1995). Atmospheric limitations to repeat-track radar interferometry. *Geophysical research letters*, 22, 2517-2517.
- Goldstein, R. M., & Werner, C. L. (1998). Radar interferogram filtering for geophysical applications. *Geophysical Research Letters*, 25(21), 4035-4038.
- Gong, W., Thiele, A., Hinz, S., Meyer, F. J., Hooper, A., & Agram, P. S. (2016). Comparison of Small Baseline Interferometric SAR Processors for Estimating Ground Deformation. *Remote Sensing*, 8(4), 330.
- Got, J. L., & Okubo, P. (2003). New insights into Kilauea's volcano dynamics brought by large-scale relative relocation of microearthquakes. *Journal of Geophysical Research: Solid Earth*, 108(B7).
- Got, J. L., Peltier, A., Staudacher, T., Kowalski, P., & Boissier, P. (2013). Edifice strength and magma transfer modulation at Piton de la Fournaise volcano. *Journal of Geophysical Research: Solid Earth*, 118(9), 5040-5057.

REFERENCES

- Gourmelen, N., Amelung, F., Casu, F., Manzo, M., & Lanari, R. (2007). Mining-related ground deformation in Crescent Valley, Nevada: Implications for sparse GPS networks. *Geophysical Research Letters*, 34(9).
- Griffiths, R. W., & Fink, J. H. (1993). Effects of surface cooling on the spreading of lava flows and domes. *Journal of Fluid Mechanics*, 252, 667-702.
- Griffiths, R. W. (2000). The dynamics of lava flows. *Annual Review of Fluid Mechanics*, 32, 477-518.
- Hall, M. P., Barclay, L. W., & Hewitt, M. T. (1996). Propagation of radiowaves. In *Propagation of Radiowaves*. The Institution of Electrical Engineers, London.
- Hanssen, R., & Bamler, R. (1999). Evaluation of interpolation kernels for SAR interferometry. *IEEE Transactions on Geoscience and Remote Sensing*, 37(1), 318-321.
- Hanssen, R. F. (2001). *Radar interferometry: data interpretation and error analysis*. Kluwer Academic Publishers.
- Harris, A., (2013), *Thermal Remote Sensing of Active Volcanoes: A User's Manual.*, Cambridge University Press, U.K., 736 p.
- Heleno, S. I. N., Frischknecht, C., d'Oreye, N., Lima, J. N. P., Faria, B., Wall, R., & Kervyn, F. (2010). Seasonal tropospheric influence on SAR interferograms near the ITCZ - The case of Fogo Volcano and Mount Cameroon. *Journal of African Earth Sciences*, 58(5), 833-856.
- Heleno, S. I., Oliveira, L. G., Henriques, M. J., Falcão, A. P., Lima, J. N., Cooksley, G., Ferretti, A., Fonseca, A. M., Lobo-Ferreira, J. P. & Fonseca, J. F. (2011). Persistent scatterers interferometry detects and measures ground subsidence in Lisbon. *Remote Sensing of Environment*, 115(8), 2152-2167.
- Herrera, G., Tomás, R., López-Sánchez, J. M., Delgado, J., Mallorqui, J. J., Duque, S., & Mulas, J. (2007). Advanced DInSAR analysis on mining areas: La Union case study (Murcia, SE Spain). *Engineering Geology*, 90(3), 148-159.
- Herrera, G., Notti, D., García-Davalillo, J. C., Mora, O., Cooksley, G., Sánchez, M., Arnaud, A. & Crosetto, M. (2011). Analysis with C-and X-band satellite SAR data of the Portalet landslide area. *Landslides*, 8(2), 195-206.
- Herring, T. A., King, R. W., & McClusky, S. C. (2010). GPS analysis at MIT. *GAMIT Reference Manual, Release, 10.4*. Massachusetts Institute of Technology, Cambridge.
- Hetland, E. A., Musé, P., Simons, M., Lin, Y. N., Agram, P. S., & DiCaprio, C. J. (2012). Multiscale InSAR time series (MInTS) analysis of surface deformation. *Journal of Geophysical Research: Solid Earth*, 117(B2).

REFERENCES

- Hirn, A., L epine, J. C., Sapin, M., & Delorme, H. (1991). Episodes of pit-crater collapse documented by seismology at Piton de la Fournaise. *Journal of Volcanology and Geothermal Research*, 47(1), 89-104.
- Hooper, A., Zebker, H., Segall, P., & Kampes, B. (2004). A new method for measuring deformation on volcanoes and other natural terrains using InSAR persistent scatterers. *Geophysical research letters*, 31(23).
- Hooper, A., & Zebker, H. A. (2007). Phase unwrapping in three dimensions with application to InSAR time series. *Journal of Optical Society of America A*, 24(9), 2737-2747.
- Hooper, A., Segall, P., & Zebker, H. (2007). Persistent scatterer interferometric synthetic aperture radar for crustal deformation analysis, with application to Volc an Alcedo, Gal apagos. *Journal of Geophysical Research: Solid Earth*, 112(B7).
- Hooper, A. (2008). A multi-temporal InSAR method incorporating both persistent scatterer and small baseline approaches. *Geophysical Research Letters*, 35(16).
- Hooper, A., Bekaert, D., Spaans, K., & Arkan, M. (2012). Recent advances in SAR interferometry time series analysis for measuring crustal deformation. *Tectonophysics*, 514, 1-13.
- Huntley, J. M. (2001). Three-dimensional noise-immune phase unwrapping algorithm. *Applied Optics*, 40(23), 3901-3908.
- Hyndman, R. D., Yamano, M., & Oleskevich, D. A. (1997). The seismogenic zone of subduction thrust faults. *Island Arc*, 6(3), 244-260.
- Intrieri, E., Di Traglia, F., Del Ventisette, C., Gigli, G., Mugnai, F., Luzi, G., & Casagli, N. (2013). Flank instability of Stromboli volcano (Aeolian Islands, Southern Italy): integration of GB-InSAR and geomorphological observations. *Geomorphology*, 201, 60-69.
- Jenkinson, M. (2003). Fast, automated, N-dimensional phase-unwrapping algorithm. *Magnetic resonance in medicine*, 49(1), 193-197.
- Jo, M. J., Jung, H. S., Won, J. S., & Lundgren, P. (2015). Measurement of three-dimensional surface deformation by Cosmo-SkyMed X-band radar interferometry: Application to the March 2011 Kamoamoao fissure eruption, K ilauea Volcano, Hawai'i. *Remote Sensing of Environment*, 169, 176-191.
- Jolivet, R., Grandin, R., Lasserre, C., Doin, M. P., & Peltzer, G. (2011). Systematic InSAR tropospheric phase delay corrections from global meteorological reanalysis data. *Geophysical Research Letters*, 38(17).

REFERENCES

- Jolivet, R., Lasserre, C., Doin, M. P., Guillaso, S., Peltzer, G., Dailu, R., & Sun, J. (2012). Shallow creep on the Haiyuan fault (Gansu, China) revealed by SAR interferometry. *Journal of Geophysical Research: Solid Earth*, 117(B6).
- Jolivet, R., Agram, P. S., Lin, N. Y., Simons, M., Doin, M. P., Peltzer, G., & Li, Z. (2014). Improving InSAR geodesy using global atmospheric models. *Journal of Geophysical Research: Solid Earth*, 119(3), 2324-2341.
- Joughin, I. R., Winebrenner, D. P., & Fahnestock, M. A. (1995). Observations of ice-sheet motion in Greenland using satellite radar interferometry. *Geophysical Research Letters*, 22(5), 571-574.
- Just, D., & Bamler, R. (1994). Phase statistics of interferograms with applications to synthetic aperture radar. *Applied optics*, 33(20), 4361-4368.
- Kelfoun, K., Giachetti, T., & Labazuy, P. (2010). Landslide-generated tsunamis at Réunion Island. *Journal of Geophysical Research: Earth Surface*, 115(F04012).
- Kieffer, G. (1990). Grands traits morphologiques de l'île de La Réunion. *Le volcanisme de La Réunion Monographie*, 75-114.
- King, P.L., Ramsey, M.S., Swayze, G. (2004) Infrared spectroscopy of silicate glasses with application to natural system, , *Mineral. assoc. Canada*, 33 , pp. 93–132.
- Kositsky, A. P., & Avouac, J. P. (2010). Inverting geodetic time series with a principal component analysis-based inversion method. *Journal of Geophysical Research: Solid Earth*, 115(B3).
- Kumar, V., Venkataramana, G., & Høgda, K. A. (2011). Glacier surface velocity estimation using SAR interferometry technique applying ascending and descending passes in Himalayas. *International Journal of Applied Earth Observation and Geoinformation*, 13(4), 545-551.
- Kwoh, L. K., Chang, E. C., Heng, W. C. A., & Lim, H. (1994). DTM generation from 35-day repeat pass ERS-1 interferometry. In *Geoscience and Remote Sensing Symposium, 1994. IGARSS'94. Surface and Atmospheric Remote Sensing: Technologies, Data Analysis and Interpretation, International (Vol. 4, pp. 2288-2290)*. IEEE.
- Labazuy, P. (1996). Recurrent landslides events on the submarine flank of Piton de la Fournaise volcano (Reunion Island). *Geological Society, London, Special Publications*, 110(1), 295-306.
- Lahr, J. C., Chouet, B. A., Stephens, C. D., Power, J. A., & Page, R. A. (1994). Earthquake classification, location, and error analysis in a volcanic environment: Implications for the magmatic system of

REFERENCES

- the 1989–1990 eruptions at Redoubt Volcano, Alaska. *Journal of Volcanology and Geothermal Research*, 62(1), 137-151.
- Lanari, R., Lundgren, P., & Sansosti, E. (1998). Dynamic deformation of Etna volcano observed by satellite radar interferometry. *Geophysical Research Letters*, 25(10), 1541-1544.
- Lanari, R., Mora, O., Manunta, M., Mallorquí, J. J., Berardino, P., & Sansosti, E. (2004a). A small-baseline approach for investigating deformations on full-resolution differential SAR interferograms. *Geoscience and Remote Sensing, IEEE Transactions on*, 42(7), 1377-1386.
- Lanari, R., Lundgren, P., Manzo, M., & Casu, F. (2004b). Satellite radar interferometry time series analysis of surface deformation for Los Angeles, California. *Geophysical Research Letters*, 31(23).
- Lasserre, C., Peltzer, G., Crampé, F., Klinger, Y., Van Der Woerd, J., & Tapponnier, P. (2005). Coseismic deformation of the 2001 Mw= 7.8 Kokoxili earthquake in Tibet, measured by synthetic aperture radar interferometry. *Journal of Geophysical Research: Solid Earth*, 110(B12).
- Lasserre, C., Cavalié, O., Peltzer, G., Socquet, A., Doin, M. P., Sun, J., Xu, X., Shen, Z. K., Wang, Q. & Gaudemer, Y. (2007). Interseismic strain across the Altyn Tagh and Haiyuan faults at the northern edge of the Tibetan plateau, measured by space geodesy. *Geophysical Research Abstracts CDROM*, 9, 10102.
- Lauknes, T. R., Shanker, A. P., Dehls, J. F., Zebker, H. A., Henderson, I. H. C., & Larsen, Y. (2010). Detailed rockslide mapping in northern Norway with small baseline and persistent scatterer interferometric SAR time series methods. *Remote Sensing of Environment*, 114(9), 2097-2109.
- Le Friant, A., Lebas, E., Clément, V., Boudon, G., Deplus, C., de Voogd, B., & Bachèlery, P. (2011). A new model for the evolution of La Réunion volcanic complex from complete marine geophysical surveys. *Geophysical Research Letters*, 38(9).
- Le Maitre, R. W., Streckeisen, A., Zanettin, B., Le Bas, M. J., Bonin, B., Bateman, P., & Lameyre, J. (2002). Igneous rocks: a classification and glossary of terms: recommendations of the International Union of Geological Sciences. In *Subcommission on the Systematics of Igneous Rocks*. Cambridge University Press.
- Lee, J. S., Papathanassiou, K. P., Ainsworth, T. L., Grunes, M. R., & Reigber, A. (1998). A new technique for noise filtering of SAR interferometric phase images. *Geoscience and Remote Sensing, IEEE Transactions on*, 36(5), 1456-1465.
- Lénat, J. F., Vincent, P., & Bachèlery, P. (1989). The off-shore continuation of an active basaltic volcano: Piton de la Fournaise (Réunion Island, Indian Ocean); structural and geomorphological

REFERENCES

- interpretation from sea beam mapping. *Journal of Volcanology and Geothermal Research*, 36(1), 1-36.
- Lénat, J. F., Bachèlery, P., Bonneville, A., Galdéano, A., Labazuy, P., Rousset, D., & Vincent, P. (1990). Structure and morphology of the submarine flank of an active volcano: Piton de la Fournaise (Reunion Island, Indian Ocean). *Oceanologica Acta* 10, 211–223.
- Lénat, J. F., Gibert-Malengreau, B., & Galdéano, A. (2001). A new model for the evolution of the volcanic island of Reunion (Indian Ocean). *Journal of Geophysical Research: Solid Earth*, 106(B5), 8645-8663.
- Lénat, J. F., Bachèlery, P., & Merle, O. (2012). Anatomy of Piton de la Fournaise volcano (La Réunion, Indian Ocean). *Bulletin of volcanology*, 74(9), 1945-1961.
- Li, F. K., & Goldstein, R. M. (1990). Studies of multibaseline spaceborne interferometric synthetic aperture radars. *Geoscience and Remote Sensing, IEEE Transactions on*, 28(1), 88-97.
- Li, Z., Muller, J. P., & Cross, P. (2003). Comparison of precipitable water vapor derived from radiosonde, GPS, and Moderate-Resolution Imaging Spectroradiometer measurements. *Journal of Geophysical Research: Atmospheres*, 108(D20).
- Li, Z. (2005). Correction of Atmospheric Water vapour Effects on repeat-Pass SAR interferometry Using GPS, MODIS, and MERIS data. *PhD thesis*, 224 pp, College London, London.
- Li, Z., Muller, J. P., Cross, P., & Fielding, E. J. (2005). Interferometric synthetic aperture radar (InSAR) atmospheric correction: GPS, Moderate Resolution Imaging Spectroradiometer (MODIS), and InSAR integration. *Journal of Geophysical Research: Solid Earth*, 110(B3).
- Li, Z., Fielding, E. J., Cross, P., & Muller, J. P. (2006a). Interferometric synthetic aperture radar atmospheric correction: GPS topography-dependent turbulence model. *Journal of Geophysical Research: Solid Earth*, 111(B2).
- Li, Z., Fielding, E., Cross, P., & Muller, J.-P. (2006b). Interferometric synthetic aperture radar atmospheric correction: Medium Resolution Imaging Spectrometer and Advanced Synthetic Aperture Radar integration. *Geophysical Research Letters*, 33(6), L06816.
- Li, Z., Fielding, E. J., Cross, P., & Preusker, R. (2009). Advanced InSAR atmospheric correction: MERIS/MODIS combination and stacked water vapor models. *International Journal of Remote Sensing*, 30(13), 3343-3363.

REFERENCES

- Li, Z. W., Xu, W. B., Feng, G. C., Hu, J., Wang, C. C., Ding, X. L., & Zhu, J. J. (2012a). Correcting atmospheric effects on InSAR with MERIS water vapour data and elevation-dependent interpolation model. *Geophysical Journal International*, *189*(2), 898-910.
- Li, Z., Pasquali, P., Cantone, A., Singleton, A., Funning, G., & Forrest, D. (2012b). MERIS atmospheric water vapor correction model for wide swath interferometric synthetic aperture radar. *IEEE Geoscience and Remote Sensing Letters*, *9*(2), 257-261.
- Lin, Y. N. N., Simons, M., Hetland, E. A., Muse, P., & DiCaprio, C. (2010a). A multiscale approach to estimating topographically correlated propagation delays in radar interferograms. *Geochemistry, Geophysics, Geosystems*, *11*(9).
- Lin, Y. N. N., Kositsky, A. P., & Avouac, J. P. (2010b). PCAIM joint inversion of InSAR and ground-based geodetic time series: Application to monitoring magmatic inflation beneath the Long Valley Caldera. *Geophysical Research Letters*, *37*(23).
- Lu, Z., Fatland, R., Wyss, M., Li, S., Eichelberger, J., Dean, K., & Freymueller, J. (1997). Deformation of New Trident Volcano measured by ERS-1 SAR interferometry, Katmai National Park, Alaska. *Geophysical Research Letters*, *24*(6), 695-698.
- Lu, Z., Masterlark, T., & Dzurisin, D. (2005). Interferometric synthetic aperture radar study of Okmok volcano, Alaska, 1992–2003: Magma supply dynamics and postemplacement lava flow deformation. *Journal of Geophysical Research: Solid Earth*, *110*(B2).
- Lu, Z., & Dzurisin, D. (2014). InSAR Imaging of Aleutian Volcanoes: Monitoring a Volcanic Arc From Space. *Springer Praxis Books, Geophys. Sci.*, 388 pp., Springer, New York.
- Lundgren, P., & Rosen, P. A. (2003). Source model for the 2001 flank eruption of Mt. Etna volcano. *Geophysical research letters*, *30*(7).
- Lundgren, P., Berardino, P., Coltelli, M., Fornaro, G., Lanari, R., Puglisi, G., Sansosti, M., & Tesauro, M. (2003). Coupled magma chamber inflation and sector collapse slip observed with synthetic aperture radar interferometry on Mt. Etna volcano. *Journal of Geophysical Research: Solid Earth*, *108*(B5).
- Lundgren, P., Poland, M., Miklius, A., Orr, T., Yun, S. H., Fielding, E., Liu, Z., Tanaka, A., Szeliga, W., & Hensley, S. (2013). Evolution of dike opening during the March 2011 Kamoamoā fissure eruption, Kīlauea Volcano, Hawai'i. *Journal of Geophysical Research: Solid Earth*, *118*(3), 897-914.
- Machado, A., Azevedo, J.M., Almeida, D. M., Chemale, JR. F. (2008). Geochemistry of Volcanic Rocks from Faial Island (Azores), *Rev. Elect. Ciências da Terra*, *5*, 1, ISSN 1645-0388.

REFERENCES

- Malengreau, B., Lénat, J. F., & Froger, J. L. (1999). Structure of Réunion Island (Indian Ocean) inferred from the interpretation of gravity anomalies. *Journal of Volcanology and Geothermal Research*, 88(3), 131-146.
- Mardia, K. V., & P. E. Jupp (2000). *Directional Statistics*, 429 pp., New York, Wiley.
- Massonnet, D., & Rebaute, T. (1985). Etude de principe d'une détection de mouvements tectoniques par radar. *Int. Memo*, 326.
- Massonnet, D., Rossi, M., Carmona, C., Adragna, F., Peltzer, G., Feigl, K., & Rabaute, T. (1993). The displacement field of the Landers earthquake mapped by radar interferometry. *Nature*, 364(6433), 138-142.
- Massonnet, D., & Rabaute, T. (1993). Radar interferometry: limits and potential. *Geoscience and Remote Sensing, IEEE Transactions on*, 31(2), 455-464.
- Massonnet, D., Feigl, K., Rossi, M., & Adragna, F. (1994). Radar interferometric mapping of deformation in the year after the Landers earthquake. *Nature*, 369(6477), 227-230.
- Massonnet, D., & Feigl, K. L. (1995). Discrimination of geophysical phenomena in satellite radar interferograms. *Geophysical research letters*, 22(12), 1537-1540.
- Massonnet, D., Briole, P., & Arnaud, A. (1995). Deflation of Mount Etna monitored by spaceborne radar interferometry. *Nature*, 375(6532), 567-570.
- Massonnet, D., & Feigl, K. L. (1998). Radar interferometry and its application to changes in the Earth's surface. *Reviews of geophysics*, 36(4), 441-500.
- Massonnet, D., & Sigmundsson, F. (2000). Remote sensing of volcano deformation by radar interferometry from various satellites. *Remote sensing of active volcanism*, Geophys. Monogr., edited by P. Mouginiis-Mark, J. A. Crisp, and J. H. Fink, pp. 207–221, AGU, Washington, D. C.
- Matsushima, T., & Takagi, A. (2000). GPS and EDM monitoring of Unzen volcano ground deformation. *Earth, planets and space*, 52(11), 1015-1018.
- McGuire, W. J. (1996). Volcano instability: a review of contemporary themes. *Geological Society, London, Special Publications*, 110(1), 1-23.
- Merle, O., & Lénat, J. F. (2003). Hybrid collapse mechanism at Piton de la Fournaise volcano, Reunion Island, Indian Ocean. *Journal of Geophysical Research: Solid Earth*, 108(B3).
- Mesinger, F. et al. (2006). North American regional reanalysis. *Bulletin of the American Meteorological Society*, 87(3), 343-360.

REFERENCES

- Michon, L., Saint-Ange, F., Bachelery, P., Villeneuve, N., & Staudacher, T. (2007a). Role of the structural inheritance of the oceanic lithosphere in the magmato-tectonic evolution of Piton de la Fournaise volcano (La Réunion Island). *Journal of Geophysical Research: Solid Earth*, 112(B4).
- Michon, L., Staudacher, T., Ferrazzini, V., Bachèlery, P., & Marti, J. (2007b). April 2007 collapse of Piton de la Fournaise: a new example of caldera formation. *Geophysical Research Letters*, 34(21).
- Michon, L., & Saint-Ange, F. (2008). Morphology of Piton de la Fournaise basaltic shield volcano (La Réunion Island): Characterization and implication in the volcano evolution. *Journal of Geophysical Research: Solid Earth*, 113(B3).
- Michon, L., Villeneuve, N., Catry, T., & Merle, O. (2009). How summit calderas collapse on basaltic volcanoes: New insights from the April 2007 caldera collapse of Piton de la Fournaise volcano. *Journal of Volcanology and Geothermal Research*, 184(1), 138-151.
- Michon, L., Massin, F., Famin, V., Ferrazzini, V., & Roult, G. (2011). Basaltic calderas: Collapse dynamics, edifice deformation, and variations of magma withdrawal. *Journal of Geophysical Research: Solid Earth*, 116(B3).
- Mogi, K. (1958), Relations between the eruptions of various volcanoes and the deformation of the ground surface around them. *Bulletin Earthquake Research Institute of Tokyo*, 36, 99-134.
- Mora-Stock, C., Thorwart, M., Wunderlich, T., Bredemeyer, S., Hansteen, T. H., & Rabbel, W. (2014). Comparison of seismic activity for Llaima and Villarrica volcanoes prior to and after the Maule 2010 earthquake. *International Journal of Earth Sciences*, 103(7), 2015-2028.
- Moreno, H., Naranjo, J. A., Pena, P., Munoz, J., Basualto, D., Delgado, D., Gallegos, C., Dungan, C., & Bouvet de Maisonneuve, C. (2009). El ciclo eruptivo 2007–2009 del volcan Llaima, Andes del sur, paper presented at XII Congreso geologico Chileno, Santiago, 22–26.
- Morgan, W. J. (1981). 13. Hotspot tracks and the opening of the Atlantic and Indian Oceans. *The Sea, ideas and observations on progress in the study of the seas*, 7, 443-487.
- Naranjo, J. A., & Moreno, H. (1991). Actividad explosiva postglacial en el Volcán Llaima, Andes del Sur (38°45'S). *Revista Geologica de Chile*, 18(1), 69-80.
- Naranjo, J. A., & Moreno, H. (2005). Geología del volcán Llaima, Región de la Araucanía. Servicio Nacional de Geología y Minería, Carta Geológica de Chile, Serie Geología Básica, No. 88, 33p., 1 mapa escala 1:50.000, Santiago, Chile.

REFERENCES

- Neri, M., Casu, F., Acocella, V., Solaro, G., Pepe, S., Berardino, P., Sansosti, E., Caltabiano, T., Lundgren, P., & Lanari, R. (2009). Deformation and eruptions at Mt. Etna (Italy): a lesson from 15 years of observations. *Geophysical Research Letters*, *36*(2).
- Oehler, J. F., Labazuy, P., & L  nat, J. F. (2004). Recurrence of major flank landslides during the last 2-Ma history of Reunion Island. *Bulletin of Volcanology*, *66*(7), 585-598.
- Oehler, J. F., L  nat, J. F., & Labazuy, P. (2008). Growth and collapse of the Reunion Island volcanoes. *Bulletin of Volcanology*, *70*(6), 717-742.
- Onn, F., & Zebker, H. A. (2006). Correction for interferometric synthetic aperture radar atmospheric phase artifacts using time series of zenith wet delay observations from a GPS network. *Journal of Geophysical Research: Solid Earth*, *111*(B9).
- Osmanođlu, B., Dixon, T. H., Wdowinski, S., Cabral-Cano, E., & Jiang, Y. (2011). Mexico City subsidence observed with persistent scatterer InSAR. *International Journal of Applied Earth Observation and Geoinformation*, *13*(1), 1-12.
- Palano, M., Puglisi, G., & Gresta, S. (2008). Ground deformation patterns at Mt. Etna from 1993 to 2000 from joint use of InSAR and GPS techniques. *Journal of Volcanology and Geothermal Research*, *169*(3), 99-120.
- Palano, M., Gresta, S., & Puglisi, G. (2009). Time-dependent deformation of the eastern flank of Mt. Etna: After-slip or viscoelastic relaxation? *Tectonophysics*, *473*(3), 300-311.
- Pavez, A., Remy, D., Bonvalot, S., Diament, M., Gabalda, G., Froger, J. L., Julien, P., Legrand, D., & Moisset, D. (2006). Insight into ground deformation at Iascar volcano (Chile) from SAR interferometry, photogrammetry and GPS data: Implication on volcano dynamics and future space monitoring. *Remote Sensing of Environment*, *100*, 307-320.
- Peltier, A., Staudacher, T., & Bach  lery, P. (2007). Constraints on magma transfers and structures involved in the 2003 activity at Piton de La Fournaise from displacement data. *Journal of Geophysical Research: Solid Earth*, *112*(B3).
- Peltier, A., Famin, V., Bach  lery, P., Cayol, V., Fukushima, Y., & Staudacher, T. (2008). Cyclic magma storages and transfers at Piton de La Fournaise volcano (La R  union hotspot) inferred from deformation and geochemical data. *Earth and Planetary Science Letters*, *270*(3), 180-188.
- Peltier, A., Bach  lery, P., & Staudacher, T. (2009a). Magma transport and storage at Piton de La Fournaise (La R  union) between 1972 and 2007: A review of geophysical and geochemical data. *Journal of Volcanology and Geothermal Research*, *184*(1), 93-108.

REFERENCES

- Peltier, A., Staudacher, T., Bachèlery, P., & Cayol, V. (2009b). Formation of the April 2007 caldera collapse at Piton de La Fournaise volcano: Insights from GPS data. *Journal of Volcanology and Geothermal Research*, 184(1), 152-163.
- Peltier, A., Bianchi, M., Kaminski, E., Komorowski, J. C., Rucci, A., & Staudacher, T. (2010a). PSInSAR as a new tool to monitor pre-eruptive volcano ground deformation: Validation using GPS measurements on Piton de la Fournaise. *Geophysical Research Letters*, 37(12).
- Peltier, A., Staudacher, T., & Bachèlery, P. (2010b). New behaviour of the Piton de La Fournaise volcano feeding system (La Réunion Island) deduced from GPS data: Influence of the 2007 Dolomieu caldera collapse. *Journal of Volcanology and Geothermal Research*, 192(1), 48-56.
- Peltier, A., Massin, F., Bachèlery, P., & Finizola, A. (2012). Internal structure and building of basaltic shield volcanoes: the example of the Piton de La Fournaise terminal cone (La Réunion). *Bulletin of volcanology*, 74(8), 1881-1897.
- Peltier, A., Got, J. L., Villeneuve, N., Boissier, P., Staudacher, T., Ferrazzini, V., & Walpersdorf, A. (2015a). Long-term mass transfer at Piton de la Fournaise volcano evidenced by strain distribution derived from GNSS network. *Journal of Geophysical Research: Solid Earth*, 120(3), 1874-1889.
- Peltier, A., Poland, M., & Staudacher, T. (2015b). Are Piton de la Fournaise (La Réunion) and Kīlauea (Hawai 'i) really "analog volcanoes". *Hawaiian volcanoes: from source to surface. Geophysical monograph series*, 208, 507-531.
- Peltier, A., Beauducel, F., Villeneuve, N., Ferrazzini, V., Di Muro, A., Aiuppa, A., Derrien, A., Jourde, K., & Taisne, B. (2016a). Deep fluid transfer evidenced by surface deformation during the 2014–2015 unrest at Piton de la Fournaise volcano. *Journal of Volcanology and Geothermal Research*, 321, 140-148.
- Peltier, A., Froger, J.L., Villeneuve, N., & Catry, T. (2016b). Assessing the reliability and consistency of InSAR and GNSS data for rapid volcano deformation, the example of the 2015 Piton de la Fournaise eruptions. *Journal of Volcanological and Geothermal Research*. Submitted.
- Pepe, A., & Lanari, R. (2006). On the extension of the minimum cost flow algorithm for phase unwrapping of multitemporal differential SAR interferograms. *IEEE transactions on geoscience and remote sensing*, 44(9), 2374-2383.
- Perfettini, H., Avouac, J. P., Tavera, H., Kositsky, A., Nocquet, J. M., Bondoux, F., Chlieh, M., Sladen, A., Audin, L., Farber, D. L., & Soler, P. (2010). Seismic and aseismic slip on the Central Peru megathrust. *Nature*, 465(7294), 78-81.

REFERENCES

- Pinel, V., Hooper, A., De la Cruz-Reyna, S., Reyes-Davila, G., Doin, M. P., & Bascou, P. (2011). The challenging retrieval of the displacement field from InSAR data for andesitic stratovolcanoes: Case study of Popocatepetl and Colima Volcano, Mexico. *Journal of Volcanology and Geothermal Research*, 200(1), 49-61.
- Pinel, V., Poland, M. P., & Hooper, A. (2014). Volcanology: Lessons learned from synthetic aperture radar imagery. *Journal of Volcanology and Geothermal Research*, 289, 81-113.
- Plattner, C., Amelung, F., Baker, S., Govers, R., & Poland, M. (2013). The role of viscous magma mush spreading in volcanic flank motion at Kīlauea Volcano, Hawai'i. *Journal of Geophysical Research: Solid Earth*, 118(5), 2474-2487.
- Prati, C., & Rocca, F. (1990). Limits to the resolution of elevation maps from stereo SAR images. *International Journal of Remote Sensing*, 11(12), 2215-2235.
- Prati, C., Ferretti, A., & Perissin, D. (2010). Recent advances on surface ground deformation measurement by means of repeated space-borne SAR observations. *Journal of Geodynamics*, 49(3), 161-170.
- Pritchard, M. E., & Simons, M. (2002). A satellite geodetic survey of large-scale deformation of volcanic centres in the central Andes. *Nature*, 418(6894), 167-171.
- Pritchard, M. E., & Simons, M. (2004). An InSAR-based survey of volcanic deformation in the central Andes. *Geochemistry, Geophysics, Geosystems*, 5(2), Q02002.
- Pritt, M. D. (1996). Phase unwrapping by means of multigrid techniques for interferometric SAR. *Geoscience and Remote Sensing, IEEE Transactions on*, 34(3), 728-738.
- Puyssegur, B., Michel, R., & Avouac, J. P. (2007). Tropospheric phase delay in interferometric synthetic aperture radar estimated from meteorological model and multispectral imagery. *Journal of Geophysical Research: Solid Earth*, 112(B5).
- Rançon, J.P., Lerebour, P., & Augé, T. (1989). The Grand Brule exploration drilling: New data on the deep framework of the Piton de la Fournaise volcano. Part 1: Lithostratigraphic units and volcano structural implications. *Journal of Volcanology and Geothermal Research*, 36, (1), 113-127.
- Raucoules, D., & De Michele, M. (2010). Assessing ionospheric influence on L-band SAR data: implications on coseismic displacement measurements of the 2008 Sichuan earthquake. *IEEE Geoscience and Remote Sensing Letters*, 7(2), 286-290.
- Raynolds M., Magnússon B., Metúsalemsson S. and Magnússon S.H., (2015), Warming, Sheep and Volcanoes: Land Cover Changes in Iceland Evident in Satellite NDVI Trends , *Remote Sens.*, 7, 9492-9506; doi:10.3390/rs70809492.

REFERENCES

- Remy, D., Bonvalot, S., Briole, P., & Murakami, M. (2003). Accurate measurements of tropospheric effects in volcanic areas from SAR interferometry data: Application to Sakurajima volcano (Japan). *Earth and Planetary Science Letters*, 213(3), 299-310.
- Remy, D., Falvey, M., Bonvalot, S., Chlieh, M., Gabalda, G., Froger, J. L., & Legrand, D. (2011). Variability of atmospheric precipitable water in northern Chile: Impacts on interpretation of InSAR data for earthquake modeling. *Journal of South American Earth Sciences*, 31(2), 214-226.
- Remy, D., Froger, J. L., Perfettini, H., Bonvalot, S., Gabalda, G., Albino, F., Cayol, V., Legrand, D., & Saint Blanquat, M. D. (2014). Persistent uplift of the Lazufre volcanic complex (Central Andes): New insights from PCAIM inversion of InSAR time series and GPS data. *Geochemistry, Geophysics, Geosystems*, 15(9), 3591-3611.
- Remy, D., Chen, Y., Froger, J. L., Bonvalot, S., Cordoba, L., & Fustos, J. (2015). Revised interpretation of recent InSAR signals observed at Llama volcano (Chile). *Geophysical Research Letters*, 42(10), 3870-3879.
- Rienecker, M. M., et al. (2011). MERRA: NASA's modern-era retrospective analysis for research and applications. *Journal of Climate*, 24(14), 3624-3648.
- Rivet, D., Brenguier, F., Clarke, D., Shapiro, N. M., & Peltier, A. (2014). Long-term dynamics of Piton de la Fournaise volcano from 13 years of seismic velocity change measurements and GPS observations. *Journal of Geophysical Research: Solid Earth*, 119(10), 7654-7666.
- Roman, D. C., & Cashman, K. V. (2006). The origin of volcano-tectonic earthquake swarms. *Geology*, 34(6), 457-460.
- Rosen, P. A., Hensley, S., Zebker, H. A., Webb, F. H., & Fielding, E. J. (1996). Surface deformation and coherence measurements of Kilauea Volcano, Hawaii, from SIR-C radar interferometry. *Journal of Geophysical Research: Planets*, 101(E10), 23109-23125.
- Rosen, P. A., Hensley, S., Joughin, I. R., Li, F. K., Madsen, S. N., Rodriguez, E., & Goldstein, R. M. (2000). Synthetic aperture radar interferometry. *Proceedings of the IEEE*, 88(3), 333-382.
- Roult, G., Peltier, A., Taisne, B., Staudacher, T., Ferrazzini, V., & Di Muro, A. (2012). A new comprehensive classification of the Piton de la Fournaise activity spanning the 1985–2010 period. Search and analysis of short-term precursors from a broad-band seismological station. *Journal of Volcanology and Geothermal Research*, 241, 78-104.
- Rufino, G., Moccia, A., & Esposito, S. (1998). DEM generation by means of ERS tandem data. *Geoscience and Remote Sensing, IEEE Transactions on*, 36(6), 1905-1912.

REFERENCES

- Salfity, M. F., Ruiz, P. D., Huntley, J. M., Graves, M. J., Cusack, R., & Beauregard, D. A. (2006). Branch cut surface placement for unwrapping of undersampled three-dimensional phase data: application to magnetic resonance imaging arterial flow mapping. *Applied optics*, 45(12), 2711-2722.
- Sandwell, D. T., Myer, D., Mellors, R., Shimada, M., Brooks, B., & Foster, J. (2008). Accuracy and resolution of ALOS interferometry: Vector deformation maps of the Father's Day intrusion at Kilauea. *IEEE Transactions on Geoscience and Remote Sensing*, 46(11), 3524-3534.
- Sansosti, E., Casu, F., Manzo, M., & Lanari, R. (2010). Space-borne radar interferometry techniques for the generation of deformation time series: An advanced tool for Earth's surface displacement analysis. *Geophysical Research Letters*, 37(20).
- Schaefer, L. N., Lu, Z., & Oommen, T. (2015). Dramatic volcanic instability revealed by InSAR. *Geology*, 43(8), 743-746.
- Shirzaei, M., Bürgmann, R., Foster, J., Walter, T. R., & Brooks, B. A. (2013). Aseismic deformation across the Hilina fault system, Hawaii, revealed by wavelet analysis of InSAR and GPS time series. *Earth and Planetary Science Letters*, 376, 12-19.
- Sigmundsson, F., Durand, P., & Massonnet, D. (1999). Opening of an eruptive fissure and seaward displacement at Piton de la Fournaise volcano measured by RADARSAT satellite radar interferometry. *Geophysical Research Letters*, 26(5), 533-536.
- Simons, M., Fialko, Y., & Rivera, L. (2002). Coseismic deformation from the 1999 Mw 7.1 Hector Mine, California, earthquake as inferred from InSAR and GPS observations. *Bulletin of the Seismological Society of America*, 92(4), 1390-1402.
- Skone, S., & Cannon, M. E. (1999). Ionospheric effects on differential GPS applications during auroral substorm activity. *ISPRS journal of photogrammetry and remote sensing*, 54(4), 279-288.
- Smith Jr, E. K., & Weintraub, S. (1953). The constants in the equation for atmospheric refractive index at radio frequencies. *Proceedings of the IRE*, 41(8), 1035-1037.
- Solaro, G., Acocella, V., Pepe, S., Ruch, J., Neri, M., & Sansosti, E. (2010). Anatomy of an unstable volcano from InSAR: Multiple processes affecting flank instability at Mt. Etna, 1994–2008. *Journal of Geophysical Research: Solid Earth*, 115(B10).
- Solheim, F. S., Vivekanandan, J., Ware, R. H., & Rocken, C. (1999). Propagation delays induced in GPS signals by dry air, water vapor, hydrometeors, and other particulates. *Journal of geophysical research*, 104(D8), 9663-9670.
- Sparks, R. S. J. (2003). Forecasting volcanic eruptions. *Earth and Planetary Science Letters*, 210, 1-15.

REFERENCES

- Staudacher, T., Sarda, P., & Allègre, C. J. (1990). Noble gas systematics of Réunion Island, Indian Ocean. *Chemical geology*, 89(1), 1-17.
- Staudacher, T., & Allègre, C. J. (1993). Ages of the second caldera of Piton de la Fournaise volcano (Réunion) determined by cosmic ray produced ^3He and ^{21}Ne . *Earth and Planetary Science Letters*, 119(3), 395-404.
- Staudacher, T., Ferrazzini, V., Peltier, A., Kowalski, P., Boissier, P., Catherine, P., Lauret, F., & Massin, F. (2009). The April 2007 eruption and the Dolomieu crater collapse, two major events at Piton de la Fournaise (La Réunion Island, Indian Ocean). *Journal of Volcanology and Geothermal Research*, 184(1), 126-137.
- Staudacher, T., & Peltier, A. (2015). Ground deformation at Piton de la Fournaise (La Réunion Island), a review from 20 years of GNSS monitoring. In: *Bachèlery P, Lénat, JF, Di Muro A, Michon L (ed) Active Volcanoes of the Southwest Indian Ocean: Piton de la Fournaise and Karthala. Active Volcanoes of the World*. Springer, Berlin, 139-170. Doi: 10.1007/978-3-642-31395-0_9.
- Staudacher, T., Peltier, A., Ferrazzini, V., Di Muro, A., Boissier, P., Catherine, P., Kowalski, P., & Lauret, F. (2015). Fifteen years of intense eruptive activity (1998–2013) at Piton de La Fournaise volcano: a review. In: *Bachèlery P, Lénat, JF, Di Muro A, Michon L (ed) Active Volcanoes of the Southwest Indian Ocean: Piton de la Fournaise and Karthala*. Springer Berlin and Heidelberg.
- Stevens, N. F., Wadge, G., & Murray, J. B. (1999). Lava flow volume and morphology from digitised contour maps: a case study at Mount Etna, Sicily. *Geomorphology*, 28(3), 251-261.
- Stevens, N. F., Wadge, G., Williams, C. A., Morley, J. G., Muller, J. P., Murray, J. B., & Upton, M. (2001a). Surface movements of emplaced lava flows measured by synthetic aperture radar interferometry. *Journal of Geophysical Research: Solid Earth*, 106(B6), 11293-11313.
- Stevens, N. F., Wadge, G., & Williams, C. A. (2001b). Post-emplacment lava subsidence and the accuracy of ERS InSAR digital elevation models of volcanoes. *International Journal of Remote Sensing*, 22(5), 819-828.
- Stramondo, S., Trasatti, E., Albano, M., Moro, M., Chini, M., Bignami, C., Polcari, M., & Saroli, M. (2016). Uncovering deformation processes from surface displacements. *Journal of Geodynamics (In Press)*.
- Sun, Q., Zhang, L., Ding, X. L., Hu, J., Li, Z. W., & Zhu, J. J. (2015). Slope deformation prior to Zhouqu, China landslide from InSAR time series analysis. *Remote Sensing of Environment*, 156, 45-57.
- Swanson, D. A., Duffield, W. A., & Fiske, R. S. (1976). Displacement of the south flank of Kilauea Volcano; the result of forceful intrusion of magma into the rift zones. *U.S. Geol. Surv. Prof. Pap.* 963, 39.

REFERENCES

- Symonds, R. B., Rose, W. I., Bluth, G. J., & Gerlach, T. M. (1994). Volcanic-gas studies; methods, results, and applications. *Reviews in Mineralogy and Geochemistry*, 30(1), 1-66.
- Taylor, M., & Peltzer, G. (2006). Current slip rates on conjugate strike-slip faults in central Tibet using synthetic aperture radar interferometry. *Journal of Geophysical Research: Solid Earth*, 111(B12).
- Thayer, G. D. (1974). An improved equation for the radio refractive index of air. *Radio Science*, 9(10), 803-807.
- Tinard, P. (2007). *Caractérisation et modélisation des déplacements du sol associés à l'activité volcanique du Piton de la Fournaise, île de La Réunion, à partir de données interférométriques. Août 2003–Avril 2007* (Doctoral dissertation, Université Blaise Pascal-Clermont-Ferrand II).
- Usai, S. (2003). A least squares database approach for SAR interferometric data. *IEEE Transactions on Geoscience and Remote Sensing*, 41(4), 753-760.
- Vadon, H., & Sigmundsson, F. (1997). Crustal deformation from 1992 to 1995 at the Mid-Atlantic Ridge, southwest Iceland mapped by satellite radar interferometry. *Science*, 275, 193-197.
- Villeneuve, N., & Bachèlery, P. (2006). Revue de la typologie des éruptions au Piton de La Fournaise, processus et risques volcaniques associés. *Cybergeo: European Journal of Geography. Environnement, Nature, Paysage* 336, URL: <http://cybergeo.revues.org/index2536.html>.
- Wadge, G., et al. (2002). Atmospheric models, GPS and InSAR measurements of the tropospheric water vapour field over Mount Etna. *Geophysical Research Letters*, 29.
- Wadge, G., Mattioli, G. S., & Herd, R. A. (2006). Ground deformation at Soufriere Hills Volcano, Montserrat during 1998-2000 measured by radar interferometry and GPS. *Journal of Volcanology and Geothermal Research*, 152(1), 157-173.
- Walters, R. J., Elliott, J. R., Li, Z., & Parsons, B. (2013). Rapid strain accumulation on the Ashkabad fault (Turkmenistan) from atmosphere-corrected InSAR. *Journal of Geophysical Research: Solid Earth*, 118(7), 3674-3690.
- Webley, P. W., Bingley, R. M., Dodson, A. H., Wadge, G., Waugh, S. J., & James, I. N. (2002). Atmospheric water vapour correction to InSAR surface motion measurements on mountains: results from a dense GPS network on Mount Etna. *Physics and Chemistry of the Earth, Parts A/B/C*, 27(4), 363-370.
- Wessel, P., & Smith, W. H. (1991). Free software helps map and display data. *Eos, Transactions American Geophysical Union*, 72(41), 441-446.

REFERENCES

- Williams, S., Bock, Y., & Fang, P. (1998). Integrated satellite interferometry: Tropospheric noise, GPS estimates and implications for interferometric synthetic aperture radar products. *Journal of geophysical research*, 103(B11), 27051-27067.
- Wright, T. J., Parsons, B. E., & Lu, Z. (2004). Toward mapping surface deformation in three dimensions using InSAR. *Geophysical Research Letters*, 31(1), L01607.
- Zebker, H. A., & Goldstein, R. M. (1986). Topographic mapping from interferometric synthetic aperture radar observations. *Journal of Geophysical Research: Solid Earth*, 91(B5), 4993-4999.
- Zebker, H. A., Rosen, P. A., & Hensley, S. (1997). Atmospheric effects in interferometric synthetic aperture radar surface deformation and topographic maps. *Journal of Geophysical Research: Solid Earth*, 102(B4), 7547-7563.

REFERENCES

APPENDIX

Appendix 1. Summary of SAR acquisitions of TSX/TDX and CSK data.

* indicates the SAR acquisitions that acquired by TDX.

Satellite - Pass	TSX/TDX - A		TSX/TDX - D		CSK - A		CSK - D	
	Orbit number	Date	Orbit number	Date	Orbit number	Date	Orbit number	Date
1	9587	20090307	8304	20081213	19967	20110215	19974	20110215
2	10088	20090409	8471	20081224	20204	20110303	20211	20110303
3	10589	20090512	8805	20090115	20441	20110319	20448	20110319
4	12593	20090921	9306	20090217	20678	20110404	20685	20110404
5	12927	20091013	9807	20090322	20915	20110420	20922	20110420
6	13094	20091024	10308	20090424	21152	20110506	21159	20110506
7	13595	20091126	10809	20090527	21389	20110522	21396	20110522
8	14096	20091229	11310	20090629	21626	20110607	21633	20110607
9	14597	20100131	11811	20090801	21863	20110623	21870	20110623
10	15098	20100305	12312	20090903	22100	20110709	22107	20110709
11	15599	20100407	12813	20091006	22337	20110725	22344	20110725
12	16100	20100510	12980	20091017	22574	20110810	22581	20110810
13	16601	20100612	13147	20091028	22811	20110826	22818	20110826
14	17102	20100715	13314	20091108	23048	20110911	23055	20110911
15	17603	20100817	13815	20091211	23285	20110927	23292	20110927
16	18104	20100919	14316	20100113	23522	20111013	23528	20111013
17	18605	20101022	14817	20100215	23759	20111029	23766	20111029
18	7219*	20111009	15318	20100320	23996	20111114	24003	20111114
19	7553*	20111031	15819	20100422	24233	20111130	24240	20111130
20	7887*	20111122	16320	20100525	24707	20120101	24714	20120101
21	8889*	20120127	16821	20100627	24944	20120117	24951	20120117
22	9223*	20120218	17322	20100730	25181	20120202	25188	20120202
23	9557*	20120311	17823	20100901	25418	20120218	25425	20120218
24	10559*	20120516	18658	20101026	29684	20130604	29691	20130604
25	10893*	20120607	2095*	20101106	14235	20130624	14242	20130624
26	11227*	20120629	7439*	20111024	33002	20130714	33009	20130714
27	11561*	20120721	26173	20120304	30632	20130807	30639	20130807
28	12229*	20120903	10111*	20120417	33713	20130831	33720	20130831
29	12563*	20120925	27843	20120622	31343	20130924	31350	20130924
30	13231*	20121108	35525	20131110	34424	20131018	34431	20131018

APPENDIX

31	13565*	20121130	36527	20140115	32054	20131111	32061	20131111
32	13899*	20121222	36861	20140206	35135	20131205	35142	20131205
33	14233*	20130113	37195	20140228	32765	20131229	32772	20131229
34	14734*	20130215	40535	20141006	35846	20140122	35853	20140122
35	15402*	20130331			33476	20140215	33483	20140215
36	15736*	20130422			36557	20140311	36564	20140311
37	16070*	20130514			34187	20140404	34194	20140404
38	16404*	20130605			37268	20140428	37275	20140428
39	17072*	20130719			37979	20140615	37986	20140615
40	17406*	20130810			35609	20140709	35616	20140709
41	34470	20130901			38690	20140802	38697	20140802
42	34804	20130923			36320	20140826	36327	20140826
43	19076*	20131128			39401	20140919	39408	20140919
44	19410*	20131220						
45	19744*	20140111						
46	20078*	20140202						
47	20412*	20140224						
48	20746*	20140318						
49	21414*	20140501						
50	22082*	20140614						
51	22416*	20140706						
52	23084*	20140819						
53	23418*	20140910						
54	23752*	20141002						
55	24086*	20141024						
56	41150	20141115						

Appendix 2. TSX/TDX ascending interferograms

Interferogram number	Master	Slave	B_t (day)	B_{\perp} (m)	Altitude of ambiguity (m)
1	20090307	20090409	33	-25.9	201.5
2	20090307	20090512	66	65	-74.6
3	20090307	20090921	198	26	-198.1
4	20090307	20091013	220	68.6	-74.6
5	20090307	20091229	297	-155.1	33.1
6	20090409	20090512	33	90.9	-54.7
7	20090409	20090921	165	51.9	-98.9
8	20090409	20091013	187	94.5	-54.3
9	20090409	20091126	231	27.8	-182.5
10	20090409	20091229	264	-129.2	39.5
11	20090512	20090921	132	-39	117.1
12	20090512	20091013	154	3.6	-439.8
13	20090512	20091024	165	109.6	-49
14	20090512	20091126	198	-63.1	77.3
15	20090921	20091013	22	42.6	-118.4
16	20090921	20091024	33	148.6	-34.9
17	20090921	20091126	66	-24.1	216.1
18	20090921	20091229	99	-181.1	28.4
19	20090921	20100131	132	162.9	-32.2
20	20090921	20100407	198	193.9	-26.7
21	20090921	20100510	231	-120	42.8
22	20090921	20100612	264	-76.1	68
23	20091013	20091024	11	106	-49.2
24	20091013	20091126	44	-66.7	77.1
25	20091013	20091229	77	-223.7	22.9
26	20091013	20100131	110	120.3	-44
27	20091013	20100305	143	186	-27.8
28	20091013	20100407	176	151.3	-34.3
29	20091013	20100510	209	-162.6	31.5
30	20091013	20100612	242	-118.7	43.4
31	20091013	20100715	275	88.7	-60.9
32	20091013	20100817	308	-21	247.2
33	20091024	20091126	33	-172.7	30.1
34	20091024	20100131	99	14.3	-345.3
35	20091024	20100305	132	80	-63.5
36	20091024	20100407	165	45.3	-113.6
37	20091024	20100715	264	-17.3	245.1
38	20091126	20091229	33	-157	32.6
39	20091126	20100131	66	187	-28.1
40	20091126	20100305	99	252.7	-20.4

APPENDIX

41	20091126	20100407	132	218	-23.8
42	20091126	20100510	165	-95.9	53.4
43	20091126	20100612	198	-52	99.2
44	20091126	20100715	231	155.4	-34.2
45	20091126	20100817	264	45.7	-112.3
46	20091126	20100919	297	24.1	-204
47	20091229	20100510	132	61.1	-83.5
48	20091229	20100612	165	105	-48.4
49	20100131	20100305	33	65.7	-73
50	20100131	20100407	66	31	-148.9
51	20100131	20100612	132	-239	22
52	20100131	20100715	165	-31.6	156.3
53	20100131	20100817	198	-141.3	37.3
54	20100131	20101022	264	-14.5	340.3
55	20100305	20100407	33	-34.7	142.9
56	20100305	20100715	132	-97.3	50.5
57	20100305	20100817	165	-207	25
58	20100305	20101022	231	-80.2	61.1
59	20100407	20100510	33	-313.9	16.5
60	20100407	20100612	66	-270	19.2
61	20100407	20100715	99	-62.6	78
62	20100407	20100817	132	-172.3	30.1
63	20100407	20100919	165	-193.9	26.7
64	20100407	20101022	198	-45.5	107.1
65	20100407	20111031	572	-371.7	13.9
66	20100407	20111122	594	-262	19.8
67	20100510	20100612	33	43.9	-115.2
68	20100510	20100715	66	251.3	-20.9
69	20100510	20100817	99	141.6	-36.2
70	20100510	20100919	132	120	-42.6
71	20100510	20111031	539	-57.8	80.1
72	20100510	20111122	561	51.9	-92
73	20100612	20100715	33	207.4	-25.5
74	20100612	20100817	66	97.7	-52.2
75	20100612	20100919	99	76.1	-67.1
76	20100612	20101022	132	224.5	-23.4
77	20100612	20111009	484	221.6	-23.1
78	20100612	20111122	528	8	-200.2
79	20100612	20120127	594	224.2	-22.9
80	20100715	20100817	33	-109.7	49
81	20100715	20100919	66	-131.3	40.4
82	20100715	20101022	99	17.1	-283.1
83	20100715	20111009	451	14.2	-190.7
84	20100715	20111122	495	-199.4	26.4
85	20100715	20120127	561	16.8	-199.9
86	20100715	20120218	583	-30.7	165.9

APPENDIX

87	20100817	20100919	33	-21.6	231.7
88	20100817	20101022	66	126.8	-41.9
89	20100817	20111009	418	123.9	-41.2
90	20100817	20111031	440	-199.4	25.6
91	20100817	20111122	462	-89.7	57.5
92	20100817	20120127	528	126.5	-40.4
93	20100817	20120218	550	79	-65.1
94	20100817	20120311	572	90.8	-56.6
95	20100919	20101022	33	148.4	-35.5
96	20100919	20111009	385	145.5	-35.2
97	20100919	20111122	429	-68.1	75.9
98	20100919	20120127	495	148.1	-34.5
99	20100919	20120218	517	100.6	-50.9
100	20100919	20120311	539	112.4	-45.5
101	20101022	20111009	352	-2.9	-254.7
102	20101022	20111122	396	-216.5	24.2
103	20101022	20120127	462	-0.3	-348.5
104	20101022	20120218	484	-47.8	108.3
105	20101022	20120311	506	-36	141.6
106	20111009	20111031	22	-323.3	15.9
107	20111009	20111122	44	-213.6	24.1
108	20111009	20120127	110	2.6	-1406
109	20111009	20120218	132	-44.9	114
110	20111009	20120311	154	-33.1	153.9
111	20111009	20120721	286	-20.2	212
112	20111031	20111122	22	109.7	-46.4
113	20111031	20120311	132	290.2	-17.7
114	20111122	20120127	66	216.2	-23.8
115	20111122	20120218	88	168.7	-30.6
116	20111122	20120311	110	180.5	-28.6
117	20120127	20120218	22	-47.5	106.4
118	20120127	20120311	44	-35.7	142.1
119	20120127	20120629	154	204	-25.1
120	20120127	20120721	176	-22.8	171.6
121	20120127	20121108	286	-37.2	107.5
122	20120218	20120311	22	11.8	-414.4
123	20120218	20120629	132	251.5	-20.4
124	20120218	20120721	154	24.7	-172.3
125	20120218	20121108	264	10.3	-210.2
126	20120218	20121130	286	-14.6	327.8
127	20120311	20120629	110	239.7	-21.4
128	20120311	20120721	132	12.9	-228.9
129	20120311	20121108	242	-1.5	202.3
130	20120311	20121130	264	-26.4	184.2
131	20120516	20120607	22	49.1	-104.8
132	20120516	20120629	44	-78.5	65.3

APPENDIX

133	20120516	20120903	110	35.3	-144.5
134	20120516	20120925	132	-112.3	45.5
135	20120516	20121222	220	-103.5	49.3
136	20120607	20120629	22	-127.6	40.2
137	20120607	20120903	88	-13.8	367.8
138	20120607	20120925	110	-161.4	31.7
139	20120607	20121222	198	-152.6	33.5
140	20120607	20130331	297	18.9	-257.6
141	20120629	20120721	22	-226.8	22.5
142	20120629	20120903	66	113.8	-45
143	20120629	20120925	88	-33.8	149
144	20120629	20121108	132	-241.2	20.8
145	20120629	20121222	176	-25	201.2
146	20120629	20130422	297	-18.1	234.6
147	20120721	20120925	66	193	-26.4
148	20120721	20121108	110	-14.4	279.2
149	20120721	20121130	132	-39.3	134.4
150	20120721	20121222	154	201.8	-25.3
151	20120721	20130113	176	-137.7	37.6
152	20120721	20130215	209	10.9	-452.7
153	20120721	20130605	319	-1.5	-539
154	20120903	20120925	22	-147.6	34.5
155	20120903	20121222	110	-138.8	36.8
156	20120903	20130331	209	32.7	-154.7
157	20120903	20130422	231	-131.9	38.8
158	20120925	20121108	44	-207.4	24.2
159	20120925	20121130	66	-232.3	22.1
160	20120925	20121222	88	8.8	-561.8
161	20120925	20130215	143	-182.1	28
162	20120925	20130331	187	180.3	-28.3
163	20120925	20130422	209	15.7	-253.1
164	20120925	20130514	231	-118.6	43.4
165	20121108	20121130	22	-24.9	222.2
166	20121108	20121222	44	216.2	-23.3
167	20121108	20130113	66	-123.3	43.1
168	20121108	20130215	99	25.3	-177.3
169	20121108	20130422	165	223.1	-22.4
170	20121108	20130514	187	88.8	-54.5
171	20121108	20130605	209	12.9	-210.5
172	20121108	20130719	253	-112.9	47.3
173	20121108	20130810	275	70.8	-60.5
174	20121108	20130901	297	16.6	-146.3
175	20121130	20121222	22	241.1	-21.3
176	20121130	20130113	44	-98.4	52.1
177	20121130	20130215	77	50.2	-101
178	20121130	20130514	165	113.7	-45.1

APPENDIX

179	20121130	20130605	187	37.8	-136
180	20121130	20130719	231	-88	58.1
181	20121130	20130810	253	95.7	-54.1
182	20121130	20130901	275	41.5	-129
183	20121222	20130215	55	-190.9	26.7
184	20121222	20130331	99	171.5	-29.8
185	20121222	20130422	121	6.9	-305.3
186	20121222	20130514	143	-127.4	40.4
187	20121222	20130605	165	-203.3	25.3
188	20121222	20130810	231	-145.4	32.5
189	20130113	20130215	33	148.6	-34.7
190	20130113	20130514	121	212.1	-24.2
191	20130113	20130605	143	136.2	-37.7
192	20130113	20130719	187	10.4	-453.8
193	20130113	20130901	231	139.9	-37.4
194	20130113	20130923	253	-0.8	465.7
195	20130215	20130422	66	197.8	-25.7
196	20130215	20130514	88	63.5	-78.8
197	20130215	20130605	110	-12.4	293.7
198	20130215	20130719	154	-138.2	37.5
199	20130215	20130810	176	45.5	-87.9
200	20130215	20130901	198	-8.7	175.2
201	20130215	20130923	220	-149.4	34.2
202	20130215	20131128	286	59.5	-72
203	20130331	20130422	22	-164.6	31.1
204	20130331	20130514	44	-298.9	17.1
205	20130422	20130514	22	-134.3	38.2
206	20130422	20130605	44	-210.2	24.4
207	20130422	20130810	110	-152.3	31.9
208	20130422	20130901	132	-206.5	24.4
209	20130422	20131128	220	-138.3	34.3
210	20130422	20140224	308	5.5	-168.1
211	20130514	20130605	22	-75.9	67.6
212	20130514	20130719	66	-201.7	25.4
213	20130514	20130810	88	-18	113.9
214	20130514	20130901	110	-72.2	65.8
215	20130514	20130923	132	-212.9	24
216	20130514	20131128	198	-4	113.6
217	20130514	20140318	308	-42.3	71.3
218	20130605	20130719	44	-125.8	40.6
219	20130605	20130810	66	57.9	-87.6
220	20130605	20130901	88	3.7	537.5
221	20130605	20130923	110	-137	37.3
222	20130605	20131128	176	71.9	-71.1
223	20130605	20131220	198	-148.2	35.4
224	20130605	20140111	220	-79.6	90.1

APPENDIX

225	20130605	20140318	286	33.6	-125.2
226	20130719	20130810	22	183.7	-28.4
227	20130719	20130901	44	129.5	-40.2
228	20130719	20130923	66	-11.2	268.6
229	20130719	20131128	132	197.7	-26.5
230	20130719	20131220	154	-22.4	98.2
231	20130719	20140111	176	46.2	-55.7
232	20130719	20140202	198	-67.2	67
233	20130810	20130901	22	-54.2	94.2
234	20130810	20130923	44	-194.9	27
235	20130810	20131128	110	14	-374.8
236	20130810	20131220	132	-206.1	26.9
237	20130810	20140111	154	-137.5	53.7
238	20130810	20140224	198	157.8	-31.8
239	20130810	20140318	220	-24.3	153.3
240	20130810	20140501	264	-71.1	65.3
241	20130810	20140614	308	-25.9	110.3
242	20130901	20130923	22	-140.7	37.4
243	20130901	20131128	88	68.2	-77
244	20130901	20131220	110	-151.9	36.1
245	20130901	20140111	132	-83.3	103.6
246	20130901	20140202	154	-196.7	27.1
247	20130901	20140224	176	212	-24.1
248	20130901	20140318	198	29.9	-156.9
249	20130901	20140501	242	-16.9	161.7
250	20130901	20140614	286	28.3	-128.6
251	20130923	20131128	66	208.9	-25.4
252	20130923	20131220	88	-11.2	176.4
253	20130923	20140111	110	57.4	-53.1
254	20130923	20140202	132	-56	87.5
255	20130923	20140318	176	170.6	-32.6
256	20130923	20140501	220	123.8	-41.2
257	20131128	20131220	22	-220.1	25.3
258	20131128	20140111	44	-151.5	47.7
259	20131128	20140202	66	-264.9	20.4
260	20131128	20140224	88	143.8	-34.4
261	20131128	20140318	110	-38.3	114.1
262	20131128	20140501	154	-85.1	54.3
263	20131128	20140614	198	-39.9	89.2
264	20131128	20140706	220	151.5	-30.4
265	20131128	20140819	264	-43.7	93.7
266	20131128	20140910	286	8.4	-125.5
267	20131220	20140111	22	68.6	-53.9
268	20131220	20140202	44	-44.8	105.2
269	20131220	20140318	88	181.8	-32.5
270	20131220	20140501	132	135	-37.3

APPENDIX

271	20131220	20140614	176	180.2	-28.6
272	20131220	20141024	308	23	-182.6
273	20140111	20140202	22	-113.4	35.8
274	20140111	20140224	44	295.3	-20
275	20140111	20140318	66	113.2	-81.9
276	20140111	20140501	110	66.4	-83
277	20140111	20140614	154	111.6	-56.2
278	20140111	20140819	220	107.8	-61
279	20140111	20141024	286	-45.6	63.9
280	20140111	20141115	308	16.9	202.4
281	20140202	20140318	44	226.6	-24.9
282	20140202	20140501	88	179.8	-28.4
283	20140202	20140614	132	225	-22.8
284	20140202	20141024	264	67.8	-75.9
285	20140224	20140318	22	-182.1	26.5
286	20140224	20140501	66	-228.9	22.1
287	20140224	20140614	110	-183.7	27.8
288	20140224	20140706	132	7.7	-90.6
289	20140224	20140819	176	-187.5	27.1
290	20140224	20140910	198	-135.4	37.6
291	20140224	20141002	220	-29.9	119.2
292	20140318	20140501	44	-46.8	79.8
293	20140318	20140614	88	-1.6	-97.9
294	20140318	20140706	110	189.8	-24
295	20140318	20140819	154	-5.4	-105
296	20140318	20140910	176	46.7	-71.4
297	20140318	20141002	198	152.2	-30.2
298	20140318	20141024	220	-158.8	36.1
299	20140318	20141115	242	-96.3	65.4
300	20140501	20140614	44	45.2	-109
301	20140501	20140706	66	236.6	-21.6
302	20140501	20140819	110	41.4	-118.5
303	20140501	20140910	132	93.5	-54
304	20140501	20141002	154	199	-25.7
305	20140501	20141024	176	-112	45.2
306	20140501	20141115	198	-49.5	105.5
307	20140614	20140706	22	191.4	-26.9
308	20140614	20140819	66	-3.8	1002.6
309	20140614	20140910	88	48.3	-107.5
310	20140614	20141002	110	153.8	-33.6
311	20140614	20141024	132	-157.2	32.5
312	20140614	20141115	154	-94.7	56.9
313	20140706	20140819	44	-195.2	26.2
314	20140706	20140910	66	-143.1	35.4
315	20140706	20141002	88	-37.6	115.1
316	20140819	20140910	22	52.1	-98.6

APPENDIX

317	20140819	20141002	44	157.6	-32.7
318	20140819	20141024	66	-153.4	33.7
319	20140819	20141115	88	-90.9	60.2
320	20140910	20141002	22	105.5	-48.9
321	20140910	20141024	44	-205.5	25.3
322	20140910	20141115	66	-143	38
323	20141002	20141024	22	-311	16.7
324	20141002	20141115	44	-248.5	21.4
325	20141024	20141115	22	62.5	-75.5

Appendix 3. TSX/TDX descending interferograms

Interferogram number	Master	Slave	B_t (day)	B_{\perp} (m)	Altitude of ambiguity (m)
1	20081213	20081224	11	209.3	-29.2
2	20081213	20090115	33	-145.5	42
3	20081213	20090217	66	-134.9	45
4	20081213	20090322	99	-12.5	411.3
5	20081213	20090424	132	-202.2	30.2
6	20081213	20090527	165	-197.4	30.9
7	20081213	20090629	198	-74	84.2
8	20081213	20090801	231	-88.3	69.4
9	20081213	20090903	264	-93.4	65.4
10	20081213	20091006	297	-32.4	191.1
11	20081213	20091028	319	-5.1	395
12	20081224	20090115	22	-354.8	17.3
13	20081224	20090217	55	-344.2	17.8
14	20081224	20090322	88	-221.8	27.8
15	20090115	20090217	33	10.6	-368.5
16	20090115	20090322	66	133	-45.4
17	20090115	20090424	99	-56.7	104.6
18	20090115	20090527	132	-51.9	114.4
19	20090115	20090629	165	71.5	-83.2
20	20090115	20090801	198	57.2	-104.2
21	20090115	20090903	231	52.1	-116.1
22	20090115	20091006	264	113.1	-53.4
23	20090115	20091017	275	-10.8	558.3
24	20090115	20091108	297	64.7	-93
25	20090217	20090322	33	122.4	-49.5
26	20090217	20090424	66	-67.3	83.5
27	20090217	20090527	99	-62.5	89.7
28	20090217	20090629	132	60.9	-95.8
29	20090217	20090801	165	46.6	-128.2
30	20090217	20090903	198	41.5	-143
31	20090217	20091006	231	102.5	-58.9
32	20090217	20091017	242	-21.4	231.5
33	20090217	20091028	253	129.8	-46.6
34	20090217	20091108	264	54.1	-110
35	20090217	20091211	297	-56.4	103.5
36	20090322	20090424	33	-189.7	31.8
37	20090322	20090527	66	-184.9	32.6
38	20090322	20090629	99	-61.5	97.4
39	20090322	20090801	132	-75.8	80.2
40	20090322	20090903	165	-80.9	74.4

APPENDIX

41	20090322	20091006	198	-19.9	282.4
42	20090322	20091017	209	-143.8	42.1
43	20090322	20091028	220	7.4	-797.2
44	20090322	20091108	231	-68.3	88.5
45	20090322	20100113	297	-32.2	183.5
46	20090424	20090527	33	4.8	-1091.1
47	20090424	20090629	66	128.2	-47.1
48	20090424	20090801	99	113.9	-52.6
49	20090424	20090903	132	108.8	-55.8
50	20090424	20091006	165	169.8	-35.7
51	20090424	20091017	176	45.9	-128.3
52	20090424	20091028	187	197.1	-30.6
53	20090424	20091108	198	121.4	-49.6
54	20090424	20091211	231	10.9	-432.7
55	20090527	20090629	33	123.4	-48.9
56	20090527	20090801	66	109.1	-54.9
57	20090527	20090903	99	104	-58.4
58	20090527	20091006	132	165	-36.7
59	20090527	20091017	143	41.1	-143.5
60	20090527	20091028	154	192.3	-31.4
61	20090527	20091108	165	116.6	-51.7
62	20090527	20091211	198	6.1	-772
63	20090527	20100113	231	152.7	-39.1
64	20090629	20090801	33	-14.3	344.5
65	20090629	20090903	66	-19.4	299.6
66	20090629	20091006	99	41.6	-147.1
67	20090629	20091017	110	-82.3	72.9
68	20090629	20091028	121	68.9	-87.9
69	20090629	20091108	132	-6.8	610.2
70	20090629	20091211	165	-117.3	51.4
71	20090629	20100113	198	29.3	-193.8
72	20090629	20100215	231	40.3	-151
73	20090801	20090903	33	-5.1	655.2
74	20090801	20091006	66	55.9	-107.5
75	20090801	20091017	77	-68	87.9
76	20090801	20091028	88	83.2	-72.9
77	20090801	20091108	99	7.5	-570.9
78	20090801	20091211	132	-103	58.4
79	20090801	20100113	165	43.6	-124.5
80	20090801	20100215	198	54.6	-110
81	20090903	20091006	33	61	-99
82	20090903	20091017	44	-62.9	96.7
83	20090903	20091028	55	88.3	-68.1
84	20090903	20091108	66	12.6	-463.7
85	20090903	20091211	99	-97.9	62
86	20090903	20100113	132	48.7	-116.6

APPENDIX

87	20090903	20100215	165	59.7	-100.9
88	20090903	20100320	198	190.3	-31.7
89	20090903	20100422	231	158.3	-38.2
90	20090903	20100525	264	-107.8	55.8
91	20091006	20091017	11	-123.9	48.9
92	20091006	20091028	22	27.3	-217.1
93	20091006	20091108	33	-48.4	125.6
94	20091006	20091211	66	-158.9	38.1
95	20091006	20100113	99	-12.3	411.1
96	20091006	20100215	132	-1.3	4170.7
97	20091006	20100320	165	129.3	-46.7
98	20091006	20100422	198	97.3	-62.2
99	20091017	20091028	11	151.2	-40
100	20091017	20091108	22	75.5	-79.9
101	20091017	20091211	55	-35	172.4
102	20091017	20100113	88	111.6	-52.8
103	20091017	20100215	121	122.6	-49.3
104	20091017	20100525	220	-44.9	129.6
105	20091017	20100627	253	-30	174.8
106	20091017	20100730	286	33.8	-178.2
107	20091028	20091108	11	-75.7	79.7
108	20091028	20091211	44	-186.2	32.5
109	20091028	20100113	77	-39.6	150.8
110	20091028	20100215	110	-28.6	203.8
111	20091028	20100320	143	102	-59.3
112	20091028	20100422	176	70	-86.5
113	20091028	20100901	308	-11.3	483.6
114	20091108	20091211	33	-110.5	54.7
115	20091108	20100113	66	36.1	-148.7
116	20091108	20100215	99	47.1	-127.7
117	20091108	20100320	132	177.7	-34.1
118	20091108	20100422	165	145.7	-41.6
119	20091108	20100525	198	-120.4	49.9
120	20091108	20100627	231	-105.5	56.6
121	20091108	20100730	264	-41.7	143
122	20091108	20100901	297	64.4	-95.3
123	20091211	20100113	33	146.6	-40.5
124	20091211	20100215	66	157.6	-38.4
125	20091211	20100525	165	-9.9	348.9
126	20091211	20100627	198	5	-428.9
127	20091211	20100730	231	68.8	-88.2
128	20100113	20100215	33	11	-534.9
129	20100113	20100320	66	141.6	-43.3
130	20100113	20100422	99	109.6	-56.6
131	20100113	20100525	132	-156.5	38.1
132	20100113	20100627	165	-141.6	42.1

APPENDIX

133	20100113	20100730	198	-77.8	75.3
134	20100113	20100901	231	28.3	-230.2
135	20100215	20100320	33	130.6	-46.3
136	20100215	20100422	66	98.6	-61.5
137	20100215	20100525	99	-167.5	36
138	20100215	20100627	132	-152.6	39.5
139	20100215	20100730	165	-88.8	68
140	20100215	20100901	198	17.3	-365.8
141	20100215	20101026	253	82.1	-73.7
142	20100320	20100422	33	-32	181.6
143	20100320	20100730	132	-219.4	27.5
144	20100320	20100901	165	-113.3	53
145	20100320	20101026	220	-48.5	121.2
146	20100422	20100525	33	-266.1	22.8
147	20100422	20100627	66	-251.2	24.1
148	20100422	20100730	99	-187.4	32.3
149	20100422	20100901	132	-81.3	73.7
150	20100422	20101026	187	-16.5	340
151	20100525	20100627	33	14.9	-368.2
152	20100525	20100730	66	78.7	-76.3
153	20100525	20100901	99	184.8	-32.8
154	20100525	20101026	154	249.6	-24.3
155	20100525	20101106	165	-246.1	24.2
156	20100525	20111024	517	-6.7	210.8
157	20100627	20100730	33	63.8	-94.8
158	20100627	20100901	66	169.9	-35.8
159	20100627	20101026	121	234.7	-25.9
160	20100627	20101106	132	-261	22.7
161	20100627	20111024	484	-21.6	174.2
162	20100730	20100901	33	106.1	-57.4
163	20100730	20101026	88	170.9	-35.4
164	20100730	20101106	99	-324.8	18.4
165	20100730	20111024	451	-85.4	70
166	20100730	20120304	583	13.3	-436
167	20100901	20101026	55	64.8	-91.2
168	20100901	20101106	66	-430.9	14
169	20100901	20111024	418	-191.5	31.7
170	20100901	20120304	550	-92.8	66
171	20101026	20111024	363	-256.3	23.5
172	20101026	20120304	495	-157.6	38.5
173	20101106	20111024	352	239.4	-25
174	20101106	20120304	484	338.1	-17.7
175	20101106	20120417	528	-142.1	42.5
176	20101106	20120622	594	498	-12.1
177	20111024	20120304	132	98.7	-60
178	20111024	20120417	176	-381.5	15.7

APPENDIX

179	20111024	20120622	242	258.6	-23.3
180	20120304	20120417	44	-480.2	12.5
181	20120304	20120622	110	159.9	-37.8
182	20120304	20131110	616	41.3	-143.1
183	20120304	20140115	682	-4.2	296.3
184	20120622	20131110	506	-118.6	51.2
185	20120622	20140115	572	-164.1	37.1
186	20120622	20140206	594	-75.8	79.3
187	20131110	20140115	66	-45.5	129.2
188	20131110	20140206	88	42.8	-144
189	20131110	20140228	110	15.5	-262.6
190	20131110	20141006	330	39.9	-165.1
191	20140115	20140206	22	88.3	-68.7
192	20140115	20140228	44	61	-95.7
193	20140115	20141006	264	85.4	-74.2
194	20140206	20140228	22	-27.3	221.7
195	20140206	20141006	242	-2.9	469.7
196	20140228	20141006	220	24.4	-325.7

Appendix 4. CSK Ascending interferograms

Interferogram number	Master	Slave	B_t (day)	B_{\perp} (m)	Altitude of ambiguity (m)
1	20110215	20110303	16	210	-48.2
2	20110215	20110404	48	53.2	-196.8
3	20110215	20110420	64	-215.8	46.5
4	20110215	20110506	80	-71.6	134.9
5	20110215	20110522	96	-277.5	36.4
6	20110215	20110623	128	-131	73.3
7	20110215	20110709	144	0.3	261
8	20110215	20110810	176	69.1	-150.1
9	20110215	20110911	208	-224.5	44.8
10	20110215	20111013	240	248.9	-39.4
11	20110215	20111029	256	240.5	-40
12	20110215	20111114	272	328.8	-24.3
13	20110215	20120202	352	-55.2	157
14	20110215	20120218	368	114.8	-90.3
15	20110303	20110319	16	491.9	-22.3
16	20110303	20110404	32	-156.8	63
17	20110303	20110420	48	-425.8	23.7
18	20110303	20110506	64	-281.6	35.7
19	20110303	20110522	80	-487.5	20.8
20	20110303	20110623	112	-341	29.3
21	20110303	20110709	128	-209.7	46.3
22	20110303	20110810	160	-140.9	68.7
23	20110303	20110911	192	-434.5	23.3
24	20110303	20110927	208	322.2	-42.2
25	20110303	20111013	224	38.9	-210.5
26	20110303	20111029	240	30.5	-218.5
27	20110303	20111114	256	118.8	-48.7
28	20110303	20120202	336	-265.2	37.5
29	20110303	20120218	352	-95.2	97.4
30	20110319	20110607	80	299.4	-33.8
31	20110319	20110725	128	44.6	-195.2
32	20110319	20110826	160	78.8	-123.3
33	20110319	20110927	192	-169.7	47.3
34	20110319	20111013	208	-453	24.9
35	20110319	20111114	240	-373.1	40.5
36	20110319	20120101	288	143.9	-70.3
37	20110404	20110420	16	-269	38.1
38	20110404	20110506	32	-124.8	82.4
39	20110404	20110522	48	-330.7	31
40	20110404	20110623	80	-184.2	54.8

APPENDIX

41	20110404	20110709	96	-52.9	167.2
42	20110404	20110810	128	15.9	-623.2
43	20110404	20110911	160	-277.7	36.9
44	20110404	20111013	192	195.7	-48.4
45	20110404	20111029	208	187.3	-49.3
46	20110404	20111114	224	275.6	-27.5
47	20110404	20120202	304	-108.4	92.8
48	20110404	20120218	320	61.6	-166.7
49	20110420	20110506	16	144.2	-70.9
50	20110420	20110522	32	-61.7	164.1
51	20110420	20110623	64	84.8	-121.6
52	20110420	20110709	80	216.1	-48
53	20110420	20110810	112	284.9	-36.2
54	20110420	20110911	144	-8.7	1169.5
55	20110420	20111013	176	464.7	-21.4
56	20110420	20111029	192	456.3	-21.5
57	20110420	20120117	272	-211.5	49
58	20110420	20120202	288	160.6	-64.3
59	20110420	20120218	304	330.6	-31.1
60	20110506	20110522	16	-205.9	49.7
61	20110506	20110623	48	-59.4	156.2
62	20110506	20110709	64	71.9	-142.3
63	20110506	20110810	96	140.7	-73.7
64	20110506	20110911	128	-152.9	66.9
65	20110506	20111013	160	320.5	-30.5
66	20110506	20111029	176	312.1	-30.9
67	20110506	20111114	192	400.4	-20.6
68	20110506	20120117	256	-355.7	29
69	20110506	20120202	272	16.4	-559.8
70	20110506	20120218	288	186.4	-55.4
71	20110522	20110623	32	146.5	-70.8
72	20110522	20110709	48	277.8	-37.3
73	20110522	20110810	80	346.6	-29.7
74	20110522	20110911	112	53	-192.1
75	20110522	20120117	240	-149.8	69.4
76	20110522	20120202	256	222.3	-46.4
77	20110522	20120218	272	392.3	-26.2
78	20110607	20110725	48	-254.8	40.2
79	20110607	20110826	80	-220.6	46.4
80	20110607	20110927	112	-469.1	19.7
81	20110607	20120101	208	-155.5	63.7
82	20110623	20110709	16	131.3	-78.9
83	20110623	20110810	48	200.1	-51
84	20110623	20110911	80	-93.5	112.1
85	20110623	20111013	112	379.9	-25.7
86	20110623	20111029	128	371.5	-26

APPENDIX

87	20110623	20111114	144	459.8	-18.3
88	20110623	20120117	208	-296.3	35.1
89	20110623	20120202	224	75.8	-133.9
90	20110623	20120218	240	245.8	-41.7
91	20110709	20110810	32	68.8	-143.1
92	20110709	20110911	64	-224.8	46.3
93	20110709	20111013	96	248.6	-38.1
94	20110709	20111029	112	240.2	-38.3
95	20110709	20111114	128	328.5	-23.8
96	20110709	20120117	192	-427.6	24.3
97	20110709	20120202	208	-55.5	186.7
98	20110709	20120218	224	114.5	-88.1
99	20110725	20110826	32	34.2	-298.6
100	20110725	20110927	64	-214.3	38.5
101	20110725	20111114	112	-417.7	33.7
102	20110725	20120101	160	99.3	-101
103	20110810	20110911	32	-293.6	35.1
104	20110810	20110927	48	463.1	-26.2
105	20110810	20111013	64	179.8	-51.7
106	20110810	20111029	80	171.4	-52.6
107	20110810	20111114	96	259.7	-28.5
108	20110810	20120202	176	-124.3	82.4
109	20110810	20120218	192	45.7	-223.5
110	20110826	20110927	32	-248.5	34.2
111	20110826	20111114	80	-451.9	30.5
112	20110826	20120101	128	65.1	-151.6
113	20110911	20111013	32	473.4	-21
114	20110911	20111029	48	465	-21.1
115	20110911	20120117	128	-202.8	51
116	20110911	20120202	144	169.3	-61.2
117	20110911	20120218	160	339.3	-30.4
118	20110927	20111013	16	-283.3	52.6
119	20110927	20111029	32	-291.7	51.4
120	20110927	20111114	48	-203.4	232.9
121	20110927	20120101	96	313.6	-28.5
122	20110927	20120218	144	-417.4	29.6
123	20111013	20111029	16	-8.4	1100.6
124	20111013	20111114	32	79.9	-63.9
125	20111013	20120202	112	-304.1	31.9
126	20111013	20120218	128	-134.1	66.6
127	20111029	20111114	16	88.3	-62.4
128	20111029	20120202	96	-295.7	32.1
129	20111029	20120218	112	-125.7	66.9
130	20111029	20130604	584	202.7	-51.1
131	20111114	20120202	80	-384	21.2
132	20111114	20120218	96	-214	32.5

APPENDIX

133	20111114	20130604	568	114.4	-90.3
134	20111130	20120117	48	384.2	-27.1
135	20120101	20130604	520	-402.6	25.7
136	20120101	20130624	540	84.6	-74.8
137	20120101	20130714	560	-206.8	46.1
138	20120101	20130807	584	213.7	-41.9
139	20120117	20120202	16	372.1	-27.8
140	20120202	20120218	16	170	-60.4
141	20120202	20130604	488	498.4	-20.8
142	20120218	20130604	472	328.4	-31.6
143	20120218	20130714	512	524.2	-19.9
144	20120218	20130924	584	150	-60.5
145	20130604	20130624	20	487.2	-21.3
146	20130604	20130714	40	195.8	-53.2
147	20130604	20130831	88	318.7	-32.5
148	20130604	20130924	112	-178.4	58.4
149	20130604	20131018	136	-86.1	119.7
150	20130604	20131111	160	286.6	-36.2
151	20130604	20131229	208	149.2	-69.2
152	20130604	20140404	304	380.1	-27.1
153	20130604	20140428	328	347.6	-29.9
154	20130604	20140826	448	-132.7	76.8
155	20130604	20140919	472	107.9	-97.1
156	20130624	20130714	20	-291.4	35.5
157	20130624	20130807	44	129.1	-81.2
158	20130624	20130831	68	-168.5	60.8
159	20130624	20131111	140	-200.6	51.7
160	20130624	20131229	188	-338	30.7
161	20130624	20140215	236	-28.1	348.4
162	20130624	20140311	260	265.1	-38.9
163	20130624	20140404	284	-107.1	84.2
164	20130624	20140428	308	-139.6	66.5
165	20130624	20140709	380	-113	78.6
166	20130624	20140802	404	-124.4	64.7
167	20130714	20130807	24	420.5	-24.7
168	20130714	20130831	48	122.9	-83
169	20130714	20130924	72	-374.2	28
170	20130714	20131018	96	-281.9	36.9
171	20130714	20131111	120	90.8	-111.3
172	20130714	20131229	168	-46.6	214.4
173	20130714	20140215	216	263.3	-39.3
174	20130714	20140404	264	184.3	-54.9
175	20130714	20140428	288	151.8	-66.9
176	20130714	20140709	360	178.4	-56.8
177	20130714	20140802	384	167	-59.3
178	20130714	20140919	432	-87.9	66.9

APPENDIX

179	20130807	20130831	24	-297.6	34.9
180	20130807	20131111	96	-329.7	31.6
181	20130807	20131229	144	-467.1	22.3
182	20130807	20140215	192	-157.2	66.3
183	20130807	20140311	216	136	-74.2
184	20130807	20140404	240	-236.2	42.5
185	20130807	20140428	264	-268.7	37.1
186	20130807	20140709	336	-242.1	41.1
187	20130807	20140802	360	-253.5	37.5
188	20130831	20130924	24	-497.1	21
189	20130831	20131018	48	-404.8	25.6
190	20130831	20131111	72	-32.1	229.9
191	20130831	20131229	120	-169.5	60.5
192	20130831	20140215	168	140.4	-73.8
193	20130831	20140311	192	433.6	-23.9
194	20130831	20140404	216	61.4	-150.6
195	20130831	20140428	240	28.9	-237.5
196	20130831	20140709	312	55.5	-164
197	20130831	20140802	336	44.1	-139.4
198	20130831	20140919	384	-210.8	39
199	20130924	20131018	24	92.3	-114.6
200	20130924	20131111	48	465	-22.4
201	20130924	20131205	72	-411.1	25
202	20130924	20131229	96	327.6	-31.8
203	20130924	20140122	120	-380	27.1
204	20130924	20140615	264	-275.2	37.3
205	20130924	20140826	336	45.7	-116.4
206	20130924	20140919	360	286.3	-42.1
207	20131018	20131111	24	372.7	-27.8
208	20131018	20131229	72	235.3	-44
209	20131018	20140122	96	-472.3	22
210	20131018	20140404	168	466.2	-22.2
211	20131018	20140428	192	433.7	-24
212	20131018	20140615	240	-367.5	28.1
213	20131018	20140826	312	-46.6	128.6
214	20131018	20140919	336	194	-60
215	20131111	20131229	48	-137.4	75.5
216	20131111	20140215	96	172.5	-59.8
217	20131111	20140311	120	465.7	-22.2
218	20131111	20140404	144	93.5	-91.7
219	20131111	20140428	168	61	-117.6
220	20131111	20140709	240	87.6	-96
221	20131111	20140802	264	76.2	-87.9
222	20131111	20140826	288	-419.3	25.7
223	20131111	20140919	312	-178.7	42.1
224	20131205	20140122	48	31.1	-174

APPENDIX

225	20131205	20140615	192	135.9	-64.8
226	20131229	20140215	48	309.9	-33.5
227	20131229	20140404	96	230.9	-43.5
228	20131229	20140428	120	198.4	-50.6
229	20131229	20140709	192	225	-44.9
230	20131229	20140802	216	213.6	-46.5
231	20131229	20140826	240	-281.9	38.2
232	20131229	20140919	264	-41.3	80
233	20140122	20140615	144	104.8	-93
234	20140122	20140826	216	425.7	-22.8
235	20140215	20140311	24	293.2	-35.3
236	20140215	20140404	48	-79	110.5
237	20140215	20140428	72	-111.5	82.1
238	20140215	20140709	144	-84.9	98.5
239	20140215	20140802	168	-96.3	79.6
240	20140215	20140919	216	-351.2	25.6
241	20140311	20140404	24	-372.2	27.5
242	20140311	20140428	48	-404.7	25.1
243	20140311	20140709	120	-378.1	26.9
244	20140311	20140802	144	-389.5	25.6
245	20140404	20140428	24	-32.5	291.4
246	20140404	20140709	96	-5.9	895.7
247	20140404	20140802	120	-17.3	273.9
248	20140428	20140709	72	26.6	-376.9
249	20140428	20140802	96	15.2	-358.1
250	20140428	20140826	120	-480.3	23.1
251	20140428	20140919	144	-239.7	36.8
252	20140615	20140826	72	320.9	-30.1
253	20140709	20140802	24	-11.4	339.6
254	20140709	20140919	72	-266.3	33.6
255	20140802	20140826	24	-495.5	22.6
256	20140802	20140919	48	-254.9	35.7
257	20140826	20140919	24	240.6	-61.7

Appendix 5. CSK descending interferograms

Interferogram number	Master	Slave	B_t (day)	B_{\perp} (m)	Altitude of ambiguity (m)
1	20110215	20110303	16	-71.1	153.6
2	20110215	20110404	48	65.2	-179
3	20110215	20110506	80	150.2	-64.2
4	20110215	20110623	128	436.2	-30.5
5	20110215	20110709	144	322.8	-52.3
6	20110215	20110725	160	-329.3	34.6
7	20110215	20110810	176	160.5	-60.2
8	20110215	20110826	192	-377.8	30.3
9	20110215	20110927	224	-223.5	50.6
10	20110215	20111013	240	-43.9	232.6
11	20110215	20111029	256	-79.3	140.9
12	20110215	20111114	272	-312.8	37.2
13	20110215	20120218	368	3.8	553.4
14	20110303	20110404	32	136.3	-82.9
15	20110303	20110506	64	221.3	-45.3
16	20110303	20110709	128	393.9	-39.1
17	20110303	20110725	144	-258.2	44.7
18	20110303	20110810	160	231.6	-43.3
19	20110303	20110826	176	-306.7	37.8
20	20110303	20110927	208	-152.4	75.6
21	20110303	20111013	224	27.2	-424.8
22	20110303	20111029	240	-8.2	1627.5
23	20110303	20111114	256	-241.7	49
24	20110303	20120218	352	74.9	-160.5
25	20110319	20110607	80	-29.8	332.9
26	20110319	20110725	128	265.3	-45.4
27	20110319	20110826	160	216.8	-55.5
28	20110319	20110927	192	371.1	-32.2
29	20110319	20111114	240	281.8	-41.7
30	20110319	20120101	288	-174.7	69.4
31	20110404	20110420	16	448.8	-29.6
32	20110404	20110506	32	85	-99.9
33	20110404	20110623	80	371	-36.7
34	20110404	20110709	96	257.6	-73.8
35	20110404	20110725	112	-394.5	29.1
36	20110404	20110810	128	95.3	-90.7
37	20110404	20110911	160	408.3	-32.8
38	20110404	20110927	176	-288.7	39.6
39	20110404	20111013	192	-109.1	102.8
40	20110404	20111029	208	-144.5	79.1

APPENDIX

41	20110404	20111114	224	-378	30.8
42	20110404	20120202	304	275.7	-66.2
43	20110404	20120218	320	-61.4	167.7
44	20110420	20110506	16	-363.8	42.1
45	20110420	20110522	32	81.4	-137.1
46	20110420	20110623	64	-77.8	152.4
47	20110420	20110709	80	-191.2	49.3
48	20110420	20110810	112	-353.5	43.9
49	20110420	20110911	144	-40.5	301.4
50	20110420	20111130	224	346.3	-34.2
51	20110420	20120117	272	-39.8	250.4
52	20110420	20120202	288	-173.1	53.5
53	20110506	20110522	16	445.2	-32.2
54	20110506	20110623	48	286	-58
55	20110506	20110709	64	172.6	-281.3
56	20110506	20110810	96	10.3	-961.5
57	20110506	20110911	128	323.3	-49
58	20110506	20110927	144	-373.7	28.4
59	20110506	20111013	160	-194.1	50.7
60	20110506	20111029	176	-229.5	44.2
61	20110506	20120117	256	324	-50.3
62	20110506	20120202	272	190.7	-194.9
63	20110506	20120218	288	-146.4	62.8
64	20110522	20110623	32	-159.2	72.7
65	20110522	20110709	48	-272.6	36.4
66	20110522	20110810	80	-434.9	33.3
67	20110522	20110911	112	-121.9	94.6
68	20110522	20111130	192	264.9	-45.3
69	20110522	20120117	240	-121.2	89
70	20110522	20120202	256	-254.5	38.6
71	20110607	20110725	48	295.1	-40.8
72	20110607	20110826	80	246.6	-48.8
73	20110607	20110927	112	400.9	-29.8
74	20110607	20111114	160	311.6	-37.4
75	20110607	20120101	208	-144.9	83.4
76	20110623	20110709	16	-113.4	72.9
77	20110623	20110810	48	-275.7	61.6
78	20110623	20110911	80	37.3	-308.2
79	20110623	20111130	160	424.1	-27.9
80	20110623	20120117	208	38	-311.8
81	20110623	20120202	224	-95.3	81.8
82	20110709	20110810	32	-162.3	396.7
83	20110709	20110911	64	150.7	-59
84	20110709	20111013	96	-366.7	43
85	20110709	20111029	112	-402.1	38.2
86	20110709	20120117	192	151.4	-60.6

APPENDIX

87	20110709	20120202	208	18.1	-446.5
88	20110709	20120218	224	-319	51.5
89	20110725	20110826	32	-48.5	249
90	20110725	20110927	64	105.8	-109.5
91	20110725	20111013	80	285.4	-40.6
92	20110725	20111029	96	250	-45.8
93	20110725	20111114	112	16.5	-258.2
94	20110725	20120218	208	333.1	-35.3
95	20110810	20110911	32	313	-51.4
96	20110810	20110927	48	-384	27.6
97	20110810	20111013	64	-204.4	48.3
98	20110810	20111029	80	-239.8	42.3
99	20110810	20120117	160	313.7	-52.7
100	20110810	20120202	176	180.4	-228.2
101	20110810	20120218	192	-156.7	59.1
102	20110826	20110927	32	154.3	-75.8
103	20110826	20111013	48	333.9	-34.8
104	20110826	20111029	64	298.5	-38.7
105	20110826	20111114	80	65	-145.6
106	20110826	20120101	128	-391.5	30.9
107	20110826	20120218	176	381.6	-30.9
108	20110911	20111130	80	386.8	-30.7
109	20110911	20120117	128	0.7	696.9
110	20110911	20120202	144	-132.6	65.1
111	20110927	20111013	16	179.6	-64.4
112	20110927	20111029	32	144.2	-78.7
113	20110927	20111114	48	-89.3	134.4
114	20110927	20120218	144	227.3	-51.8
115	20111013	20111029	16	-35.4	338.8
116	20111013	20111114	32	-268.9	44
117	20111013	20120202	112	384.8	-40.4
118	20111013	20120218	128	47.7	-261.5
119	20111029	20111114	16	-233.5	50.5
120	20111029	20120202	96	420.2	-36.1
121	20111029	20120218	112	83.1	-147.8
122	20111029	20130604	584	321.9	-37.7
123	20111114	20120101	48	-456.5	26.1
124	20111114	20120218	96	316.6	-37.7
125	20111114	20130604	568	555.4	-21.8
126	20111114	20130624	588	-145.6	63.5
127	20111130	20120117	48	-386.1	30.3
128	20120101	20130624	540	310.9	-38
129	20120101	20130807	584	345.5	-34.4
130	20120117	20120202	16	-133.3	67.6
131	20120117	20120218	32	-470.4	27.9
132	20120117	20130604	504	-231.6	52.6

APPENDIX

133	20120117	20130714	544	-414.7	29.8
134	20120117	20130831	592	-561.4	21.8
135	20120202	20120218	16	-337.1	47.6
136	20120202	20130604	488	-98.3	122.4
137	20120202	20130714	528	-281.4	51.5
138	20120202	20130831	576	-428.1	31.7
139	20120218	20130604	472	238.8	-50.6
140	20120218	20130624	492	-462.2	24.9
141	20120218	20130714	512	55.7	-117.8
142	20120218	20130807	536	-427.6	26.9
143	20120218	20130831	560	-91	77
144	20120218	20130924	584	339.7	-35.5
145	20130604	20130714	40	-183.1	65.9
146	20130604	20130831	88	-329.8	36.7
147	20130604	20130924	112	100.9	-121.3
148	20130604	20131018	136	13.9	-709.2
149	20130604	20131111	160	-267.1	45.4
150	20130604	20131205	184	393.2	-30.7
151	20130604	20131229	208	-171.5	70.6
152	20130604	20140404	304	-310	39.1
153	20130604	20140428	328	-63.8	196.9
154	20130604	20140709	400	-85.2	145.9
155	20130604	20140802	424	-101.8	120.7
156	20130624	20130807	44	34.6	-345.3
157	20130624	20130831	68	371.2	-32.2
158	20130624	20131111	140	433.9	-27.7
159	20130624	20140215	236	119.7	-99.8
160	20130624	20140311	260	289.9	-39.5
161	20130714	20130831	48	-146.7	82.1
162	20130714	20130924	72	284	-43.3
163	20130714	20131018	96	197	-62.6
164	20130714	20131111	120	-84	145.4
165	20130714	20131229	168	11.6	-837.2
166	20130714	20140215	216	-398.2	30.3
167	20130714	20140311	240	-228	53
168	20130714	20140404	264	-126.9	87.8
169	20130714	20140428	288	119.3	-72.6
170	20130714	20140709	360	97.9	-81.1
171	20130714	20140802	384	81.3	-70.8
172	20130807	20130831	24	336.6	-35.5
173	20130807	20131111	96	399.3	-30.1
174	20130807	20140215	192	85.1	-139.9
175	20130807	20140311	216	255.3	-44.6
176	20130807	20140404	240	356.4	-31.9
177	20130831	20130924	24	430.7	-28.6
178	20130831	20131018	48	343.7	-35.5

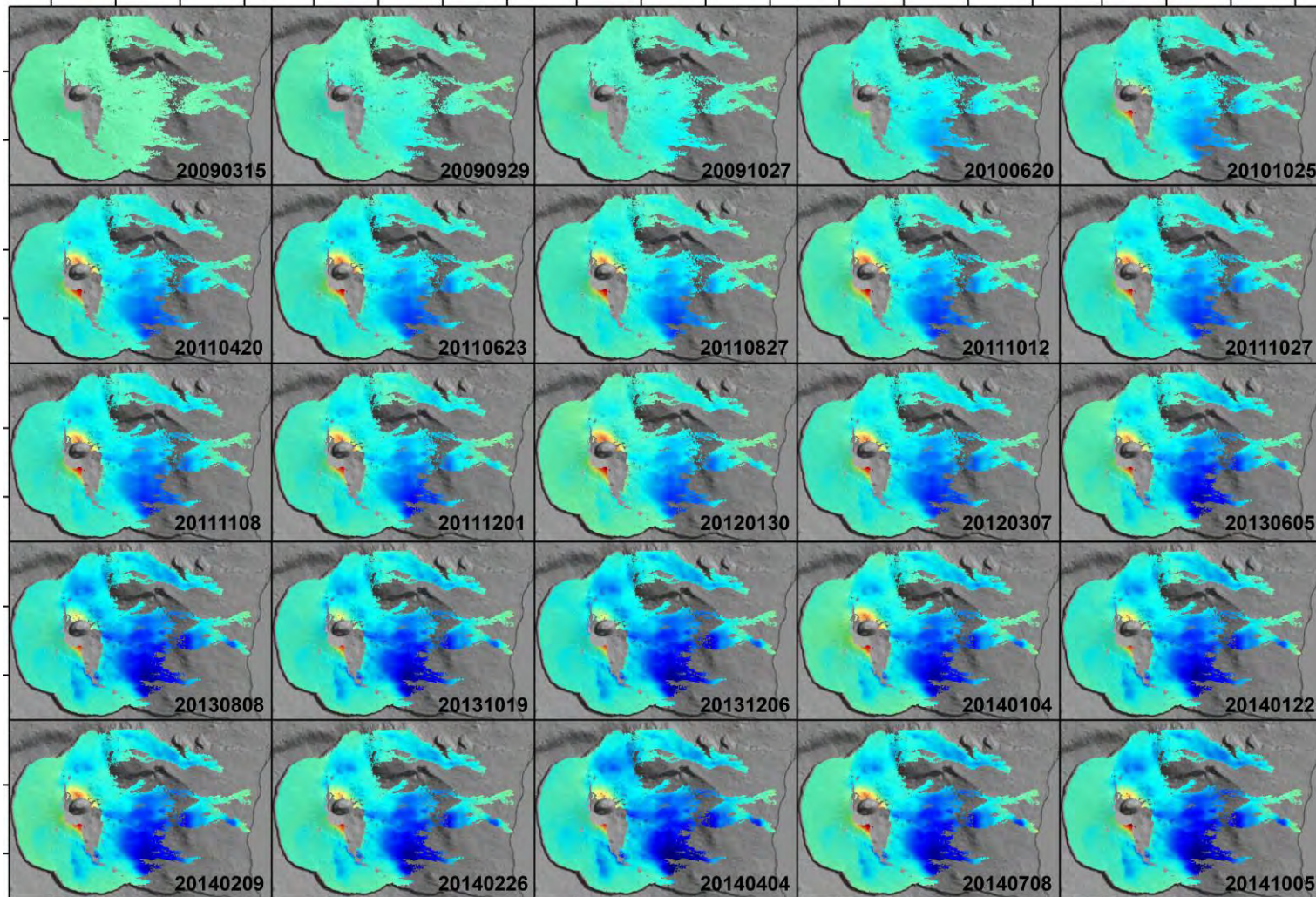
APPENDIX

179	20130831	20131111	72	62.7	-177.4
180	20130831	20131229	120	158.3	-74.7
181	20130831	20140215	168	-251.5	47.5
182	20130831	20140311	192	-81.3	145.6
183	20130831	20140404	216	19.8	-199.7
184	20130831	20140428	240	266	-39.7
185	20130831	20140709	312	244.6	-42.7
186	20130831	20140802	336	228	-40.7
187	20130924	20131018	24	-87	124.2
188	20130924	20131111	48	-368	33.4
189	20130924	20131205	72	292.3	-40
190	20130924	20131229	96	-272.4	45.1
191	20130924	20140122	120	349.6	-34
192	20130924	20140404	192	-410.9	30.5
193	20130924	20140428	216	-164.7	99.4
194	20130924	20140709	288	-186.1	82.7
195	20130924	20140802	312	-202.7	83.4
196	20130924	20140919	360	226.1	-53.4
197	20131018	20131111	24	-281	43.9
198	20131018	20131205	48	379.3	-31.4
199	20131018	20131229	72	-185.4	67
200	20131018	20140122	96	436.6	-27.4
201	20131018	20140311	144	-425	28.8
202	20131018	20140404	168	-323.9	37.5
203	20131018	20140428	192	-77.7	154.3
204	20131018	20140709	264	-99.1	121
205	20131018	20140802	288	-115.7	103.3
206	20131018	20140919	336	313.1	-37.6
207	20131111	20131229	48	95.6	-126.1
208	20131111	20140215	96	-314.2	38.4
209	20131111	20140311	120	-144	80
210	20131111	20140404	144	-42.9	138.7
211	20131111	20140428	168	203.3	-49
212	20131111	20140709	240	181.9	-52.9
213	20131111	20140802	264	165.3	-49.3
214	20131205	20140122	48	57.3	-210
215	20131205	20140615	192	228.1	-52.3
216	20131205	20140826	264	57.1	-138.6
217	20131205	20140919	288	-66.2	96.8
218	20131229	20140215	48	-409.8	29.5
219	20131229	20140311	72	-239.6	49.8
220	20131229	20140404	96	-138.5	78.7
221	20131229	20140428	120	107.7	-77.3
222	20131229	20140709	192	86.3	-84.6
223	20131229	20140802	216	69.7	-74.3
224	20140122	20140615	144	170.8	-70

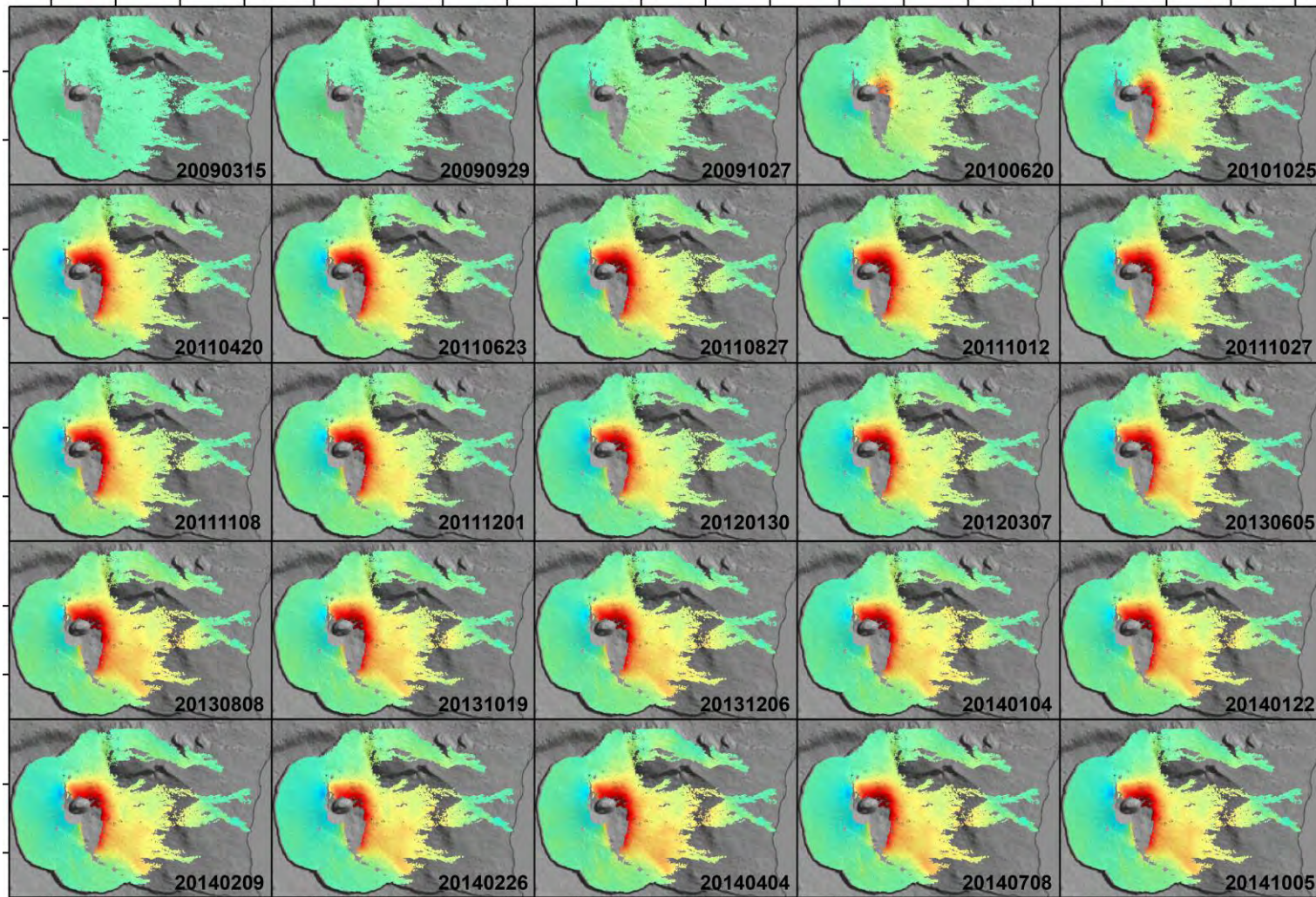
APPENDIX

225	20140122	20140826	216	-0.2	213.5
226	20140122	20140919	240	-123.5	77.8
227	20140215	20140311	24	170.2	-65.2
228	20140215	20140404	48	271.3	-41.3
229	20140311	20140404	24	101.1	-112.6
230	20140311	20140428	48	347.3	-31.8
231	20140311	20140709	120	325.9	-33.9
232	20140311	20140802	144	309.3	-32.8
233	20140404	20140428	24	246.2	-43.9
234	20140404	20140709	96	224.8	-48.1
235	20140404	20140802	120	208.2	-46.2
236	20140428	20140709	72	-21.4	474.8
237	20140428	20140802	96	-38	350.9
238	20140428	20140919	144	390.8	-35.5
239	20140615	20140826	72	-171	68.8
240	20140615	20140919	96	-294.3	39.4
241	20140709	20140802	24	-16.6	-525.6
242	20140709	20140919	72	412.2	-33.4
243	20140802	20140919	48	428.8	-34.4
244	20140826	20140919	24	-123.3	91.9

Appendix 6. Subset of vertical (U-D) component of ground displacement for TSX/TDX – CSK merged InSAR time series



Appendix 7. Subset of horizontal (E-W) component of ground displacement for TSX/TDX – CSK merged InSAR time series



Appendix 8. Examples for effectiveness test of GAMs (Cases 3 - 5)

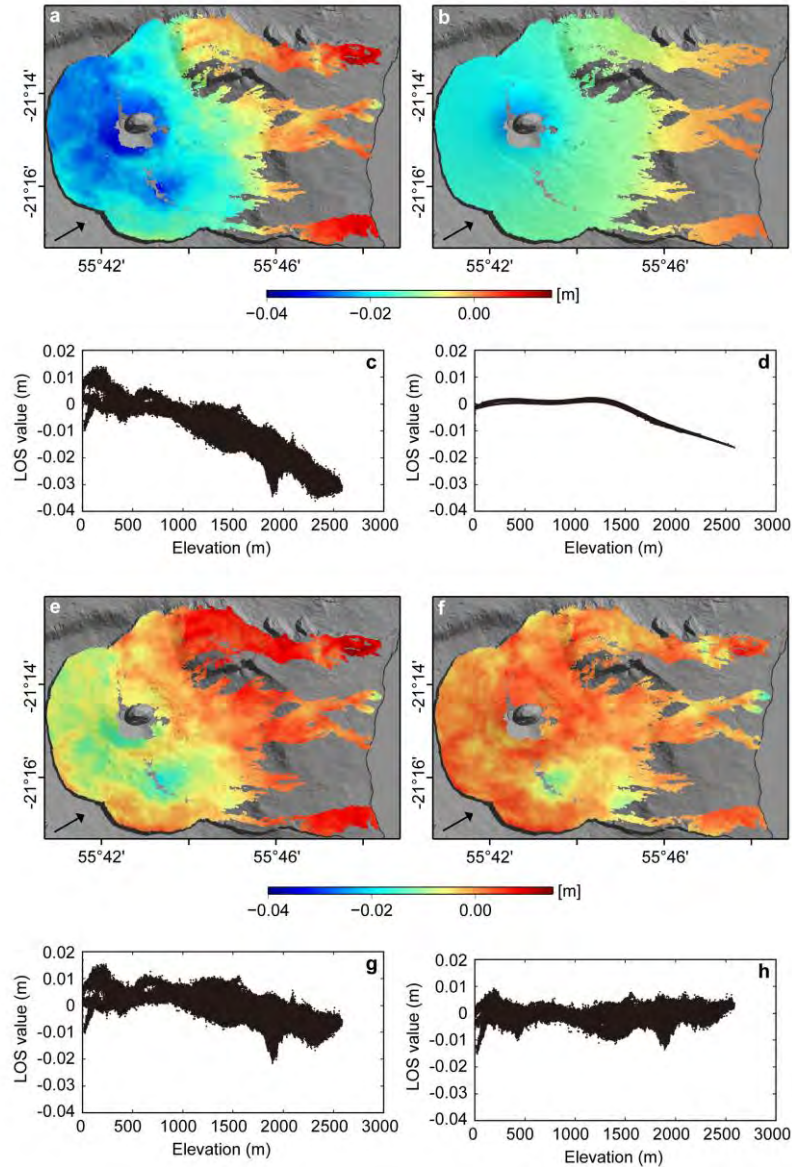


Figure Case 3 (a) An interferogram over Piton de la Fournaise from TSX/TDX SAR acquisitions on 7 June 2012 and 29 June 2012. (b) Stratified tropospheric delay predicted using ERA-Interim. (c) and (d) are the corresponding phase/elevation plots to (a) and (b). (e) Residuals after correction with the ERA-Interim prediction. (f) Residuals after correction with proposed method. (g) and (h) are the corresponding phase/elevation plots to (e) and (f). Maps are draped on a shaded DEM and projected in Geographic Lat/Lon referenced to WGS-84 Datum. Black arrows indicate the LOS directions.

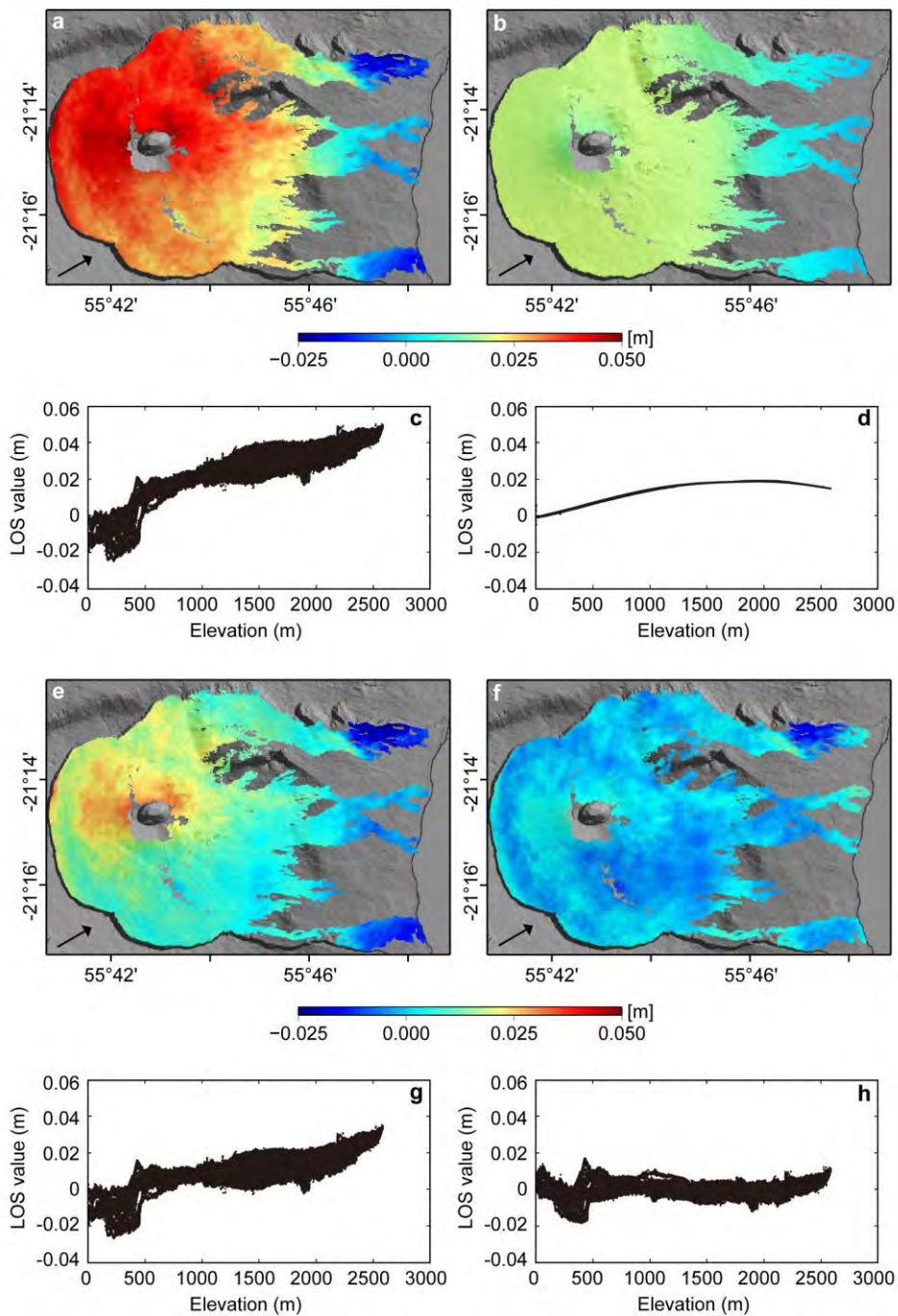


Figure Case 4 An interferogram over Piton de la Fournaise from TSX/TDX SAR acquisitions on 3 September 2012 and 25 September 2012. (b) Stratified tropospheric delay predicted using ERA-Interim. (c) and (d) are the corresponding phase/elevation plots to (a) and (b). (e) Residuals after correction with the ERA-Interim prediction. (f) Residuals after correction with proposed method. (g) and (h) are the corresponding phase/elevation plots to (e) and (f). Maps are draped on a shaded DEM and projected in Geographic Lat/Lon referenced to WGS-84 Datum. Black arrows indicate the LOS directions.

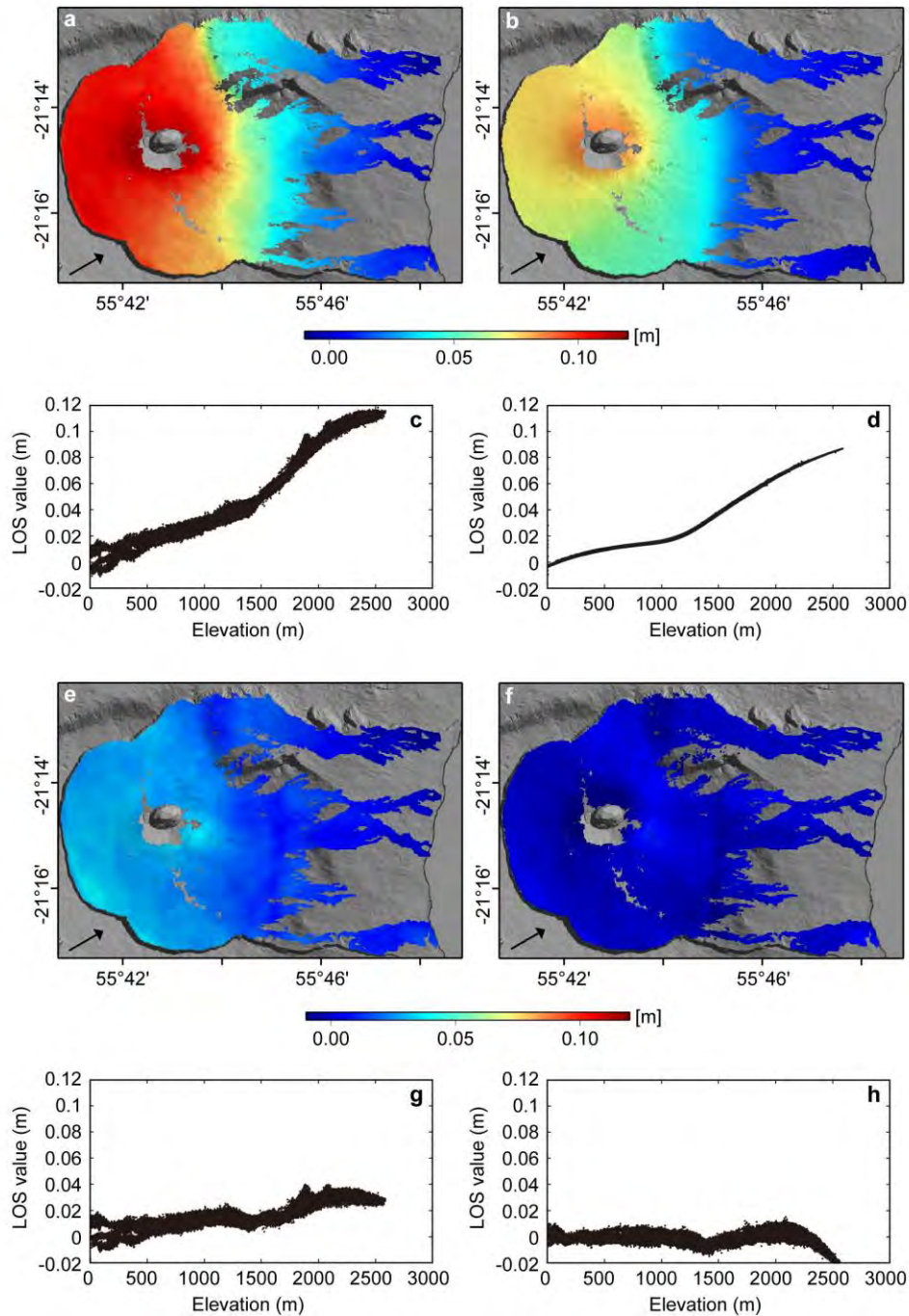
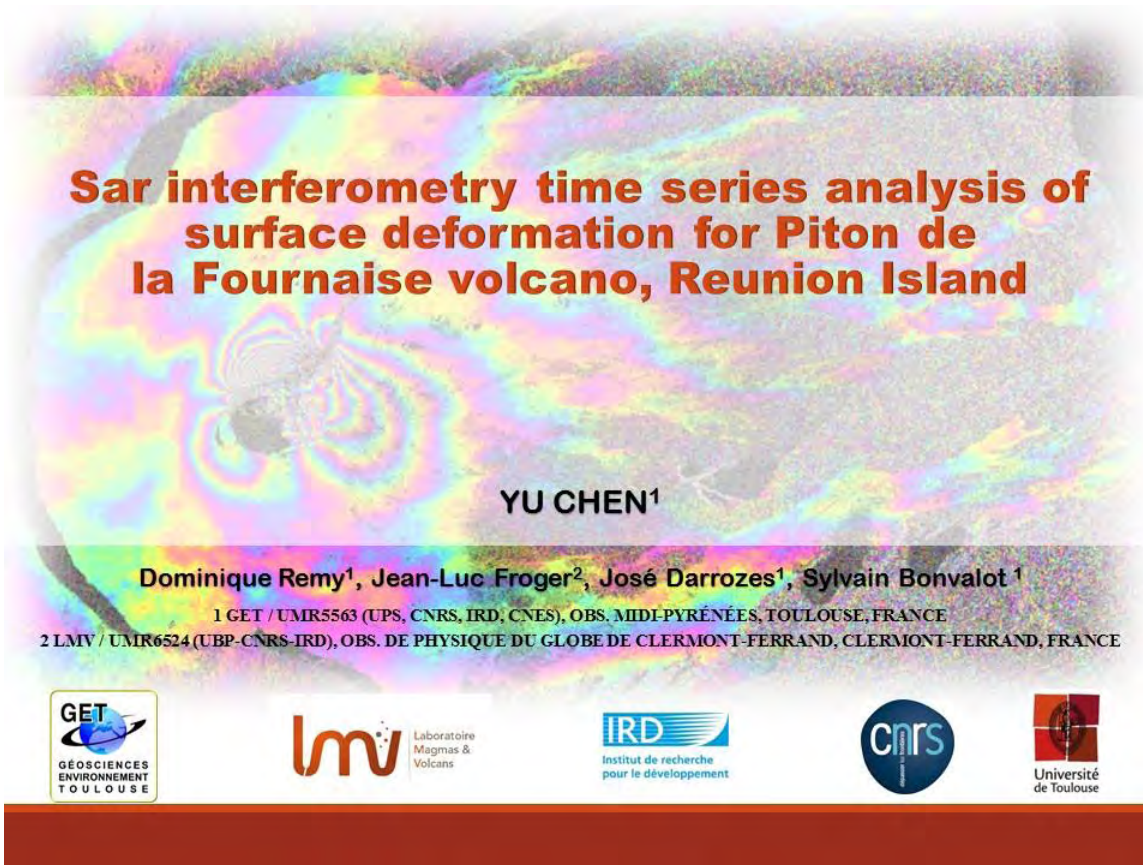


Figure Case 5 (a) An interferogram over Piton de la Fournaise from TSX/TDX SAR acquisitions on 31 October 2011 and 22 November 2011. (b) Stratified tropospheric delay predicted using ERA-Interim. (c) and (d) are the corresponding phase/elevation plots to (a) and (b). (e) Residuals after correction with the ERA-Interim prediction. (f) Residuals after correction with proposed method. (g) and (h) are the corresponding phase/elevation plots to (e) and (f). Maps are draped on a shaded DEM and projected in Geographic Lat/Lon referenced to WGS-84 Datum. Black arrows indicate the LOS directions.

**Appendix 9. Oral presentation and abstract in EGU 2015,
Vienna, Austria**








**Sar interferometry time series analysis of
surface deformation for Piton de
la Fournaise volcano, Reunion Island**

YU CHEN¹

Dominique Remy¹, Jean-Luc Froger², José Darrozes¹, Sylvain Bonvalot¹

1 GET / UMR5563 (UPS, CNRS, IRD, CNES), OBS. MIDI-PYRÉNÉES, TOULOUSE, FRANCE
2 LMV / UMR6524 (UBP-CNRS-IRD), OBS. DE PHYSIQUE DU GLOBE DE CLERMONT-FERRAND, CLERMONT-FERRAND, FRANCE




Sar interferometry time series analysis of surface deformation for Piton de la Fournaise volcano, Reunion Island

Yu Chen (1), Dominique Remy (1), Jean-Luc Froger (2), José Darrozes (1), and Sylvain Bonvalot (1)

(1) GET / UMR5563 (UPS, CNRS, IRD, CNES), Obs. Midi-Pyrénées, Toulouse, France., (2) LMV / UMR6524 (UBP-CNRS-IRD), Obs. de Physique du Globe de Clermont-Ferrand, Clermont-Ferrand, France

Piton de la Fournaise, located on the south-eastern side of Réunion Island in the Indian Ocean, is a hotspot oceanic basaltic shield volcano whose activity began more than 500,000 years ago. It is one of the most active volcanoes in the world with a high eruptive frequency on average one eruption every 9 months since 1998. In April 2007, Piton de la Fournaise experienced an exceptional eruption which is considered as the largest historical eruption ever observed during the 20th and 21st centuries, characterized by an effusion of 210×10^6 m³ volume of lava with a 340 m consequent collapse of the Dolomieu crater and the onset of a landslide on the eastern flank. ENVISAT and ALOS data analysis showed that the subsidence of central cone and landslide of eastern flank continued deforming after this eruption at least until June 2008, but no clear ground deformation has been detected after this date from Band-C or Band-L radar images. We so perform a detailed spatio-temporal analysis of ground motions on Piton de la Fournaise using X-band InSAR time series acquired from 2009 to 2014. X-Band was chosen because it provides high spatial resolution (up to 1 m), short revisit period (minimum 11 days) and a highest sensibility to ground deformation. Our large dataset of X-band radar images is composed of 106 COSMO-SkyMed and 96 TerraSAR-X Single-Look Complex images acquired in ascending and descending orbits. The interferograms were generated using DORIS. A high resolution reference Digital Elevation Model (DEM) (5m x 5m Lidar DEM) was used to model and remove the topographic contribution from the interferograms. We employed next StaMPS/MTI (Hooper et al., 2012) to generate the displacement time series and we analyzed the time-dependant behavior of surface displacement using a principal component analysis (PCA) decomposition. This analysis clearly reveals that the large eastward motion affecting the eastern flank of Piton de la Fournaise remained active (LOS velocity of about 25 mm.y⁻¹) at least until July 2012. Another important result is that the displacement maps show evidence of time-dependant processes acting at the central cone.

Appendix 9. Poster presentation and conference paper in IGARSS 2015, Milan, Italy





GEOSCIENCES
ENVIRONNEMENT
TOULOUSE


SAR INTERFEROMETRY TIME SERIES ANALYSIS OF GROUND DISPLACEMENT FOR PITON DE LA FOURNAISE VOLCANO, REUNION ISLAND


Yu Chen¹, Dominique Remy², Jean-Luc Froger³, José Darrozes¹, Sylvain Bonvalot²

¹Université Paul Sabatier, Toulouse, France
²Institut de Recherche pour le Développement, Toulouse, France
³Université Blaise Pascal, Clermont-Ferrand, France









1. INTRODUCTION

Piton de la Fournaise (La Réunion, France) is one of the most active volcanoes in the world with 36 eruptions since 1998 [1]. In March-April 2007, it experienced the largest eruption ever observed during the 20th and 21th centuries. A large amplitude of widespread seaward sliding on the Eastern Flank during the co-eruptive period was observed from ASAR (C band) and PALSAR (L band) interferometric Synthetic Aperture Radar (InSAR) measurements. In addition, a time-dependent detachment slip of the Eastern Flank had remained deforming from the end of the eruption to at least July 2008, presenting an exponential decay [2] [3]. In order to investigate the spatio-temporal ground displacement evolution at Piton de la Fournaise in the following years after the 2007 eruption, we performed a detailed time series InSAR analysis using an enhanced Small Baseline Subset (SBAS) approach on X band COSMO-SkyMed data acquired between 2011 and 2014. 2D components of mean velocities were calculated. Clear time-dependent displacement was observed both at the Central Cone and on the Eastern Flank. Our results show the persistence of large-scale downslope displacement of the Eastern Flank triggered by the 2007 eruption.

2. SAR DATASET

Table 1 Summary of the processed COSMO-SkyMed data		
Swath	15	18
Pass	Ascending	Descending
Acquisitions	43	43
Time Intervals	2011/02/15 - 2014/09/19	2011/02/15 - 2014/09/19
Incident Angle	48.8°	52.2°
Wavelength	0.031 m	0.031 m
Ground Resolution	3 m	3 m
Interferograms	257	244

3. INSAR TIME SERIES ANALYSIS

SLC

↓

SBAS

↓

StaMPS

↓

SDFPs

↓

Correction
Orbital
+Spline

↓

Inversion

↓

Time Series

↓

2D calculation

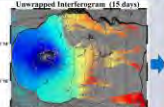
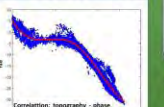
↓

Velocity

Fig. 2. Working flow

(5). Tropospheric Correction

a. Spline Estimation
 b. Correlation: phase & topography
 (6). Uncertainty
 a. 1-sigma: 8 mm
 b. From pixels in stable areas

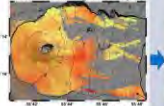
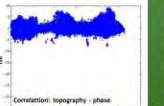
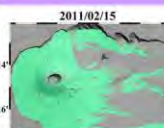
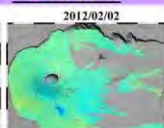



Fig. 3. Tropospheric correction

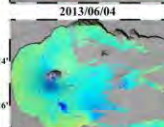
4. RESULTS



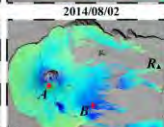
2011/02/15



2012/02/02



2013/06/04



2014/08/02

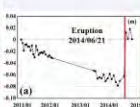
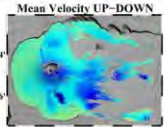
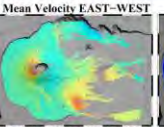


Fig. 5. Temporal behavior measured in (a) point A, and (b) point B in Figure 4

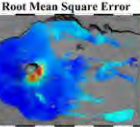
Fig. 4. Subset of time series displacement maps of COSMO-SkyMed ascending orbit (R is the reference point)



Mean Velocity UP-DOWN



Mean Velocity EAST-WEST



Root Mean Square Error

Fig. 6. 2D mean velocities and Root Mean Square Error between observed and modelled data

(1). The Central Cone

a. Point A presents a similar linear subsidence along the LOS direction until June 2014. An eruption in the southeastern part of the Central Cone occurred on June 21, 2014 producing a transient uplift of ~ 80 mm at point A from ascending orbit (Fig. 5a).
 b. The northwestern Central Cone experienced a centripetal subsidence (up to 30 mm/year downward and up to 18 mm/year eastward, Fig. 6)

(2). The Eastern Flank

a. The Eastern Flank displays a large trapezoidal displacement pattern covering ~ 20 km² area with amplitudes from ~ -50 to -100 mm (Fig. 4)
 b. Point B shows a linear temporal behavior with an overall subsidence along the LOS direction of ~ 100 mm over the study period (Fig. 5b).
 c. The displacement are uniformly downward and eastward and the downward displacement (up to 25 mm/year) has a higher rate than that of eastward displacement (up to 15 mm/year), implying a large-scale downslope movement of the Eastern Flank.

(3). RMSE Estimation (Fig. 6)

a. Majority < 8 mm indicating a good explanation by a uniform slip rate.
 b. Significant residuals in the southeastern Central Cone due to the transient displacements.

5. CONCLUSION

This study has presented a time series analysis of ground displacement at Piton de la Fournaise from 2011 to 2014. Results show that the displacement of the Eastern Flank observed is a part of the post-eruptive activities of the 2007 eruption. That is to say the displacement of the Eastern Flank continued deforming since the end of the eruption until present, which gives an important evidence of a large-scale flank destabilization that may represent the major source of potential hazard. X band SAR data has shown its powerful capabilities for accurate InSAR analysis.

Acknowledgements: This study will not be possible without the generosity of the Agence Nationale de la Recherche (ANR) through the framework of GEOSUD, ANR-10-EQPX-20 project, the Italian Space Agency (ASI) through the CSK 2080 project for our CSK images.

References:
 [1] M. Urbi, N. Gueb, and T. Staudacher, "Size and volume evaluation of the caldera collapse on Piton de la Fournaise volcano during the April 2007 eruption Using ASTER stereo imagery," *Geophysical Research Letters*, vol. 34, pp. 12238, 2007.
 [2] J.-L. Froger, V. Famin, V. Cayol, A. Augier, L. Midon, and J.-F. Lénat, "Time-dependent displacements during and after the April 2007 eruption of Piton de la Fournaise, revealed by interferometric data," *Volcanol. Geotherm. Res.*, vol. 236, pp. 55-68, 2013.
 [3] A. Augier, "Etude de l'éruption d'avril 2007 au Piton de la Fournaise (le de la Réunion) à partir de données d'interferométrie RADAR et GPS, Développement et application de procédure de modélisation," Ph.D. Thesis, Université Blaise Pascal, Clermont-Ferrand, France, 2011.
 [4] A. Hooper, H. Zebker, "Phase Unwrapping in three dimensions with application to InSAR time series," *Journal of the Optical Society of America*, vol. 24, no. 9, pp. 2722-2742, 2007.
 [5] A. Pepe, R. Lanari, "On the Extension of the Minimum Cost Flow Algorithm for Phase Unwrapping of Multitemporal Differential SAR Interferograms," *IEEE Transactions on Geoscience and remote sensing*, vol. 44, no. 5, pp. 2374-2383, 2006.

313

SAR INTERFEROMETRY TIME SERIES ANALYSIS OF GROUND DISPLACEMENT FOR PITON DE LA FOURNAISE VOLCANO, REUNION ISLAND

Yu Chen¹, Dominique Remy², Jean-Luc Froger³, José Darrozes¹, Sylvain Bonvalot²

¹Université Paul Sabatier, Toulouse, France

²Institut de Recherche pour le Développement, Toulouse, France

³Université Blaise Pascal, Clermont-Ferrand, France

ABSTRACT

We performed a detailed time series Interferometric Synthetic Aperture Radar (InSAR) analysis using an enhanced Small Baseline Subset (SBAS) approach on COSMO-SkyMed data acquired between 2011 and 2014 over Piton de la Fournaise volcano in the Réunion Island. 2-Dimensional components of mean velocities were calculated from ascending and descending orbits. Clear time-dependent displacement was observed both at the Central Cone and on the Eastern Flank. Our results show the persistence of large-scale downslope displacement of the Eastern Flank triggered by the March-April 2007 eruption.

Index Terms— Piton de la Fournaise, volcano ground displacement, Small Baseline Subset Interferometric Synthetic Aperture Radar (SBAS-InSAR), time series analysis, COSMO-SkyMed

1. INTRODUCTION

Piton de la Fournaise (2632 m a.s.l.), located on the southeastern side of La Réunion Island (21°14'33"S, 55°42'32"E) in the Indian Ocean, is a hotspot oceanic basaltic shield volcano whose activity began more than 500,000 years ago [1]. It is one of the most active volcanoes in the world with 36 eruptions since 1998 [2]. Most historical eruptions of Piton de la Fournaise occurred in a ~ 13 × 10 km EW elongated horseshoe shaped depression opened eastward to the Ocean (Enclos Fouqué-Grand Brûlé structure) [3], in particular at the Central Cone (built up by Bory crater and Dolomieu crater), or along the N25-30 and N120 rift zones (see Fig. 1) [4]. In March-April 2007, Piton de la Fournaise experienced the largest historical eruption ever observed during the 20th and 21th centuries, characterized by an effusion of 210 × 10⁶ m³ volume of lava [5] with a 340 m consequent collapse of the Dolomieu crater [6]. Besides, Froger et al. [3] observed a large amplitude of widespread seaward sliding on the Eastern Flank triggered by magma transfer during the co-eruptive period from ASAR (C band) and PALSAR (L band) Interferometric

Synthetic Aperture Radar (InSAR) measurements. It is quite notable that a time-dependent detachment slip of the Eastern Flank had remained deforming from the end of the eruption to at least July 2008, presenting an exponential decay [3] [7]. Augier [7] observed a subsidence rate of ~ 320 mm/year at the beginning of the exponential decay and a rate of ~ 50 mm/year at the end from a point on the south central Eastern Flank, using ASAR ascending data. Without InSAR, this displacement of the Eastern Flank would have gone unnoticed due to the lack of geodetic and seismic networks at the time of the eruption. Furthermore, the dynamic of the Eastern Flank in the following years remains poorly known, which therefore is the main objective of this study.

In order to perform a rigorous investigation of the ground displacement behaviors of the Eastern Flank over a long time period, we chose an X band COSMO-SkyMed SAR dataset in this study. It is not only because X band provides finer spatial resolution (~ 3 m), about one order of magnitude higher than medium resolution C band and L band data along the ground range direction, leading to an excellent performance on high coherency targets identification and on high accuracy mapping, but also because the short revisit time (16 days in this study) allows a temporally detailed ground displacement analysis [8]. In addition, the shorter wavelength (~ 0.03 m) of X band increases the sensitivity to ground displacement, making it more capable than longer wavelength bands to detect low or very low varying displacement, which is the case of the Eastern Flank whose displacement rate is expected to be even lower than 50 mm/year after July 2008.

Although successful applications of conventional InSAR at Piton de la Fournaise have been carried out by previous studies [3] [7] [9], advanced InSAR such as Persistent Scatterers InSAR (PS-InSAR), Small Baseline Subset InSAR (SBAS-InSAR) and Multi-Temporal InSAR (MT-InSAR) can perform better in dealing with a large amount of dataset. Additionally, advanced InSAR has powerful capacities to prevent temporal and geometrical decorrelations [10] [11] and to mitigate atmospheric artifacts that can be significant in the study area due to the complex tropical and coastal contexts [7]. Therefore, in

order to investigate the spatio-temporal ground displacement evolution at Piton de la Fournaise, we developed an enhanced SBAS-InSAR approach based on the approach of Hopper et al. [12] and performed a detailed time series analysis using available X-band COSMO-SkyMed SAR data from 2011 to 2014.

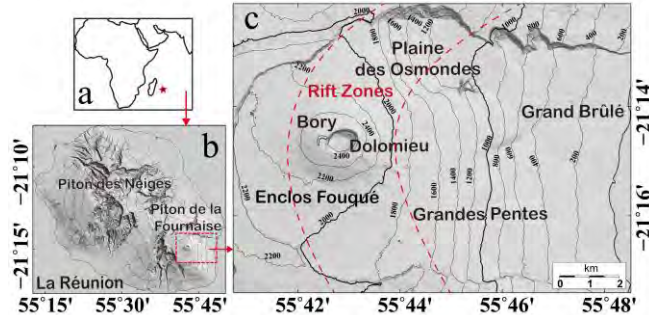


Fig. 1. a) Location of La Réunion Island in the Indian Ocean. b) Location of Piton de la Fournaise. c) Topography of Piton de la Fournaise with 200 m elevation contours. The red dashed lines represent the borders of the Rift Zones where eruptive vents and fissures are preferentially located.

2. SAR DATASET

A total of 86 COSMO-SkyMed Single-Look Complex (SLC) images (in HIMAGE acquisition mode) acquired between 15 February 2011 and 19 September 2014 over Piton de la Fournaise volcano were used in this study (Table 1). 43 of them are from ascending pass (swath 15), and 43 are from descending pass (swath 18). Swath 15 and swath 18 share the same date for each acquisition.

Table 1 Summary of the processed COSMO-SkyMed data

Swath	15	18
Pass	Ascending	Descending
Acquisitions	43	43
Time Intervals	2011/02/15 - 2014/09/19	2011/02/15 - 2014/09/19
Incident Angle	48.8°	52.2°
Wavelength	0.031 m	0.031 m
Ground Resolution	3 m	3 m
Interferograms	257	244

3. INSAR TIME SERIES ANALYSIS

The enhanced SBAS approach used in this study consists of a SBAS method referred to as Stanford Method for Persistent Scatterers (StaMPS) [13], an orbital correction module and a tropospheric correction module.

We firstly applied the StaMPS method on the dataset. In this method, all the interferograms with perpendicular baselines shorter than 600 m and temporal baselines shorter than 600 days for both swath 15 and 18 were generated by DORIS software using a 5×5 m Lidar Digital Elevation Model (DEM) for both coregistration and modelling of the

topographic contributions. Single look was used to form interferograms aiming to retain the highest spatial resolution. A filtering in range prior to the generation of interferograms was applied to further reduce the geometric decorrelation and a filtering in azimuth as well, to discard non-overlapping Doppler frequencies [12]. The good temporal coherence of study area allowed the interferograms spanning close to 2 years to be included into the subsets. On the other hand, interferograms with evident turbulent atmospheric artifacts were discarded under the condition of ensuring the soundness of the interferogram combination. The coherent pixels refer to as slowly-decorrelating filtered phase (SDFP) pixels were selected based on a statistical analysis of amplitude difference dispersion and the phase stability [14]. 3D unwrapping method [14] [15] (the time as the third dimension) was adopted to unwrap the phases of SDFP pixels for the purpose of getting access to more reliable unwrapped results. We finally obtained two subsets of 257 and 244 unwrapped interferograms from ascending and descending orbits, respectively.

Due to the overlapped spatial patterns and comparable amplitudes of orbital and displacement contributions, we modelled and estimated the orbital ramps of each interferogram with a linear function by masking out the expected displacement areas including the Central Cone and the Eastern Flank. The results of correction indicated that this module can effectively reduce ~ 20 % of variances in the interferograms.

Although the tropospheric phase delays can be theoretically maximum mitigated when a large small baseline subset used, important residuals can nevertheless remain especially in areas that have significant topography [11] [16], as is the case of Piton de la Fournaise. In the atmospheric correction module, we applied a spline model to simulate the long wavelength tropospheric phase delays remained on several interferograms based on their correlations with topography [16]. Even though this approach generally well mitigates the stratified tropospheric contributions in the interferograms, in some interferograms, complicated tropospheric moisture patterns still affect the accuracy of InSAR measurements.

Once the orbital and tropospheric contributions were removed from the unwrapped interferograms, the time series displacement maps relative to the first acquisition were inverted by least square method. We assume a 1-sigma uncertainty to be 8 mm for the resulting time series measurements from the analysis of the dispersion of points located in stable areas.

4. RESULTS

4.1. Time series results

Four of the time series displacement maps from COSMO-SkyMed ascending pass at Piton de la Fournaise are given in Fig. 2. Clear time-dependent displacement signals present in

a majority part of volcano edifice. In this paper, we focus mainly on the displacement at the Central Cone and on the Eastern Flank. The Eastern Flank displays a large trapezoidal displacement pattern which coincides with the one observed during the post-eruptive period of March-April eruption [3] [7]. This pattern covers $\sim 20 \text{ km}^2$ area with amplitudes ranging from ~ -50 to -100 mm . The temporal displacement behaviors at two locations (Fig. 2) are shown in Fig. 3. The point *A* located to the south of the Dolomieu crater presents a similar linear subsidence along the line-of-sight (LOS) direction until June 2014 (Fig. 3a). An eruption in the southeastern part of the Central Cone after four years of dormancy occurred on June 21, 2014 producing a transient uplift of $\sim 80 \text{ mm}$ at point *A* from ascending orbit. The displacement at point *B* on the Eastern Flank shows a likely linear temporal behavior with a displacement rate of $\sim 28 \text{ mm/year}$, or an overall subsidence along the LOS direction of $\sim 100 \text{ mm}$ over the whole study period (Fig. 3b), which is about one order of amplitude lower when compared to the exponentially decreasing subsidence of the Eastern Flank between April 2007 and July 2008 (overall subsidence of $\sim 230 \text{ mm}$ within one year) observed by Froger et al. [3] and Augier [7].

4.2. 2-Dimensional (2D) mean velocities

SAR images acquired from ascending and descending orbits provide different perspectives on ground displacement, which allows the investigation of 3D ground displacement and velocity fields. But we only have two different orbits and it is not possible to compute more than 2D components. Considering the fact that for near-polar orbiting satellites and right-looking images, the N-S component is especially more sensitive to the errors of InSAR measurements than the E-W and U-D components [17], we calculated the E-W and U-D components of velocity fields at Piton de la Fournaise from February 2011 to September 2014 under a linear displacement assumption. The northwestern part of the Central Cone experienced a centripetal subsidence (up to 30 mm/year downward and up to 18 mm/year eastward) as shown in the 2D components of mean velocities (Fig. 4a). The displacement of the Eastern Flank are uniformly downward and eastward over the entire trapezoidal zone and the downward displacement (up to 25 mm/year) has a higher rate than that of eastward displacement (up to 15 mm/year), implying a large-scale downslope movement of the Eastern Flank. The low RMSE values (see Fig. 4b) between the observed and modelled data (generally $< 8 \text{ mm}$) indicate that both the horizontal and vertical motions of the Eastern Flank are well explained by a uniform slip rate during the study period. Obviously, significant residuals are observed in the southeastern part of the Central Cone due to the transient displacements that occurred during the June 21, 2014 eruption. Some patterns of strong residuals are also observed on relatively young lava flows indicating that the

displacement could be more linked to the subsidence of the cooling lava flows. An interesting feature is that no displacement is observed in the lower part of the Eastern Flank suggesting that this area acts as a structural barrier that stops the movement observed in the upper part.

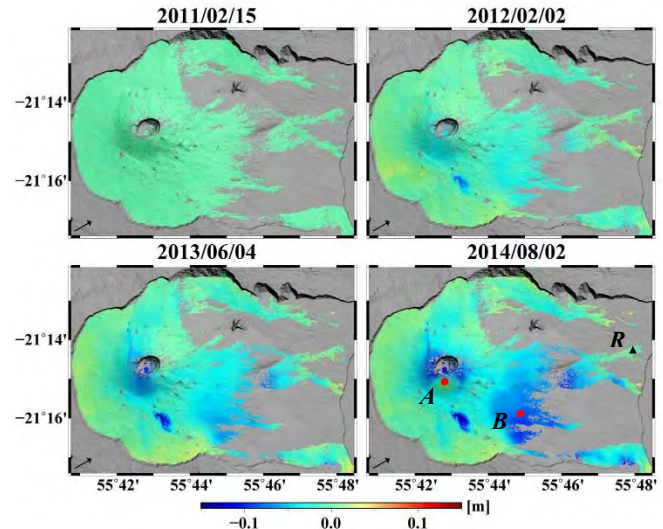


Fig. 2. Subset of time series displacement maps of COSMO-SkyMed ascending orbit at Piton de la Fournaise, referenced temporally to the first image acquired on 2011/02/15, referenced spatially to the point *R* (supposedly stable, similarly hereinafter). The negative values correspond to movements away from the satellite.

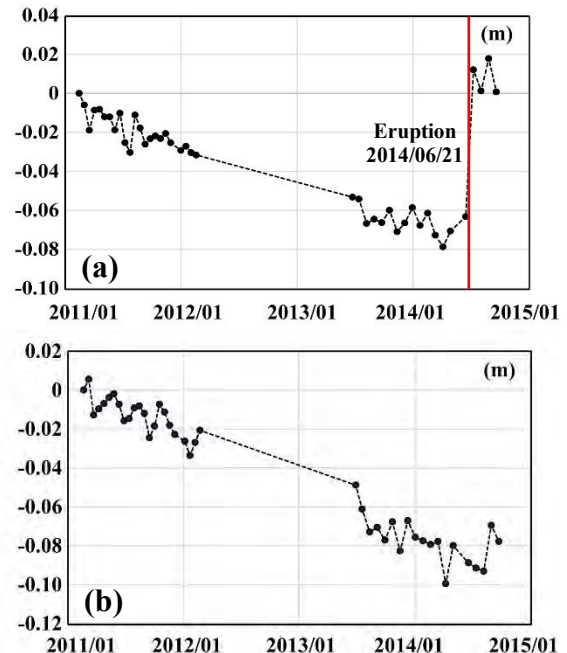


Fig. 3. Time series displacement of COSMO-SkyMed ascending measured in (a) point *A* in Fig. 2 at the Central Cone, and (b) point *B* in Fig. 2 on the Eastern Flank. The eruption on June 21, 2014 is marked with a vertical red line in (a).

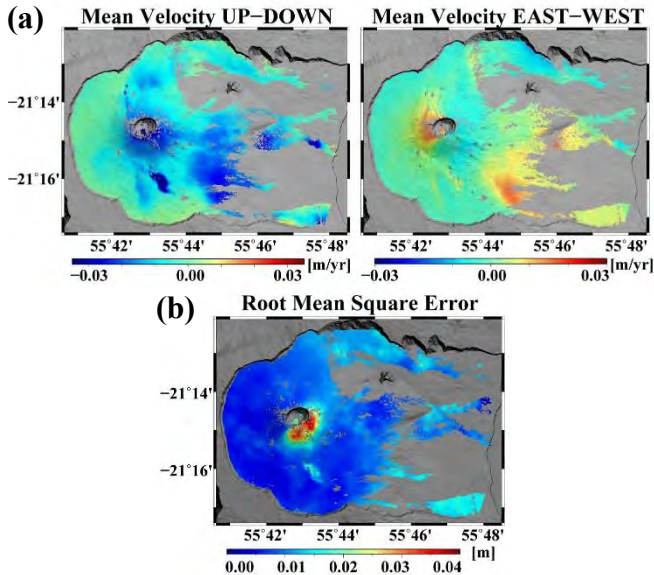


Fig. 4. (a) 2D mean velocities at Piton de la Fournaise during the study period. (b) Root Mean Square Error between the observed and the modelled data.

5. CONCLUSIONS

This paper has presented a time series analysis of ground displacement at Piton de la Fournaise volcano between February 2011 and September 2014 based on COSMO-SkyMed InSAR data. An enhanced SBAS approach has been used and has made a good performance on time series processing. By comparing the spatial pattern and the temporal behavior of displacement with previous studies, we conclude that the displacement of the Eastern Flank observed in this study is a part of the post-eruptive activities of March-April 2007 eruption, which leads us to say that the displacement of the Eastern Flank continued deforming since the end of the historical eruption until present. This displacement gives an important evidence of a large-scale flank destabilization that may represent the major source of potential hazard, emphasizing that continuous monitoring is imminently needed. The spatial continuity, the high resolution and the short revisit time of the InSAR data used in this study made it possible to produce accurate ground displacement maps and to better characterize the temporal displacement behavior of study area, improving our knowledge of the kinematic setting of Piton de la Fournaise.

6. ACKNOWLEDGMENTS

This study will not be possible without the generosity of the Agence Nationale de la Recherche (ANR) through the framework of GEOSUD, ANR-10-EQPX-20 project, the Italian Space Agency (ASI) through the CSK 2080 project for our CSK images.

7. REFERENCES

- [1] P. -Y. Gillot, P. Nativel, "Eruptive history of the Piton de la Fournaise volcano, Réunion island, Indian Ocean," *J. Volcanol. Geotherm. Res.*, vol. 36, pp. 53-65, 1989.
- [2] M. Urai, N. Geshi, and T. Staudacher, "Size and volume evaluation of the caldera collapse on Piton de la Fournaise volcano during the April 2007 eruption Using ASTER stereo imagery," *Geophys. Res. Lett.*, vol. 34, pp. L22318, 2007.
- [3] J. -L. Froger, V. Famin, V. Cayol, A. Augier, L. Michon, and J.-F. Lénat, "Time-dependent displacements during and after the April 2007 eruption of Piton de la Fournaise, revealed by interferometric data," *J. Volcanol. Geotherm. Res.*, vol. 296, pp. 55-68, 2015.
- [4] L. Michon, F. Saint-Ange, P. Bachèlery, N. Villeneuve, and T. Staudacher, "Role of the structural inheritance of the oceanic lithosphere in the magmato-tectonic evolution of Piton de la Fournaise volcano (La Réunion Island)," *J. Geophys. Res.*, vol. 112, pp. B04205, 2007.
- [5] P. Bachèlery, F. Saint-Ange, N. Villeneuve, B. Savoye, A. Normand, E. Le Drezen, A. Barre, J.-P. Quod, and C. Deplus, "Huge lava flow into the sea and caldera collapse, April 2007, Piton de la Fournaise," *IAVCEI Third Workshop on Collapse Calderas*, La Réunion, pp. 73-74, 2010.
- [6] T. Staudacher, V. Ferrazzini, A. Peltier, P. Kowalski, P. Boissier, P. Catherine, F. Lauret, and F. Massin, "The April 2007 eruption and the Dolomieu crater collapse, two major events at Piton de la Fournaise (La Réunion Island, Indian Ocean)," *J. Volcanol. Geotherm. Res.*, vol. 184, pp. 126-137, 2009.
- [7] A. Augier, "Etude de l'éruption d'avril 2007 du Piton de la Fournaise (île de la Réunion) à partir de données d'interférométrie RADAR et GPS, développement et application de procédure de modélisation," *Ph.D. Thesis*, Université Blaise Pascal, Clermont-Ferrand, France, 2011.
- [8] F. Bovenga, J. Wasowski, D. O. Nitti, R. Nutricato, and M. T. Chiaradia, "Using COSMO/SkyMed X-band and ENVISAT C-band SAR interferometry for landslides analysis," *Remote Sensing of Environment*, vol. 119, pp. 272-285, 2012.
- [9] J. -L. Froger, Y. Fukushima, P. Briole, T. Staudacher, T. Souriot, and N. Villeneuve, "The deformation field of the August 2003 eruption at Piton de la Fournaise, Reunion Island, mapped by ASAR interferometry," *Geophys. Res. Lett.*, vol. 31, pp. L14601, 2004.
- [10] A. Peltier, M. Bianchi, E. Kaminski, J. -C. Komorowski, A. Rucci, and T. Staudacher, "PSInSAR as a new tool to monitor pre-eruptive volcano ground deformation: Validation using GPS measurements on Piton de la Fournaise," *Geophys. Res. Lett.*, vol. 37, pp. L12301, 2010.
- [11] A. Ferretti, C. Prati, and F. Rocca, "Permanent scatterers in SAR interferometry," *IEEE Transactions on Geoscience and Remote Sensing*, vol. 39, no. 1, pp. 8-20, 2001.
- [12] A. Hooper, "A multi-temporal InSAR method incorporating both persistent scatterer and small baseline approaches," *Geophys. Res. Lett.*, vol. 35, pp. L16302, 2008.
- [13] A. Hooper, D. Bekaert, K. Spaans, and M. Arkan, "Recent advances in SAR interferometry time series analysis for measuring crustal deformation," *Tectonophysics*, vol. 514-517, pp.1-13, 2012.
- [14] A. Hooper, H. Zebker, "Phase unwrapping in three dimensions with application to InSAR time series," *Journal of the Optical Society of America*, vol. 24, Iss. 9, pp. 2737-2747, 2007.
- [15] A. Pepe, R. Lanari, "On the Extension of the Minimum Cost Flow Algorithm for Phase Unwrapping of Multitemporal Differential SAR Interferograms," *IEEE Transactions on Geoscience and remote sensing*, vol. 44, no. 9, pp. 2374-2383, 2006.
- [16] D. Remy, S. Bonvalot, P. Briole, and M. Murakami, "Accurate measurements of tropospheric effects in volcanic areas from SAR interferometry data: application to Sakurajima volcano (Japan)," *Earth and Planetary Science Letters*, vol. 213, Iss. 3-4, pp. 299-310, 2003.
- [17] T. J. Wright, B. E. Parsons, and Z. Lu, "Toward mapping surface deformation in three dimensions using InSAR," *Geophys. Res. Lett.*, vol. 31, pp. L01607, 2004.